THERMAL SPRAY CLADDING OPTIMIZATION

FOR STEEL DRILL PIPE

by

Wesley L. Ott

A thesis submitted to the Faculty and the Board of Trustees of the Colorado School of Mines in partial fulfillment of the requirements for the degree of Master of Science (Metallurgical and Materials Engineering).

Golden, Colorado

Date _____

Signed: _____
Wesley L. Ott

Signed: _____
Dr. Zhenzhen Yu
Thesis Advisor

Golden, Colorado

Date _____

Signed: _____
Dr. Angus Rockett
Professor and Department Head
George S. Ansell Department of Metallurgical and Materials Engineering

ABSTRACT

Thermal spraying is commonly used to apply a hard and wear resistant coating to the outside of drill pipe. These coatings, however, are susceptible to impact damage and brittle fracture. A fundamental understanding is needed for the relationship among wire composition, spray parameters, and developed microstructure to improve coating toughness and bonding strength to the substrate. Characterization of the coating's main features was determined by optical microscopy (OM) and scanning electron microscopy (SEM) analysis. Effect of process parameter voltage was evaluated by four-point bend testing with digital image correlation and Vickers and nano-indentation testing across the coating-substrate interface. It was found that as the voltage increased, the number of defects, primarily oxides, decreased. The decrease in oxide content led to increased coating strength at the higher voltage conditions. The oxide concentration did not exhibit a linear relationship with voltage, indicating that no significant change would occur above 36.5V.

A new composition coating was proposed to increase strength and toughness while still maintaining wear properties. The new multi principle element alloy (MPEA) coating composition ($Fe_{0.32}Co_{0.08}Cr_{0.2}Ni_{0.32}Mo_{0.07}Ta_{0.01}$) was based on favorable findings reported for the $FeCoCrNiMo_{0.2}$ MPEA. Two wires of different material were arced together to form the final coating. The effect of spray pressure on the mechanical properties of the coatings was evaluated by four-point bend testing, Vickers hardness, and dry sand rubber wheel wear testing. OM and SEM characterizations were performed on the new coatings. It was found that the anode and cathode wires did not mix within the arc, during flight, or upon deposition resulting in a coating with two different splat compositions. An increase in spray pressure from 172 to 310 kPa, resulted in the dramatic increase in oxide concentration from 21% to 64% but an 8% decrease in outer-fiber stress. The maximum new coating strength was found to be two times that of the HH1 coating. The wear rate was over three times greater than that of the HH1 coating. The two spray pressure conditions tested exhibited virtually the same wear rate suggesting that the spinel oxides responsible for the exceptional wear behavior of the $FeCoCrNiMo_{0.2}$ MPEA did not form due to the lack of mixing.

TABLE OF CONTENTS

ABSTRACT iii

LIST OF FIGURES ix

LIST OF TABLES xvi

ACKNOWLEDGMENTS xvii

CHAPTER 1: INTRODUCTION 1

1.1 Industrial Relevance 1

1.2 Motivation for Research 1

1.3 Object and Approach 1

CHAPTER 2: LITERATURE REVIEW 3

2.1 Thermal Spray Overview 3

2.2 Thermal Spray Processes 3

2.3 Twin-Wire Arc Thermal Spray 5

2.3.1 TWAS Equipment 7

2.3.2 Droplet Formation 9

2.3.3 In-Flight Droplet Behavior 12

2.3.3.1 Secondary Atomization 12

2.3.3.2 In-Flight Oxidation 14

2.3.3.3 In-Flight Nucleation 16

2.3.4 Droplet Impact and Solidification 19

2.3.4.1 Substrate Surface Preparation 20

2.3.4.2 Splat Formation 21

2.3.4.3 Splat Oxidation 23

2.3.4.4 Phase Transformations and Residual Stress 25

2.4 Process Parameters 28

2.4.1 Effect of Voltage 29
2.4.2 Effect of Amperage 33
2.4.3 Effect of Air Pressure and Atomizing Gas 35
2.4.4 Effect of Spray Distance 36
2.5 Solidification Modeling 37
2.5.1 Early Theoretical Model 37
2.5.2 Recent Modeling Developments 45
2.6 Thermal Sprayed High Entropy Alloy Coatings 51
2.6.1 HEA Overview 51
2.6.2 HEA Principles 52
2.6.2.1 High Entropy Effect 52
2.6.2.2 Severe Lattice Distortion 53
2.6.2.3 Sluggish Diffusion 53
2.6.2.4 Cocktail Effect 54
2.6.3 Wear Resistant HEA Coatings 54
2.6.3.1 Thermal Sprayed $Ni_{0.2}Co_{0.6}Fe_{0.2}CrSi_{0.2}AlTi_{0.2}$ 55
2.6.3.2 Thermal Sprayed AlCoCrFeNiTi 55
2.6.3.3 Thermal Sprayed $FeCoCrNiMo_{0.2}$ 57
CHAPTER 3: EXPERIMENTAL PROCEDURES 60
3.1 Thermal Sprayed Sample Preparation 60
3.2 Optical Microscopy 62
3.2.1 Porosity Measurement 63
3.3 SEM Imaging 64
3.4 X-ray Computed Tomography 65
3.5 Hardness 66

3.5.1 Vickers 66

3.5.2 Nano-Indentation 66

3.6 Four-Point Bend Testing with Digital Image Correlation 66

3.6.1 Sample Generation 66

3.6.2 Four-Point Bend Testing 67

3.6.3 Digital Image Correlation 68

3.6.4 Bend Sample Fractography 70

3.6.5 Wear Testing 70

3.7 New Thermal Spray Wire Composition 71

3.7.1 Approach 71

3.7.1.1 Base Composition 71

3.7.1.2 New Composition 73

3.7.2 New Composition Thermal Spraying 75

3.7.3 Testing 76

3.7.3.1 Wear Testing 77

CHAPTER 4: RESULTS 78

4.1 Thermal Sprayed HH1 Coating 78

4.1.1 Area Percent Defects 78

4.1.1.1 Area Percent Defects Statistical Significance 80

4.1.2 Vickers Hardness 81

4.1.3 SEM Images and Composition Maps 82

4.1.3.1 Low Voltage Condition SEM Analysis 83

4.1.3.2 High Voltage Condition SEM Analysis 84

4.1.4 Nano-Indentation Results 88

4.1.5 Four-Point Bending Results with DIC 90

4.1.6 Fracture Surface 92

4.1.7 Wear Test – HH1 94

4.2 Thermal Sprayed New Composition Coating 95

4.2.1 Area Percent Defects 95

4.2.2 Vickers Hardness 97

4.2.3 SEM Images and Composition Maps 98

4.2.4 Four-Point Bending Results 99

4.2.5 Wear Results – New Composition 102

CHAPTER 5: DISCUSSION 105

5.1 Thermal Sprayed HH1 Coating 105

5.1.1 Coating Porosity Analysis 105

5.1.2 Voltage Effects on Oxidation Behavior 108

5.1.3 Coating Structure 109

5.1.4 Oxide Morphologies 110

5.1.5 Effect of Voltage on Residual Stress 111

5.1.6 Coating Strength 113

5.1.7 Fracture Surface Analysis 116

5.1.8 Wear Testing – HH1 120

5.2 Thermal Sprayed New Coating Composition 120

5.2.1 Coating Features 121

5.2.2 Coating Oxide Analysis 124

5.2.3 Mechanical Testing 127

5.2.3.1 Hardness 127

5.2.3.2 Coating Strength 129

5.2.3.3 Wear Testing – New Composition 131

CHAPTER 6: CONCLUSION 134

6.1 HH1 Coating 134

6.2 New Composition Coating 134

CHAPTER 7: FUTURE WORK 136

7.1 HH1 Coating 136

7.1.1 Bond Strength Test 136

7.1.2 Residual Stress Testing 137

7.2 New MPEA Composition 139

REFERENCES 140

LIST OF FIGURES

Figure 2.1 Thermal spray processes with subsets [9]. 4

Figure 2.2 Schematic diagram of the twin-wire arc thermal spray process [14]. 6

Figure 2.3 AT-400 Wire Arc Spray System used to thermal spray samples for this study. 8

Figure 2.4 AT-400 Wire Arc Spray System gun assembly [16]. 9

Figure 2.5 Atomization stages showing the breakdown of liquid sheets in to droplets [18]. 10

Figure 2.6 High-speed photograph of Al droplet formation for TWAS [12]. 10

Figure 2.7 Schematic demonstrating the three types of liquid metal breakup mechanisms. Axisymmetric breakup shown on both the anode and cathode (a). Non-axisymmetric breakup shown on the anode with membrane type breakup mechanism shown on the cathode (b) [17]. 11

Figure 2.8 Main droplet breakup modes [23]. 13

Figure 2.9 Liquid metal movement within the droplet from shear forces induced by jet stream velocity [28]. 14

Figure 2.10 Schematic of in-flight Ni – 5 wt. % Al molten droplet with oxides segregation to front (a) and TWAS Ni – 5 wt. % Al coating with solidified droplet that did not deform into splat upon impact [30]. 15

Figure 2.11 Graph showing the effect of oxygen content in a nitrogen based atomizing gas on the deposit oxygen and carbon content [14]. 16

Figure 2.12 Cross-section of atomized 7150 Al powders [33]. 17

Figure 2.13 Schematic diagram showing the nucleus originating at point O_2 on the droplet surface [34]. 18

Figure 2.14 Temperature (a) and solid fraction (b) of individual droplets during flight [33]. 18

Figure 2.15 Schematic showing partially solid droplets impacting deposit [35]. 19

Figure 2.16 Acceptable and unacceptable examples for substrate geometries for thermal spraying [37]. 20

Figure 2.17 Good and bad wetting angles between splat and substrate [43]. 22

Figure 2.18 Various cases for droplets impacting the substrate [45]. 23

Figure 2.19 Splat thickness and radius versus oxidation volume fraction [46]. 24

Figure 2.20 Schematic showing oxide shell splashing beneath splat [30]. 25

Figure 2.21 Origen of quench stress during thermal spraying progressing from before droplet impact (a), impact and quench (b), and splat stresses (c) [52]. 25

Figure 2.22 Schematic diagram for experimental set up for in-situ measurements of distortion [49]. 27

Figure 2.23 Schematic diagram for experimental set up for in-situ measurements of distortion [49]. 27

Figure 2.24 Schematic TTT diagram for electric arc sprayed steel showing cooling paths for shells sprayed with average temperatures of (a) 200 °C; (b) 255 °C; and (c) 450 °C [49, 53]. 28

Figure 2.25 Effect of input voltage on mean solidified droplet diameter for TWAS Fe-0.8 wt.% C [58]. 30

Figure 2.26 The effect of arc voltage on spray velocity (a) and spray temperature (b) at a spray distance of 150 mm, spraying with air and nitrogen atomizing gasses at a pressure of 280 kPa and 3 g s^{-1} wire feed rate [57]. 31

Figure 2.27 Voltage stages with respect to time (a) and schematic showing droplet formation at wire tip during each stage (b) [58]. 32

Figure 2.28 The effect of wire feed rate on spray velocity (a) and spray temperature (b) at a spray distance of 150 mm, spraying with air and nitrogen atomizing gasses at a pressure of 280 kPa and 34V arc voltage [57]. 33

Figure 2.29 Effect of wire feed rate on mean solidified droplet diameter for TWAS Fe-0.8C [58]. 34

Figure 2.30 The effect of gas pressure on spray velocity (a) and spray temperature (b) at a spray distance of 150 mm, spraying with air and nitrogen atomizing gasses at a wire feed rate of 3 g/s and arc voltage of 34 V [57]. 35

Figure 2.31 Effect of atomizing gas pressure on mean solidified droplet diameter for TWAS Fe-0.8C [58]. 36

Figure 2.32 Effect of spray distance and atomizing gas type on mean droplet temperature and velocity for TWAS Fe-0.8C sprayed at 34 V arc voltage, atomizing gas pressure of 280 kPa, and wire feed rate of 1 g/s [57]. 37

Figure 2.33 Photograph of alumina disks obtained from plasma spraying [61]. 38

Figure 2.34 Droplet flattening schematic for calculations [61]. 39

Figure 2.35 Flattening degree for the solidification case ($k > 0$) [61]. 44

Figure 2.36 Schematic of thermal spray deposition [64]. 46

Figure 2.37 Photograph of the solidification sequence of a liquid tin droplet on a flat stainless steel substrate [63] (a) and the calculated spreading and solidification (b) [62]. 49

Figure 2.38 Rough surface geometry types with the shape of the modeled splat. Rectangular groove (a), triangular groove (b), rectangular ridge (c), and triangular ridge (d) [62]. 49

Figure 2.39 View of droplet spreading showing flow and solidification for four times of 0.05, 0.12, 0.50, and 1.00 µm [67]. 51

Figure 2.40 Schematic of a BCC crystal (a) perfect lattice, (b) distorted lattice by one component with a different atomic radius, and (c) severe lattice distortion by many different sized atoms [79]. 53

Figure 2.41 Schematic of atmospheric plasma spraying process and apparatus [83]. 54

Figure 2.42 Cross section view of (a) as-sprayed and (b) heat treated HEA coating [72]. 55

Figure 2.43 SEM images of the cross-section of the as-sprayed AlCoCrFeNiTi coating taken at (a) lower and (b) higher magnification [73]. 56

Figure 2.44 Wear surface of the AlCoCrFeNiTi coating at (a) 25°C and (b) 700°C [73]. 57

Figure 2.45 Volume wear rates for the APS and HVOF FeCoCrNiMo0.2 HEA coatings [84]. 58

Figure 2.46 Worn surface morphologies of the APS and HVOF coatings for different friction wear test times [84]. 59

Figure 3.1 Thermach, Inc AT-400 Twin-Wire Arc Spray System with components visible (a). Spray gun where cored wires are fed together (b). [9] 61

Figure 3.2 Photo (a) and schematic (b) of thermal spraying set-up. 62

Figure 3.3 Test piece substrate geometry before thermal spraying. 62

Figure 3.4 Location where optical microscopy samples were taken for each test piece. 63

Figure 3.5 Image showing approximate locations of micrographs used for porosity measurement. 63

Figure 3.6 Metallographic image taken within the coating before thresholding (a) and after thresholding (b). 64

Figure 3.7 Cross sectioned sample resting on the FEI Quanta 600 SEM stage. 65

Figure 3.8 Schematic of specimen prepared for x-ray tomography (not to scale). 66

Figure 3.9 Test piece 1 thermal sprayed at 26.5V showing where bend test samples were water-jet cut. 67

Figure 3.10 Four-point bend test loading schematic for the "one half of support span" load configuration from ASTM D6272 with calculated dimensional values inserted in millimeters. 68

Figure 3.11 Four-point bend sample prepared with spackle for DIC during testing. 69

Figure 3.12 Four-point bend testing with DIC set-up. 69

Figure 3.13 Schematic example of four-point bend sample cutting to expose fracture surface with picture showing post cutting. 70

Figure 3.14 Thermo-Calc phase diagram generated for FeCoCrNi versus Mo with the dotted line showing the $FeCoCrNiMo_{0.2}$ composition. 72

Figure 3.15 Thermo-Calc phase diagram generated for FeMoCrNiTa versus Co with the dotted line showing the $Fe_{0.32}Co_{0.08}Cr_{0.2}Ni_{0.32}Mo_{0.07}Ta_{0.01}$ composition. 74

Figure 3.16 Schematic of how two different wires are fed together to achieve the $Fe_{0.32}Co_{0.08}Cr_{0.2}Ni_{0.32}Mo_{0.07}Ta_{0.01}$ composition. 76

Figure 4.1 Vickers hardness taken through the coating thickness for each voltage condition. 82

Figure 4.2 Vickers hardness values from Figure 4.1 that were under 500 HV. 82

Figure 4.3 Compositional maps of the 26.5V input voltage condition at the coating substrate interface for elements Fe, Mn, Si, V, O, Ni, Ti, and Al. 83

Figure 4.4 Compositional maps of the 26.5V input voltage condition within the coating for elements Fe, Mn, Si, V, O, Ni, Ti, and Al. 83

Figure 4.5 Three locations where compositional maps were taken in relation to the substrate. Vickers hardness values are overlaid next to respective indent. 84

Figure 4.6 Composition maps for Fe, Mn, Si, V, O, Ni, Ti, and Al at location (a) of Figure 4.5. 85

Figure 4.7 Spot scans taken within location (a) of Figure 4.5. 85

Figure 4.8 Composition maps for Fe, Mn, Si, V, O, Ni, Ti, and Al at location (b) of Figure 4.5. 86

Figure 4.9 Spot scans taken within location (b) of Figure 4.5. 86

Figure 4.10 Composition maps for Fe, Mn, Si, V, O, Ni, Ti, and Al at location (c) of Figure 4.5. 87

Figure 4.11 Spot scans taken within location (c) of Figure 4.5. 88

Figure 4.12 OM images taken at each nano-indentation grid across the coating-substrate interface. 88

Figure 4.13 Nano-indentation results for each voltage condition. 89

Figure 4.14 Four point bend samples water-jet cut from each voltage test piece. 90

Figure 4.15 Location where four-point bend sample dimensions were taken. 90

Figure 4.16 Strain image taken 90 seconds into the second bend test of the low input voltage condition overlaid onto the sample image inside the bending fixture (a) with sample posttest with DIC paint spatter cleaned off showing location of cracks. 91

Figure 4.17 Load versus time for the second bend test of the low input voltage condition with strain images correlated each load drop. 92

Figure 4.18 Fracture surface of the first bend test of the 26.5V input voltage condition. 92

Figure 4.19 SEM image of bend test fracture surface. 93

Figure 4.20 Cleaved splat showing river lines with spot scan taken at apparent initiation point. 94

Figure 4.21 Image of wear test samples posttest. 95

Figure 4.22 Vickers hardness taken through the coating thickness for the high and low pressure conditions. 98

Figure 4.23 Compositional maps taken of the 241 kPa coating overlaid on the SEM image from the same location. 99

Figure 4.24 Compositional maps taken at the coating-substrate interface overlaid on the SEM image from the same location. 100

Figure 4.25 Low spray pressure bend samples outer-fiber stress versus strain. 101

Figure 4.26 Outer-fiber stress versus strain for 241 kPa spray condition (a) and 310 kPa spray condition (b). 102

Figure 4.27 Post wear test sample of the 241 kPa spray pressure condition. 103

Figure 4.28 Wear surface of the 241 kPa spray pressure condition at different magnifications of (a) 126X, (b) 612X, and (c) 1030X. 103

Figure 4.29 Compositional maps taken of the wear surface. 104

Figure 4.30 Location and result for spot scans taken of wear surface. 104

Figure 5.1 Graph showing the relationship between input parameter voltage and area percentage porosity. 106

Figure 5.2 Processed image (a) and SEM (b) images taken from the same area of 26.5V voltage condition with red circles showing large oxides that show up as dark regions on the processed OM image. 107

Figure 5.3 X-ray CT data of the HH-1 31.5 voltage condition rendered in 3D giving the distribution of oxides, pores, and cracks through the coating thickness. 108

Figure 5.4 Optical image of the 26.5V (a) and 36.5V condition (b) comparing the oxidation on the splat surface. Schematic drawings (not-to-scale) showing droplet size and splat surface oxidation for the 26.5V (c) and 36.5V condition (d). 109

Figure 5.5 SEM image (a) and EDS maps of Ni (b) and V (c) of the 36.5V condition taken at the same location. 110

Figure 5.6 EDS Mapping of the 36.5V condition for O, Si, Al, and Ti. 112

Figure 5.7 Average indentation values at various distances into the substrate starting at the interface. 113

Figure 5.8 Load versus time for each bend sample. Each input voltage condition had two bend samples tested. 114

Figure 5.9 Average indentation values at various distances into the substrate starting at the interface. 115

Figure 5.10 Schematic of the I-T diagram for type 1080 steel approximated for the twin-wire arc sprayed HH-1 [114]. 116

Figure 5.11 Fracture surface after bend test showing delamination from substrate. 117

Figure 5.12 Spots scans taken along fracture surface with schematic showing where image was taken and photo of posttest bend sample showing where the crack changes from perpendicular to parallel to bend stress. 118

Figure 5.13 Fracture surface of post bend test samples showing location of spot scans at crack initiation points. 119

Figure 5.14 *Splat 1* (a) and *Splat 2* composition (b) with elemental maps and spot scans showing the distribution and composition of splat types for the 241 kPa spray pressure condition. 121

Figure 5.15 High speed image taken from the anode side of the metal breakup during TWAS [124]. .. 122

Figure 5.16 Jet flow melting behavior, and disintegration of solid wires (a) and cored wires (b) [124]. 123

Figure 5.17 High speed image of TWAS of cored wires [124]. 124

Figure 5.18 Graph showing the relationship between spray pressure and area percentage oxides, pores, and cracks. 125

Figure 5.19 OM images of the 172 kPa (a), 241 kPa (b), and 310 kPa (c) spray pressure conditions. ... 125

Figure 5.20 Oxygen compositional map overlaid on SEM image showing the location of two spot scans. 126

Figure 5.21 Vickers hardness values taken through the coating thickness of the low pressure condition showing which indents correspond to which splat type. 128

Figure 5.22 Fe-Co-Cr ternary phase diagrams at 1000°C (a) and at 700°C (b) [127]. 128

Figure 5.23 Bend test outer-fiber stress versus strain for each new composition spray pressure condition bend test plotted with HH1 coating results for comparison. 129

Figure 5.24 Effect of atomizing gas pressure on mean droplet diameter [58] (a) and effect of flight distance on particle velocity for various spray pressures [128] (b). 130

Figure 5.25 Volume wear rates for thermal sprayed coatings. 132

Figure 7.1 Schematic and transparent SolidWorks model of the pin and ring test proposed to measure the coating bond strength. 137

Figure 7.2 Sprayed sample showing curved radius developed after spraying with the definition of curvature parameter, *K* [139]. 138

Figure 7.3 Hole-drilling set-up on the HH1 coating (a), magnified image of the strain gauge rosette (b), and image of drill positioned over the middle of the strain gauge. 139

LIST OF TABLES

Table 2.1 Thermal spray process comparisons for gas flow, gas temperature, particle impact velocity, and the relative adhesive strength [6, 13]. 5

Table 2.2 Thermal spray process comparisons for coating strength, oxide content, process cost, spray rate, and power [6, 13]. 7

Table 2.3 Cooling rate vs. splat thickness for an Fe splat an Cu substrate and 30°C [41]. 21

Table 2.4 TWAS rates for various materials [9]. 34

Table 3.1 TWAS standard process parameters for HH1. 60

Table 3.2 Element properties for Fe, Co, Cr, Ni, and Mo [74, 103]. 73

Table 3.3 Composition and element properties for $Fe_{0.32}Co_{0.08}Cr_{0.2}Ni_{0.32}Mo_{0.07}Ta_{0.01}$ [74, 103]. 75

Table 3.4 TWAS process parameters for the $Fe_{0.32}Co_{0.08}Cr_{0.2}Ni_{0.32}Mo_{0.07}Ta_{0.01}$ composition. 76

Table 4.1 Chemical analysis of wires used for thermal spraying. 78

Table 4.2 Area Percent Defects for HH1 sprayed at Varying Voltages 79

Table 4.3 Statistical Analysis of Area Percent Defects with Input Voltage. 81

Table 4.4 Bend sample dimensions. 91

Table 4.5 Wear Results. 94

Table 4.6 Area Percent Defects for $Fe_{0.32}Co_{0.08}Cr_{0.2}Ni_{0.32}Mo_{0.07}Ta_{0.01}$ composition sprayed at varying pressures. 96

Table 4.7 Bend Sample Dimensions. 100

Table 4.8 Wear Results for New Composition. 102

ACKNOWLEDGMENTS

The present work would not have been possible without the financial support of National Science Foundation Industry-University Cooperative Research Center (NSF IUCRC) with Manufacturing and Materials Joining Innovation Center (Ma2JIC) and Devasco International, Inc. Joe Scott, Hai Nguyen, and Tien Le have are gratefully acknowledged for the production of sprayed samples and polished samples as, well as, continues technical support for the life of the project.

I would like to thank my advisor, Dr. Zhenzhen Yu, for giving me the opportunity study at the Colorado School of Mines. Her excitement, guidance, and support have pushed me to become a better researcher. It has been an honor to be part of the Center for Welding, Joining, and Coatings Research lead by Dr. Stephen Liu who has been an invaluable resource and constant guide exemplifying what it means to truly be the leader of a field. I would like to thank my committee (Dr. Zhenzhen Yu, Dr. Stephan Liu, and Dr. Emmanuel De Moor) for the comments and feedback which has improved the quality of this work. My CWJCR colleagues and friends; Cheryl Hawk, Devon Gonzales, Ethan Sullivan, Davis Wilson, Ben Schneiderman, Brian Rodger, Juan Wei, Scott Gordon, Xin Wu, Ezequiel Pessoa, Drew White, Michelle Gilbert, Jordan Ream, Tim Pickle, Abdelrahman Abdelmotagly, Erzhuo Gao, and Xiaoxu Li.

I would finally like to thank the love of my life and wife, Mimi, for her patience, love, and support.

CHAPTER 1: INTRODUCTION

1.1 Industrial Relevance

Oil country tubular goods (OCTG) are subjected to high amounts of wear during drilling operations. With advancements in directional drilling, drilling with casing, and premium wedge connections; operations torque has greatly increased and wear has become a big concern for tubulars in the oilfield [1]. Drill pipes are often hard-faced in order to increase wear resistance and extend the life of the drill string [2, 3]; however, hardfacing requires that the surface is melted to form a metallurgical interface [4]. Thermal spray, on the other-hand, forms a mechanical bond with a rough surface and does not affect the substrate properties. Additionally, thermal sprayed coatings can significantly reduce the friction between the tool joint and surrounding casing increasing the life of both the drill and casing strings [5].

1.2 Motivation for Research

This research expands the knowledge of process parameters on metallurgical and mechanical properties of a new cored wire composition (HH-1) developed by White Horse Technology. HH-1 was developed for applications on drill pipe and downhole tools to improve wear resistance and reduce friction in order to extend operating life. The main issue faced with these types of thermally sprayed coatings is low impact resistance, wherein, sections varying in size can chip off of the substrate upon impact during transportation, handling on the rig, or down-hole. Improving the coatings toughness while maintaining acceptable wear resistance would greatly reduce the occurrence of this issue in both transportation and in service.

1.3 Object and Approach

The objective of the present research is to characterize the main features of the HH-1 thermal sprayed coating. Features such as oxides and porosity are quantified and characterized utilizing optical microscopy (OM), scanning electron microscope (SEM) imaging, and X-ray computed tomography (X-ray CT). Coating mechanical properties were determined from hardness and four-point bend testing. The effect of thermal sprayed droplet characteristics on coating microstructures and properties are evaluated by varying the input voltage parameter. Coating morphologies and properties are discussed in connection with

the in-flight and deposited droplet conditions to better understand the relationship among the input voltage, droplet temperature, oxidation, and final coating structure and properties.

A new coating composition was developed in order to achieve improved strength and toughness while maintaining wear properties. Thermodynamic calculations using Thermo-Calc software were performed to predict splat phases and compared with the coatings characteristics reported in literature. OM and SEM imaging was also performed to characterize the coatings obtained using the new composition. Mechanical properties are determined from Vickers hardness, four-point bend testing, and dry sand rubber wheel wear testing. The effect of spray pressure on coating strength and wear rate was evaluated by varying input spray pressure.

CHAPTER 2: LITERATURE REVIEW

2.1 Thermal Spray Overview

Thermal spray is commonly used in various industrial sectors including automotive, oil and gas, mining, aerospace, biomedical, ect. [6]. Thermal spray technologies are advancing and are regarded as key environmentally friendly means to modify properties of selected surfaces of critical components [7]. The global thermal spray market is expected to reach 12.783 billion USD by the year 2024 with major growth in the aerospace and automotive sectors on cylinders, engine parts, and turbine blades to enhance corrosion resistance, thermal efficiency, and sliding wear [8]. Market forces have driven the demand for improved efficiency and improved part life leading to many opportunities for thermal spray coatings which apply a thin layer of higher performing material tailored to the specific application.

2.2 Thermal Spray Processes

Thermal spray is a general term that covers a group of processes used to apply metallic, ceramic, or cermet coatings [9]. The sprayed particles can be applied as molten, semi-molten, or as solid particles. A coating is generated as these particles impact, deform, and build onto the substrate which is accomplished by either molten droplets or solid droplets deposited at sufficiently high velocities [10]. Thermal spraying can be classified by process based on the input energy and droplet characteristics. The four main categories are flame, plasma arc, electric, and cold spray [9]. As shown in Figure 2.1, each of these categories can be further broken down with each having their own subsets and unique coating characteristics as they vary with velocity, temperature, and droplet size.

When comparing the coatings of different thermal spray processes it is important to understand the temperatures, velocities, and spray environment differences that the spray particles are exposed to. The thermal spray process can be simply viewed as a high speed thermal treatment where sprayed material is heated to some temperature over a given period of time. The heat over time is governed by the jet. This jet can be engineered by utilizing various nozzle designs which the pressurizing gas flows through [11, 12]. How long the sprayed material is in the air, or the particle dwell time, is a function of the jet velocity and the specific particle characteristics such as material properties and particle morphologies. The temperature

of a given particle, on the other hand, is a function of spray process in-put heat, thermal properties of the particle, and composition and pressure of the jet.

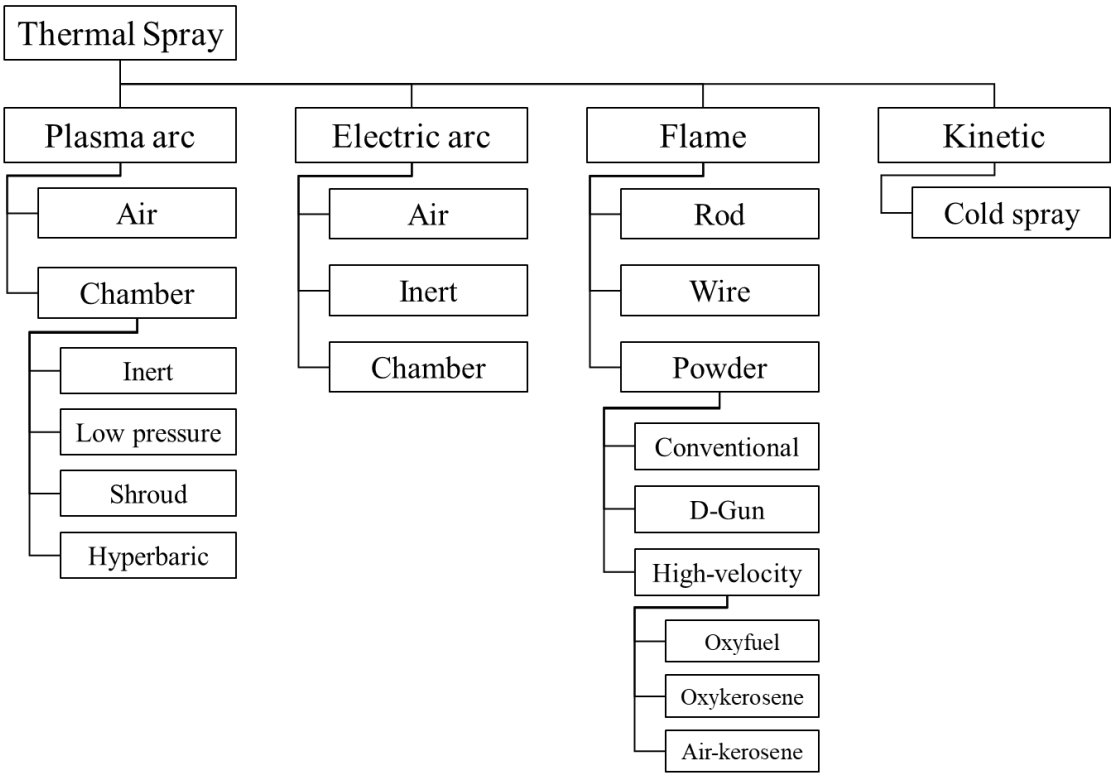

Figure 2.1 Thermal spray processes with subsets [9].

Temperature can vary wildly between processes as shown in Table 2.1. Flame spray, depending on the fuel, has gas temperatures that range from 2540 to 3150°C representing the low temperature spray process. On the opposite end with the highest jet temperature is wire arc thermal spray having jet temperatures reaching over 24,000°C with plasma spray next in line with typical temperatures reaching 20,000°C. These jet temperatures are well above any known material melting temperature. The temperature gradient of the jet is severe on the order of several thousand degrees. This is mainly due to the differences between the hot jet core and the colder surrounding environment. This causes a temperature gradient both as a distance from the nozzle but also radially as the drop in temperature reduces the gas velocity at the core and increases the gas velocity near the outer boundary [9].

Table 2.1 Thermal spray process comparisons for gas flow, gas temperature, particle impact velocity, and the relative adhesive strength [6, 13].

Process	Gas flow		Process gas temperature		Particle impact velocity		Relative adhesive strength (i)
	m^3/h	ft^3/h	°C	°F	m/s	ft/s	
Flame powder	11	400	2200	4000	30	100	3
Flame wire	71	2500	2800	5000	180	600	4
High velocity oxyfuel	28–57	1000–2000	3100	5600	610–1060	2000–3500	8
Detonation gun	…	…	3900	7000	1200	3900	8
Wire arc	71	2500	5500	10,000	240	800	6
Conventional plasma	4.2	150	5500	10,000	240	800	6
High-energy plasma	17–28	600–1000	8300	15,000	240–1220	800–4000	8
Vacuum plasma	8.4	300	8300	15,000	240–610	800–2000	9

(i) 1 (low) to 10 (high). (ii) ppm levels.

Higher jet velocities result in higher velocity particles and higher particle temperatures. It is generally desirable to have higher particle velocities resulting in higher impact energies and more deformation on impact producing a denser coating with higher bond strength. Additionally, the less time that a particle/droplet has in-flight to solidify or partially solidify, increases the coating density and quality [9]. Longer dwell times can be compensated by increasing the jet enthalpy and thus particle temperatures. This relationship is shown in Table 2.1 comparing the spray processes including the gas flow and temperature with particle speeds and coating strengths. For this work, the thermal spray process studied was wire arc spray, commonly referred to as twin-wire arc spray (TWAS).

2.3 Twin-Wire Arc Thermal Spray

TWAS process, also known as electric arc spray, twin-wire arc, arc spray, or wire arc spray, works by feeding two wires together in the gun head where a direct-current electric (dc) arc is struck between the wire tips melting them as showing in Figure 2.2 [9, 14]. Compressed air, fed from behind the arc, atomizes the molten material and propels molten droplets towards the substrate. Arc temperatures reach temperatures above 5000°C well above the melting temperature of any know material [15]. Unlike the other thermal

spray processes that use indirect heating to melt particles, TWAS utilizes a dc electric arc to melt the material directly making it the most thermal efficient process. This is shown in Table 2.2, where the TWAS process uses drastically less power than any of the other spray processes. Additionally, the TWAS has the lowest process cost with similar strength and densities to similar combustion processes, making it an attractive thermal spray option [6, 15].

Due to low spraying costs, moderately high deposition rates, and high cohesive strengths, TWAS has found many applications including wear resistant coatings, corrosion resistant coatings, and/or thermal barrier coatings. Thermal spray coatings have been widely used across many industries including oil and gas, automotive, and aerospace to improve wear resistance, heat resistance, or other key performance factors. Due to the ease of application, a TWAS coating can be applied to worn or corroded components to restore dimensional accuracy commonly seen on mining and infrastructure components.

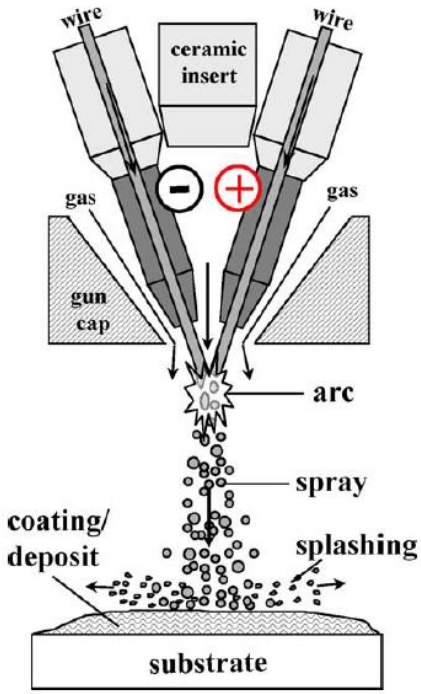

Figure 2.2 Schematic diagram of the twin-wire arc thermal spray process [14].

Table 2.2 Thermal spray process comparisons for coating strength, oxide content, process cost, spray rate, and power [6, 13].

Process	Cohesive strength	Oxide content, %	Relative process cost (i)	Maximum spray rate		Power	
				kg/h	lb/h	kW	hp
Flame powder	Low	6	3	7	15	25–75	34–100
Flame wire	Medium	4	3	9	20	50–100	70–135
High velocity oxyfuel	Very high	0.2	5	14	30	100–270	135–360
Detonation gun	Very high	0.1	…	…	…	…	…
TWAS (wire arc)	High	0.5–3	1	16	35	4–6	5–8
Conventional plasma	High	0.5–1	5	5	10	30–80	40–110
High-energy plasma	Very high	0.1	4	23	50	100–250	135–335
Vacuum plasma	Very high	(ii)	10	10	24	50–100	70–135

(i) 1 (low) to 10 (high).

2.3.1 TWAS Equipment

For TWAS, two consumable wire electrodes are fed together in a gun head by guiding the wires through contact tips. There are several wire-feeding design types including feeders that push, pull, or are a combination of push and pull designs. For the pull-type design, motors in the gun pull the wires from the spools where the motor type determines pull distance and type of wire spool depending on torque limitations. For the push-type design, the motor is located by the spool and is remotely controlled by the gun resulting in a lighter weight gun easier to handle by the spray operator. The gun-to-feeder distance is now determined by the wire column strength instead of limited by the motor type. However, for this design softer or smaller diameter wires are difficult to use in the push-type without buckling. Both push and pull type designs are limited to an approximate gun-to-feeder distance of 6 m (20 ft) [9]. If greater distances are required, the combination push/pull design can be used to achieve gun-to-feeder distances of greater than 15 m (50 ft). This is because the push/pull design unitizes both a gun and drive motor. Limitations exist with a heavy gun due to the motor, just like the pull type design, which fatigues operators and can cause quality issues that arise from out of synch drive and gun motors. For this study the push-type AT-400 Wire Arc Spray System was used as shown in Figure 2.3.

The push-type AT-400 Wire Arc Spray System requires electrically conductive material in wire form with sizes between 11 and 14 gauge, or wire diameters between 1.57 mm (0.062”) to 2.31 mm (0.091”). A three phase constant potential dc power source provides arc voltages between 18 and 40 volts and can operate between 15 and 400 amps. The wire feeder consists of four-drive roll per wire. Debris and dust is blown off of each wire before entering the coaxial cables by bypass air routed through the drive housing and coaxial cables. The coaxial cables are insulated power cables charged positive and negative and provide a path for the consumable wires from the wire-feeder to the gun head.

Figure 2.3 AT-400 Wire Arc Spray System used to thermal spray samples for this study.

The two axial cables and the air pressure line all connect to the gun head. The consumable wires are fed through copper wire guide tips into the high velocity air cap as shown in Figure 2.4. This assembly is then connected to a detachable gun handle with an on/off trigger switch that an operator can use to control spray. Once the gun handle trigger is activated, the consumable wires begin to be fed forward to the point where an arc is struck across the wire tips. The air cap directs the high velocity air across the arc zone and produces the spray jet.

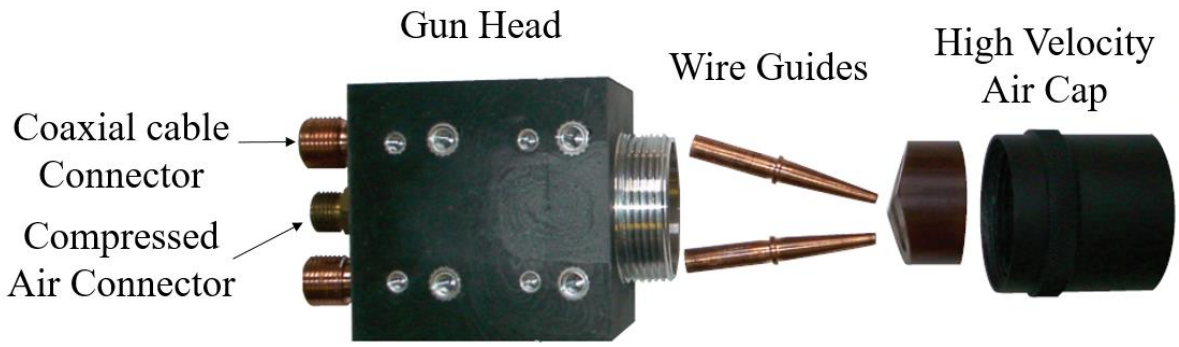

Figure 2.4 AT-400 Wire Arc Spray System gun assembly [16].

2.3.2 Droplet Formation

As discussed in Section 2.3.1, molten metal droplets are formed when compresses air is passed over the arc zone propelling the molten material away from the gun nozzle. Compressed air removes molten material from the arc in the form of ribbons as a result of the transfer of kinetic energy from the gas to the molten material [17]. Atomization of the molten material occurs from Rayleigh instabilities that form on the surface of molten ribbons producing droplets. This is visualized in three stages as shown in Figure 2.5. The first stage represents the formation and growth of disturbance waves, followed by the fragmentation of liquid sheets in stage 2, before finally forming the droplets in stage 3 [18]. The droplets undergo further changes due to surface tension and additional pressure forces. Droplet size is dependent on the thermodynamic properties of the spray material and pressurizing gas, as well as the processing parameters. For metals, spheroidization of molten metal thermal spray droplets is rapid due to large surface tension forces (60-2,400 mJ/m^2) and low viscosities (0.602-6.92 mPa s) [19].

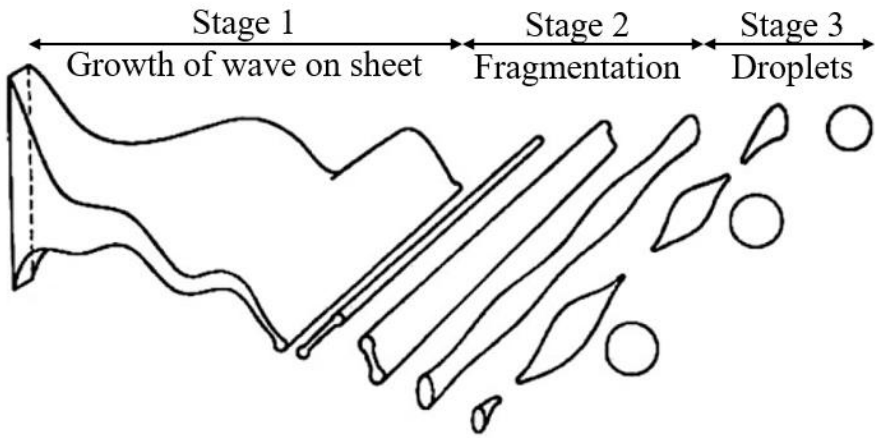

Figure 2.5 Atomization stages showing the breakdown of liquid sheets in to droplets [18].

During TWAS, the melting of the anode and cathode is asymmetric as the cathode is consumed more rapidly. The cathode has a more constricted arc attachment as compared with the diffuse arc attachment at the anode resulting in higher melting rates. This has been visualized during the TWAS spraying of aluminum by utilizing high-speed photography with a shadowgraph setup [12]. Figure 2.6 shows the high-speed photograph taken of the asymmetric Al melting behavior of the anode and cathode wires. It was found that the slower melting anode had an elongated molten stream resulting in larger droplets [12].

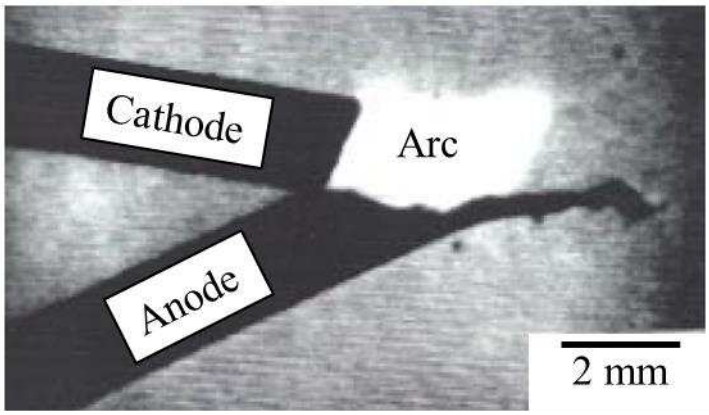

Figure 2.6 High-speed photograph of Al droplet formation for TWAS [12].

Hussary (2007) further explored the melting within the TWAS arc for TAFA 30T medium carbon steel and categorized the metal breakup into three types: Rayleigh axisymmetric breakup, Rayleigh non-

axisymmetric breakup, and membrane breakup [17]. Figure 2.7 shows a schematic of each type of liquid metal breakup mechanism with Figure 2.7 (a) showing the Rayleigh axisymmetric breakup mechanism and Figure 2.7 (b) showing both the Rayleigh non-axisymmetric breakup and membrane breakup mechanisms. The Rayleigh axisymmetric breakup is characterized by the molten metal stretched parallel to the jet axis. This parallel stretching is the result of forces acting in opposite directions on the liquid sheet. The aerodynamic drag force acts in the downstream direction with the surface tension force acting in the upstream direction. This results in amplified Kelvin-Helmholts instabilities breaking up droplets having trajectories parallel to the jet axis [20]. The Rayleigh non-axisymmetric breakup results from forces in the transverse direction from converting eddies. These eddies arise from complex jet flow generated in the shear layer [21].

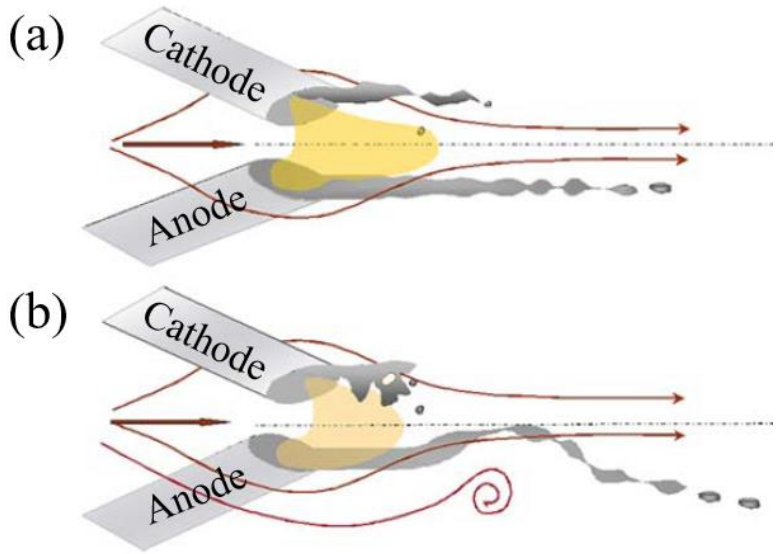

Figure 2.7 Schematic demonstrating the three types of liquid metal breakup mechanisms. Axisymmetric breakup shown on both the anode and cathode (a). Non-axisymmetric breakup shown on the anode with membrane type breakup mechanism shown on the cathode (b) [17].

The membrane breakup is categorized by a hole that develops in the center of thinly stretched molten sheets of material at the edge of the electrode. This hole develops on molten material near the electrode due to the high surface tension of liquid metal at the edges of the membrane pulling the liquid metal into a ring shape. The molten ring then further breaks up into droplets down the jet stream by either

Rayleigh axisymmetric breakup or Rayleigh non-axisymmetric breakup mechanisms [17]. This study will focus on TWAS of metals noting that thermal spraying of a variety of materials and composites is possible.

2.3.3 In-Flight Droplet Behavior

2.3.3.1 Secondary Atomization

After droplet formation and just after leaving the arc, droplets undergo further changes from additional pressure forces and undergo more disintegration if the dynamic pressure forces from gas stream velocity exceed the surface tension forces of the droplet [19]. This relationship is given by the maximum stability criterion expression [22]:

$$0.5\rho_g(\Delta V)^2 = C\left(\frac{\sigma_d}{d_d}\right) \tag{2.1}$$

where ρ_g is the atomizing gas density, ΔV is the difference between the atomizing gas and droplet velocities, the constant C represents an empirical value dependent of the spray system, droplet surface tension is given by σ_d, and droplet diameter given as d_d. This results in an unequal pressure distribution and deformation from the original spherical shape generated in stage 3 of droplet formation discussed in Section 2.3.2. This process of droplet deformation from aerodynamic forces causing fragmentation, is termed secondary atomization. Deformation is resisted by the droplet surface tension (σ) and viscosity (μ). The main dimension parameters affecting secondary atomization are the Weber number (We) and the Ohnesorge number (Oh) which are represented by the following expressions:

$$We = \frac{\rho_g U_{rel}^2 d_d}{\sigma} \tag{2.2}$$

and

$$Oh = \frac{\mu_d}{\sqrt{\rho_d d_d \sigma}} \tag{2.3}$$

where U_{rel} is the relative velocity, and ρ_d is the droplet density [23]. The Weber number represents the ratio of the aerodynamic force for disrupting the droplet to the surface tension force resisting. The Ohnesorge number represents the ratio between the viscous and surface tension forces. Higher We indicates higher fragmentation while a higher Oh indicates less fragmentation.

Secondary atomization occurs by various breakup modes identified by Pilch and Erdman [24] and termed by Hsiang and Faeth [25]. These breakup modes include vibrational, bag, multimode, sheet-thinning, and catastrophic [26]. Figure 2.8 shows a schematic of the three most common break-up modes in sequence of increasing We [23]. The first mode, having the lowest We, is termed bag breakup. The droplet deforms into a disk leading to a positive pressure difference between the front and wake resulting in the center of the droplet moving downstream forming the thin "bag" shape. Once a critical bag size is formed, the deformed droplet will fragment forming a large number of small droplets at the front with larger droplets forming from the rim at the back.

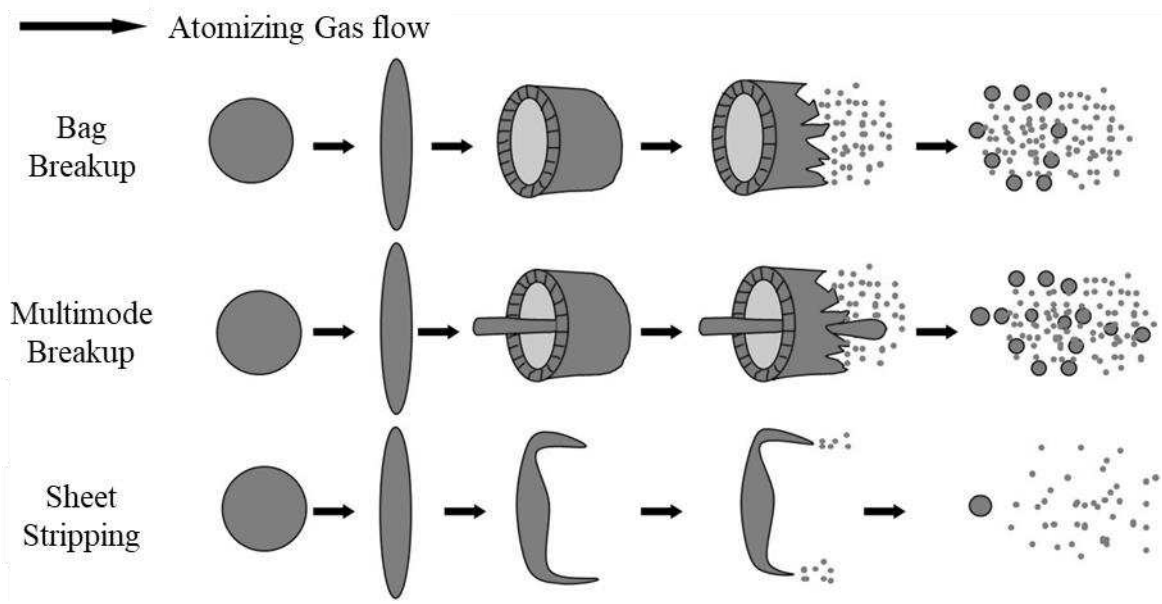

Figure 2.8 Main droplet breakup modes [23].

Multimode breakup is the second mode and resembles bag breakup but with the front stamen forming a long ligament in the center of the bag. The front edges form fine particles like bag breakup with the back rim and stamen forming larger droplets. The third breakup mode has the highest We and involves the droplet deforming into a thin disk where sheets are created and form around the rim due to Kelvin-Helmholtz (K-H) waves. As the sheets are drawn, fine droplets are fragmented around the edges with this continuing until the core droplet in the middle is at a stable diameter with the surrounding aerodynamic

forces. Webber number can be targeted to result in a break-up mode that reduces the variability in droplet diameter while considering the simultaneous oxidation and temperature effects of changing spray pressure.

2.3.3.2 In-Flight Oxidation

During flight the molten metal particles are exposed to the jet environment where oxidation is largely dependent on the oxygen content of the atomizing gas. Oxidation of metals is a time dependent process with linear and parabolic fundamental types [27]. Linear is a character of alkaline metals with a non-continuous oxide film where the evolution of mass and exposed time are $\Delta m \sim t$ respectively. Parabolic has a continuous oxide film, $\Delta m \sim t^{0.5}$, and is present for metals such as nickel and iron. During flight, the molten droplets are subjected to shear forces acting on the surface from the high-velocity gas flow. This creates convection motion of the liquid in the droplet resulting in higher rates of oxidation as fresh liquid is continuously brought to the droplet surface to react with oxygen [10]. The motion of liquid within the droplet is schematically shown in Figure 2.9.

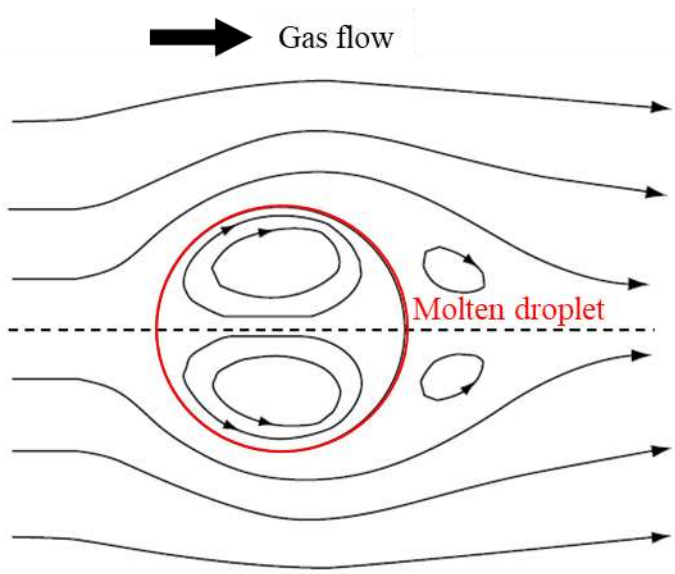

Figure 2.9 Liquid metal movement within the droplet from shear forces induced by jet stream velocity [28].

In-flight oxidation can be characterized by the formation of metastable oxides and spherical oxide inclusions [10]. A study on APS sprayed 316L austenitic stainless steel powders found that in-flight

reactions formed metastable oxides of spinel type $Fe_{3-x}Cr_xO_4$ (1.90 > x > 1.56) with mixed cations of Cr, Fe, Mn, and Si [29]. Oxides form by either chemical reactions between the droplet surface liquid and oxygen or by the diffusion of oxygen into the liquid. Observations of thermal sprayed Ni – 5 wt. % Al by APS and TWAS suggest that oxides start to segregate towards the front of the droplet during flight [30]. Figure 2.10 (a) shows a schematic of the droplet during flight where the Al_2O_3 shell builds up at the front with Figure 2.10 (b) showing an oxidized particle that was found within the TWAS sprayed coating that did not form a splat due to solidifying before impact with the substrate. The oxides segregate to the front of the droplet due to velocity effects where the lower viscosity liquid metal moves to the rear of the droplets thus pushing the oxides forward. Capillary flow in the droplets pushes the liquid aluminum oxide away from the hot region in the back of the droplet to the cooling front end.

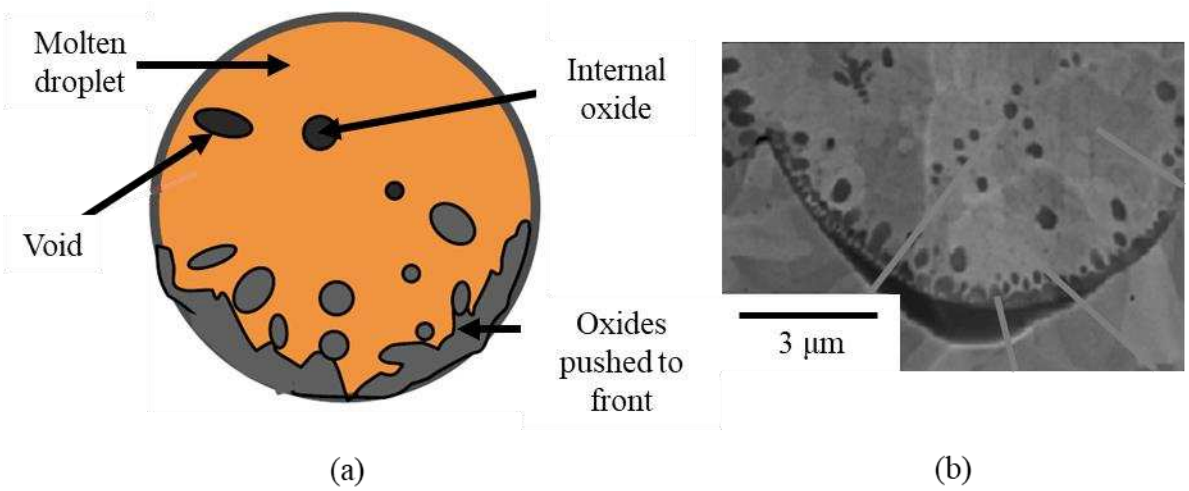

Figure 2.10 Schematic of in-flight Ni – 5 wt. % Al molten droplet with oxides segregation to front (a) and TWAS Ni – 5 wt. % Al coating with solidified droplet that did not deform into splat upon impact [30].

Oxidation of droplets is not limited to spraying with air atomizing gas but is also observed when nitrogen is used due to the inevitable entrapment of oxygen into the spray plume from the surrounding air [31]. A study of TWAS sprayed 1.6 mm plain carbon steel (TAFA 38T) wire found that when incrementally increasing the oxygen content of the atomizing gas, the spray temperature increased, deposit carbon content decreased, and deposit oxygen content increased [14]. Figure 2.11 shows the relationship between oxygen

content in a nitrogen based atomizing gas on the deposit oxygen and carbon content. At the wire tips, the metal is heated well above the melting point resulting in vaporization of iron and carbon which, in the presence of oxygen, reacts to form Fe_3O_4 dust and carbon dioxide respectively.

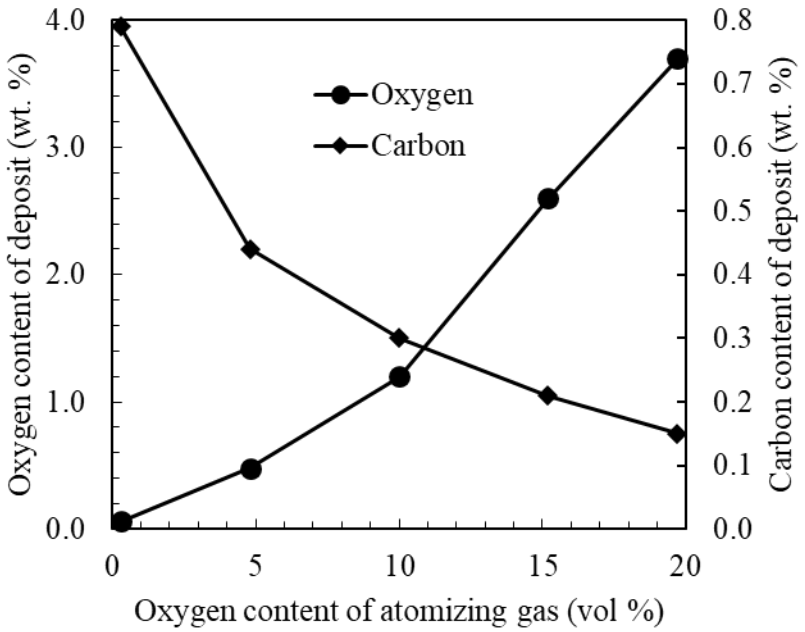

Figure 2.11 Graph showing the effect of oxygen content in a nitrogen based atomizing gas on the deposit oxygen and carbon content [14].

2.3.3.3 In-Flight Nucleation

Solidification during flight occurs primarily heterogeneously by one or more of the following scenarios: (i) heterogeneous nucleation within the droplet, (ii) surface oxidation, and (iii) inter-particle collisions [19]. For homogeneous nucleation, the droplets need to be sufficiently small to allow the necessary undercooling [32]. A study on atomized 7150 Al powders found that nucleation occurred primarily at the droplet surface and then developed dendrite arms in a fan shaped manner around and into the droplet [33]. Figure 2.12 (a) shows a powder particle intercepted by a copper plate where two nucleation events were observed starting at the droplet surface. Figure 2.12 (b) shows a similar situation but has three nucleation events with one of them starting within the droplet. Even though surface nucleation is the dominant mechanism, there were

still cases where nucleation occurred within the interior of the droplet which was attributed to nucleation sites such as inclusions or surficial oxides.

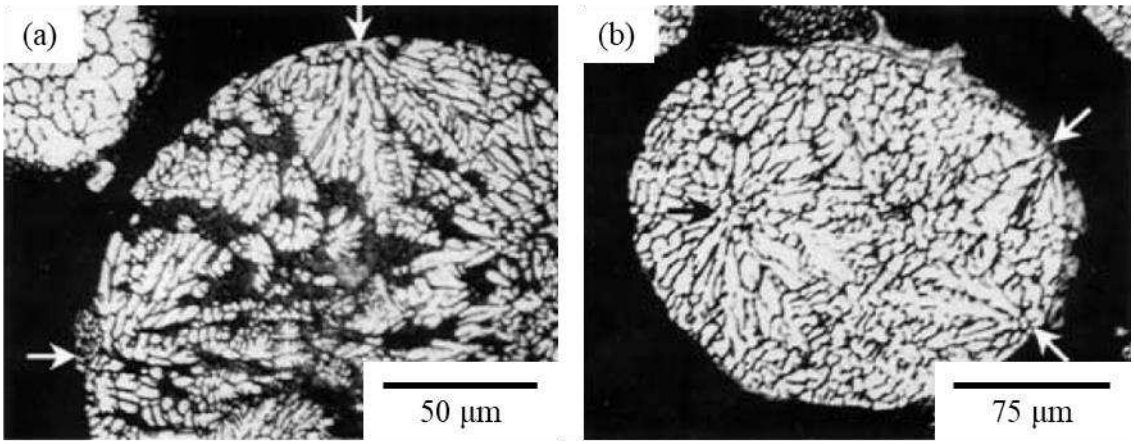

Figure 2.12 Cross-section of atomized 7150 Al powders [33].

As the Al droplets move down the spray stream away from the gun-head, heat is rapidly lost due to convection from the atomizing gas. Nucleation occurs at some temperature below the liquidus temperature. Figure 2.12 shows that there are several nucleation events per droplet. Based on experimental observations, there are six nucleation events on each droplet irrespective of its size (N = 6) [33]. Assuming isotropic growth, the extended volume fraction (x_{ex}^{he}) of the heterogeneous nuclei within a droplet can be calculated as:

$$x_{ex}^{he} = N\frac{1}{d^4}\left(4d - 3\left(\int_0^t V[T(t)]dt\right)\right)\left(\int_0^t V[T(t)]dt\right)^4 \tag{2.4}$$

where N is the number of nucleation sites, V is volume, T is temperature, and t is time. The growth of the nucleus will start on the droplet surface and grow into the droplet forming spherical caps as shown in Figure 2.13 at location O_2.

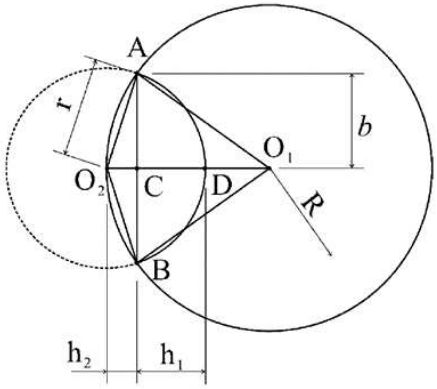

Figure 2.13 Schematic diagram showing the nucleus originating at point O_2 on the droplet surface [34].

Nucleation was followed by a rapid recalescence from the release of the latent heat during solidification. This was followed by an increase in droplet temperature approaching the equilibrium transformation temperature which is shown in Figure 2.14 (a). In contrast to the Scheil's rule, eutectic plateaus did not appear resulting in a final microstructure obtained containing no eutectic composition. Droplets of various sizes experience different undercooling and, as a result, smaller particles experience rapid recalescence as the crystalline embryos quickly grow into the deeply undercooled liquid. This effect is shown in Figure 2.14 (b). [33]

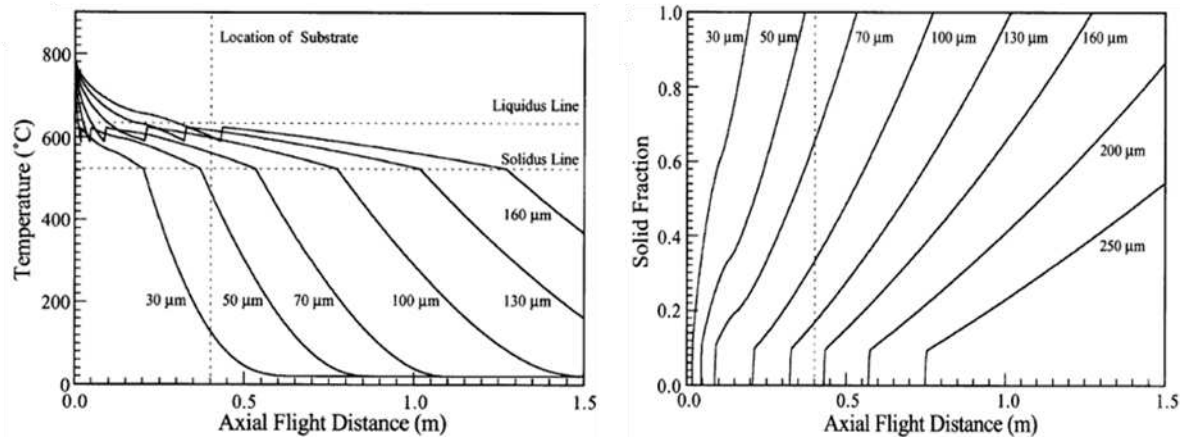

(a) (b)

Figure 2.14 Temperature (a) and solid fraction (b) of individual droplets during flight [33].

2.3.4 Droplet Impact and Solidification

Once droplets impact the surface they deform into a splat. Droplets impact the surface as either liquid, partially solid, or fully solid. There exists a complex thermal history of undercooling, nucleation, decalescence, and equilibrium solidification. The heterogeneous mixture of the microstructure is thus dependent on the solidification characteristics of the in-flight droplets, interaction of droplet and substrate on impact and splat to splat interactions [19]. During the deposition phase, the repeated impact of droplets causes fragmentation of the droplet and deposit dendrite arms as is shown schematically in Figure 2.15 [35]. During deposition, when a droplet impinges onto the previously deposited layer, rapid heat transfer occurs across the layer which is analogous to rapid quenching, and thus, homogeneous nucleation becomes the dominant mechanism [36]. The mechanism by which the particles adhere to the substrate and underlying coating layer is primarily by mechanical anchorage [10]. Thus, the surface of the substrate has to be prepared in order for there to be adhesion.

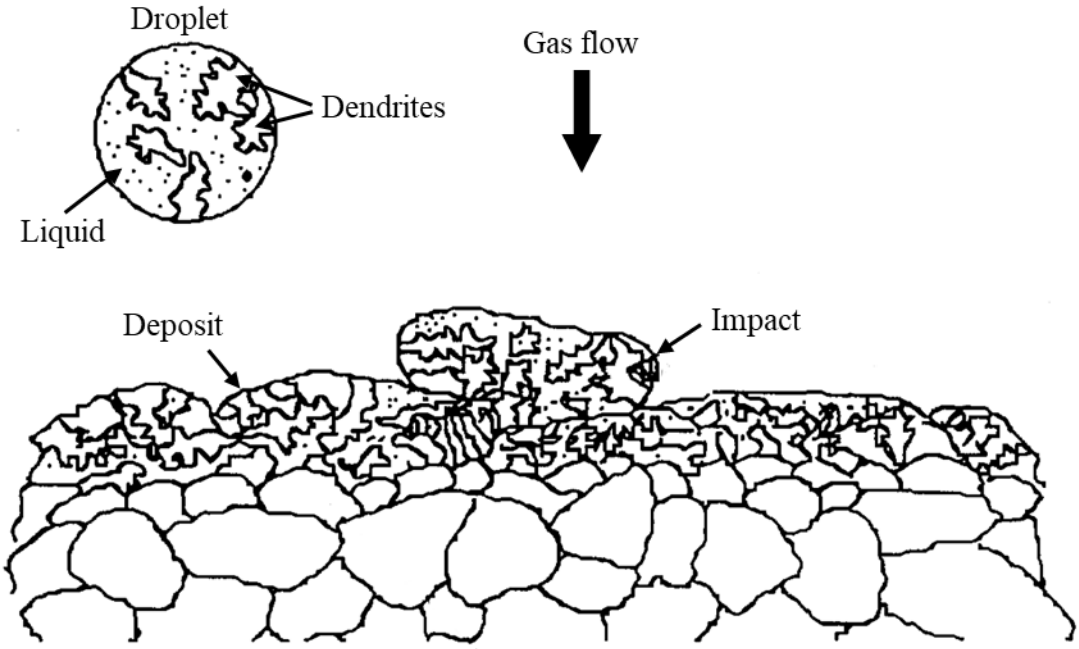

Figure 2.15 Schematic showing partially solid droplets impacting deposit [35].

2.3.4.1 Substrate Surface Preparation

In order to ensure that the coating will adhere to the substrate, the surface needs to be prepared by cleaning, shaping if necessary, and activation [10]. Cleaning of the substrate is a broad concept ranging from removal of grease to the removal of old coating. After cleaning, the substrate needs to be shaped depending on the geometry. If substrate geometries have sharp edges or areas difficult to spray, the adherence of the coating will be poor. Some examples of acceptable and unacceptable substrate geometries are provided in Figure 2.16.

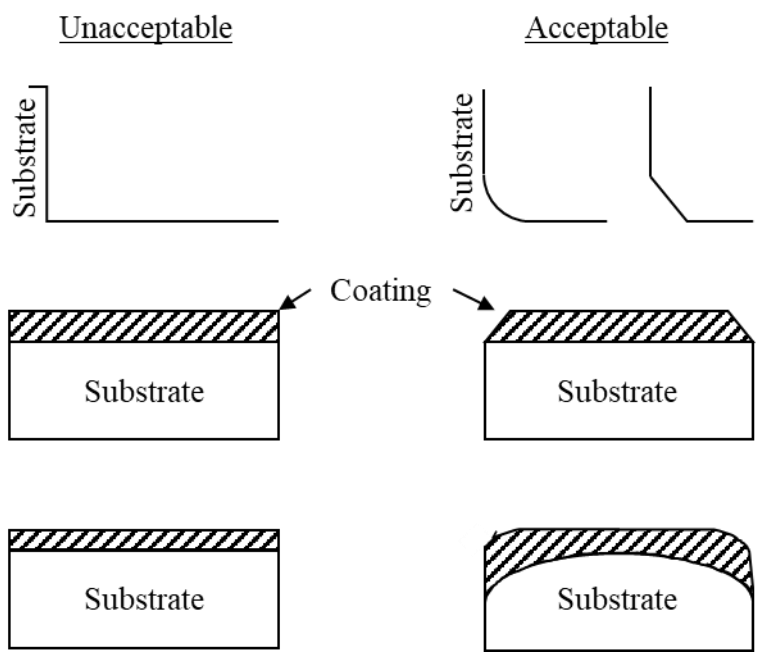

Figure 2.16 Acceptable and unacceptable examples for substrate geometries for thermal spraying [37].

Shaping can be performed by machining, grinding, or designed into the substrate depending on the application and coating material. Some substrates do not require shaping if they already have curved surfaces such as pipes, pistons, and rollers. The last step, activation, requires roughening the surface so that adherence is possible. The most common activation technique is abrasive grit blasting which involves hard grit particles accelerated to the surface by compressed air resulting in a roughened surface that the spray can anchor to. Commonly used grits include ceramic grits such as alumina or silica, and metals such as cast iron or steel in spherical or irregular shapes [38]. The size of the grit is selected based on the desired coating

characteristics with finer grits typically used for thinner coatings. The surface activation influences the adhesion strength, with higher surface roughness resulting in improved coating bonding.

2.3.4.2 Splat Formation

After a droplet impacts the substrate, it deforms into a splat which is the fundamental building block of the thermal spray coating [39]. As the splat flattens, heat is rapidly removed from the splat into the underlying substrate with solidification rates between 10^5 and 10^8 °C/s. The cooling rate is related to the degree of flatting that the droplet experiences on impact which is governed by droplet size, temperature, velocity, and material, as well as the thermal conductivity of the substrate [40]. A relationship between splat thickness and cooling rate has been developed and tested for various material systems [40, 41]. Table 2.3 shows the cooling rates versus splat thickness of an iron splat on a copper substrate. Particle deformation and solidification happen almost simultaneously and are dependent on such factors as wettability, substrate temperature, liquid droplet viscosity and surface temperature, and phase content within droplet between solid and liquid [10].

Table 2.3 Cooling rate vs. splat thickness for an Fe splat an Cu substrate and 30°C [41].

Splat Thickness (cm)	Average Cooling Rate (°C/s)
0.1 (1 mm)	8.1×10^3
0.01 (100 µm)	8.1×10^5
10^{-3} (10 µm)	8.1×10^7
10^{-4} (1.0 µm)	8.1×10^9
10^{-5} (0.1 µm)	8.1×10^{11}

Splats occur in two main morphologies called *pancake* and *flower* depending on the wetting between the splat and underlying layer. Wetting examples are shown in Figure 2.17 where increasing angle α improves wetting and results in a *pancake-type* splat permitting the formation of close contact between the substrate and splat lamella [42]. If the liquid droplet does not wet well with the substrate, the contact surface area is reduced resulting in a fragmentation of the droplet producing the *flower-type* splat.

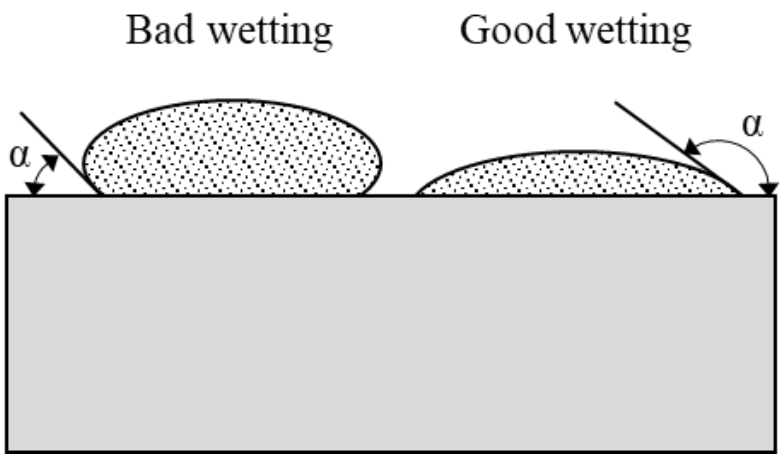

Figure 2.17 Good and bad wetting angles between splat and substrate [43].

Experimental results for plasma-sprayed niobium particles on steel, alumina, and glass substrates found that droplets impacting the steel and alumina formed *pancake-type* splats while droplets impacting the glass substrate exploded and formed the *flower-type* splat [44]. Due to the lower thermal conductivity of the glass, the splat maintained a higher temperature resulting in a higher contact temperature. The combination of weak wetting between the liquid niobium and higher contact temperature promoted the droplet fragmentation into flower morphology. The cooling rate of sprayed niobium particles on glass was approximately 5-6 $\times$ 10^7 K/s where on the steel substrate it was an order of magnitude higher at approximately 2×10^8 K/s.

Innumerous cases exist for how a splat can impact a substrate depending on factors such as particle oxidation, speed, substrate roughness, in-flight collision, and coating thickness effects [10]. In order to simplify the splat formation cases, it is useful to consider a single droplet impacting an idealized substrate. A range of cases was considered for the formation of plasma-sprayed ceramic thermal barrier coatings to develop models for splat formation with schematics for each case shown in Figure 2.18 [45].

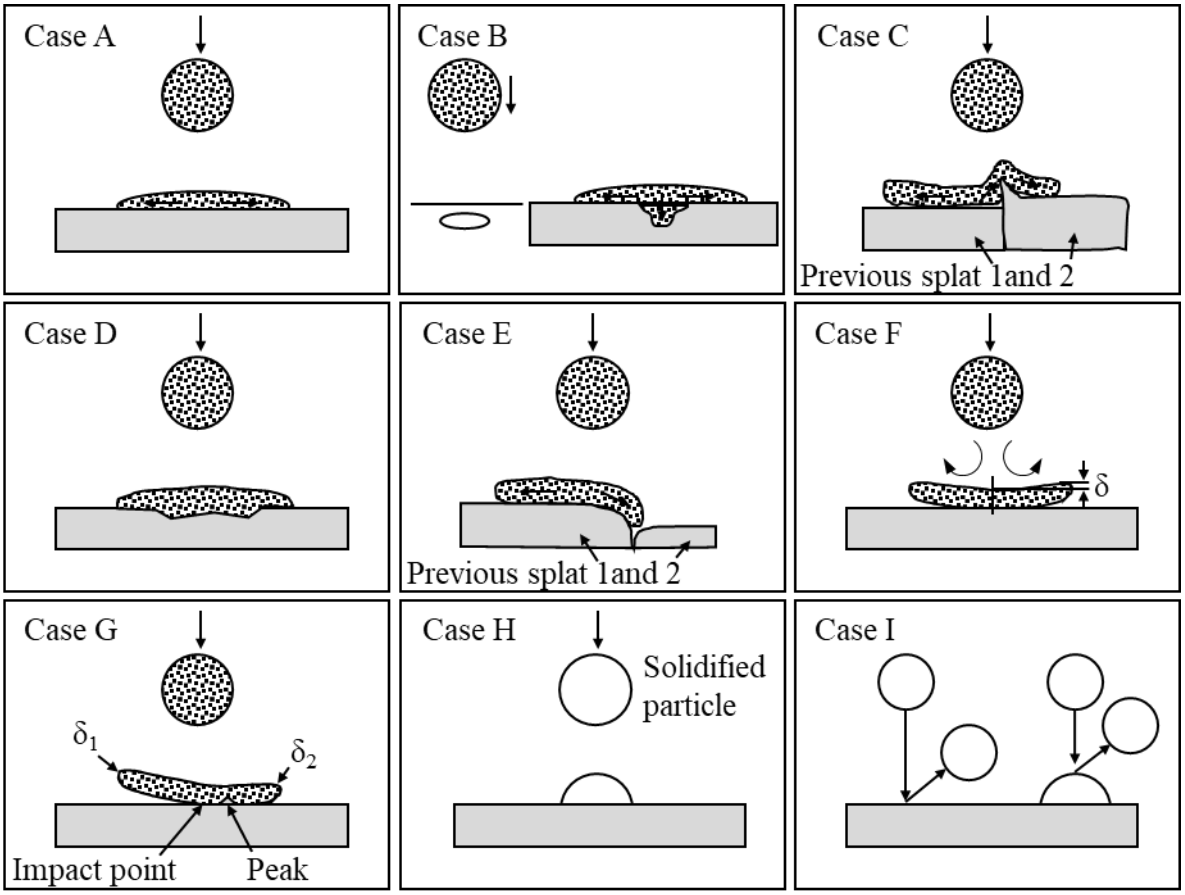

Figure 2.18 Various cases for droplets impacting the substrate [45].

Case A represents a splat forming on a flat surface with case B identical to case A but with porosity under the impact region restricting flattening. For case C, the splat encounters another splat boundary and must fill the space available before flowing over creating an interlocking mechanism. Cases D and E represent rough surfaces that the splat flows over with Case E experiencing a steep slope created by other splats which it flows down. Cases F and G, represent the top layer of the coating where the splat to curls up due to temperature differences between the top and bottom with Case G having a peak which pins the splat, modifying its curl. Lastly, Case H and I represent the impact of solidified solid droplets which impact and bounce off instead of adhering.

2.3.4.3 Splat Oxidation

After droplets impact, deforming into splats, oxides begin to form as cooling progresses. The top surface of the splat is exposed to oxygen containing atmosphere which oxidizes the surface as the splat cools. Oxide

layer thickness is several orders of magnitude less than the splat thickness where turbulent mixing of the splat liquid distributes oxides which slow down the solidification by decreasing the thermal diffusivity of the liquid phase [43]. Oxidation also contributes to splat splashing which results in greater oxidation. Increasing the splat initial temperature results in increased oxidation kinetics and splat solidification time both increasing the final oxide content. It has been observed for plasma sprayed molybdenum that increases in oxide content reduced the splat radius and increased the thickness as shown in Figure 2.19 [46]. This is due to an increase in liquid metal viscosity reducing flattening, as well as, a decrease in solidification rate at the bottom of the splat.

In addition to splat surface oxidation, oxides are also present under the splat from in-flight oxidation. Observation of thermal sprayed Ni – 5 wt. % Al by APS and TWAS found that oxides start to segregate towards the front of the droplet forming an oxide shell during flight which splashes under the metal splat upon impact [30]. This is shown schematically in Figure 2.20 where the dark region represents oxide shell spreading under the splat. This behavior was only observed for TWAS and APS and did not occur for HVOF spraying where in-flight oxidation was reduced due to higher particle velocities and lower temperature [47]. Without the formation of oxides during flight, the molten droplet instead contains dissolved oxygen which improves wetting and increases flattening [48].

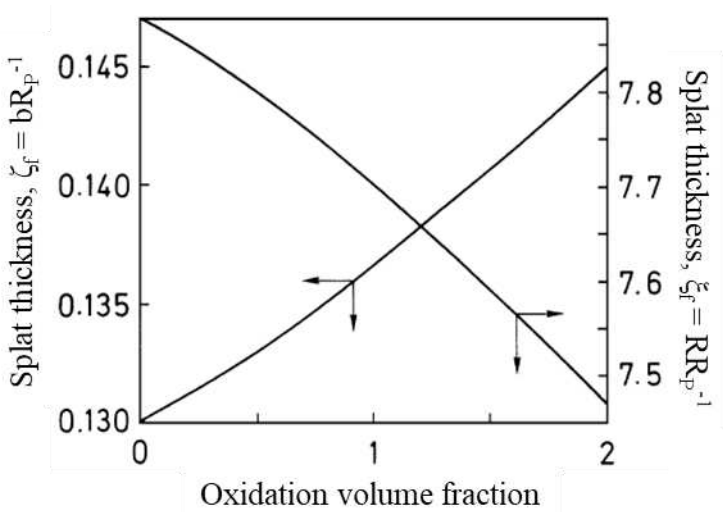

Figure 2.19 Splat thickness and radius versus oxidation volume fraction [46].

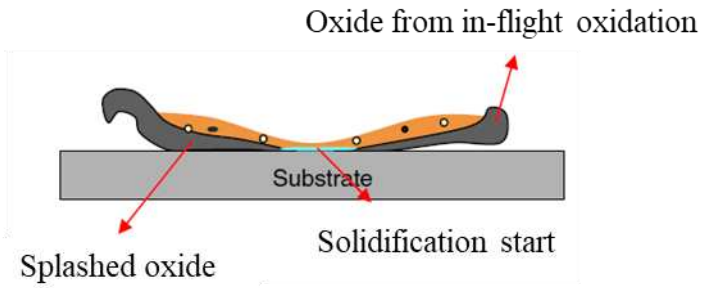

Figure 2.20 Schematic showing oxide shell splashing beneath splat [30].

2.3.4.4 Phase Transformations and Residual Stress

Molten droplets impact the substrate and undergo rapid solidification resulting in thermal contraction as the splat is restrained by the cooler underlying material [49]. This thermal contraction generates tensile stress in the splat known as quench stress which generates bulk residual stresses in the deposit that can lead to coating peeling, warping, and loss of dimensional tolerances [49-51]. Figure 2.21 shows a schematic of this process where (a) shows the molten droplet before impact, (b) shows the droplet deforming across the substrate with the rapid heat flow from the droplet to the underlying layer, and (c) showing the quench stresses present within the droplet.

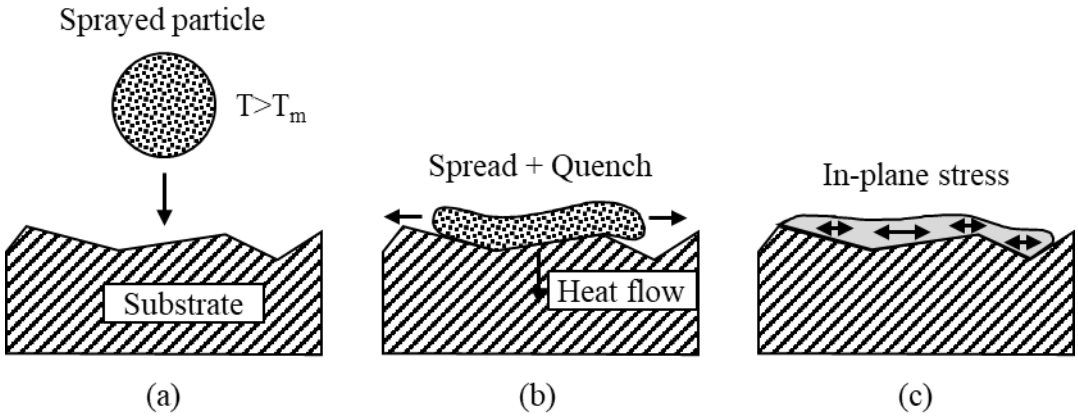

Figure 2.21 Origen of quench stress during thermal spraying progressing from before droplet impact (a), impact and quench (b), and splat stresses (c) [52].

A study was conducted on TWAS sprayed copper-coated, 1.6mm 38T wire (Fe-0.8 wt. %C) sprayed at various surface temperatures. The goal was to control the phases generated, namely the expansive bainite transformation, to counteract the tensile quench stresses [49]. In this study, a series of shells were manufactured with steady-state average temperatures ranging from 170°C and 450°C in 25°C intervals to determine the relationship between distortion and surface temperature. Spraying was carried out on steel plates as shown in Figure 2.22 with a spring-loaded linear position sensor that could measure distortion over spray time of the substrate and shell.

It was found that residual stress varied greatly with the substrate temperatures. Figure 2.23 shows that there were three shell states; concave distortion driven by thermal contraction tensile stress (quench stresses), convex distortion driven by phase transformation compressive stress, and zero distortion where compressive and tensile stresses balance [49]. The competing phases were the austenite and bainite, as the substrate temperatures were above the martensite start (M_s) temperature. The phase transformation paths can be viewed on the time-temperature-transformation (TTT) diagram shown in Figure 2.25 which estimates that the spay composition will behave similarly to 1018 steel. Path *a* represents the cooling path for a droplet impacting the substrate preheated to 200°C. In this case, splats experienced quench stresses from rapid cooling from A_1 = 723°C to 200°C which can be represented by:

$$\sigma_Q = \left(\frac{E}{1-v}\right)\alpha\Delta T \tag{2.5}$$

where E and v are the sprayed shell Young's modulus and poisons ratio respectively, α is the coefficient of thermal expansion, and ΔT is the change in temperature from A_1 to controlled surface temperature. This resulted in a σ_Q value of 937 MPa that caused the convex distortion shown in Figure 2.23.

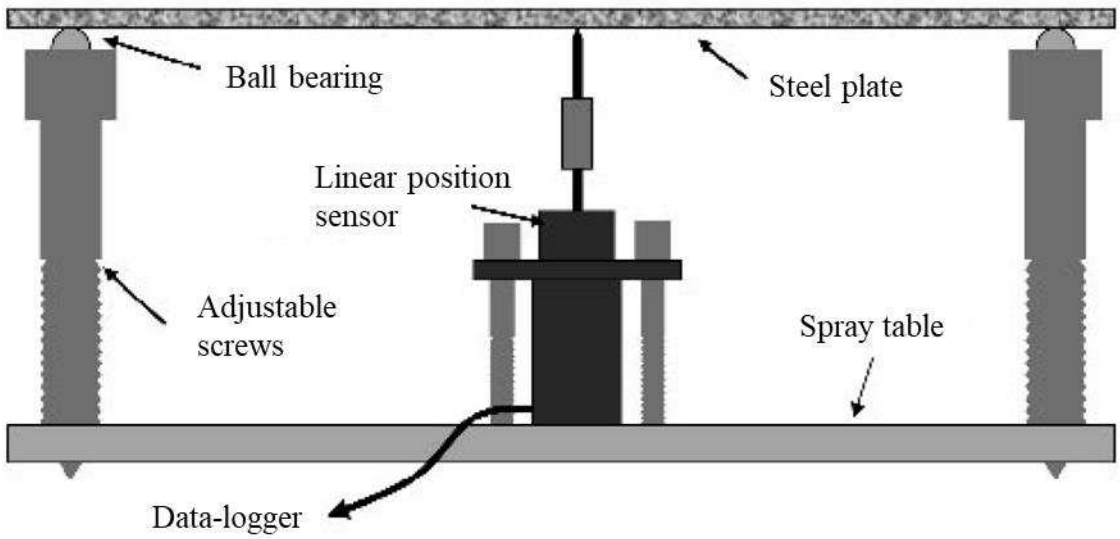

Figure 2.22 Schematic diagram for experimental set up for in-situ measurements of distortion [49].

Near the end of the spraying time for path *a*, some of the austenite was speculated to decompose to bainite but with slow kinetics. The limited expansive bainite transformation was not enough to counteract the tensile stresses and the convex distortion. For a surface temperature maintained at 255 °C during spraying, the cooling was expected to follow path *b*. Like with the 200 °C case, the quench rate was too rapid to allow diffusional phase transformations. However, unlike the 200 °C case, there was a significant time spent in the bainite region on the TTT diagram allowing the diffusional lower bainite transformation to take place for a significant volume fraction.

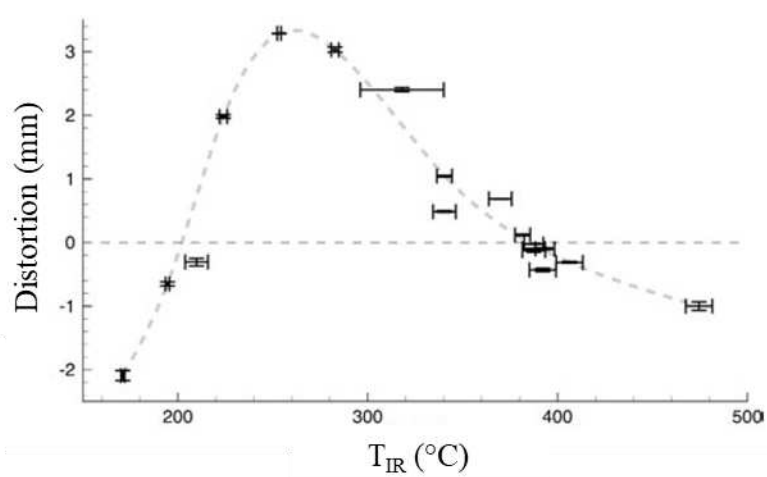

Figure 2.23 Schematic diagram for experimental set up for in-situ measurements of distortion [49].

The expansive transformation resulted in a net compressive stress state as observed in Figure 2.23. For path *c*, unlike the 255 °C case, bainite formation did not progress significantly over the spray time. This resulted in a net tensile or convex distortion like the 200°C case. This study showed that there existed a range of temperatures between approximately 210°C and 390°C where the expansive transformation dominated resulting in a net concave distortion. Thus, there are two temperatures where a net residual stress state of zero could be achieved. [49]

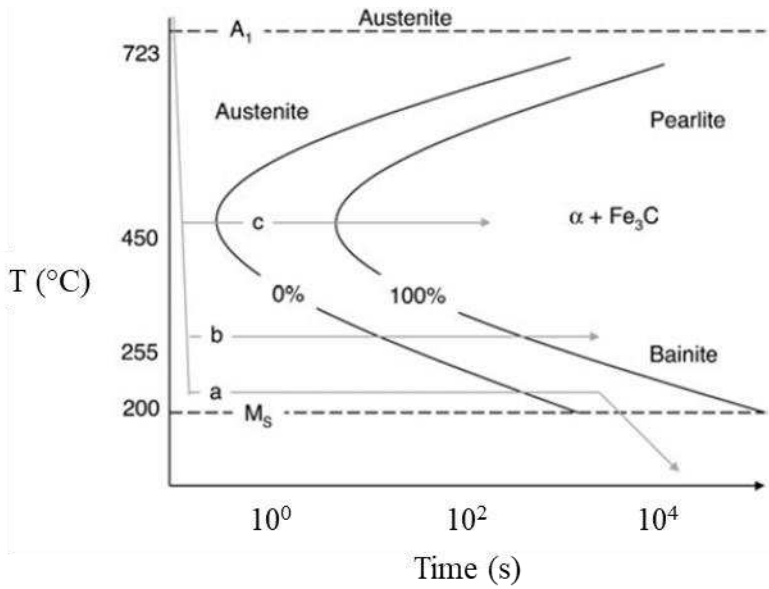

Figure 2.24 Schematic TTT diagram for electric arc sprayed steel showing cooling paths for shells sprayed with average temperatures of (a) 200 °C; (b) 255 °C; and (c) 450 °C [49, 53].

2.4 Process Parameters

Thermal spraying has many variables that can be manipulated to produce the desired finial coating structure. Thermal spray process variables are commonly categorized into manipulation control, time, temperature, and mass variables [54]. For TWAS, the manipulable variables include surface speed, standoff distance, pitch increment, and spray angle. Surface speed represents the relation between gun and part speeds, the standoff distance is defined as the distance between the gun-face and sprayed substrate, the pitch increments are the distances that the gun moves per pass or revolution example being the coating of a pipe set at some revolutions per minute (rpm) and forward advancing speed, and lastly the spray angle is given

as some angle between 0° and 90° to the substrate. The time variables include air pressure, atomizing gas characteristics, and arc characteristics. Air pressure can be influenced by various gun designs and greatly influences the jet speed [11, 15, 55]. Atomizing gas characteristics include gas type or mixture, density, and thermal conductivity. Arc characteristics are affected by voltage and amperage which influence material breakup, and thus, the speed and flow of sprayed material. The third process variable category is temperature and includes available energy, consumable material characteristics, and spray environment. The energy supplied to the system is governed by the input amperage and voltage as well as how quickly the material is being removed and thermal heat dispersed. Consumable material characteristics include wire composition, mass, thermal properties, electrical properties, and wire type such as solid or cored. The spray environment is defined as the atomizing gas type, spray speed, in-flight reactions such as oxidation, and distance the spray material has to travel which influence the droplet temperature on impact [54, 56].

2.4.1 Effect of Voltage

Arc voltage ranges typically from 20-40V and is set before spraying depending on the material, air pressure, and spray distance [10]. Input voltage influence the mean droplet size, droplet speed, and droplet impact temperature which are critical to final coating structure as it relates directly to cooling rates [9]. Studies on the iron sprays have found that as voltage is increased, the mean droplet diameter on impact was decreased [9, 57-59]. In a study of TWAS of Fe-0.8 wt. % C, it was found that mean droplet diameter decreased by approximately 15 μm when increasing the input voltage from 27 to 40 V [58]. Figure 2.25 shows the effect of voltage on mean solidified droplet diameter (d_m) produced by TWAS Fe-0.8 wt.% C 1.6 mm diameter steel wires using N_2 atomizing gas at 280 k Pa gas pressure and 3 gs^{-1} wire feed rate. Mean droplet diameter was determined by mounting the spray gun on the top of the 2.6 m vertical chamber and spraying without a substrate so that the droplets could fully solidify mid-air and be collected from the chamber base.

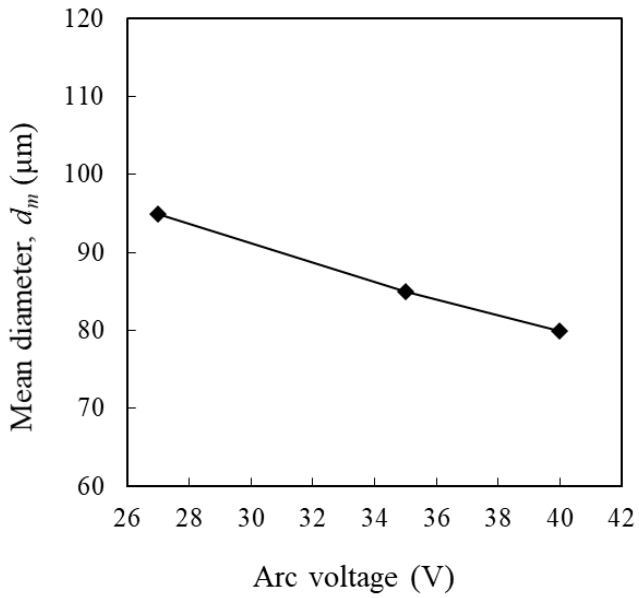

Figure 2.25 Effect of input voltage on mean solidified droplet diameter for TWAS Fe-0.8 wt.% C [58].

As voltage increased, droplet velocity decreased and temperature increased. A study using in-flight particle pyrometry on Fe-0.8 wt.% C TWAS found that as input voltage was increased from 27 to 41V the spray temperature increased from approximately 2000°C to 2200°C at a spray distance of 150 mm using nitrogen atomizing gas [57]. Increasing voltage leads to an increase in arc temperature resulting in more rapidly heated spray before leaving the arc. The decrease in droplet velocity was dependent on the spray distance. As voltage increased, droplet size decreased resulting in particles that were accelerated more rapidly; however, at the spray distance of 150 mm, these smaller droplets were more easily slowed down by the rapidly decreasing gas velocity. Figure 2.26 shows the effect of input voltage on velocity and temperature. The degree of influence voltage has on velocity and temperature was found to be different for different atomizing gasses depending on gas thermal properties and degree of exothermic oxidation that occurred.

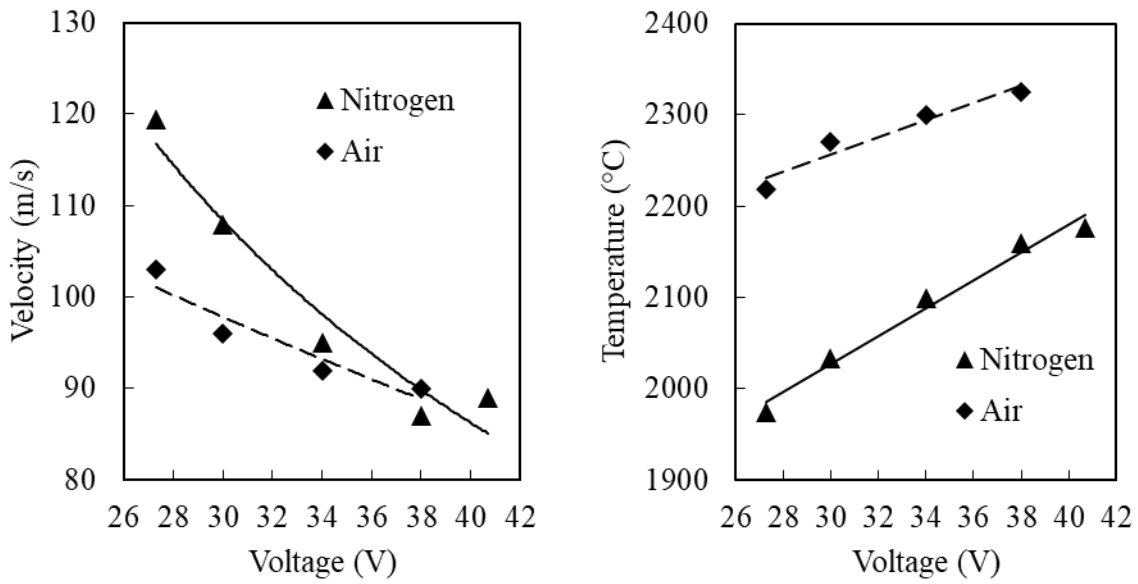

(a) (b)

Figure 2.26 The effect of arc voltage on spray velocity (a) and spray temperature (b) at a spray distance of 150 mm, spraying with air and nitrogen atomizing gasses at a pressure of 280 kPa and 3 g s^{-1} wire feed rate [57].

There exist voltage fluctuations during the formation of droplets that arise from the arc movement during spraying resulting in periodic removal of molten material from the wire tips. Newbery proposed that a relationship exists between arc voltage and droplet diameter that occurred in three stages [58]. Figure 2.27 (a) shows the voltage stages over time with Figure 2.27 (b) showing a schematic of the voltage stages as they relate to droplet formation. Stage 1 is when voltage is relatively high and the arc is stable, extending toward the wire tips. A small amount of molten material begins to form a layer and starts to build up at the wire tip. Stage 2 is characterized by a sharp drop in arc voltage as a result of the arc becoming unstable after the critical volume of molten material has developed at the wire tip. The critical molten metal volume is dependent on drag forces from the atomizing gas which removes the molten material. The rapid decrease in voltage occurs as the arc returns to the shortest wire separation. Stage 3 occurs after the molten droplets are removed and the arc begins to extend again before the cycle occurs again. This voltage cycle was measured during spraying using a software which logs time resolved voltages at 100 kHz over 2.62 s at steady state spraying.

As voltage increased, there was an increase in energy supplied to the arc resulting in a higher temperature arc [60]. Higher arc temperature results in faster melting and, as a result, the wire tips grow further apart and increase the arc width. Higher temperature molten material has reduced viscosity and surface tension reducing the time for material removal with increased velocity resulting in a reduction of d_m [58].

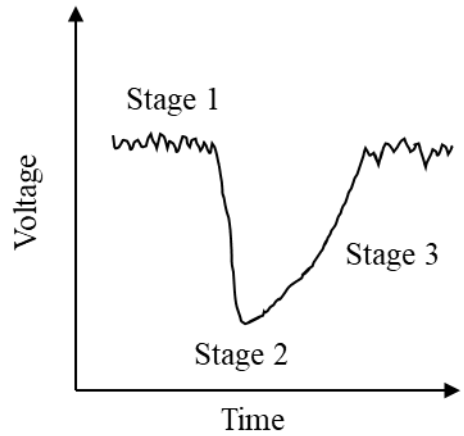

(a)

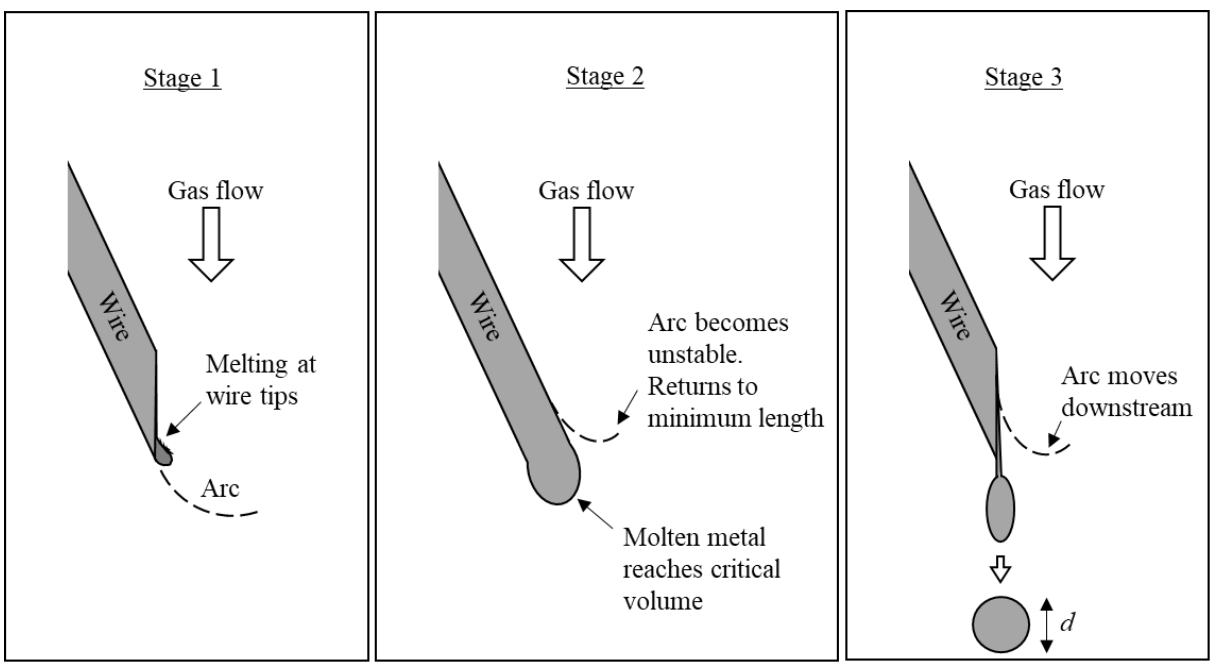

(b)

Figure 2.27 Voltage stages with respect to time (a) and schematic showing droplet formation at wire tip during each stage (b) [58].

2.4.2 Effect of Amperage

For TWAS, amperage relates directly to wire feed rate. Amperage can be controlled between 15-400 amps [16]. Changes in amperage affect deposition rates, spray temperature, and droplet velocities. The effects of the amperage are more complex because for increases or decreases in feed rate there is a machine calibrated electric current adjustment supplied to the arc to compensate and help maintain stable melting and deposition [58]. A study was conducted on Fe-0.8 wt. % C steel wires sprayed at various amperages with results presented as wire feed rate [57]. Thus, even though amperage is a controllable parameter on the TWAS machine, it is more practical to provide wire feed rate because electric current is constantly being adjusted to maintain this value.

It was found that increased wire feed rate reduced the spray velocity, as shown in Figure 2.28 (a), as a result of the increased mass in the jet stream. Wire feed rate had little effect on the spray temperature as shown in Figure 2.28 (b). This is because the molten material can be removed at a certain temperature where the liquid viscosity and surface tension are low enough for the atomizing gas to remove it. Thus, material is removed at approximately the same temperature regardless of the feed rate [57].

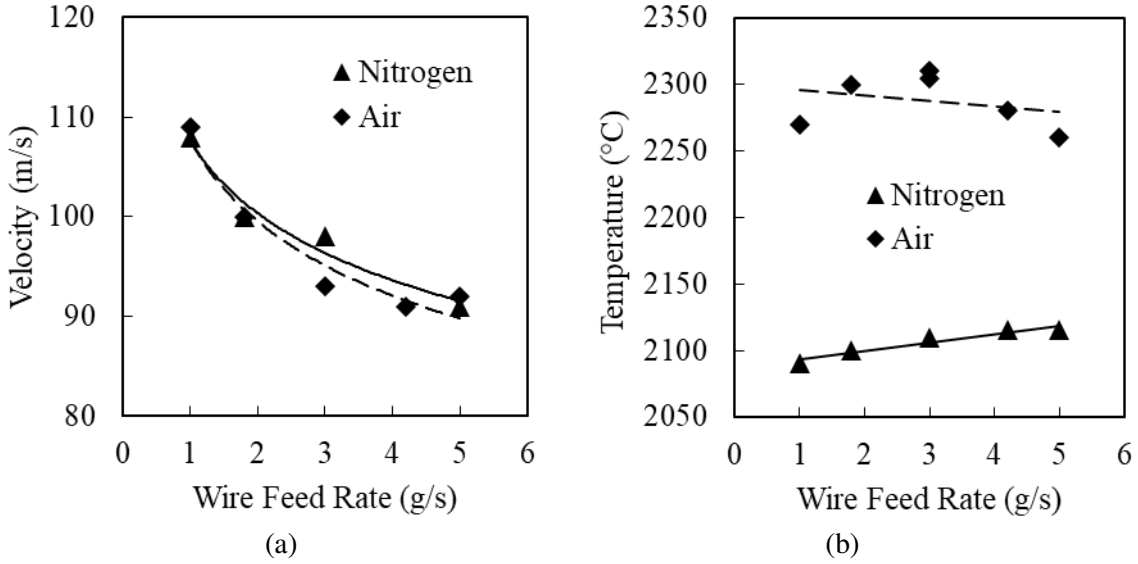

Figure 2.28 The effect of wire feed rate on spray velocity (a) and spray temperature (b) at a spray distance of 150 mm, spraying with air and nitrogen atomizing gasses at a pressure of 280 kPa and 34V arc voltage [57].

Amperage also has an effect on the droplet diameter. As wire feed rate increases, droplet diameter increases as shown in Figure 2.29 [58]. Increasing the amperage results in an increase in wire feed rate thus increasing the amount of material melted per unit time. More material builds up at the wire tips before being removed, resulting in an increase of droplet diameter. Steel has been selected as the example for the amperage effects on velocity, temperature, and size; however, it is worth noting that every power supply design works differently with different alloys. Table 2.4 provides spray rates and amperage for various materials [9].

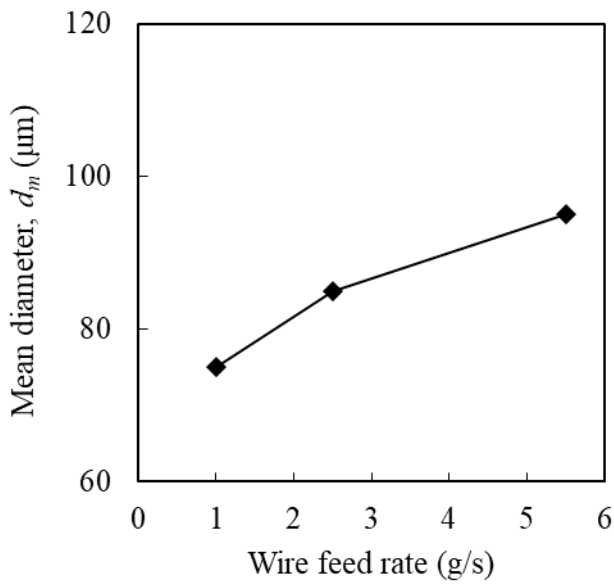

Figure 2.29 Effect of wire feed rate on mean solidified droplet diameter for TWAS Fe-0.8C [58].

Table 2.4 TWAS rates for various materials [9].

Wire	g/min (lb/h)/100 A dc
Aluminum	45 (6)
Steel	76 (10)
Stainless steel	76 (10)
Tin	341 (45)
Titanium	23 (3)
Zinc	182 (24)

2.4.3 Effect of Air Pressure and Atomizing Gas

Air pressures typically used for TWAS range between 100 to 700 kPa [10]. Increasing gas pressure increases spray velocity, decreases spray temperature, and reduces droplet size [9, 10, 57]. The most commonly used atomizing gasses used for TWAS are nitrogen and dried processed air. A study on the effect of atomizing gas pressure for TWAS of Fe-0.8 wt. % C steel found that when air pressure was increased from 140 to 410 kPa, spray velocity increased by 50 m/s as shown in Figure 2.30 (a) [57]. In this study it was also found that over this pressure range, spray temperature 150 mm from the spray gun was reduced by 80°C which is shown in Figure 2.30 (b) [57]. Similar findings were also reported for AS850 cored wires and solid nickel wires [59].

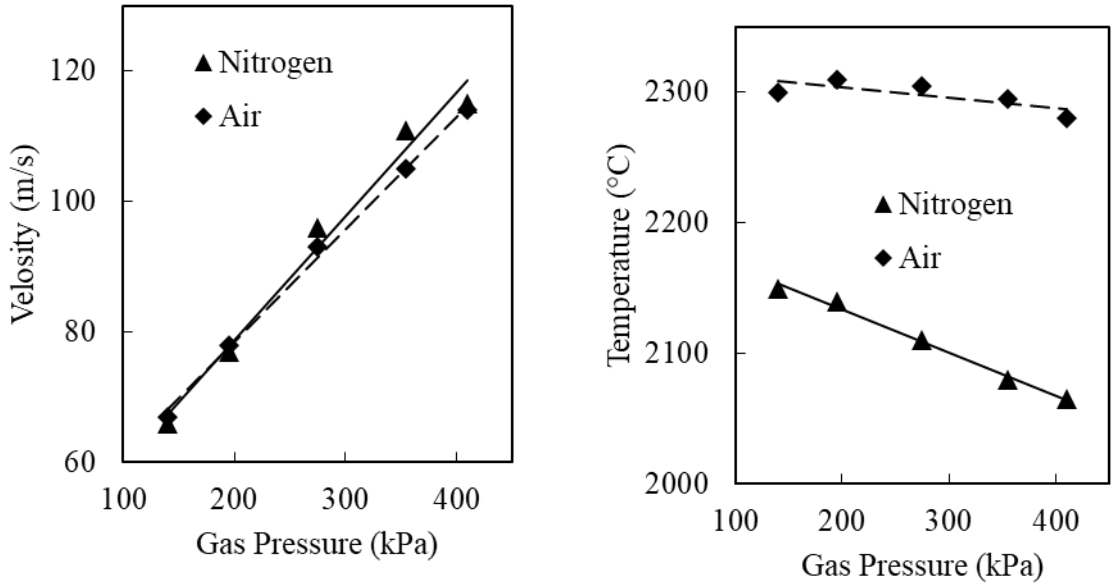

(a) (b)

Figure 2.30 The effect of gas pressure on spray velocity (a) and spray temperature (b) at a spray distance of 150 mm, spraying with air and nitrogen atomizing gasses at a wire feed rate of 3 g/s and arc voltage of 34 V [57].

Atomizing gas type does not have a significant effect on spray velocity but has a significant effect on spray temperature as shown in Figure 2.30 (b) where at any given pressure the spray temperature of air was over 100°C greater. Oxidation reactions occur at a much higher rate when spraying with air due to the oxygen content which is not as present when spraying with nitrogen [14]. The oxidation reactions are

exothermic and significantly raise the temperature of the arc. Additionally, higher spray pressures also increase oxide content which is why the temperature difference between nitrogen and air increased at higher pressures [12, 57].

Air pressure has the greatest process parameter effect on mean particle size. This is because the main factor generating droplets are the drag forces removing molten material from the wire tips within the arc. For Fe-0.8 wt. % C steel TWAS, droplet diameter was reduced by more than half when increasing the gas pressure from 150 to 550 kPa which is shown in Figure 2.31 [58].

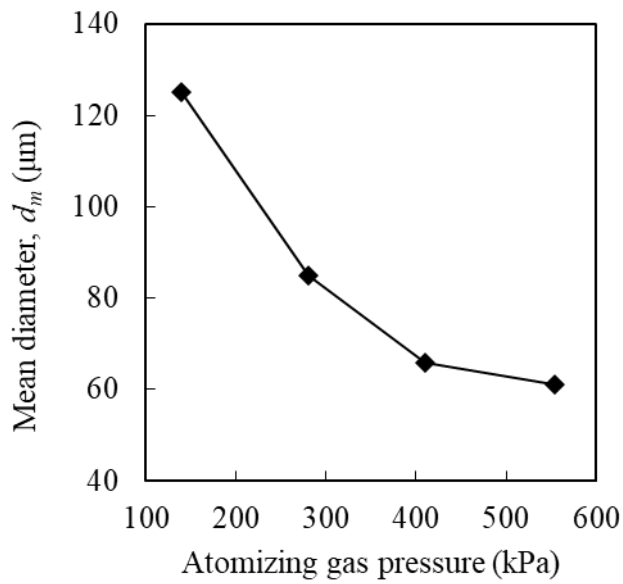

Figure 2.31 Effect of atomizing gas pressure on mean solidified droplet diameter for TWAS Fe-0.8C [58].

2.4.4 Effect of Spray Distance

Spray distance, along with velocity, determine how long a droplet will be in flight which influences the droplet impact temperature and velocity. Figure 2.32 shows the relationship between velocity and temperature for TWAS sprayed Fe-0.8 wt. % C steel wires [57]. As expected, the mean droplet temperature continuously decreases for increased spray distances due to the droplet loosing heat to the surrounding jet stream. Velocity, on the hand, reaches a maximum value at some spray distance before continuously

decreasing. This is because droplets are accelerated by the atomizing gas to a maximum velocity at some spray distance before the droplets begin to be slowed by drag forces of the rapidly decreasing gas velocity.

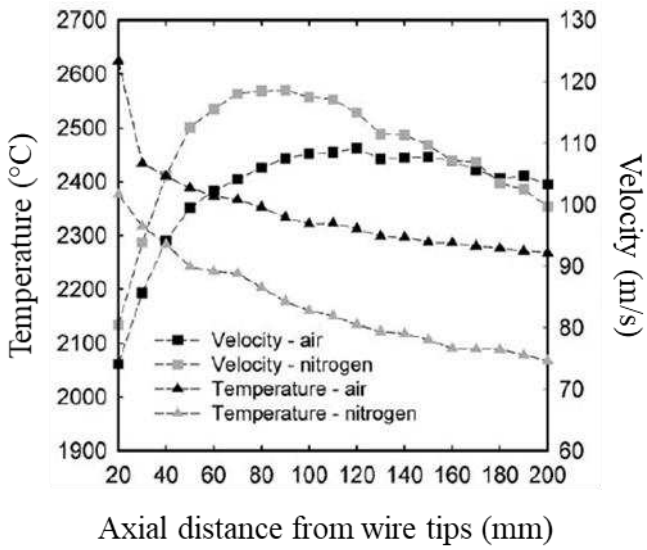

Figure 2.32 Effect of spray distance and atomizing gas type on mean droplet temperature and velocity for TWAS Fe-0.8C sprayed at 34 V arc voltage, atomizing gas pressure of 280 kPa, and wire feed rate of 1 g/s [57].

As was previously shown in Figure 2.14, increasing the spray distance results in a larger volume fraction of the droplet solidified before impact as was observed for spray forming of 7150 Al powders [33]. The microstructure of the coating is heavily dependent upon the solidification condition of the impinging droplet where the solidified dendrites fracture upon impact and act as nucleation sites. This creates a mix of small grains from the rapid solidification and large grains from the in-flight solidification.

2.5 Solidification Modeling

2.5.1 Early Theoretical Model

Early modeling of the thermal spray atomization and deposit was performed by Madejski which determined the degree of flattening of the solidifying droplets [61]. The problem consists of the two simultaneous processes of the liquid motion and of the solidification. The model was related to experimental measurements of individual droplets of alumina (Al_2O_3) as shown in Figure 2.33 sprayed at a velocity of 200 ms^{-1} with droplet diameters of $4 \cdot 10^{-5}$ m [61].

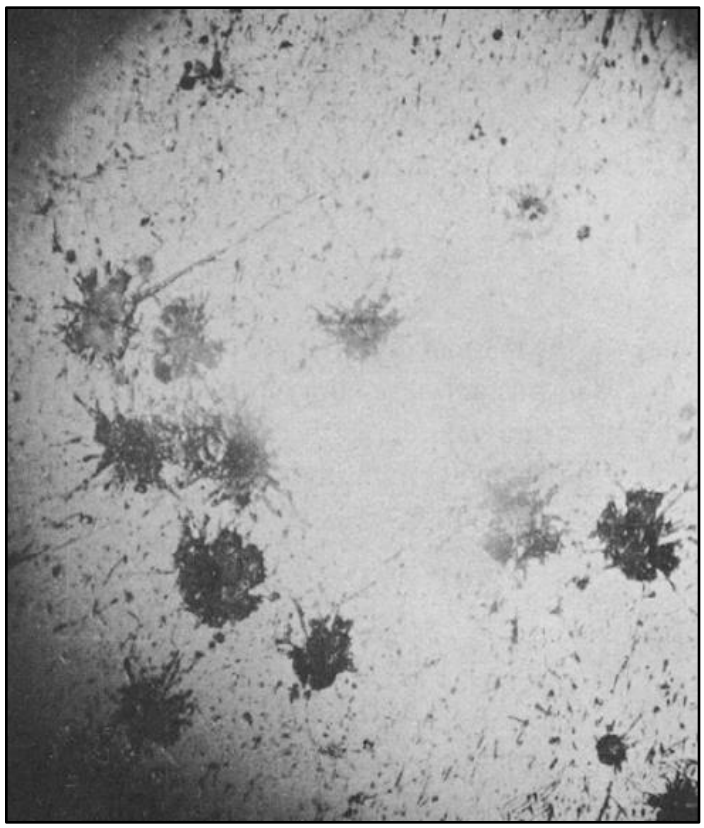

Figure 2.33 Photograph of alumina disks obtained from plasma spraying [61].

The area covered by the droplet was estimated by the ratio shown in Equation (2.6) where ξ_m is the maximum flattening ratio, D is the droplet diameter, and A is the surface area covered by the droplet. Initial theoretical calculations assume the splat is a regular circle as opposed to the jagged shape shown in Figure 2.33 for the model. Thus, a droplet of diameter D impinging perpendicularly on the cold surface flattens to form a cylinder shaped splat of radius $R(t')$ growing at time t'. See Figure 2.34 for a visual of calculation model.

$$\xi_m = \frac{2}{D}\sqrt{\frac{A}{\pi}} \tag{2.6}$$

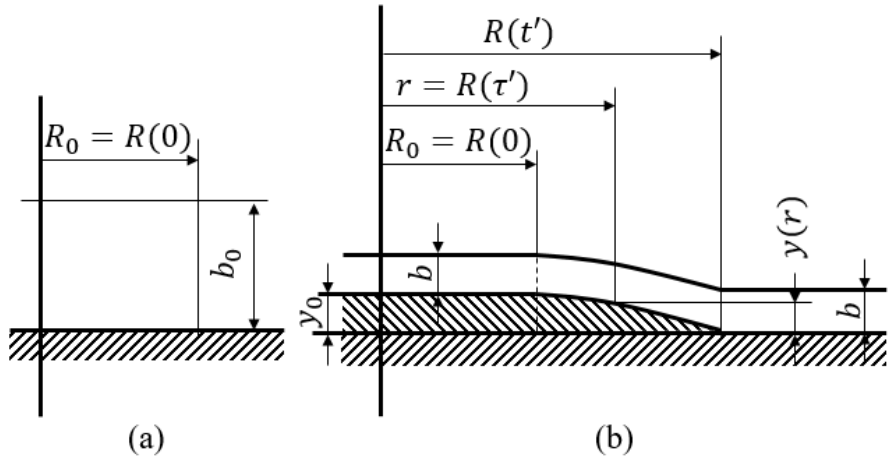

Figure 2.34 Droplet flattening schematic for calculations [61].

The solidified layer (y) is greater in the center than on the periphery because of radius growth. From the Stephan problem, thickness is then:

$$y = U\sqrt{at'} \tag{2.7}$$

The value a is the thermal diffusivity of the layer and U is the freezing constant depending on the Jakob number. Freezing begins at r in the moment τ' when $r = R(\tau')$. For $r > R_0$ there is:

$$y(r) = U\sqrt{a(t' - \tau')} \tag{2.8}$$

For $r < R_0 = R(0)$ there is:

$$y_0 = U\sqrt{at'} \tag{2.9}$$

The volume of the solid layer can be calculated as:

$$V_s = \pi R_0^2 y_0 + \int_{\tau'=0}^{\tau'=t'} 2\pi R(\tau') \cdot y \cdot dR(\tau') \tag{2.10}$$

or

$$V_s = \pi R_0^2 U\sqrt{at'} + \int_0^{t'} 2\pi R(\tau') \frac{dR(\tau')}{d\tau'} U\sqrt{a(t' - \tau')} d\tau' \tag{2.11}$$

Using the simplifying assumption that liquid layer thickness b depending only upon the time t'. Therefore the mass balance of the disk can be represented as:

$$m = \frac{\pi}{6} D^3 \rho' = \rho V_s + \pi R^2 b \rho' \tag{2.12}$$

where, m is the mass balance of the droplet, b is the liquid layer thickness, ρ is the density of the solid, and ρ' is the density of the liquid. The layer can then be represented by the function:

$$b(t') = \frac{\frac{\pi}{6}D^3\rho' - \rho V_s}{\pi R^2 \rho'} \tag{2.13}$$

The motion or flattening of the disk droplet is described by the energy equation:

$$\frac{d}{dt'}\left(E_k + E_p + L_f\right) = 0 \tag{2.14}$$

where E_k is the kinetic energy, E_p is the potential energy, and L_f is the work friction forces.

Velocity field functions (velocity distribution) used to determine the kinetic energy and work of friction are:

$$w_x = -Cx^2 \tag{2.15}$$

and

$$w_r = Cxr \tag{2.16}$$

The variables w_x and w_r are the velocity components with the constant term C expressed in terms of the disk expansion ($\frac{dR}{dt'}$). The continuity equation can then be fulfilled as:

$$\frac{\partial}{\partial r}(rw_r) + \frac{\partial}{\partial x}(rw_x) = 0 \tag{2.17}$$

Next, the disk expansion average velocity on the periphery can be represented by the expression:

$$\frac{dR}{dt'} = \frac{1}{b}\int_0^b w_r dx = \frac{CbR}{2} \tag{2.18}$$

where

$$C = \frac{2}{Rb}\frac{dR}{dt'} \tag{2.19}$$

From there the kinetic energy can then be calculated as:

$$E_k = 2\pi \int_0^R r dr \int_0^b dx \cdot \frac{1}{2}\rho'(w_x^2 + w_r^2) \tag{2.20}$$

The kinetic energy equation can then be modified by using Equations (2.15), (2.16), and (2.19) to achieve the following expression:

$$E_k = \frac{\pi}{3}\rho'\left(\frac{dR}{dt'}\right)^2 \cdot \left(bR^2 + \frac{6}{5}b^3\right) = E_k(t') \tag{2.21}$$

At the start time (t') of zero, the value of kinetic energy (E_k) is that of the falling droplet. Thus, this can be expressed as:

$$E_k(0) = \frac{\pi}{6}D^3\rho'\frac{w^2}{2} \tag{2.22}$$

The initial radius can then be assumed as some portion of droplet diameter given by:

$$R(0) = R_0 = \varepsilon D \tag{2.23}$$

where D is the droplet diameter and ε constant representing the relation between the splat radius and droplet diameter. The initial radial expansion of the splat is then calculated as:

$$\frac{dR(0)}{dt'} = w\sqrt{\frac{\frac{3}{2}}{1 + \frac{1}{30\varepsilon^6}}} \tag{2.24}$$

The work of friction mentioned in Equation (2.14) can now be represented by friction power expression:

$$\frac{dL_f}{dt'} = \int_0^R 2\pi r dr \tau \overline{w_r} \tag{2.25}$$

The shear stress (τ) can be related to dynamic viscosity (μ) by:

$$\tau = \mu\frac{\partial w_r}{\partial x} = \mu C r = \frac{2\mu r}{Rb}\cdot\frac{dR}{dt'} \tag{2.26}$$

The average radial velocity is expressed as:

$$\overline{w_r} = \frac{1}{b}\int_0^b w_r dx = \frac{r}{R}\frac{dR}{dt'} \tag{2.27}$$

From here the shear stress Equation (2.26) and the average radial velocity Equation (2.27) can be substituted into the friction power Equation (2.25) to get:

$$\frac{dL_f}{dt'} = \frac{\pi R^2\mu}{b}\cdot\left(\frac{dR}{dt'}\right)^2 \tag{2.28}$$

Potential energy due to the surface tension (σ) acting on the disk surface is:

$$E_p = \sigma(\pi R^2 + 2\pi R b) \tag{2.29}$$

The energy will be equal to the potential energy of the droplet at $t' = 0$ and is given by:

$$E_{pg} = \pi\sigma D^2 \tag{2.30}$$

Though, by substituting the initial radius as a portion of the droplet diameter from Equation (2.23) the potential energy can then be calculated as:

$$E_p(0) = \pi\sigma D^2\left(\varepsilon^2 + \frac{1}{3\varepsilon}\right) \tag{2.31}$$

The model, however, does not have a value for the constant ε that will satisfy $E_{pg} = E_p(0)$. To work around this, $\varepsilon = 0$ is assumed resulting in an error value of 8% for the initial value of potential energy.

Continuing with the model, the dimensionless variables for the radius, thickness, and time are introduced as:

$$\xi = \frac{R}{R_0} \tag{2.32}$$

$$\varphi = \frac{b}{R_0} \tag{2.33}$$

$$t = \frac{wt'}{R_0} \tag{2.34}$$

As well as, introducing the Weber, Reynolds, and Péclet expressions:

$$We = \frac{\rho' D w^2}{\sigma} \tag{2.35}$$

$$Re = \frac{\rho' D w^2}{\mu} \tag{2.36}$$

$$Pe = \frac{wD}{a} \tag{2.37}$$

and the parameter:

$$k = 6\varepsilon^2 U \frac{\rho}{\rho'}\sqrt{\frac{\varepsilon}{Pe}} \tag{2.38}$$

Taking now the kinetic energy Equation (2.21), friction power Equation (2.28), potential energy Equation (2.29) with the dimensionless variable Equations of (2.35), (2.36), and (2.37), as well as, the Weber, Reynolds, and Péclet numbers and parameter k and substituting all into the energy of flattening the disk droplet Equation (2.14), the following equation is achieved:

$$\frac{d}{dt}\left[\frac{\varepsilon}{3}\dot{\xi}\varphi\left(\xi^2+\frac{6}{5}\varphi^2\right)+\frac{1}{We}\xi(\xi+2\varphi)\right]+\frac{\xi^2\dot{\xi}^2}{\varphi Re}=0 \tag{2.39}$$

where

$$\varphi=\frac{1}{6\varepsilon^3\xi^2}\left\{1-k\left[\sqrt{t}+2\int_0^t\xi(\tau)\dot{\xi}(\tau)\sqrt{t-\tau}d\tau\right]\right\} \tag{2.40}$$

The point over the dimensionless disk radius variable (ξ) denote differentiation with respect to the dimensionless time. Boundary conditions are expressed as:

$$\xi(0)=1 \text{ and } \xi(0)=\sqrt{\frac{\frac{3}{2}}{1+\frac{1}{30\varepsilon^6}}} \tag{2.41}$$

With this the solution for $\xi(t)$, the maximum value ξ_m at $\dot{\xi}=0$ can be found. This value, as defined in Equation (2.6), is a function of constant *k*, *Re*, and *We*. The general formula for ξ_m is difficult to find and, as such, several cases were viewed numerically by Madejski [61]. When $k=0=Re^{-1}$, it was found that:

$$\xi_m=\sqrt{\frac{We}{3}} \tag{2.42}$$

for $We>100$ and for $k=0=We^{-1}$ the equation becomes:

$$\xi_m=1.2941(Re+0.9517)^{\frac{1}{5}} \tag{2.43}$$

for $Re>100$. This can be simplified resulting in

$$\xi_m=1.2941Re^{\frac{1}{5}} \tag{2.44}$$

The equation for the flattening of a droplet without solidification when $k=0$ is thus given as:

$$\frac{3\xi_m}{We}+\frac{1}{Re}\left(\frac{\xi_m}{1.2941}\right)^5=1 \tag{2.45}$$

Provided the conditions are met where $We > 100$ and $Re > 100$ illustrates this relationship between the flattening degree and solidification parameter k. It was found that for the cases where $Re^{-1} = 0 = We^{-1}$, the degree of flattening could be expressed by the approximate formula:

$$\xi_m = 1.5344k^{-0.395} \tag{2.46}$$

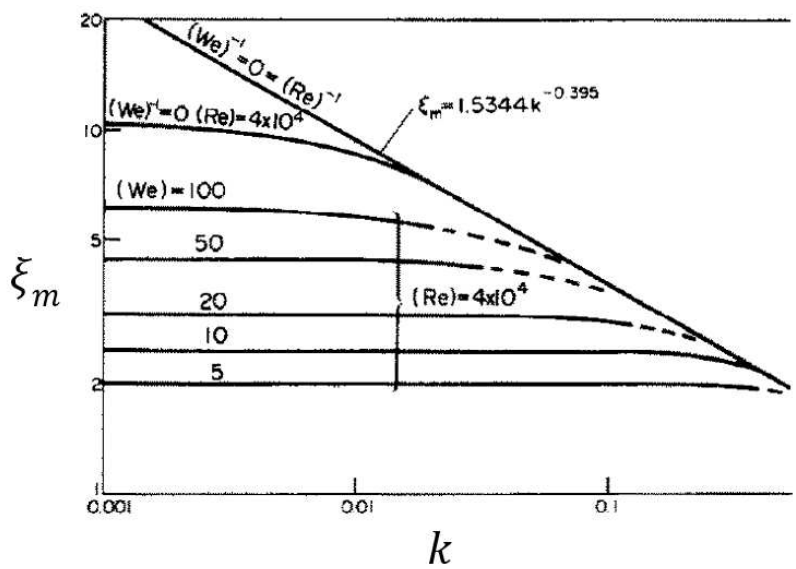

Figure 2.35 Flattening degree for the solidification case ($k > 0$) [61].

In order to determine the freezing constant (U) during the experiment, the Stefan problem was expressed for solidification of a half-space super-heated liquid of temperature $T_p' > T_s'$. Stephan problem can then be written as:

$$\frac{U}{2}\sqrt{\pi} = \frac{T_0}{\left[erf\frac{U}{2} + \sqrt{\frac{\lambda c\rho}{\lambda_f c_f \rho_f}}\right] e^{\frac{U^2}{4}}} - \frac{T_p\sqrt{\frac{\lambda' c' \rho'}{\lambda c \rho}}}{erfc\left(\frac{U}{2}\sqrt{\frac{a}{a'}}\right) \cdot \exp\left(-\frac{U^2 a}{4a'}\right)} \tag{2.47}$$

where

$$T_0 = \frac{\lambda(T_s' - T_0')}{a\rho\Delta h} \text{ and } T_p = \frac{\lambda(T_p' - T_s')}{a\rho\Delta h} \tag{2.48}$$

The initial temperature of the mold is represented by T_0', Δh is the latent heat of fusion, T_s' is the temperature of fusion, λ_f is the heat conductivity of the mold, c_f is the specific heat of the mold, ρ_f is the density of the mold, and a_f is the thermal diffusivity of the mold ($a_f = \frac{\lambda_f}{c_f \rho_f}$).

It was observed that the thermal properties of the cold surface that the droplets solidify on had no impact on the value of ξ_m. The isothermal case in which $\sqrt{\frac{\lambda c \rho}{\lambda_f c_f \rho_f}} = 0$ could be expressed as:

$$T_0 = \frac{\lambda(T_s' - T_0')}{a\rho\Delta h} = \sqrt{\pi}\frac{U}{2}\mathrm{erf}\left(\frac{U}{2}e^{\frac{U^2}{4}}\right) \tag{2.49}$$

Through experimentation, it was found that the theory of one-dimensional flow of liquid was inadequate to predict the behavior [61]. Madejski analytical model outlined above for $We^{-1} = 0 = Re^{-1}$, gave slightly lower values for ξ_m as compared with actual values. Further developments would need to be incorporated into the model to better predict flattening and broaden its application to more material systems.

2.5.2 Recent Modeling Developments

Resent thermal spray modelling work by Ha have included the aspect of a rough surface which is more common among thermal spray operations [62]. This work was an advancement on previous numerical models and experiments performed by Pasandideh-Fard *et al.* [63] and Tong and Holt [64] which predicted the fluid flow of the impacted droplet and heat transfer to substrate. Defects on the surface were shown to have an effect on the droplet formation and spreading.

The model first considers the simple condition of a single droplet deposit on the substrate as shown in the Figure 2.36 schematic. The fluid flow model considers the Navier-Stokes equation with two-dimensional axisymmetric incompressible flow [65]. In the model the stationary solid substrate Θ does not undergo a phase change. Continuity and momentum equations are considered and are given as:

$$\nabla \cdot (\Theta \mathrm{V}) = 0 \tag{2.50}$$

and

$$\Theta\frac{\partial V}{\partial t} + \nabla \cdot (\Theta \mathrm{VV}) = -\frac{\Theta}{\rho}\nabla p + \frac{\Theta}{\rho}\nabla \cdot \tau + \Theta \mathrm{F}_b + \Theta \mathrm{S} \tag{2.51}$$

where Θ corresponds to a cell without a substrate volume fraction, S is the Darcy source term modeling the velocity reduction of the solidified droplet, V is velocity (m/s), t is time, ρ is the density (kg/m^3), τ is the viscous stress tensor, and F_b the body force.

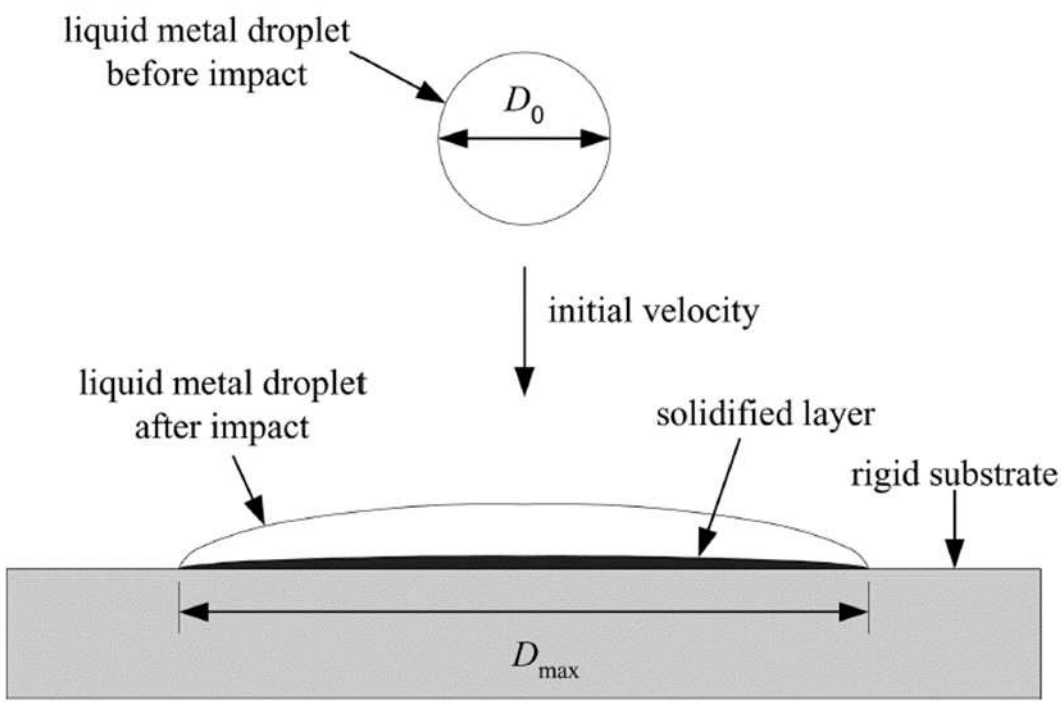

Figure 2.36 Schematic of thermal spray deposition [64].

for the two step projection, Equation (2.51) can be approximated as:

$$\Theta\frac{\tilde{V}-V^n}{\delta t} = -\nabla\cdot(\Theta VV)^n + \frac{\Theta}{\rho}\nabla\cdot\tau^n + \Theta F_b{}^n \tag{2.52}$$

and

$$\Theta\frac{V^{n+1}-\tilde{V}}{\delta t} = -\frac{\Theta}{\rho}\nabla p^{n+1} \tag{2.53}$$

where $\tilde{V}$ is the auxiliary velocity computed from incremental change in V^n, and *n* is the old time value.

Equations (2.50) and (2.53) can be combined as a single pressure Poisson equation:

$$\nabla\cdot\left[\frac{\Theta}{\rho^n}\nabla p^{n+1}\right] = \frac{\nabla\cdot\left(\Theta\tilde{V}\right)}{\delta t} \tag{2.54}$$

The volume-of-fluid (VOF) transport equation is given as the function F. Surface tension is modeled using volume forces:

$$\frac{\partial}{\partial t}(\Theta \mathrm{F}) + \nabla \cdot (\Theta \mathrm{FV}) = 0 \tag{2.55}$$

In order to determine the surface tension the use of the continuum surface force (CSF) method was employed which interprets surface tension as a continuous, three-dimensional effect, across an interface, rather than as a boundary value condition on the interface [66]. This method was used with the volume force to achieve the following expression:

$$\mathrm{F}_b = F_{sv} = \sigma_K \nabla F \tag{2.56}$$

where F_{sv} is the continuous surface force and σ_K is the surface tension. From here the adhesion bound at the contact of fluid meeting the wall or a solidified obstacle can be calculated using a unit vector normal to the free surface in the same manner of volume forces:

$$\hat{n} = \hat{n}_w \cos\theta + \hat{t}_w \sin\theta \tag{2.57}$$

The unit vector normal to the free surface is given as $\hat{n}$, $\hat{n}_w$ represents the unit vector normal to the wall, $\hat{t}_w$ is the unit vector tangent to the wall, θ is the static contact angle between fluid and substrate. The static contact angle on the substrate had grooves and ridges with the angle assumed to be 90° as the average value of moving contact angles.

The solidification process can be described by the energy equation (2.58) where g is the volume fraction of the non-solidified metal droplet versus total droplet volume. The specific heat (c), temperature (T), thermal conductivity (k), and latent heat of fusion (ΔH) can then be expressed together as:

$$\frac{\partial}{\partial t}(\rho c T) + \nabla \cdot (\rho c V T) = \nabla \cdot (k \nabla T) - \rho \Delta H \frac{\partial g}{\partial t} \tag{2.58}$$

Equation (2.58) can then be integrated to get the non-linear equation:

$$a_P T_P^{m+1} = a_P^n T_P^n + \sum_{nb} a_{nb} T_{nb}^{m+1} + \rho \Delta H (g_P^n - g_P^{m+1}) \tag{2.59}$$

where m is the iteration level, and nb are the neighboring nodes to the node point P. Using a Taylor series, the g^{m+1} term can then be expanded to:

$$g^{m+1} = g^m + \frac{dg}{dT}(T^{m+1} - T^m) \tag{2.60}$$

Substitute Equation (2.60) into Equation (2.59), the linear source term can then be expressed as:

$$\left(a_P + \rho\Delta H\frac{dg}{dT}\right)T_P^{m+1} = a_P^n T_P^n + \rho\Delta H\frac{dg}{dT}T_P^m + \sum_{nb} a_{nb}T_{nb}^{m+1} + \rho\Delta H(g_P^n - g_P^m) \tag{2.61}$$

The mushy region momentum equation can now be modified by this source term to get:

$$S = -\frac{C(1-g)^2}{g^3 + \varepsilon}V \tag{2.62}$$

where C represents the porosity of the solidified metal droplet with ε as a constant.

A comparison was drawn between the mathematical model and experimental results for tin droplets impacting a stainless steel substrate which is shown in Figure 2.37. The model predicts the behavior accurately for times less than three seconds; however, after that the model predicts a faster solidification at the edge [63]. It was estimated that the difference is due to the model which is two-dimensional axisymmetric not able to predict the three dimensional instability [62].

With developments of modelling of the droplet solidification on a smooth surface, more complex models could be developed that considered surface roughness. Various surface roughness conditions were considered and are shown in Figure 2.38. It was found that all surface defects greatly reduced the spreading of the droplet and affected the splat diameter and the thickness [62]. For both groove types, air gaps were observed as the droplet solidified before filling in the bottom with the rectangular grove having large pores in the bottom corners and the triangle grove having one at the bottom point. For the ridge conditions, the solidification layer is not uniform and forms a pore on the side of the ridge away from the droplet impact. These pores hinder heat transfer between the splat and substrate resulting in reduced solidification thickness directly above the pore.

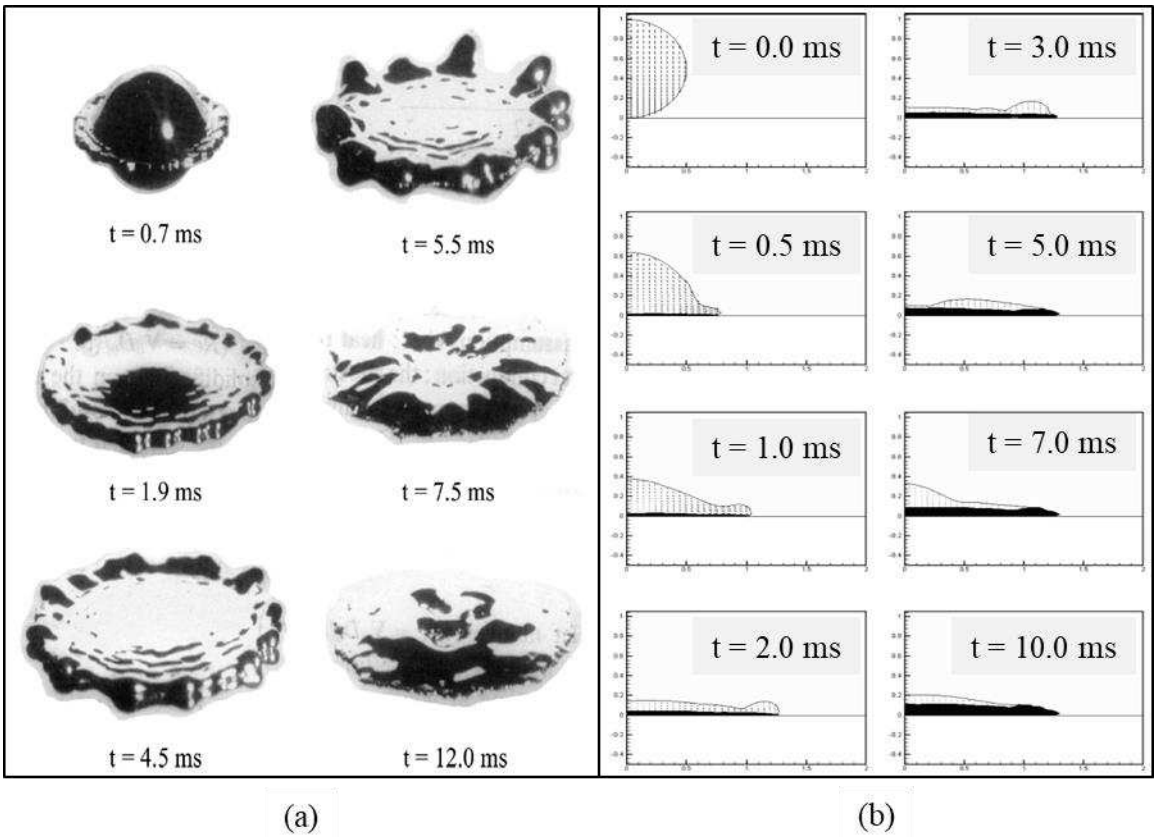

Figure 2.37 Photograph of the solidification sequence of a liquid tin droplet on a flat stainless steel substrate [63] (a) and the calculated spreading and solidification (b) [62].

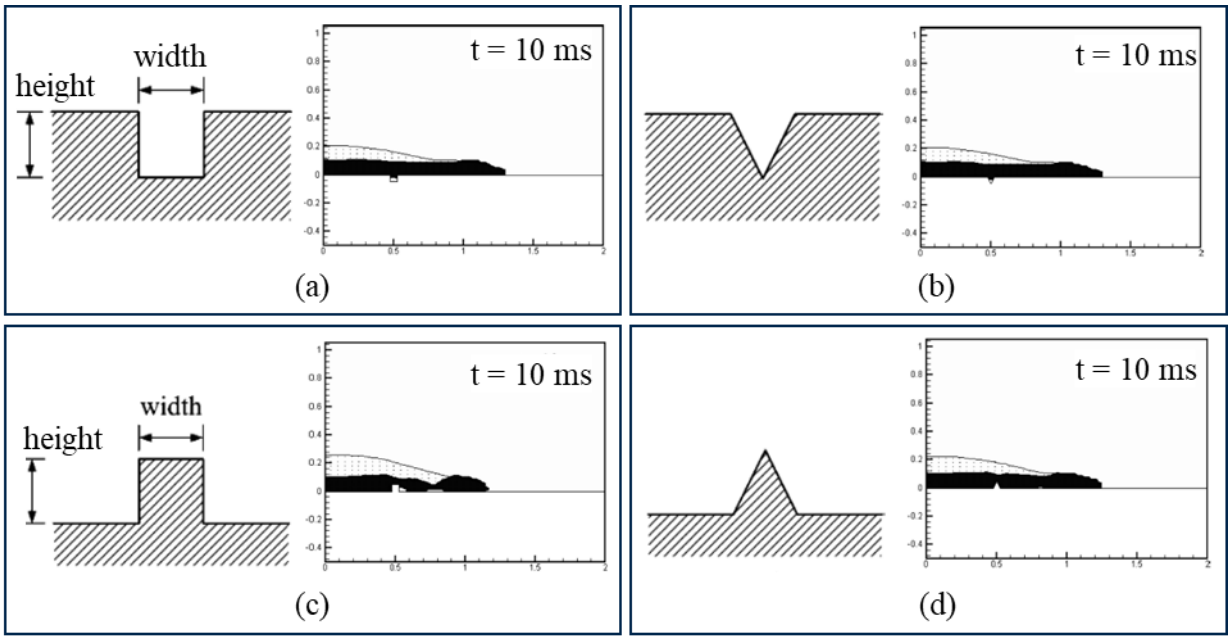

Figure 2.38 Rough surface geometry types with the shape of the modeled splat. Rectangular groove (a), triangular groove (b), rectangular ridge (c), and triangular ridge (d) [62].

These models however are limited to the first droplets solidification and may not accurately predict next layer of droplets solidification behavior where the substrate, being the last deposited layer, is not at the same temperature. Interfacial heat transfer plays a key role in droplet spreading behavior. Figure 2.39 shows the modeled solidification behavior with a nickel droplet plasma sprayed onto a stainless steel substrate at 300°C [67]. The solidification model uses the enthalpy-porosity method for the melt interface and the FLUENT software with β representing the liquid fraction parameter [68]. The total enthalpy is calculated as the sensible enthalpy h and the latent heat, ΔH.

$$H = h + \Delta H \text{ where } h = h_{ref} + \int_{T_{ref}}^{T} CpdT \tag{2.63}$$

The solidification interface (mushy zone) are represented by values of β between 0 and 1. In this zone the solid and liquid phases exist together with boundary conditions of:

$$\beta = \begin{cases} 0 & if\ T < T_{solidus} \\ 1 & if\ T > T_{liquidus} \\ \dfrac{T - T_{solidus}}{T_{liquidus} - T_{solidus}} & if\ T_{solidus} < T < T_{liquidus} \end{cases} \tag{2.64}$$

Latent heat of liquid, *L*, dissipates as the temperature decreases and is represented as:

$$\Delta H = \beta L \tag{2.65}$$

The solidification is calculated in the whole velocity field for this method and treats the mushy zone as a porous medium. The velocity goes to zero when the computation cell is fully solidified. The source term $\vec{S}_m$ can then be represented as:

$$\vec{S}_m = \frac{(1-\beta)^2}{(\beta^2 + 0.01)} A_{mush} \vec{v} \tag{2.66}$$

where β is the liquid fraction and A_{mush} is the mushy zone constant. It was found that the liquid nickel droplet-air interface with bubble formation could be accurately modeled. Material jetting occurred from the rapid growth of the bottom solid layer which causes fluid instabilities near the surface. An increase in substrate temperatures from 27°C to 300°C was found to slow solidification and promote substrate melting.

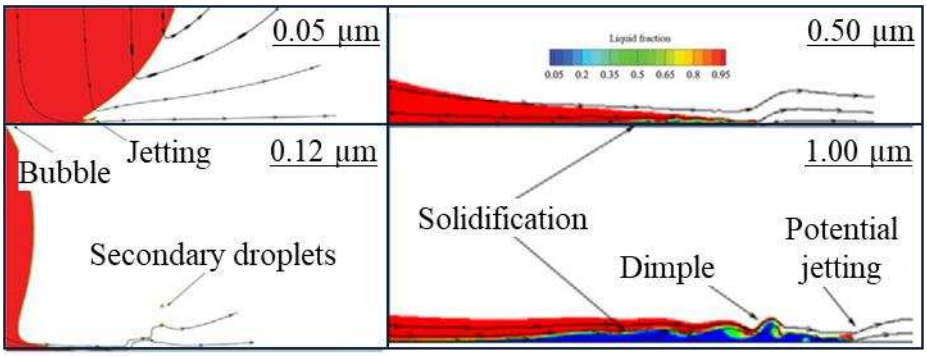

Figure 2.39 View of droplet spreading showing flow and solidification for four times of 0.05, 0.12, 0.50, and 1.00 µm [67].

2.6 Thermal Sprayed High Entropy Alloy Coatings

In the last decade, high-entropy alloys (HEAs) have gained increasing interest for their favorable mechanical and corrosion resistant properties. However, due to the high percentage inclusion of more expensive elements such as Nb, W, Cr, V, and Ni, the use of these materials has aroused interest as a film or coating on lower cost material substrates [69]. Thermal spray, which is used across a wide variety of industries improve key performance factors such as wear and corrosion resistance, offers an effective process to apply HEAs. Due to the limited literature on TWAS sprayed HEA coatings, this section will focus on the thermal spraying of HEA coatings by atmospheric plasma spraying (APS) as this process has similar temperatures, oxidizing environments, and particle velocities to TWAS.

2.6.1 HEA Overview

The HEA term was first coined by Yeh in the 1996 thesis which described an alloy system with 5 or more components and contained far fewer phases than the maximum possible predicted by the Gibbs phase rule [70]. The recent, well-accepted, definition of HEAs is a crystalline system based on four or more elements that each constitute between 5-35 at. % having a microstructure containing at least one random solid solution (RSS) phase [71]. Thus, as long as there is at least one RSS phase, the HEA may include intermetallic, ordered and/or precipitate phases, and additional alloying elements less than 5 at. %. With the expansive amount of alloys that fit this definition, HEAs have been further classified into single phase HEAs, multi-phase HEAs, and complex engineering HEAs. Recent studies of thermally sprayed HEAs

have focused on wear-resistant coatings that contain a RSS, ordered phases, and precipitate phases, thus classified as complex HEAs [72, 73].

2.6.2 HEA Principles

HEAs, as a new class of materials, have exhibited a wide range of properties from increased strength and toughness maintained at elevated temperatures outperforming superalloys [74], to HEAs having two times the wear resistance of SUJ2 bearing steel [72]. Yeh proposed four core effects distinguishing HEAs: high-entropy, severe lattice distortion, sluggish diffusion, and the cocktail effect [75]. The first three core effects represent the initial hypotheses and have been critiqued based on published data collected over the past 12 years. The fourth, "cocktail" effect, is more of a separate characteristic of HEAs as opposed to a hypothesis [74, 76].

2.6.2.1 High Entropy Effect

The high entropy effect is the namesake concept of HEAs and proposes that increasing the configurational entropy will favor a RSS over competing intermetallic (IM) phases. Yeh defined HEAs as having mixing entropies larger than 1.5R, where R is the ideal gas constant. This is based on the ideal configuration entropy of a 5-element alloy being 1.61R [77]. Configurational entropy is calculated as:

$$\Delta S_{config} = -R \sum_{i=1}^{n} X_i \ln X_i \tag{2.67}$$

where X_i is the concentration of the *i*th constituent. The configuration entropy is approximated to represent the mixing entropy as it is considered the dominant term compared with vibrational, electronical, and magnetic contributions [78].

Miracle critiqued this definition, and highlights that entropy-based definitions have conceptual problems, as the ideal configurational entropy of disordered solid solutions ($S^{SS,\ ideal}$) can poorly estimate total entropy (S^{SS}). Of the four major terms (H^{SS}, S^{SS}, H^{IM}, S^{IM}), no single term or pair of terms consistently dominates phase selection [74]. It is more practical to consider the compositional based definition as opposed to the entropy-based definition. In this sense, multi-principle element alloys (MPEAs) and

complex, concentrated alloys (CCAs) which evoke the essential features of the field and do not imply a magnitude of entropy offer more appealing acronyms.

2.6.2.2 Severe Lattice Distortion

The severe lattice distortion effect, in the RSS phase, arises from the atomic misfit and is an extension of the solid solution strengthening mechanism in conventional alloys. However, because there is no difference between solute and solvent, every lattice site experiences some displacement. This effect is depicted in Figure 2.40, showing the distortion of a body center cubic (BCC) crystal by one component alloy and then by a five component HEA [79]. This distortion has been shown experimentally with the diminished x-ray diffraction peak intensities as the number of constituent elements was increased from pure Cu to the HEA system AlSiCrFeCoNiCu [80].

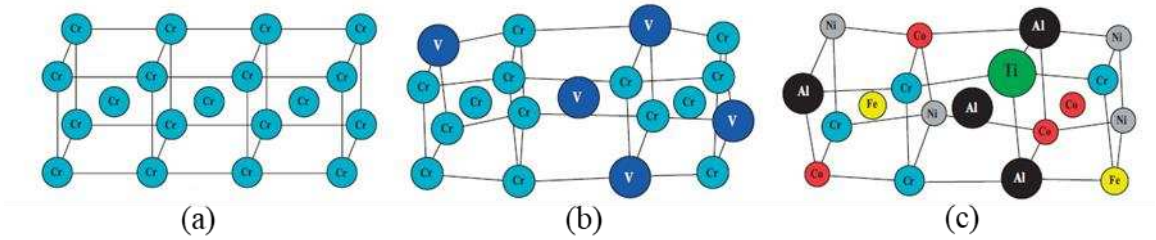

Figure 2.40 Schematic of a BCC crystal (a) perfect lattice, (b) distorted lattice by one component with a different atomic radius, and (c) severe lattice distortion by many different sized atoms [79].

This severe lattice distortion has been linked to increased hardness, reduced electrical and thermal conductivity, and reduced temperature dependence of these properties [81]. It should be noted that there still exists missing evidence separating the severe lattice distortion effect from other possible contributions such as shear modulus mismatch, hardening contribution, or local bond state's influence on electrical and thermal conductivities [74].

2.6.2.3 Sluggish Diffusion

Sluggish diffusion refers to a decrease in diffusion kinetics, compared with pure materials, caused by local lattice potential energy fluctuations caused by the varying constitute elements forming deep traps which inhibit diffusion. This was supported by results showing that CoCrFeMnNi HEAs had the slowest

self-diffusion rate compared with austenitic steels and pure metal systems [82]. The sluggish diffusion effect has only been studied in a few publications and further, carefully designed, experiments are needed [71].

2.6.2.4 Cocktail Effect

The fourth core effect refers to the selection of elements for an HEA composition based on the properties of that element, like a composite of elements [71]. This "core effect", unlike the other effects, is not a hypothesis and requires no proof but as Miracle describes it "the 'cocktail' effect reminds us that exceptional materials properties often result from unexpected synergies" [74].

2.6.3 Wear Resistant HEA Coatings

APS is commonly used to apply thermal barrier coatings (TBC) to turbine blades or aero-engine parts that operate at elevated temperatures [72]. As previously discussed in Section 2.2, APS is the process by which an arc is generated between an anode and the cathode which ionizes the flowing gasses into the plasma state. Powder feedstock is injected into the plasma jet, melted, and propelled to substrate [83] as shown in the schematic provided in Figure 2.41. Plasma arc temperatures are typically 20,000°C and capable of melting any element [9]. $Ni_{0.2}Co_{0.6}Fe_{0.2}CrSi_{0.2}AlTi_{0.2}$, AlCoCrFeNiTi, $FECoCrNiMo_{0.2}$ are three recently published thermal sprayed HEAs coatings that have promising wear resistance and high-temperature properties [72, 73, 84].

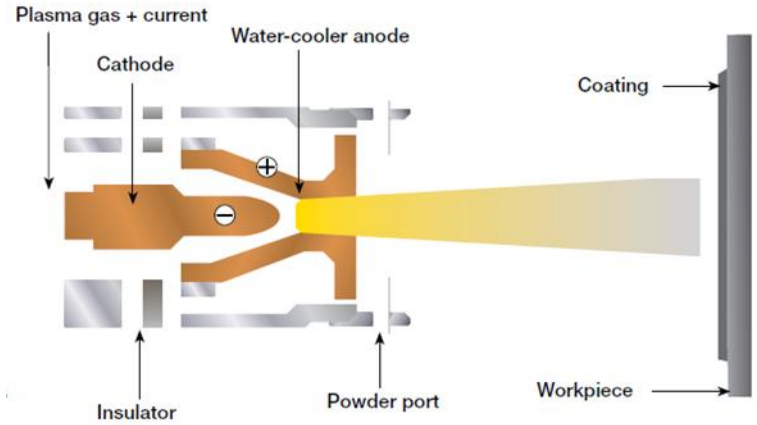

Figure 2.41 Schematic of atmospheric plasma spraying process and apparatus [83].

2.6.3.1 Thermal Sprayed $Ni_{0.2}Co_{0.6}Fe_{0.2}CrSi_{0.2}AlTi_{0.2}$

$Ni_{0.2}Co_{0.6}Fe_{0.2}CrSi_{0.2}AlTi_{0.2}$ HEA TBC was proposed by Hsu (2017) as an alternative to advanced bond coatings such as MCrAlY (M=Co and/or Ni) which often fail due to high-temperature wear of turbine blades [72]. The coating was applied by APS to a thickness of ~200 µm and compared to the as-sprayed condition and heat treated condition (800°C heating for 10 h and air cooled). It was found that the as-sprayed coating was composed of a lamellar structure of the gray phase and dispersed oxide stringers that formed during the high-temperature spraying process as shown in Figure 2.42 (a). The grey phase was determined by X-ray diffraction (XRD) to be one major BCC structure and the oxides determined with an energy-dispersive spectrometer (EDS) to be a mixture of Ti-Cr-Al oxides. The as-sprayed coating had a hardness of 429-450 HV. After heat treating, precipitation (white phase) occurred in the major grey phase. XRD and EDS determined the white phase to be Cr3Si, with microstructure shown in Figure 2.42 (b). After heat treating the hardness increased to 790-800 HV. The precipitation hardened HEA coating exhibited good room temperature wear resistance of 20 m/mm^3 which was significantly higher than conventional bearing steel SUJ2 (12 m/mm^3).

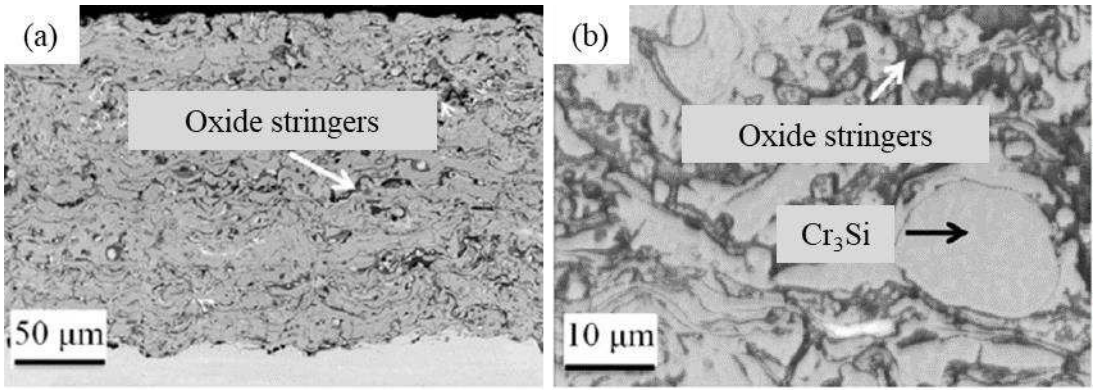

Figure 2.42 Cross section view of (a) as-sprayed and (b) heat treated HEA coating [72].

2.6.3.2 Thermal Sprayed AlCoCrFeNiTi

An AlCoCrFeNiTi HEA coating was recently studied by Tain (2016) using APS as this spray method is widely used in aerospace, petrochemical, and mining industries to apply wear resistant coatings [73]. Co, Cr, Fe, and Ni were selected due to their similar atomic diameters [85]. Al and Ti additions were added

with larger atomic radii to increase hardness and wear resistance by a solution strengthening mechanism [86]. 316 stainless steel substrates were sand-blasted and sprayed to a thickness of approximately 240 µm. XRD, bond-strength, hardness, and (ambient and elevated) wear testing was conducted. The microstructure of the as-sprayed coating was found to be a major BCC matrix phase with minor FCC phase and ordered BCC detected by XRD. Figure 2.43 (a) shows an SEM image of the full coating thickness with (b) showing a magnified region within the coating. Regions A and B correspond to the BCC matrix and ordered BCC phases, region C corresponds to the FCC phase, and regions D and E correspond to oxides that formed during spraying. The average hardness of the coating was 642 HV, approximately four times that of the substrate, and exceeded the hardness (432 HV) of previous spark plasma sintering of the same alloy [87]. The increase was attributed to the lower porosity of plasma spraying, lattice distortion of the BCC phase from Al and Ti atoms, and formation of hard oxides within the coating. No change in structure was observed after the elevated (500°C) wear test. However, after elevated wear testing above 700°C, significant changes in structure were observed as the FCC and ordered BCC phase precipitated from the BCC matric phase. In addition, tetragonal σ-CrFe precipitates and Fe_3O_4 and TiO_2 oxides were observed to form.

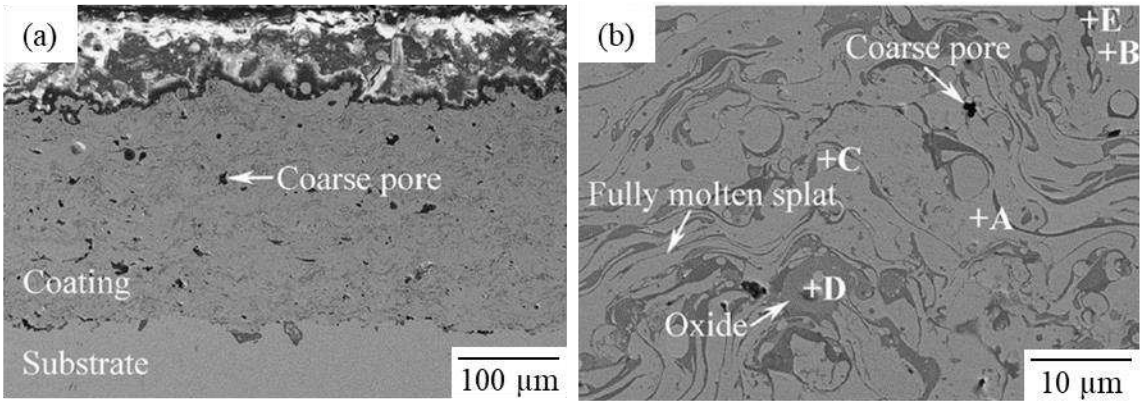

Figure 2.43 SEM images of the cross-section of the as-sprayed AlCoCrFeNiTi coating taken at (a) lower and (b) higher magnification [73].

Surface morphology revealed major adhesive wear with minor abrasion wear for temperatures between 25 and 500°C and tribo-oxidation and abrasion wear for temperatures between 700 and 900°C. At temperatures below 500°C, splats are pulled away due to the limited inter-lamellar bonding between splats

and coating as well as inter-splat oxides reducing the bonding between the metallic splats. Room temperature (25°C) wear surface is shown in Figure 5 (a). At temperatures between 700 and 900°C, oxygen diffusion promotes tribo-oxidation wear as shown in Figure 5 (b). The tribo-oxidation process involves the formation of an oxide film that acts as a solid lubricant preventing metal-metal contact and reducing the coefficient of friction [88].

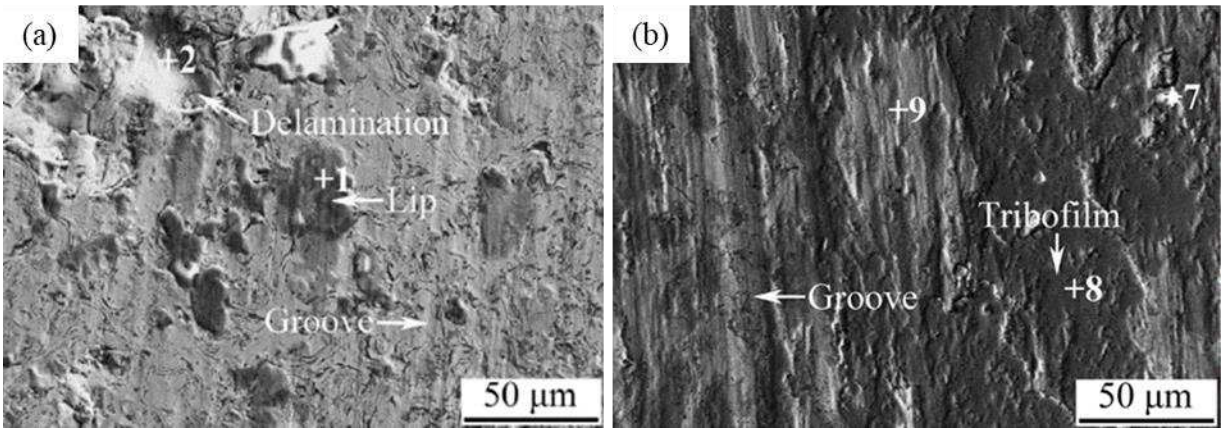

Figure 2.44 Wear surface of the AlCoCrFeNiTi coating at (a) 25°C and (b) 700°C [73].

The room temperature volume wear rate of the AlCoCrFeNiTi HEA coating was $0.77 \pm 0.01 \times 10^{-4}$ mm^3 N^{-1} m^{-1} which is approximately one-third that of the 316 stainless steel. At 700°C, the wear rate decreased to $0.23 \pm 0.01 \times 10^{-4}$ mm^3 N^{-1} m^{-1} due to the formation of tribofilms and σ phase which is hard and brittle due to the lack of multiple systems. However, at 700°C, the AlCoCrFeNiTi HEA coating was now only one-ninth that of the 316 stainless showing much better temperature resistance.

2.6.3.3 Thermal Sprayed $FeCoCrNiMo_{0.2}$

The third HEA coating reviewed was $FeCoCrNiMo_{0.2}$. Unlike the previous two coatings presented in Section 2.6.3.1 and 2.6.3.2, the $FeCoCrNiMo_{0.2}$ had a primary phase of FCC solid solution [84]. The composition was selected to be a combination of the high tensile strength (700 MPa) and elongation (56%) reported for FeCoCrNi HEA FCC solid solution [89] with the scuffing resistance of that Mo adds [90]. APS and HVOF spraying was conducted using HEA powders that were prepared by generating an $FeCoCrNiMo_{0.2}$ HEA ingot followed by re-melting through an atomizing chamber before sieving to achieve

particle size distribution of 15-42 µm. It was found that both the APS and HVOF coatings were comprised of an FCC solid solution with a mixture of Fe_3O_4, Fe_2O_3, and AB_2O_4 (A = Fe, Co, Ni and B = Fe, Cr) oxides. The oxide content varied significantly between the two thermal processes with the HVOF coating having a 12.7 % oxide content and the APS coating containing 47.0% oxides. This difference in oxide content resulted in the APS coating having an order of magnitude reduced wear rate compared to the HVOF coating as shown in Figure 2.45.

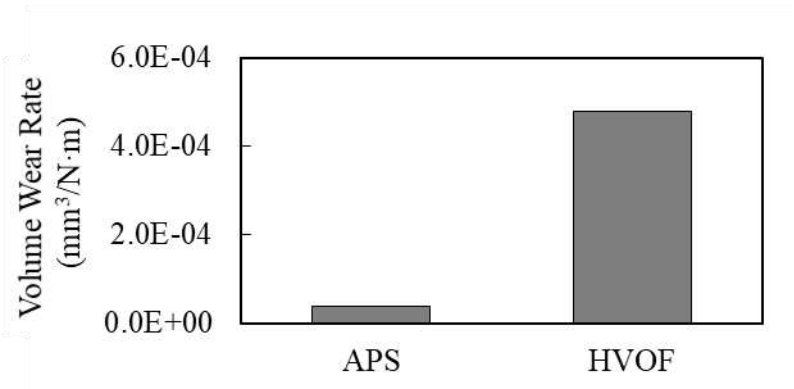

Figure 2.45 Volume wear rates for the APS and HVOF FeCoCrNiMo0.2 HEA coatings [84].

It was suggested that large differences in wear properties between the APS and HVOF coating could be attributed to a lubrication effect caused by oxide layers [91]. The oxide layer formation was divided into types: the first being the oxide inclusions formed during spraying with the second being oxides formed during oxidation of the surface during the wear test [84]. Due to the abundance of oxides in the APS coating, during the sliding wear test it was easier to compact the oxides into an oxide layer by the continuous wear stress than with the HVOF coating which had a much lower oxide content. The difference in worn surfaces of the APS coating and HVOF coating for 3, 5 and 15 min are shown in Figure 2.46.

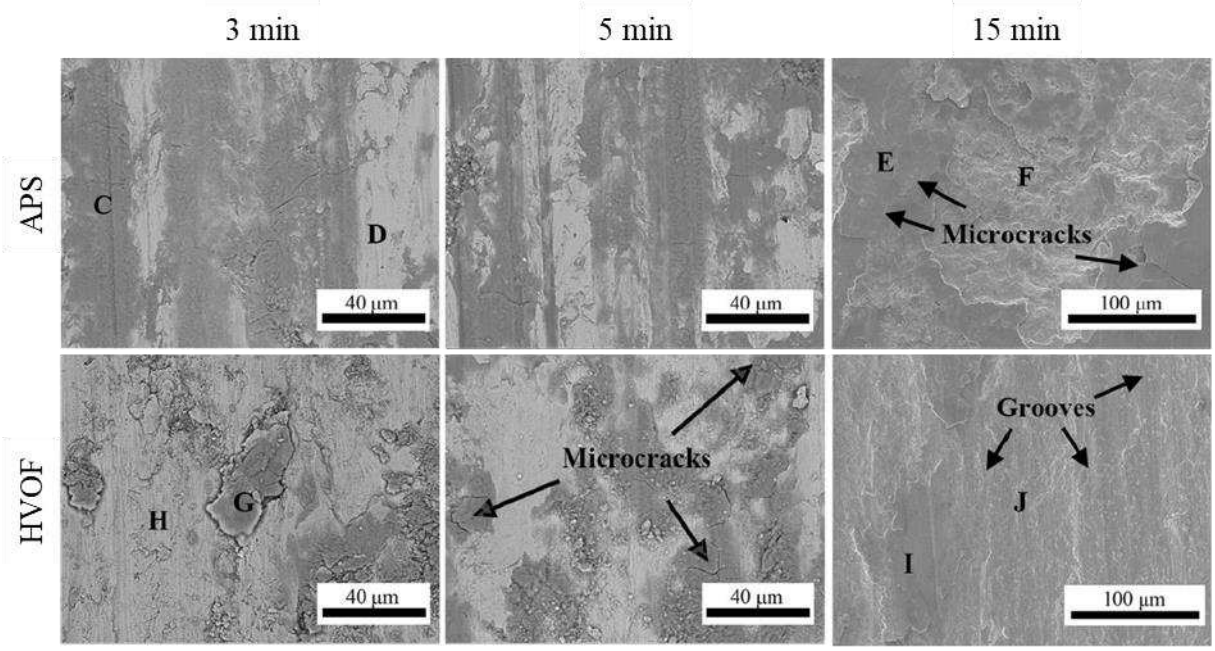

Figure 2.46 Worn surface morphologies of the APS and HVOF coatings for different friction wear test times [84].

CHAPTER 3: EXPERIMENTAL PROCEDURES

This chapter provides a description of materials, parameters, and techniques used during sample processing. Laboratory characterization, testing techniques, and equipment are described and discussed. The experimental procedure consisted of two parts. The first part involved characterizing the coating and evaluating the effect of the voltage parameter. This was accomplished by preparing sprayed samples under varied voltage conditions and characterizing the coatings microstructural and mechanical properties. The thermal spray coating was evaluated for porosity content, splat microstructure, oxide composition, hardness, strength and residual stress. The second part involved developing and testing a new wire composition targeting improved coating toughness while retaining wear resistance.

3.1 Thermal Sprayed Sample Preparation

All twin-wire arc thermal spraying (TWAS) was conducted by White Horse Technology in Tomball, Texas. Cored wires were provided by Devasco International, Inc. with powder additions of <5 wt.% Si, Ni, Al, V, Ti, and B. Before spraying, A36 steel substrates were sandblasted with 16 grit Al_2O_3 applied using 110 psi at a 60° to the substrate surface. Surface roughness was measured using PRESS-O-FILMTM and elcometer® to ensure a minimum value of 0.127mm (0.005”) was achieved. Standard thermal spraying process parameters for HH1 are shown in Table 3.1 Thermal spraying was conducted using the AT-400 Twin-Wire Arc Spray System as shown in Figure 3.1. Pressurized air used to spray was treated by compressing ambient air and filtering out moisture before transferring to an air tank where it was passed through a 5 μm filter before use.

Table 3.1 TWAS standard process parameters for HH1.

Voltage	31.5 V
Amperage	225 amps
Pressure	45 psi
Spray Distance	5 inches

(a) (b)

Figure 3.1 Thermach, Inc AT-400 Twin-Wire Arc Spray System with components visible (a). Spray gun where cored wires are fed together (b). [9]

For pipe spraying, thermal spraying is performed by fixed spray-guns set at a certain distance from the drill pipe which is rotated at a set revolution per minute (rpm) and set forward speed until a coating thickness and width is achieved around the circumference of the pipe. For this study, test pieces were sprayed by holding the spray gun at a set distance of 127 mm (5in) and traversing the spray gun back and forth until a coating thickness of 2 mm (0.079 in) was achieved. Coating thickness was measured with micrometer maintaining a tolerance of ±0.254 mm (0.010”). The surface temperature of the coating was maintained below 93°C (200°F) during spraying to match production. A schematic of the TWAS spray process and sample spraying set-up are shown in Figure 3.2.

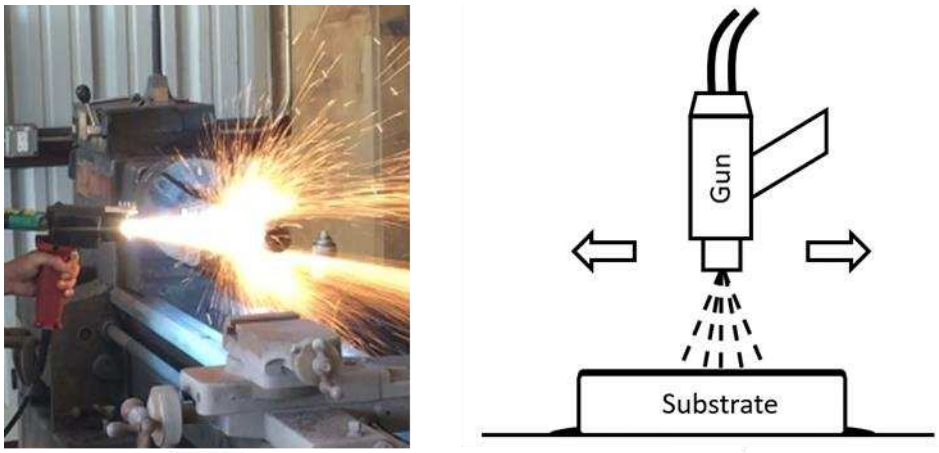

(a) (b)

Figure 3.2 Photo (a) and schematic (b) of thermal spraying set-up.

Test pieces were sprayed with varied voltages of 26.5V, 31.5V, and 36.5V. These voltage conditions represent 5V above and below the standard voltage and approximately cover the min and max voltages typically used [57-59, 92]. Three A36 steel substrates were cut to dimensions of 19.05 mm x 50.8 mm x 203.2 mm (0.75” x 2” x 2”) with the 50.8 mm x 203.2 mm surface sandblasted before being sprayed to a 2 mm coating thickness at one of the three voltage conditions with geometries shown in Figure 3.3.

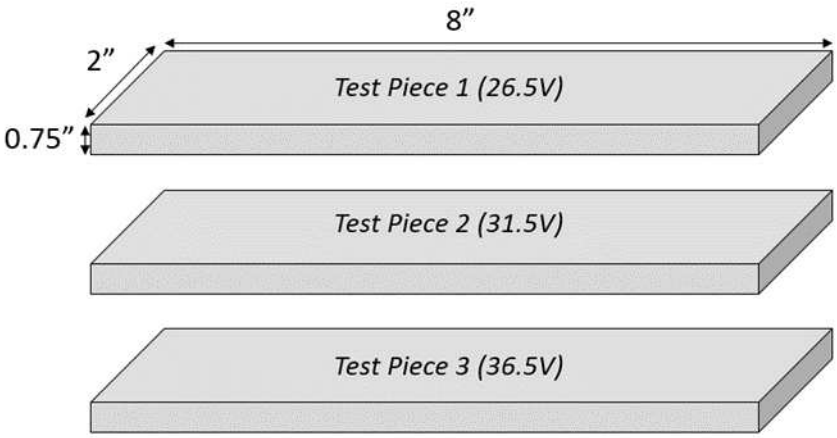

Figure 3.3 Test piece substrate geometry before thermal spraying.

3.2 Optical Microscopy

Optical microscopy (OM) samples were sectioned, mounted, and polished at ResOps Laboratory Services in Tomball, Texas. Three optical samples were taken for each voltage condition along the center

of the test piece as shown in Figure 3.4. Samples were mounted in bakelite, ground, and polished to a 1 µm diamond mirror finish for optical microscopy (OM) and scanning electron microscope (SEM) imaging. Optical images were taken for all metallographic samples using the LECO® Olympus PMG3 microscope in the as-polished condition.

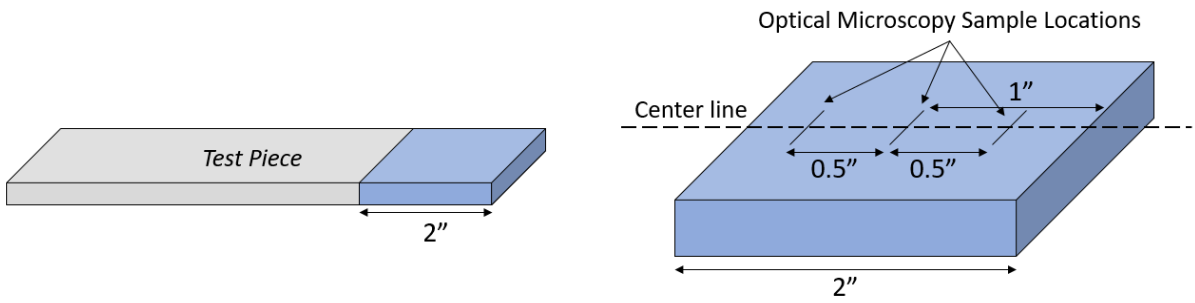

Figure 3.4 Location where optical microscopy samples were taken for each test piece.

3.2.1 Porosity Measurement

Area percentage porosity was determined following ASTM E2109 – 01 Standard Test Methods for Determining Area Percentage Porosity in Thermal Sprayed Coatings [93]. Test Method B was used to determine the area percentage by thresholding each image. Each voltage condition had three metallographic samples prepared and each metallographic sample had six optical images taken as shown in Figure 3.5. Thus, each voltage condition had 18 optical images analyzed to determine average area percent porosity.

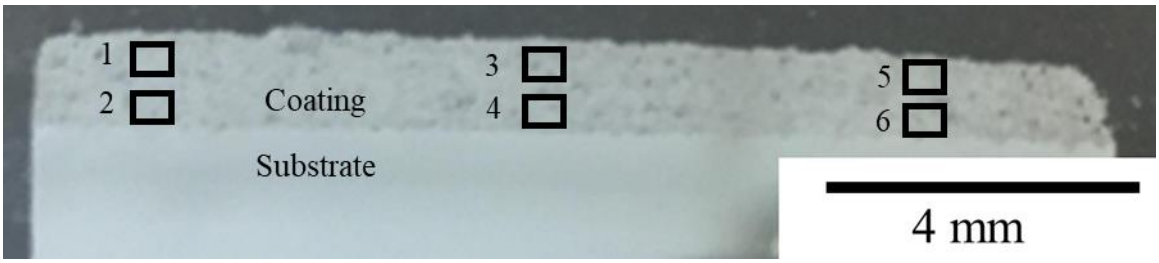

Figure 3.5 Image showing approximate locations of micrographs used for porosity measurement.

Every optical micrograph was taken on the same microscope at the same magnification and with identical image settings. All images were taken in one session. ImageJ was used to analyze images by thresholding every image to a software saturation value of 62. As the thresholding can be biased by

microscope light and magnification settings, the area percent porosity does not represent an exact value but instead a comparison between the three voltage conditions to identify any trends. Additionally, all the micrographs were taken on the same microscope during the same session increasing the reliability of the results. Figure 3.6 (a) shows an OM image taken within the coating and Figure 3.6 (b) shows the same image after thresholding where the dark area was counted as area percent porosity.

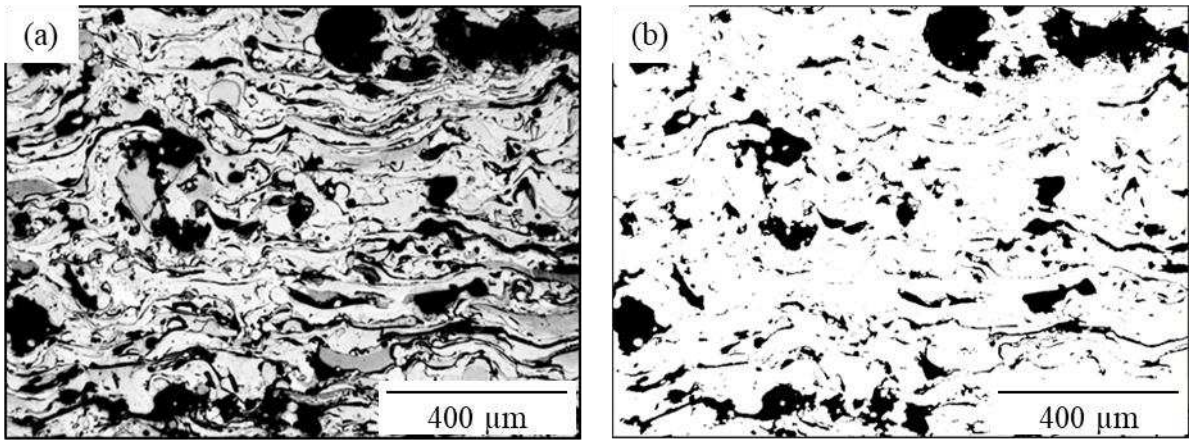

Figure 3.6 Metallographic image taken within the coating before thresholding (a) and after thresholding (b).

3.3 SEM Imaging

Samples that were sectioned and polished for OM as discussed in Section 3.2 were also analyzed with SEM. The FEI Quanta 600 scanning electron microscope (SEM) with Quanta xT operating software was used to examine the coating cross section. An accelerating voltage of 20 kV at a working distance of 10 mm was used to take images. SEM images were compared with optical images to differentiate coating features that are difficult to differentiate with OM such as pores and oxides. Figure 3.7 shows a cross-sectioned sample that has been mounted and polished placed onto the FEI Quanta 600 SEM stage. Carbon conductive adhesive tape was applied to the sample running from the substrate, away from the coating, to the base of the sample in contact with the stage.

An Energy dispersive system (EDS) with a silicon drift detector and tungsten filament was used to perform composition analysis by composition maps and spot scans utilizing EDAX 6.5.1 software. EDS maps were conducted with a dwell time of 2000 µs with 256×200 resolution for the elements Fe, O, Al, Si,

Ni, and Ti. Spot scans were taken at areas of interest revealed from the composition maps to better capture the element amounts. Spot scans were taken over 60 second intervals.

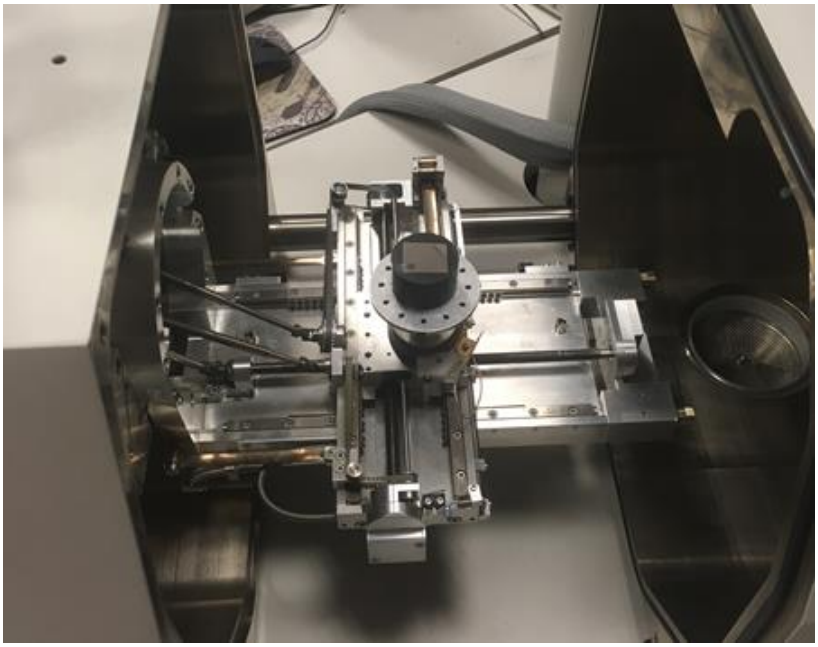

Figure 3.7 Cross sectioned sample resting on the FEI Quanta 600 SEM stage.

3.4 X-ray Computed Tomography

One specimen was sectioned from the 31.5V input voltage condition for X-ray computed tomography (X-ray CT). The sample was sectioned to dimensions of 3 mm x 3 mm x 17 mm with the 2 mm coating thickness along the 15 mm direction as shown in Figure 3.8. Testing was performed using a ZEISS 620 Versa 3D X-ray microscope to visualize how internal defects such as oxides, pores, and cracks are dispersed in the coating. The CT-scanner was operated at 120 kV of accelerating energy generating a polychromatic X-ray beam to collect results. Projections were taken over 360° rotation. A voxel size of (5.09 µm) was achieved based on the 4X optical lens behind the scintillator in combination with a geometric magnification.

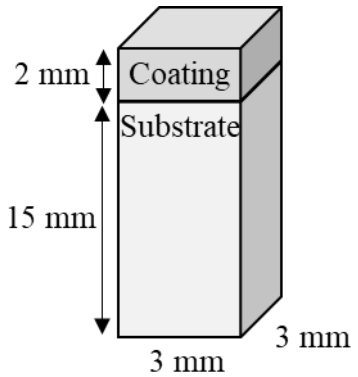

Figure 3.8 Schematic of specimen prepared for x-ray tomography (not to scale).

3.5 Hardness

3.5.1 Vickers

Vickers hardness was taken on the cross section of the coating through thickness for each sample condition. Vickers hardness indents were aimed to be placed in the center of metallic splats to indicate the phases present in the coatings. Vickers hardness tests were conducted with the Wilson Tukon Series 200 Microhardness Test. Due to the hardness differences between the substrate and coating, 300 g loads was used for reading taken of the substrate with 500 g load used within the coating. Dwell time of the loads was 10 seconds.

3.5.2 Nano-Indentation

Nano-indentation testing was conducted across the coating-substrate interface as an indication of residual stress level [94, 95]. A grid of 5×20 indents was performed across the interface at two locations per voltage condition. Indents were made with the Hysitron TI 950 TriboIndenter machine with the T1-0039 Berkovich diamond indenter. Indents were loaded at 2 mN/s with 5 second holds.

3.6 Four-Point Bend Testing with Digital Image Correlation

3.6.1 Sample Generation

After spraying, test pieces were water-jet cut to the correct dimensions for the 4-point bend testing. Figure 3.9 shows the 26.5V test pieces with dashed lines showing where it was water-jet cut. After the bend samples were water-jet cut, the edges were surface ground to the final width leaving the coating top surface

"as-sprayed". The surface grinder was used in steps of 0.001" to gradually remove material without adding significant stress to the sample as this surface would later be prepared for digital image correlation (DIC). The grinder also acted to square-up the sample as it runs parallel to the magnetic holding table. A final thickness of 4 mm was selected for the bend samples so that the coating and substrate would be approximately the same thickness. Bend samples had a final geometry of 4 x 12.7 x 76.8 mm per ASTM D6272-17 [96]. Following rules for a sample with a thickness of 1.6 mm or greater; the length (L) shall be greater than 16 times the thickness (4 mm), the width shall be less than ¼ the length, with the total specimen length being 20% longer than the length (L).

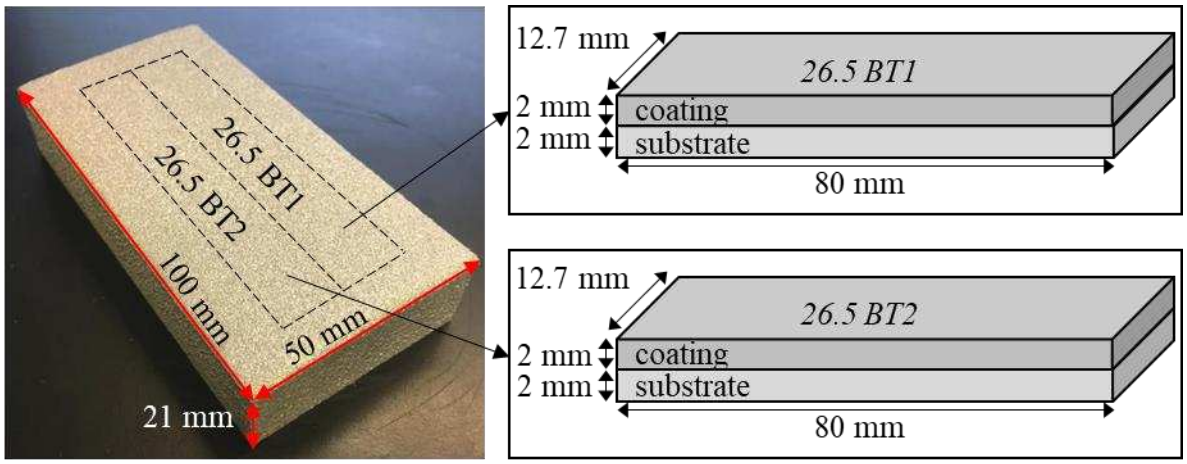

Figure 3.9 Test piece 1 thermal sprayed at 26.5V showing where bend test samples were water-jet cut.

3.6.2 Four-Point Bend Testing

Following ASTM D6272 – 17, samples were loaded in the "one half of support span" configuration. Figure 3.10 shows the loading schematic from the ASTM D6272 with dimension values used for testing. An electromechanical screw-driven MTS Alliance RT/100 load frame equipped with an MTS 89.0 kN load cell was used to perform the bend test. All samples were tested at a crosshead motion rate of 0.4275 mm/min which strains the bend sample outer-fibers (coating surface) at 0.0025 mm/mm. The crosshead motion value used was ¼ the value stated in the standard, this was done to slow the test down and collect more DIC data. The test was run until the coating had a crack running from the surface to the substrate and the coating was

beginning to peel away from the substrate. The sample was bent to this point so that post-test cutting could be easily performed without damaging the fractured surface for later observation.

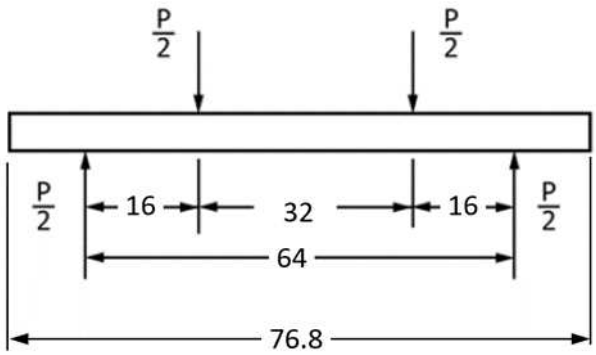

Figure 3.10 Four-point bend test loading schematic for the "one half of support span" load configuration from ASTM D6272 with calculated dimensional values inserted in millimeters.

3.6.3 Digital Image Correlation

DIC requires the surface of interest to have a solid white background spattered with fine black spots allowing the imaging software to track the movement of these spots and calculate the strain. In order to achieve this, the cross-section side of the bend-samples was polished to a 420-grit surface finish in preparation for DIC painting. The polished edge was cleaned, and spray painted with Rust-OLEUM flat white paint. Paint coats were added until the paint layer was no longer transparent achieving a smooth white surface. Once the flat white paint dried, the sample was spackled with Rust-OLEUM semi-gloss black paint. This was accomplished by spraying over the sample and slowly lowering the paint spray cloud closer to the sample allowing larger paint droplets to evenly and randomly decorate the surface. The final prepared surface for DIC is shown in Figure 3.11 which was sample 26.5 BT1. A good spackle pattern of black spots and blotches allows the DIC software to track their movements during the test and calculate strains.

Figure 3.11 Four-point bend sample prepared with spackle for DIC during testing.

Samples were then placed into the Alliance RT/100 load frame with DIC equipment positioned as shown in Figure 3.12. DIC set-up included positioning the Allied Vision Technologies camera equipped with a Schneider-Kreuznach Xenoplan 2.8/50-0902 lens approximately 60 cm from the sample. Two Lowel Pro-Lights were positioned on either side of the camera with Rosco #7300 polarizing light filters placed approximately 25 cm in front of the lights mounted on stands. A laptop with TQSnap software was connected to and used to focus the camera on the prepared sample surface. DIC images were taken every second. The loading and DIC imaging were started at the same time so that the load versus time data could be correlated directly with the DIC image number. DIC data was analyzed using Aramis software.

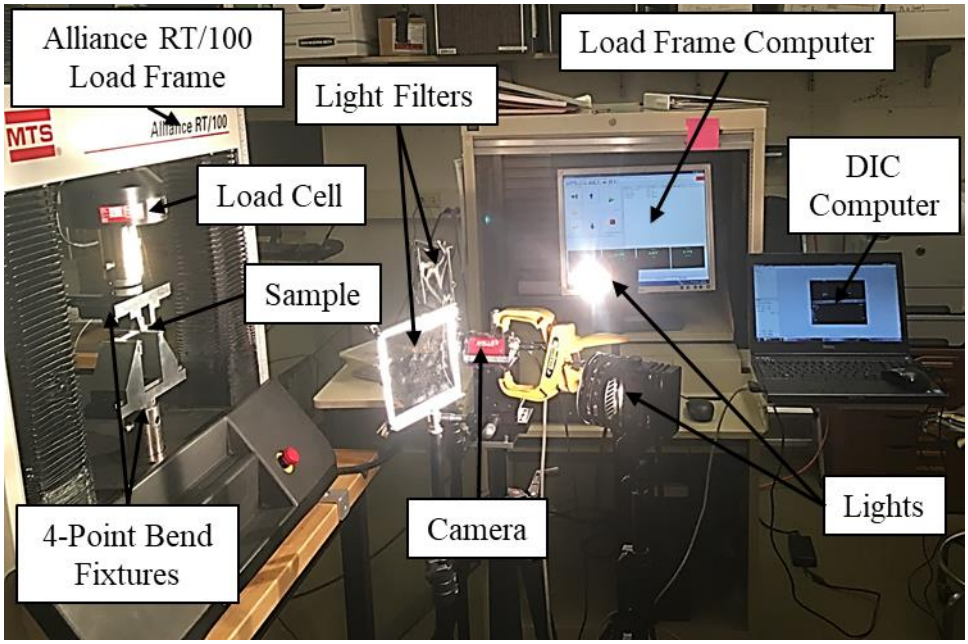

Figure 3.12 Four-point bend testing with DIC set-up.

3.6.4 Bend Sample Fractography

After bend testing, the fracture surfaces were observed with the FEI Quanta 600 scanning electron microscope (SEM) and energy dispersive spectroscopy (EDS) EDAX system previously discussed in Section 3.3. Images were taken in the high-vacuum mode at a spot size of 5 and voltage of 20.00 kV. Bend samples were cut through the substrate to the base of the crack to expose fracture surface for imaging. Figure 3.13 shows a schematic drawing of the bend sample after testing with two cracks. The substrate was sectioned to the point where the crack had propagated to the coating-substrate interface being careful to not damage the fracture surface. Also shown in Figure 3.13, is a bend sample after being cut. The cutting was never perfectly aligned with the crack and either the coating of the substrate would protrude out.

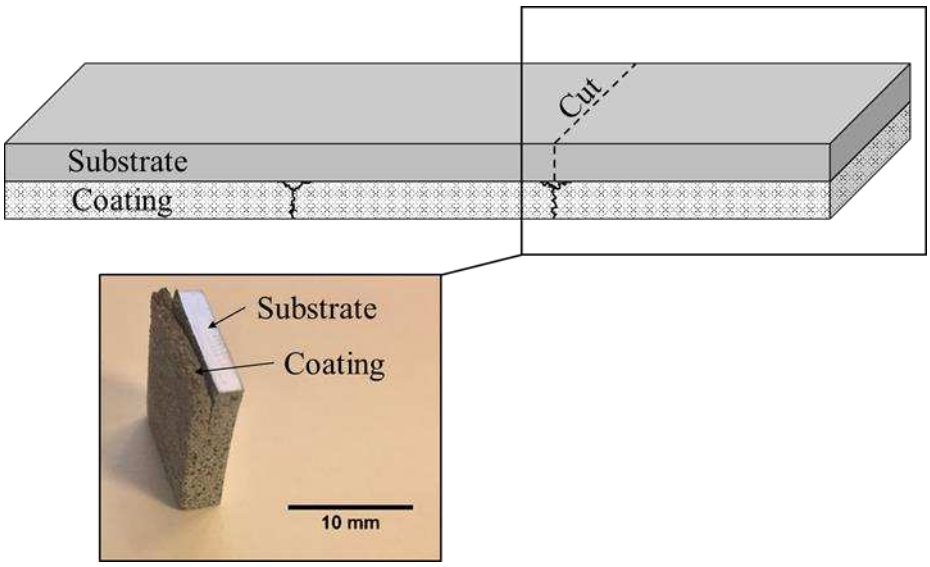

Figure 3.13 Schematic example of four-point bend sample cutting to expose fracture surface with picture showing post cutting.

3.6.5 Wear Testing

Wear of pipe is caused primarily by the rotation coupled with high contact pressure in abrasive and corrosive environments (drilling fluids). Wear and friction become of increased concern at greater depths requiring greater time and exposing the pipe to higher temperatures and corrosive environments [97]. For this work, dry sand rubber wheel wear testing was performed on the 31.5V and 36.5V voltage conditions. Testing was performed in accordance with ASTM G-65 Procedure A [98]. The load was 30 pounds run for

12,000 revolutions using a 10 inch diameter rubber wheel. Samples were weighed before and after testing to find mass loss. More information would need to be known of the specific application to develop a wear test that could take into account service temperature, contact pressure, rotation speed, and environment.

3.7 New Thermal Spray Wire Composition

3.7.1 Approach

With the goal of improving the fracture toughness while maintaining wear resistance, literature compositions were reviewed and new compositions proposed in addition to the voltage parameter research. Several HEA coatings were investigated with three literature compositions highlighted in Section 2.6.3. The MPEA coating discussed in Section 2.6.3.3 with composition of $FeCoCrNiMo_{0.2}$ had a reported wear rate of 3.90×10^{-5} mm^3/Nm when APS was used which is 30% less than HH1 [84]. The excellent wear rate of this composition was attributed to high amounts of oxides present within the coating of 47%. The oxides present were a mixture of Fe_3O_4, Fe_2O_3, and AB_2O_4 (A = Fe, Co, Ni and B = Fe, Cr) in a spinel structure with the results indicating that these oxides have a large solid solubility in each other due to the high entropy effect [99]. Additionally, this composition splat structure was FCC random solid solution (RSS) which have been characterized to have high strengths and elongation as reported for the FeCoCrNi HEA with a tensile strength of 712.5 MPa and 56% elongation [89]. It is hypothesized that combining the excellent wear behavior of a coating with these spinel oxides with a RSS FCC splat structure, that a coating could be achieved with wear rates equivalent or better than HH1 with a significantly higher toughness.

3.7.1.1 Base Composition

Using the literature $FeCoCrNiMo_{0.2}$ composition as base composition for comparison, Thermo-Calc phase diagrams were generated using the TCHEA2: High Entropy Alloys v2.0 database. In order to generate a phase diagram, four of the five elements are held in relationship to one another with the x-axis representing an incremental increase in the fifth element. Considering the $FeCoCrNiMo_{0.2}$ literature composition, the phase diagram would be FeCoCrNi versus Mo as shown in Figure 3.14. The vertical dotted line represents the $FeCoCrNiMo_{0.2}$ literature composition where the atomic percentages of the elements Fe, Co, Cr, and Ni

is 23.8% with Mo being 4.8%. At this composition, considering the high temperature of 1500 K, the structure is predicted to have a volume fraction of 93 % FCC and 7 % σ-phase. This now offers the base composition and Thermo-Calc analysis to compare new compositions to.

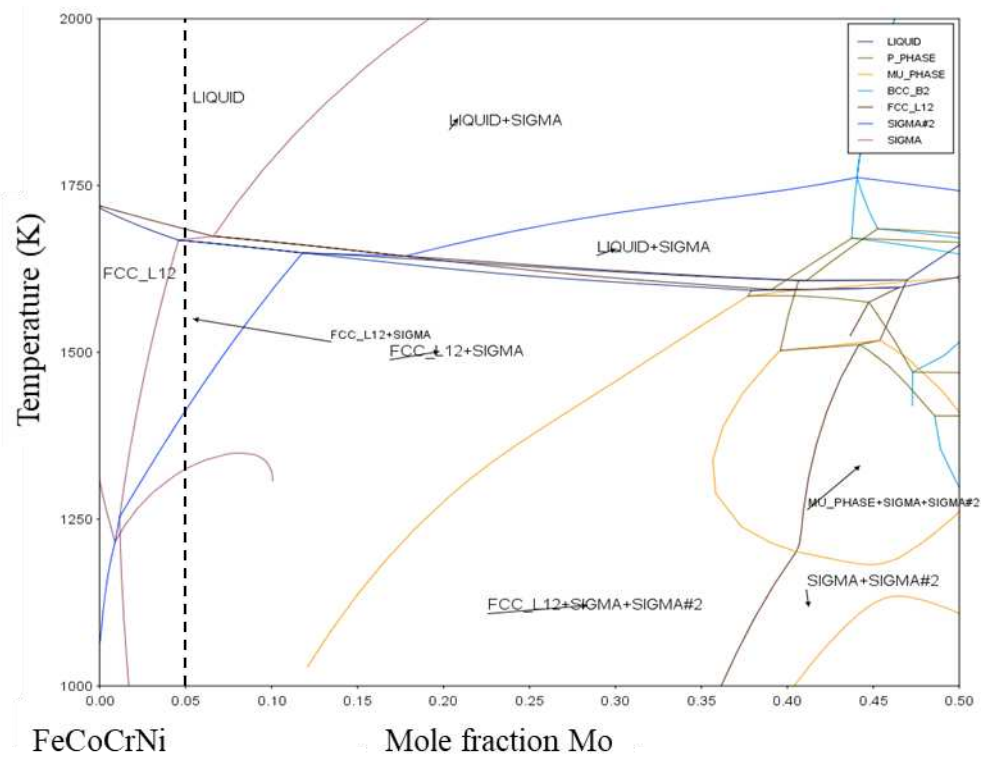

Figure 3.14 Thermo-Calc phase diagram generated for FeCoCrNi versus Mo with the dotted line showing the $FeCoCrNiMo_{0.2}$ composition.

In addition to the Thermo-Calc analysis, Hume-Rothery rules were used to identify if the alloy would form a solid solution [100, 101]. The atomic size difference (δ_r), electronegativity difference (δ_X), valence electron concentration (*VEC*) were calculated using the element properties provided in Table 3.2. The following equations were used to calculate these values:

$$\delta_r = \sqrt{\sum c_i \left(1 - \frac{r_i}{\bar{r}}\right)^2} \tag{3.1}$$

$$\delta_X = \sqrt{\sum c_i \left(1 - \frac{X_i}{\bar{X}}\right)^2} \tag{3.2}$$

$$VEC = \sum c_i VEC_i \tag{3.3}$$

where c_i represents the atom fractions of each element i, r_i is the atomic radius, $\bar{r}$ is the average atomic radius $\bar{r} = \sum c_i r_i$, X_i is the atomic electronegativity, and $\bar{X}$ is the average electronegativity $\bar{X} = \sum c_i X_i$. Solid solutions are generally formed in MPEAs when VEC was greater than 8 [102] and with δ_r less than 6.6% [79]. For the $FeCoCrNiMo_{0.2}$ literature composition, atomic size difference was calculated to be 2.0%, electronegativity deference of 6.5%, and VEC value of 8.14 which are all values favorable for the formation of FCC solid solution.

Table 3.2 Element properties for Fe, Co, Cr, Ni, and Mo [74, 103].

Element (i)	c_i	Wt. %	Structure at T_m	Atomic Radius (pm)	VEC_i	Pauling EN
Fe	0.238	22.8	BCC	124.12	8	1.83
Co	0.238	24.1	FCC	125.10	9	1.88
Cr	0.238	21.3	BCC	124.91	6	1.66
Ni	0.238	24	FCC	124.59	10	1.91
Mo	0.48	7.8	BCC	136.26	6	2.16

3.7.1.2 New Composition

Due to limited scope, budget, and schedule for the project, new MPEA wires with custom composition were unable to be produced. Instead, wires with compositions that are readily available were investigated to find a combination that closely resembled the base composition discussed in Section 3.7.1.1. Solid and cored wires were considered with the limitation of the cored wire to be 70 wt. % sheath material and 30 wt. % powder core composition. It was determined that a combination of solid Inconel 625 wire with powder cored wire of 430SS sheath and 50 wt. % Co and 50 wt. % Co produced a composition with similar phases to the base composition as predicted by Thermo-Calc. The new composition written out in MPEA terms would be $Fe_{0.32}Co_{0.08}Cr_{0.2}Ni_{0.32}Mo_{0.07}Ta_{0.01}$ considering all the reported elements of the constituent wires

and powders. Figure 3.15 shows the phase diagram generated for the new composition with FeMoCrNiTa versus Co where the dotted line represents the composition. Considering the high temperature stable phases at 1500 K, the volume fraction of phases is 93% FCC and 7% σ-phase which is approximately the same phase fraction of the base composition discussed in Section 3.7.1.1.

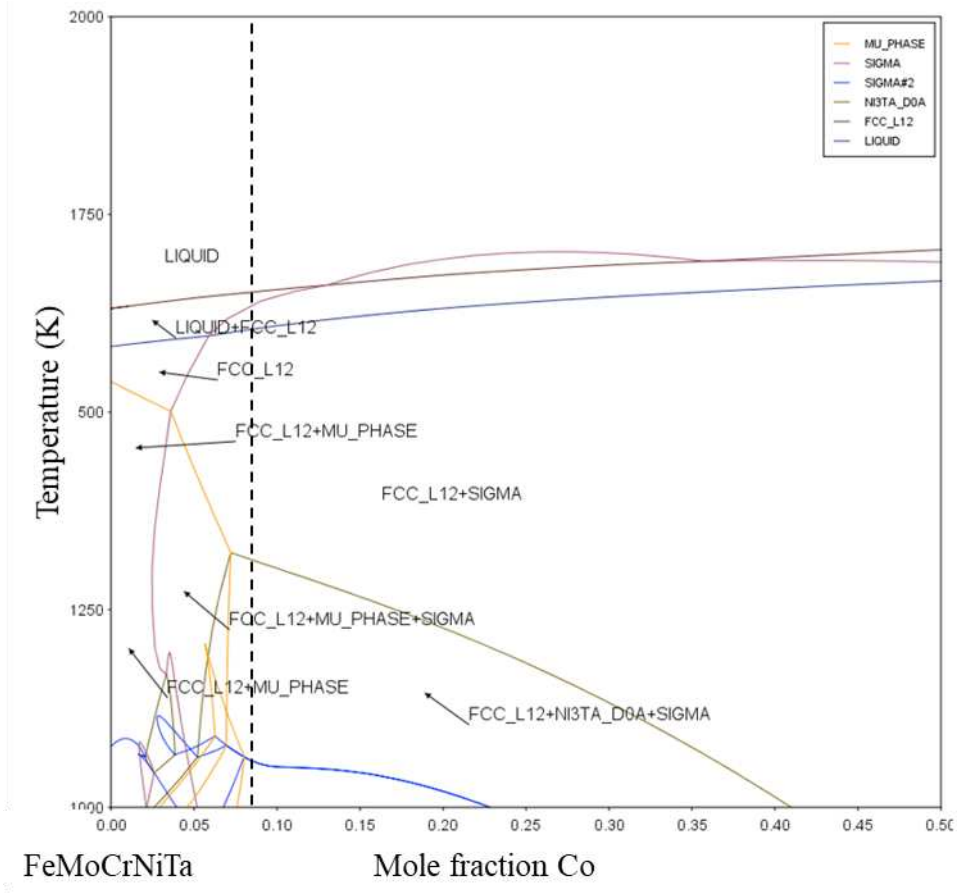

Figure 3.15 Thermo-Calc phase diagram generated for FeMoCrNiTa versus Co with the dotted line showing the $Fe_{0.32}Co_{0.08}Cr_{0.2}Ni_{0.32}Mo_{0.07}Ta_{0.01}$ composition.

In addition to the Thermo-Calc analysis, the values for atomic size difference (δ_r), electronegativity difference (δ_X), and valence electron concentration (*VEC*) were calculated using Equations (3.1) thru (3.3) and element properties shown in Table 3.3. For the new composition $Fe_{0.32}Co_{0.08}Cr_{0.2}Ni_{0.32}Mo_{0.07}Ta_{0.01}$, atomic size difference was calculated to be 2.8%, electronegativity difference of 7%, and VEC value of 8.15 which are all values favorable for the formation of FCC solid solution. Additionally, based on estimates

provided by Devasco for element costs, the new wire composition would be 27% more cost effective before considering the additional saving by using standard wire compositions versus custom compositions.

Table 3.3 Composition and element properties for $Fe_{0.32}Co_{0.08}Cr_{0.2}Ni_{0.32}Mo_{0.07}Ta_{0.01}$ [74, 103].

Element (i)	c_i	Wt. %	Density, ρ (g/cm³)	Atomic Radius (pm)	VEC_i	Pauling EN
Fe	0.32	30.0%	7.88	124.12	8	1.83
Co	0.08	7.5%	8.84	125.10	9	1.88
Cr	0.20	17.3%	7.19	124.91	6	1.66
Ni	0.32	31.7%	8.91	124.59	10	1.91
Mo	0.07	12.0%	10.23	136.26	6	2.16
Ta	0.01	1.6%	16.68	143.00	5	1.50

3.7.2 New Composition Thermal Spraying

In order to achieve a composition similar to the base composition, two different wires were used as indicated in Section 3.7.1.2. This is visualized in Figure 3.16 showing a schematic of how the two different wires were fed together with nominal wire compositions listed. The solid Inconel 625 wire was selected as the cathode due to findings revealing that cathode is consumed more rapidly for TWAS of aluminum wire previously shown in Figure 2.6 [12]. It is expected that the solid wire will be melt slower than the cored wire, thus, having it as the cathode is an attempt to have more uniform melting.

The solid wire, sheath, and powder elements will all be present within the arc; however, a risk of wires not mixing exists. To address this concern, three test pieces were sprayed at various pressure due to pressure having the greatest effect on arc characteristics as this parameter is primarily responsible for molten metal removal from wire tips as discussed previously in Section 2.4.3. The final spray parameters were chosen based on discussion with Devasco and finding a configuration that resulted in no visual peeling. The final spray parameters chosen are provided in Table 3.4. Substrate material, preparation and all other spray parameters were identical to that of HH1 spray previously provided in Section 3.1.

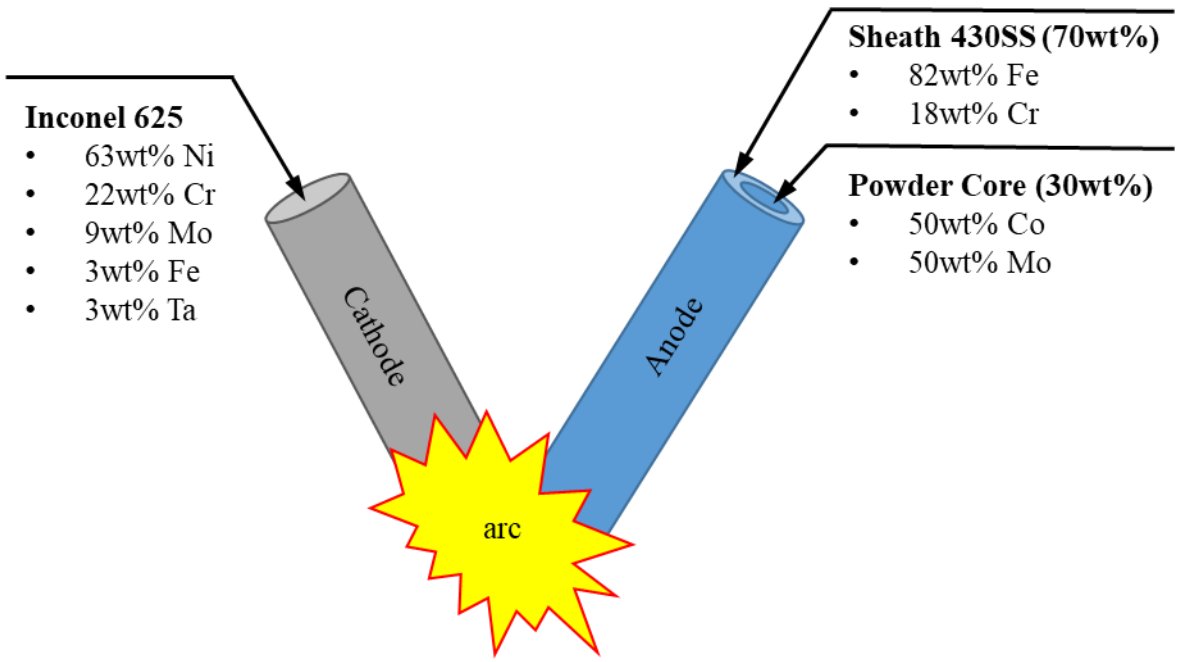

Figure 3.16 Schematic of how two different wires are fed together to achieve the $Fe_{0.32}Co_{0.08}Cr_{0.2}Ni_{0.32}Mo_{0.07}Ta_{0.01}$ composition.

Table 3.4 TWAS process parameters for the $Fe_{0.32}Co_{0.08}Cr_{0.2}Ni_{0.32}Mo_{0.07}Ta_{0.01}$ composition.

Voltage	29 V
Amperage	180 amps
Pressure	25, 35, 45 psi
Spray Distance	8 inches

Test pieces were sprayed with varied pressures of 172, 241, and 310 kPa (25, 35, and 45 psi). These pressure conditions represent 10 psi above and below the standard pressures and approximately cover the min and max pressures typically used [57-59, 92]. Three A36 steel substrates were cut to dimensions of 19.05 mm x 50.8 mm x 152.4 mm (0.75” x 2” x 6”) with the 50.8 mm x 152.4 mm surface sandblasted before being sprayed to a 2 mm coating thickness at one of the three pressure conditions.

3.7.3 Testing

The $Fe_{0.32}Co_{0.08}Cr_{0.2}Ni_{0.32}Mo_{0.07}Ta_{0.01}$ composition was subjected to various testing to determine microstructural features and mechanical properties. OM and porosity analysis was conducted in the same manner as provided in Section 3.2. SEM imaging was carried out as discussed in Section 3.3. Through coating Vickers hardness was performed as covered in Section 3.5.1. Four-point bend testing was performed

on two samples from each pressure condition and prepared in the same manner as reported in Section 3.6.1 with testing performed as described in Section 3.6.2. No DIC analysis was performed on these samples.

3.7.3.1 Wear Testing

Dry sand rubber wheel wear testing was performed on the 241 and 310 kPa pressure conditions. Testing was performed by Wear and Friction Resources, LLC in accordance with ASTM G-65 Procedure A [98]. The load was 30 pounds run for 12,000 revolutions. Samples were cleaned with mild detergent and water, rinsed with methanol and dried with compressed air.

CHAPTER 4: RESULTS

This chapter presents the findings of each experiment performed starting with the HH1 thermal sprayed coatings OM, SEM, and mechanical testing results. Additionally, a new spray coating composition was prepared with results of experiments conducted provided.

4.1 Thermal Sprayed HH1 Coating

Samples were sprayed as described in Section 3.1. Wires used to spray the samples were from two lots 14970-A and 14970-B. Chemical analysis of the wires was performed by optical emission spectroscopy per ASTM A751 [104] by A and M Technical Services Inc. with results provided in Table 4.1. Temperature was read approximately every 80 passes back and forth with the thermal spray gun using an infrared temperature gun to maintain the coating surface temperature under 93°C (200°F). Temperatures were observed to reach as high as 250°F during spraying at which point the coating was allowed to cool below 200°F before resuming thermal spraying.

Table 4.1 Chemical analysis of wires used for thermal spraying.

Lot	C	Mn	P	S	Si	Ni	Mo	Cr	Cu
14970-A	0.80	2.52	0.017	0.007	0.50	1.82	0.02	<0.02	<0.02
14970-B	0.70	2.48	0.016	0.006	0.44	1.81	0.02	<0.02	<0.02
Lot	Al	V	Ti	Nb	Co	B	W	Zr	Sn
14970-A	1.80	1.80	2.15	<0.02	<0.02	4.83	<0.02	<0.02	<0.02
14970-B	1.66	1.74	2.03	<0.02	<0.02	4.67	<0.02	<0.02	<0.02

*Reported values in weight %, balance iron.

4.1.1 Area Percent Defects

Area percent defects (oxides, pores, cracks) results are provided in Table 4.2 for varying voltages. Each test piece represents a different voltage condition as shown in Figure 3.3. Shown previously in Figure 3.4, three metallographic samples were taken along the center line of each test piece and are identified as location 1, 2, and 3. Each metallographic sample had six images taken of the coating cross section at the left-hand, middle, and right hand side with one near the substrate identified and bottom and one near the

coating surface identified as the top. Thus, the micrograph naming convention for Table 4.2 is “test piece number” + “location number” + “left/right/middle” + “top/bottom”.

Table 4.2 Area Percent Defects for HH1 sprayed at Varying Voltages

Test Piece	Location	Image	Top/Bottom	Micrograph Name	Percent Defects
1	1	Left	Top	TP1L1LT	21.33%
			Bottom	TP1L1LB	19.96%
		Middle	Top	TP1L1MT	25.83%
			Bottom	TP1L1MB	22.69%
		Right	Top	TP1L1RT	23.76%
			Bottom	TP1L1RB	21.60%
	2	Left	Top	TP1L2LT	19.69%
			Bottom	TP1L2LB	26.80%
		Middle	Top	TP1L2MT	21.89%
			Bottom	TP1L2MB	18.46%
		Right	Top	TP1L2RT	22.74%
			Bottom	TP1L2RB	20.41%
	3	Left	Top	TP1L3LT	32.00%
			Bottom	TP1L3LB	24.70%
		Middle	Top	TP1L3MT	26.22%
			Bottom	TP1L3MB	23.37%
		Right	Top	TP1L3RT	24.23%
			Bottom	TP1L3RB	26.23%
2	1	Left	Top	TP2L1LT	22.69%
			Bottom	TP2L1LB	25.54%
		Middle	Top	TP2L1MT	19.22%
			Bottom	TP2L1MB	17.92%
		Right	Top	TP2L1RT	22.78%
			Bottom	TP2L1RB	22.46%
	2	Left	Top	TP2L2LT	24.90%
			Bottom	TP2L2LB	19.18%
		Middle	Top	TP2L2MT	21.86%
			Bottom	TP2L2MB	20.65%
		Right	Top	TP2L2RT	20.25%
			Bottom	TP2L2RB	16.69%

Table 4.2 Continued

Test Piece	Location	Image	Top/Bottom	Micrograph Name	Percent Defects
2	3	Left	Top	TP2L3LT	19.48%
			Bottom	TP2L3LB	19.94%
		Middle	Top	TP2L3MT	18.13%
			Bottom	TP2L3MB	21.18%
		Right	Top	TP2L3RT	20.32%
			Bottom	TP2L3RB	18.31%
3	1	Left	Top	TP3L1LT	17.25%
			Bottom	TP3L1LB	17.18%
		Middle	Top	TP3L1MT	18.33%
			Bottom	TP3L1MB	22.32%
		Right	Top	TP3L1RT	22.05%
			Bottom	TP3L1RB	21.94%
	2	Left	Top	TP3L2LT	22.32%
			Bottom	TP3L2LB	20.39%
		Middle	Top	TP3L2MT	16.14%
			Bottom	TP3L2MB	19.34%
		Right	Top	TP3L2RT	18.27%
			Bottom	TP3L2RB	16.47%
	3	Left	Top	TP3L3LT	18.94%
			Bottom	TP3L3LB	18.97%
		Middle	Top	TP3L3MT	21.17%
			Bottom	TP3L3MB	18.48%
		Right	Top	TP3L3RT	22.78%
			Bottom	TP3L3RB	22.20%

4.1.1.1 Area Percent Defects Statistical Significance

Regression analysis was run using Microsoft Excel 2013 to determine the statistical significance of the voltage on defect content (oxides, pores, and cracks). Table 4.3 provides details of the analysis including the p-value. It was found that the p-value was significantly lower than the 0.05 null hypothesis confirming a relationship between voltage and defect content.

Table 4.3 Statistical Analysis of Area Percent Defects with Input Voltage.

Regression Statistics	
Multiple R	0.503
R Square	0.253
Adjusted R Square	0.239
Standard Error	0.027
Observations	54

ANOVA					
	df	SS	MS	F	Significance F
Regression	1	0.01260	0.01260	17.62215	0.00011
Residual	52	0.03717	0.00071		
Total	53	0.04977			

Summary Output	Voltage	Intercept
Coefficients	-0.00374	0.33043
Standard Error	0.00089	0.02831
t Stat	-4.19787	11.67226
p-value	0.00011	3.82389×10^{-16}
Lower 95%	-0.00553	0.27362
Upper 95%	-0.00195	0.38723

4.1.2 Vickers Hardness

Vickers hardness was taken through the coating thickness with indents targeted to be within splats as discussed in Section 3.5.1. Figure 4.1 shows indents taken through the coating thickness for each voltage condition. For hardness values under 500 HV, a magnified OM image was taken. Figure 4.2 shows the three hardness values from Figure 4.1 that were under 500 HV. Figure 4.2 (a) shows a Vickers indent with a hardness value of 390 HV from the 26.5V voltage condition coating. It can be seen that the indenter was not within a splat but instead broke through the coating next to a suspected large oxide inclusion. Figure 4.2 (c) shows a second indent from the 26.5V voltage condition closer to the middle of the coating with hardness reading of 403 HV. At the top of the indent it is observed that the indenter cracked through the splat resulting in the lower hardness. The third indent below 500 HV was from the 36.5V voltage condition with a hardness value of 419 HV. This indent was taken at the bottom of a splat resulting in a crack forming between two splats stacked on one another.

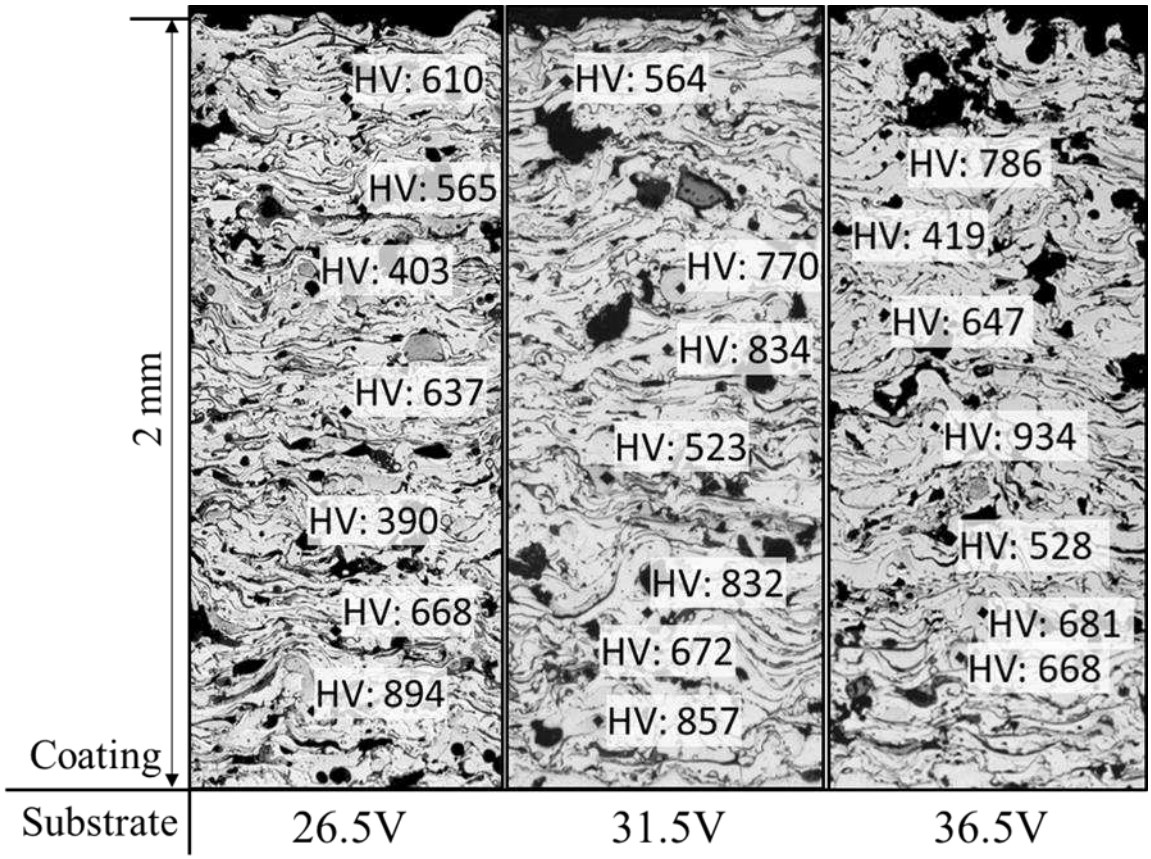

Figure 4.1 Vickers hardness taken through the coating thickness for each voltage condition.

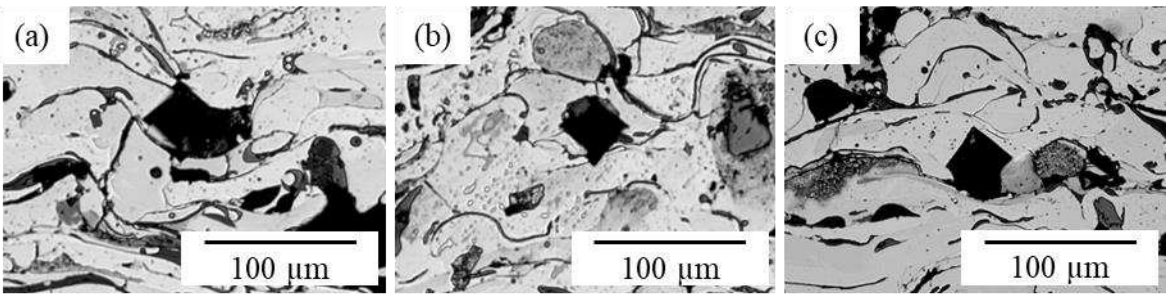

Figure 4.2 Vickers hardness values from Figure 4.1 that were under 500 HV.

4.1.3 SEM Images and Composition Maps

Composition maps were taken for each input voltage condition to identify major coating features. SEM and EDS details are provided in Section 3.3. This section will provide elemental map results and selected spot scan results for more detailed compositions.

4.1.3.1 Low Voltage Condition SEM Analysis

The low voltage condition has an input voltage of 26.5V. Several locations within the coating were selected to take composition maps. Figure 4.3 shows compositional maps taken at the interface between the coating and substrate. Figure 4.4 shows two locations where compositional maps were taken within the coating near a spherical oxide and at large crack.

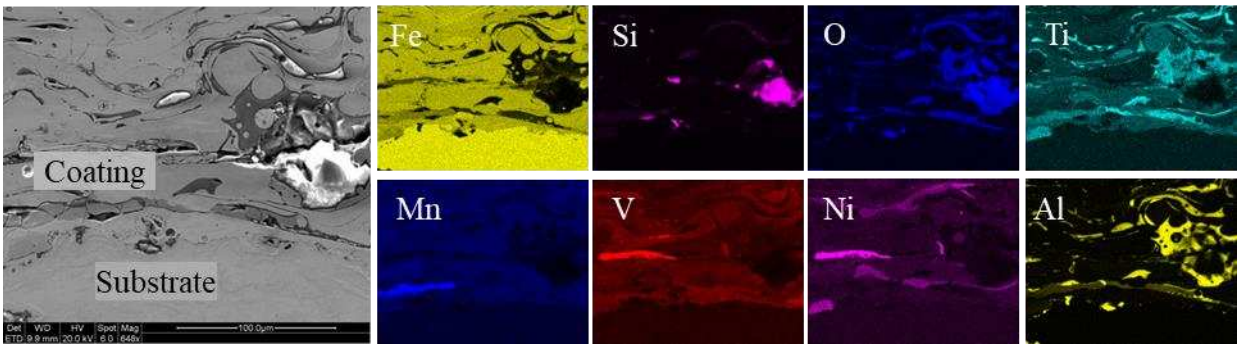

Figure 4.3 Compositional maps of the 26.5V input voltage condition at the coating substrate interface for elements Fe, Mn, Si, V, O, Ni, Ti, and Al.

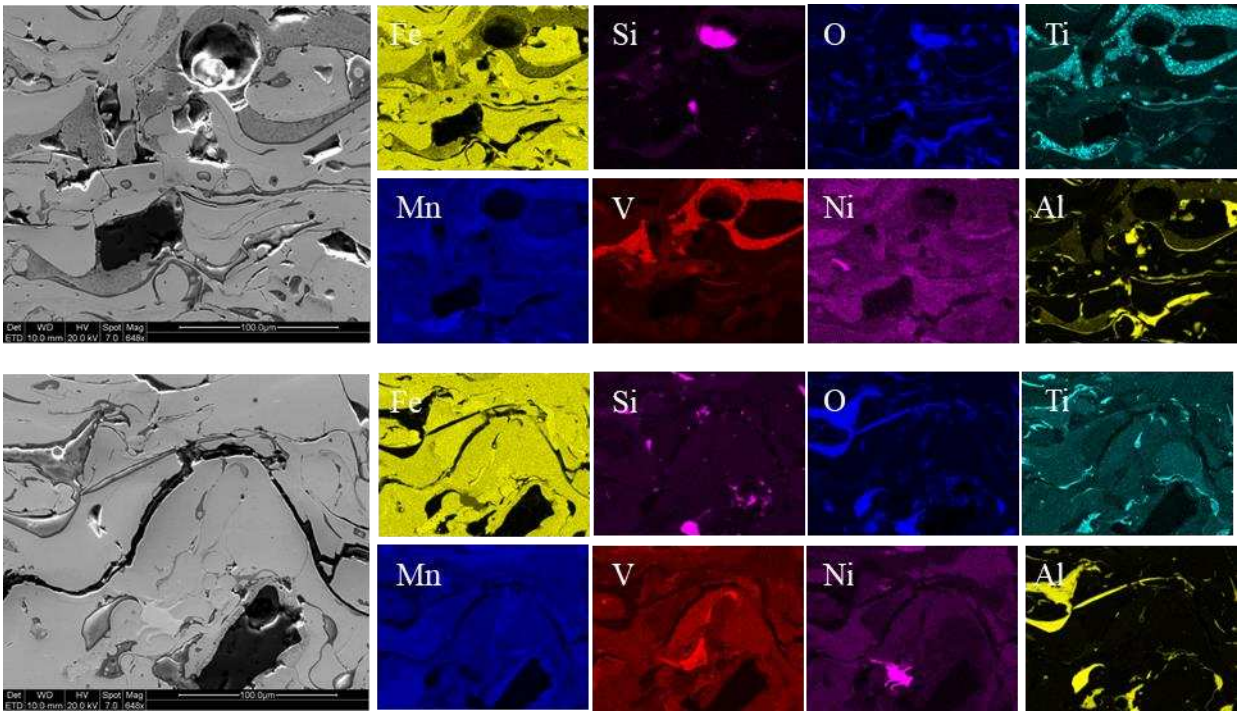

Figure 4.4 Compositional maps of the 26.5V input voltage condition within the coating for elements Fe, Mn, Si, V, O, Ni, Ti, and Al.

4.1.3.2 High Voltage Condition SEM Analysis

The low voltage condition has an input voltage of 36.5V. After Vickers hardness was taken through the coating thickness, composition maps were taken at several of the indents. Composition maps were overlaid on the SEM images to better identify particular regions. Figure 4.5 shows the three locations where compositional maps were taken in relation to the substrate. The hardness value recorded for each indent is overlaid on the SEM image and represent the three indents nearest the substrate as previously reported in Figure 4.1.

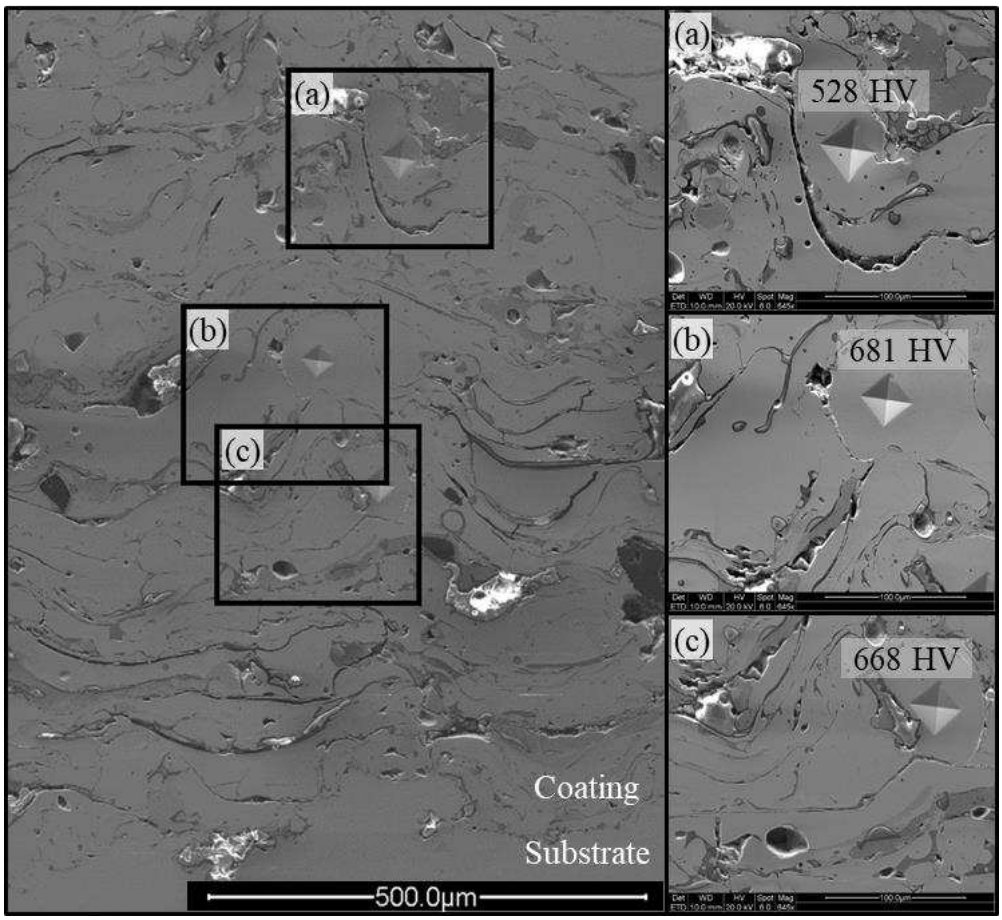

Figure 4.5 Three locations where compositional maps were taken in relation to the substrate. Vickers hardness values are overlaid next to respective indent.

Figure 4.6 shows the compositions maps for location (a) of Figure 4.5 with each element map overlaid on the SEM image for better differentiating the splats, oxides, and pore features. Looking at the oxygen composition map, it is easy to correlate other elements present at the same location and determine what

oxides are present. Additionally, areas of element concentration can be identified such as observed for the aluminum, nickel, and vanadium composition maps. Three spot scans were taken with spot 1 representing the composition at the Vickers indent, spot 2 taken within the region of aluminum concentration, and spot 3 at the round region of vanadium concentration. Location of spot scan and spot scan results are provided in Figure 4.7.

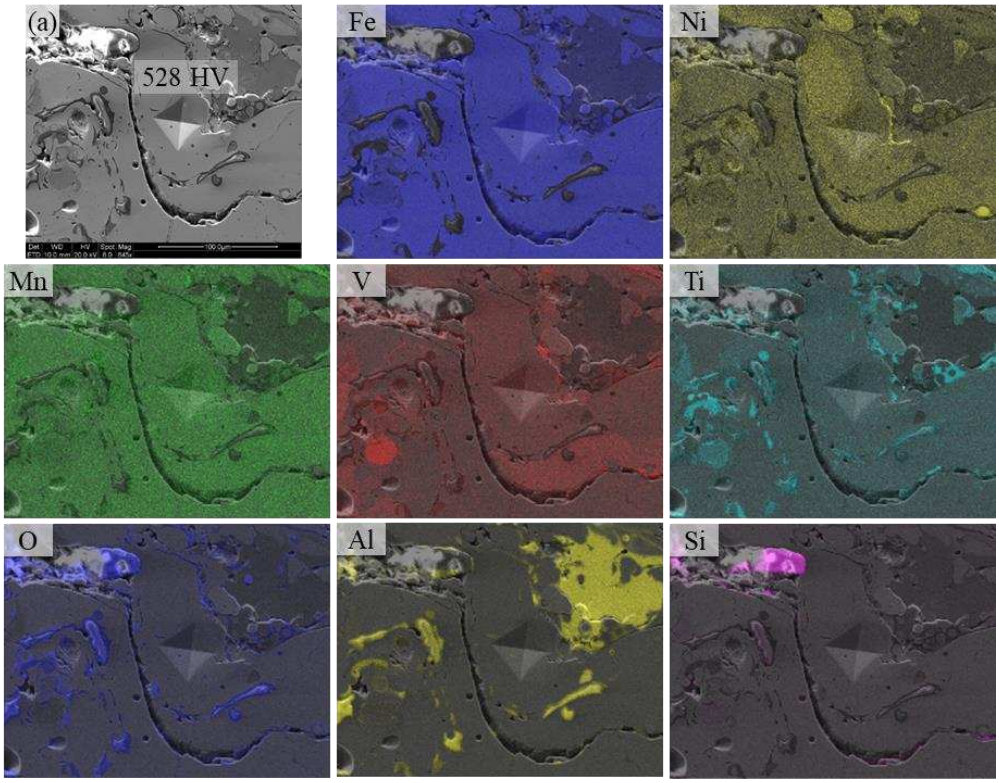

Figure 4.6 Composition maps for Fe, Mn, Si, V, O, Ni, Ti, and Al at location (a) of Figure 4.5.

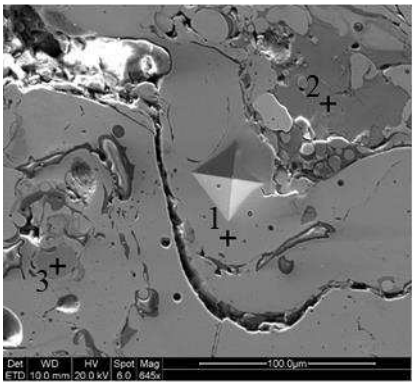

Spot 1

Element	Wt %
C K	3.02
O K	3.68
AlK	2.01
SiK	1.57
TiK	1.49
V K	1.11
MnK	3.81
FeK	81.41
NiK	1.89
Total	100.00

Spot 2

Element	Wt %
C K	2.02
O K	1.77
AlK	52.12
SiK	0.28
TiK	0.09
V K	0.32
MnK	0.36
FeK	42.90
NiK	0.15
Total	100.00

Spot 3

Element	Wt %
C K	2.45
O K	3.23
AlK	5.55
SiK	4.43
TiK	4.49
V K	7.59
MnK	2.92
FeK	68.88
NiK	0.46
Total	100.00

Figure 4.7 Spot scans taken within location (a) of Figure 4.5.

Location (b) from Figure 4.5 had composition maps taken with results shown in Figure 4.8. The Vickers indent shown was taken within the center of the splat cross-section providing a good reading for the splat material hardness. Spot scans were taken within three different splats to investigate potential splat composition variance.

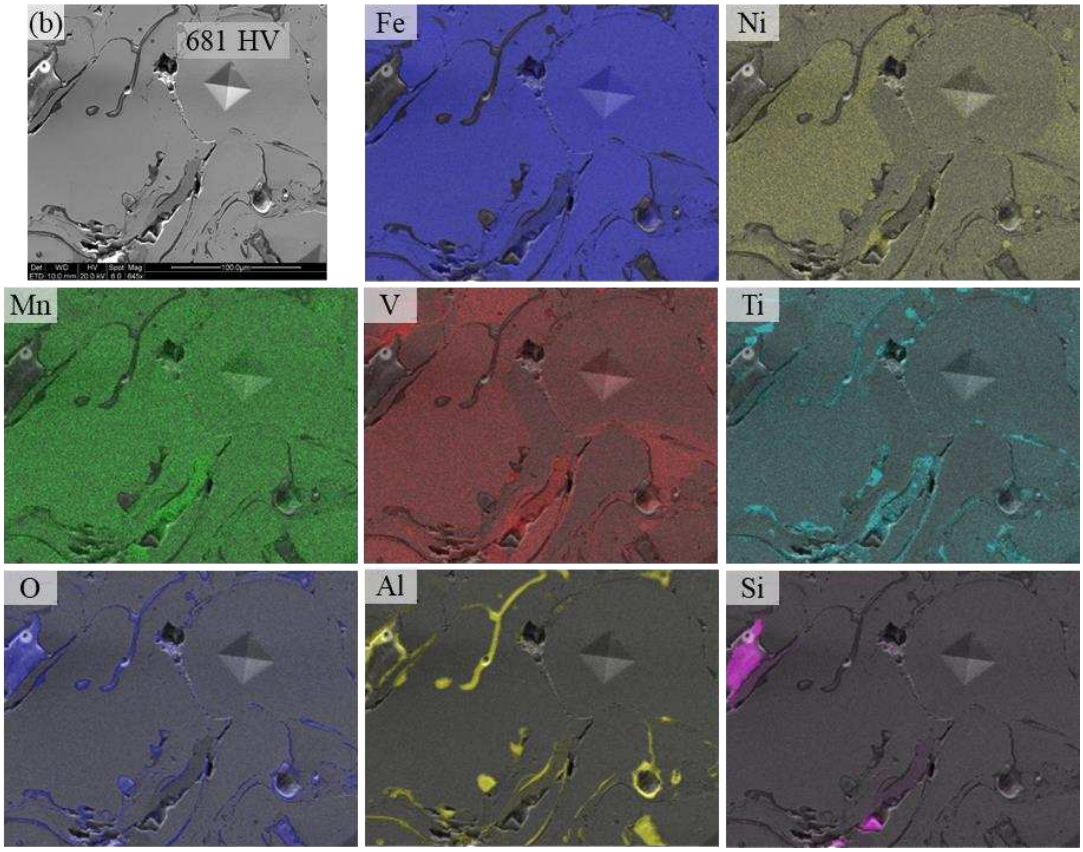

Figure 4.8 Composition maps for Fe, Mn, Si, V, O, Ni, Ti, and Al at location (b) of Figure 4.5.

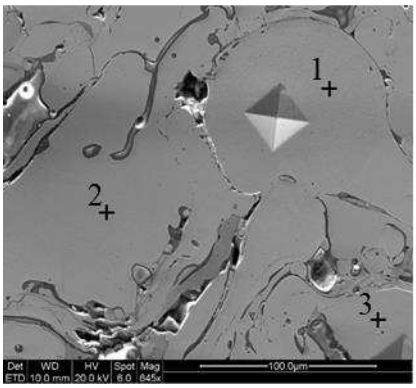

Spot 1

Element	Wt %
O K	3.55
AlK	2.08
SiK	1.68
TiK	1.15
V K	0.85
MnK	3.89
FeK	85.97
NiK	0.82
Total	100.00

Spot 2

Element	Wt %
O K	3.58
AlK	2.22
SiK	1.92
TiK	1.59
V K	1.90
MnK	4.33
FeK	80.53
NiK	3.93
Total	100.00

Spot 3

Element	Wt %
C K	2.81
O K	3.60
AlK	2.38
SiK	1.57
TiK	2.01
V K	0.67
MnK	4.07
FeK	81.52
NiK	1.37
Total	100.00

Figure 4.9 Spot scans taken within location (b) of Figure 4.5.

Results for composition maps taken at the third location, as represented by location (c) in Figure 4.8, are provided in Figure 4.10. Three spot scans were taken of the coating with spot 1 at a region of high nickel, spot 2 at a region of concentrated vanadium, and spot 3 at an aluminum and titanium oxide. Spot scan locations and results are provided in Figure 4.11.

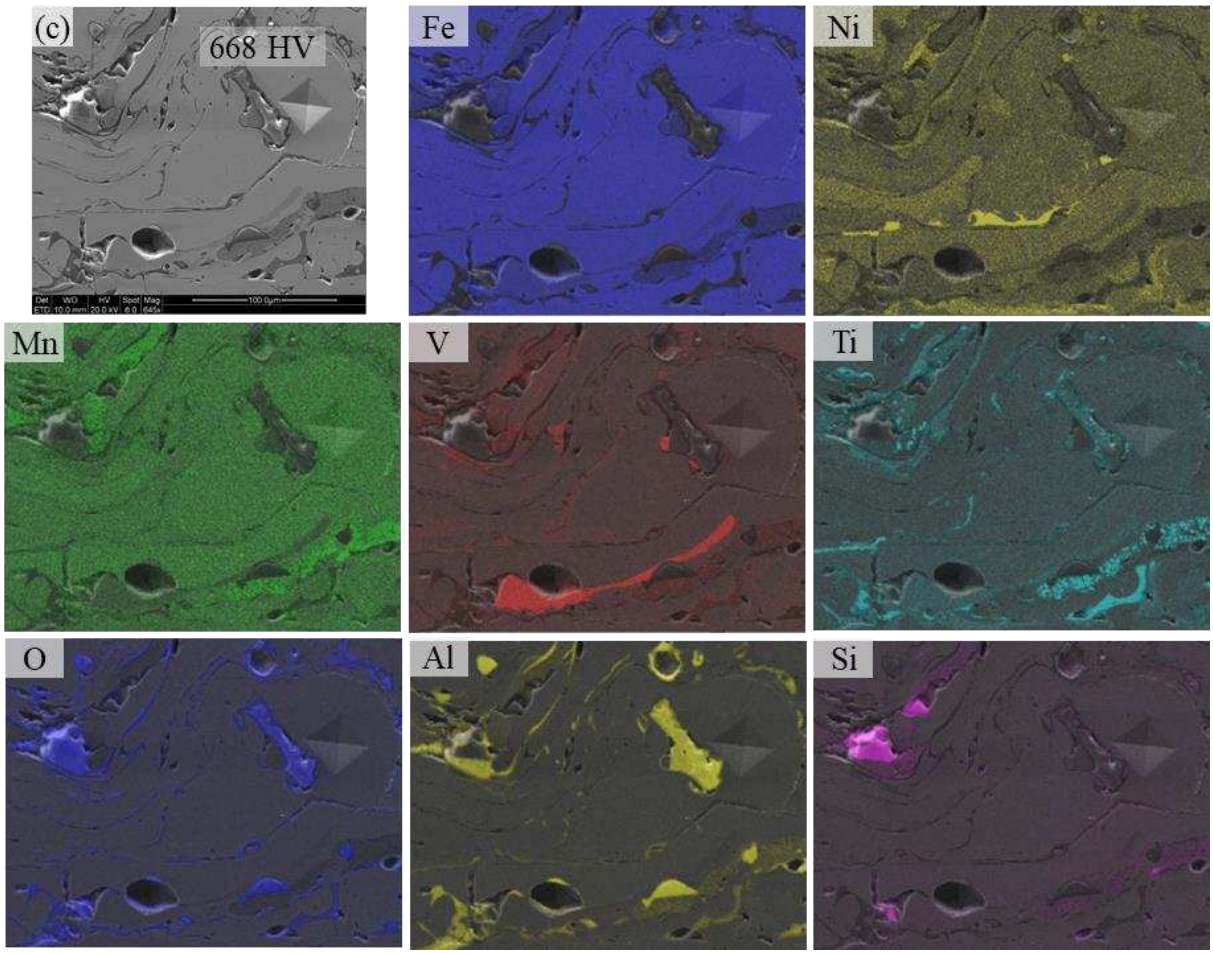

Figure 4.10 Composition maps for Fe, Mn, Si, V, O, Ni, Ti, and Al at location (c) of Figure 4.5.

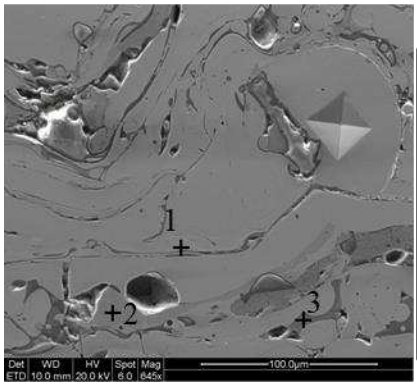

Spot 1		Spot 2		Spot 3	
Element	Wt %	Element	Wt %	Element	Wt %
O K	2.91	O K	4.70	O K	31.22
AlK	2.53	AlK	2.59	AlK	25.56
SiK	1.66	SiK	2.67	SiK	0.26
TiK	1.81	TiK	4.79	TiK	29.32
V K	1.34	V K	17.94	V K	0.70
MnK	2.18	MnK	1.44	MnK	1.70
FeK	60.67	FeK	65.52	FeK	10.75
NiK	26.90	NiK	0.35	NiK	0.48
Total	100.00	Total	100.00	Total	100.00

Figure 4.11 Spot scans taken within location (c) of Figure 4.5.

4.1.4 Nano-Indentation Results

For each voltage condition, two nano-indentation grids were taken across the coating-substrate interface of mounted and polished coating cross-sections as previously discussed in Section 3.5.2. OM images taken at each indentation grid are shown in Figure 4.12. Values in gigapascals (GPa) for each indent are provided in Figure 4.13 where the lower-left value represents the furthest value into the substrate.

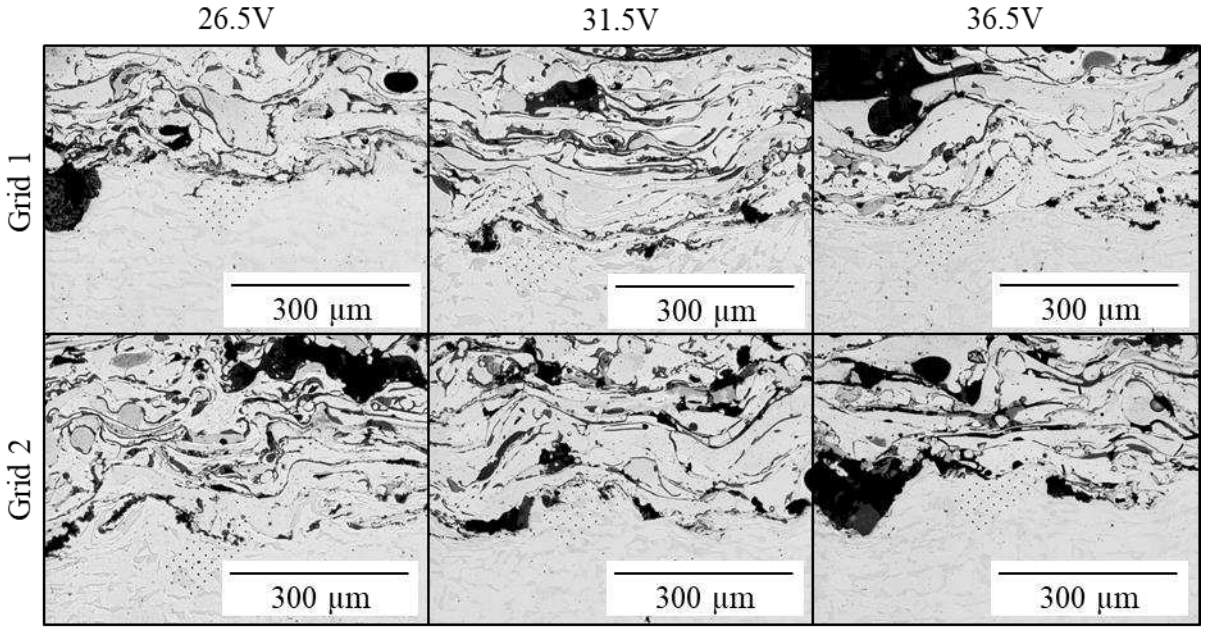

Figure 4.12 OM images taken at each nano-indentation grid across the coating-substrate interface.

Conditional formatting was applied to the grids to better visualize the distributions. Identical values with different colors are a result of rounding within the grid.

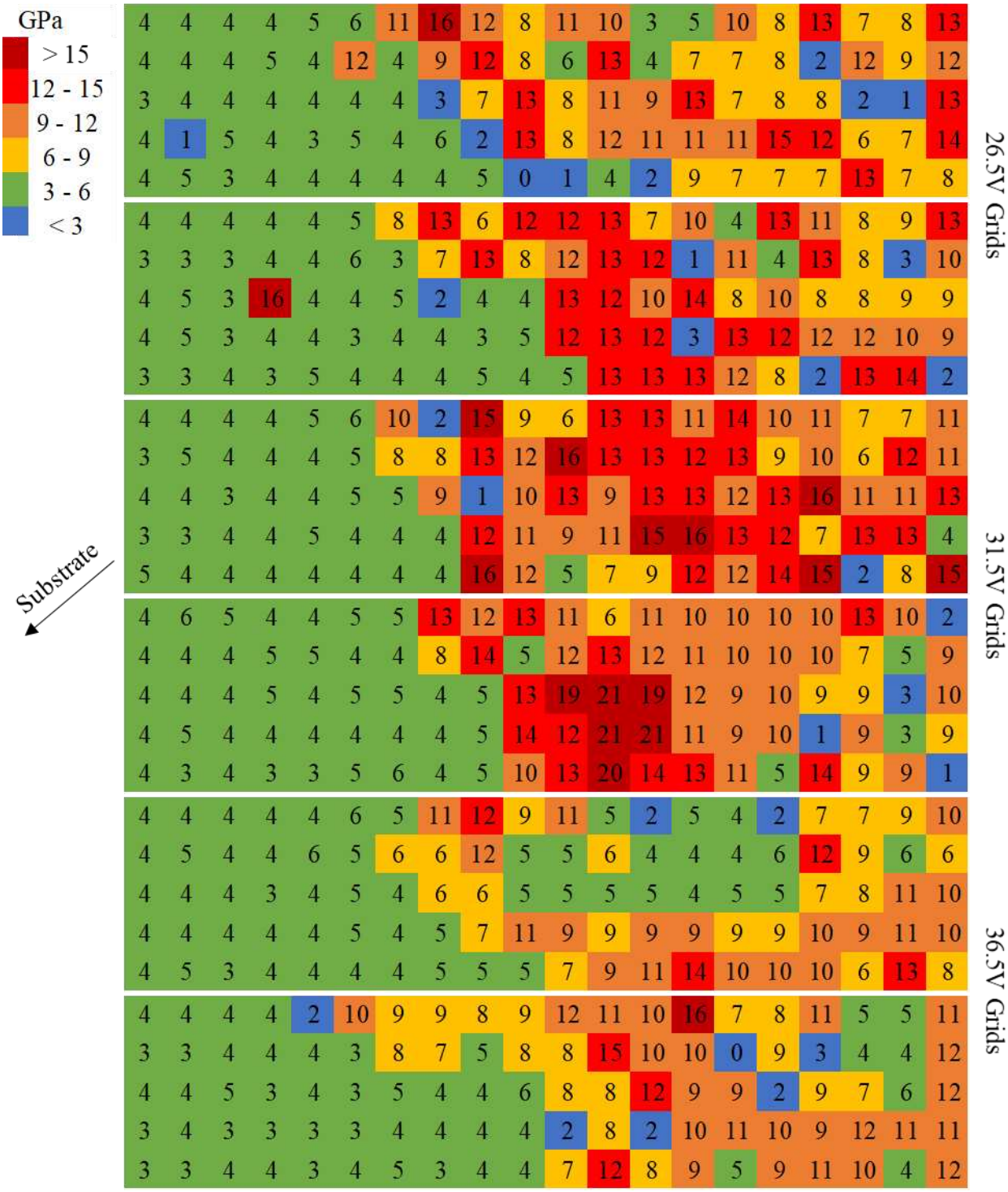

Figure 4.13 Nano-indentation results for each voltage condition

4.1.5 Four-Point Bending Results with DIC

As discussed in Section 3.6.1, six samples were prepared for bend testing. Figure 4.14 shows material that was water jet-cut before sectioning, milling, and surface grinding to final dimensions. Final dimensions were taken at locations shown in Figure 4.15 with a digital micrometer. Final sample dimensions for length, width, and thickness are provided in Table 4.4 with average values used to calculate stress and strain.

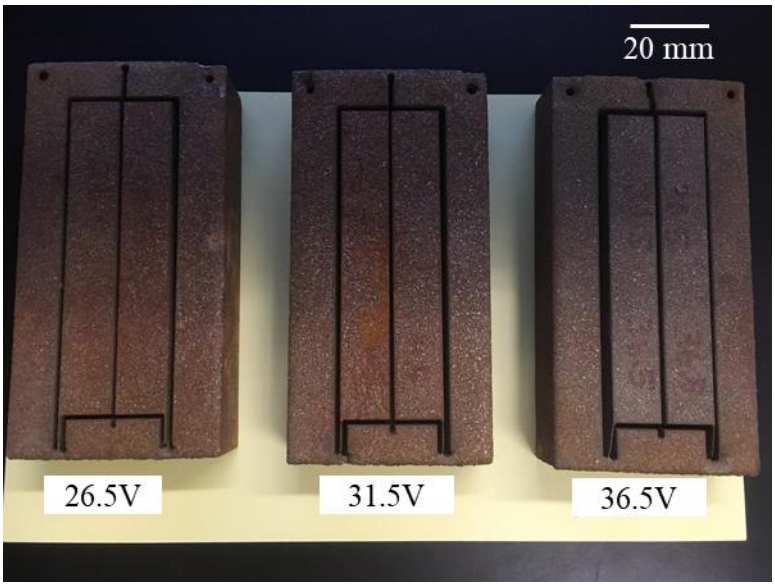

Figure 4.14 Four point bend samples water-jet cut from each voltage test piece.

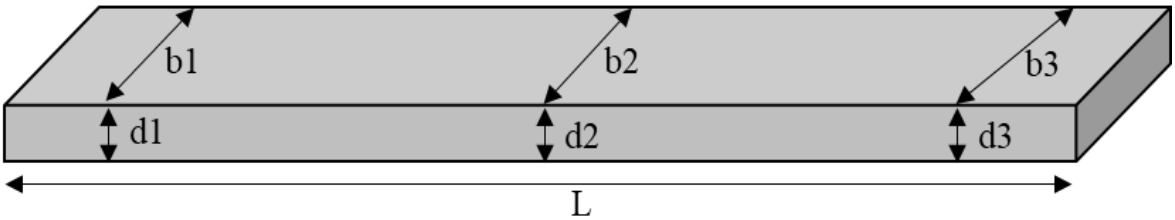

Figure 4.15 Location where four-point bend sample dimensions were taken.

Table 4.4 Bend sample dimensions.

Sample ID	Width (mm) 1	Width (mm) 2	Width (mm) 3	Thickness (mm) 1	Thickness (mm) 2	Thickness (mm) 3	Length (mm)	Thickness Average	Width Average
26.5 BT1	12.500	12.492	12.501	5.218	5.138	5.153	77.495	12.498	5.170
26.5 BT2	12.610	12.584	12.591	5.348	5.329	5.393	76.505	12.595	5.357
31.5 BT1	12.288	12.291	12.299	5.407	5.278	5.322	76.225	12.293	5.336
31.5 BT2	12.373	12.362	12.366	5.393	5.343	5.431	76.759	12.367	5.389
36.5 BT1	12.227	12.229	12.228	5.356	5.300	5.330	76.683	12.228	5.329
36.5 BT2	12.322	12.327	12.328	5.346	5.329	5.433	76.276	12.326	5.369

Bend testing was performed with DIC to track the strains during the test and correlate them with load data. The face of the sample was imaged and consisted of 2 mm thick coating at the outer-fiber with 2 mm of substrate thickness that the load was applied to. This can be viewed in Figure 4.16 (a) showing a strain image taken 90 seconds into the second bend test of the 26.5 input voltage condition overlaid onto the sample image inside the bending fixture. Figure 4.16 (b) shows the sample posttest with DIC paint spatter cleaned off showing crack locations in relationship to strain readings and loading fixtures.

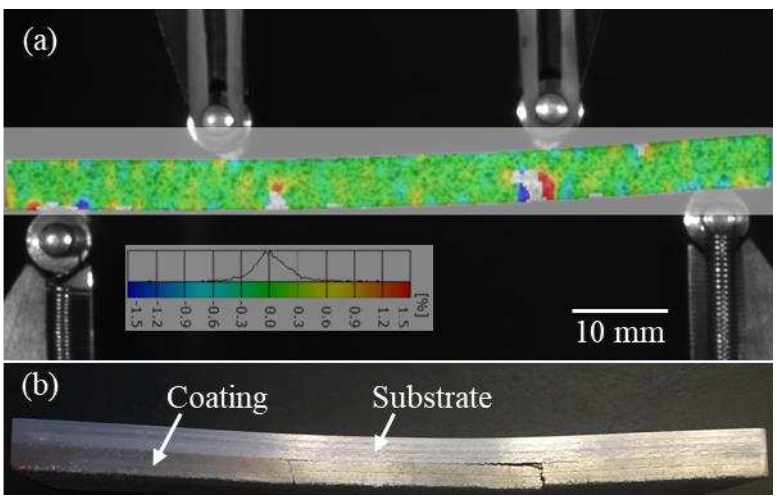

Figure 4.16 Strain image taken 90 seconds into the second bend test of the low input voltage condition overlaid onto the sample image inside the bending fixture (a) with sample posttest with DIC paint spatter cleaned off showing location of cracks.

Figure 4.17 shows an example of how the DIC data was correlated with the load results where each load drop was matched with the corresponding strain images. The load drop can be matched with strain concentrations in the area on the sample where the crack initiated. Additionally, the location of the first

crack can be determined from fracture analysis. Load versus time was compared with DIC data in the same fashion as shown in Figure 4.17.

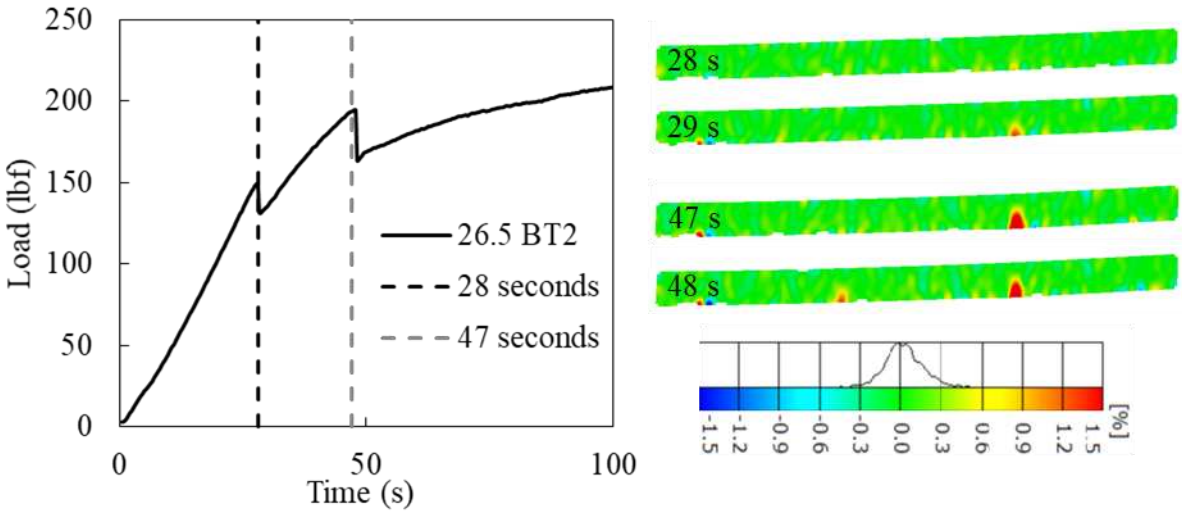

Figure 4.17 Load versus time for the second bend test of the low input voltage condition with strain images correlated each load drop.

4.1.6 Fracture Surface

Four point bend samples were sectioned as shown in Figure 3.13 to analyze the fracture surface. Figure 4.18 shows an image of the fracture surface of the first bend test of the 26.5V input voltage condition. The substrate was sectioned with a ceramic blade being careful to not damage the fracture surface; however, several of the coating layers were sectioned and would not be used in the analysis.

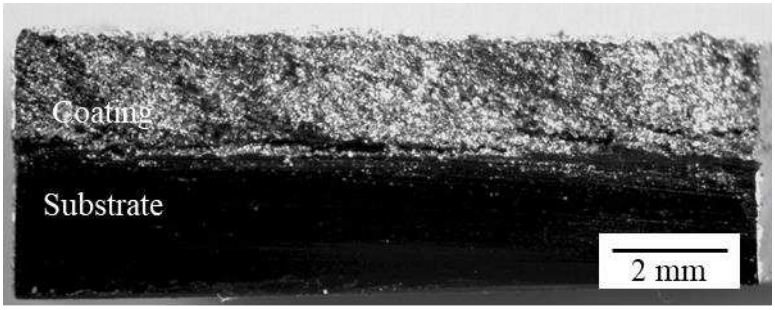

Figure 4.18 Fracture surface of the first bend test of the 26.5V input voltage condition.

The fracture surface was also analyzed with SEM. Figure 4.19 shows an SEM image of the full coating thickness fracture surface. The cutting marks can be viewed on the substrate and the first splat layer leaving

a majority of the facture surface intact for fractography. Individual splats can be observed as well as the point where the coating crack changed from transvers to longitudinal propagation to the bending stress.

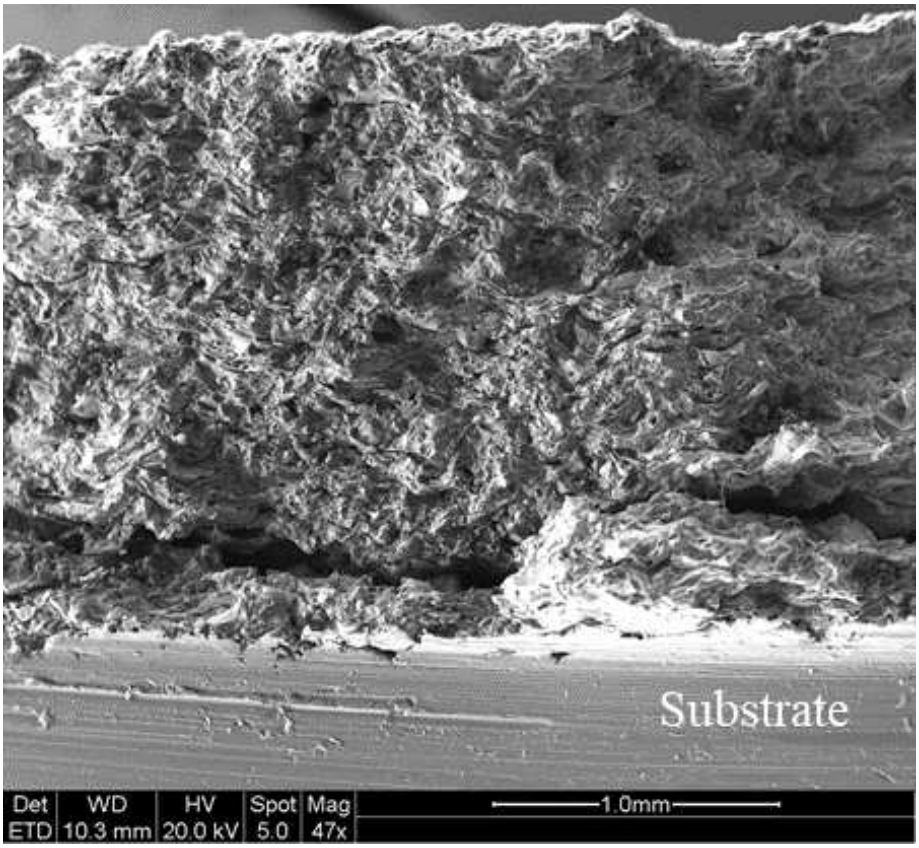

Figure 4.19 SEM image of bend test fracture surface.

SEM images were taken at various locations within the coating representative of the whole. Spot scans for compositions were taken of various features and areas suspected of crack initiation. An example of this is shown in Figure 4.20 where an image was taken of a cleaved splat with visible river-lines. A spot scan was taken at the suspected crack initiation point indicated by the river lines revealing an aluminum oxide.

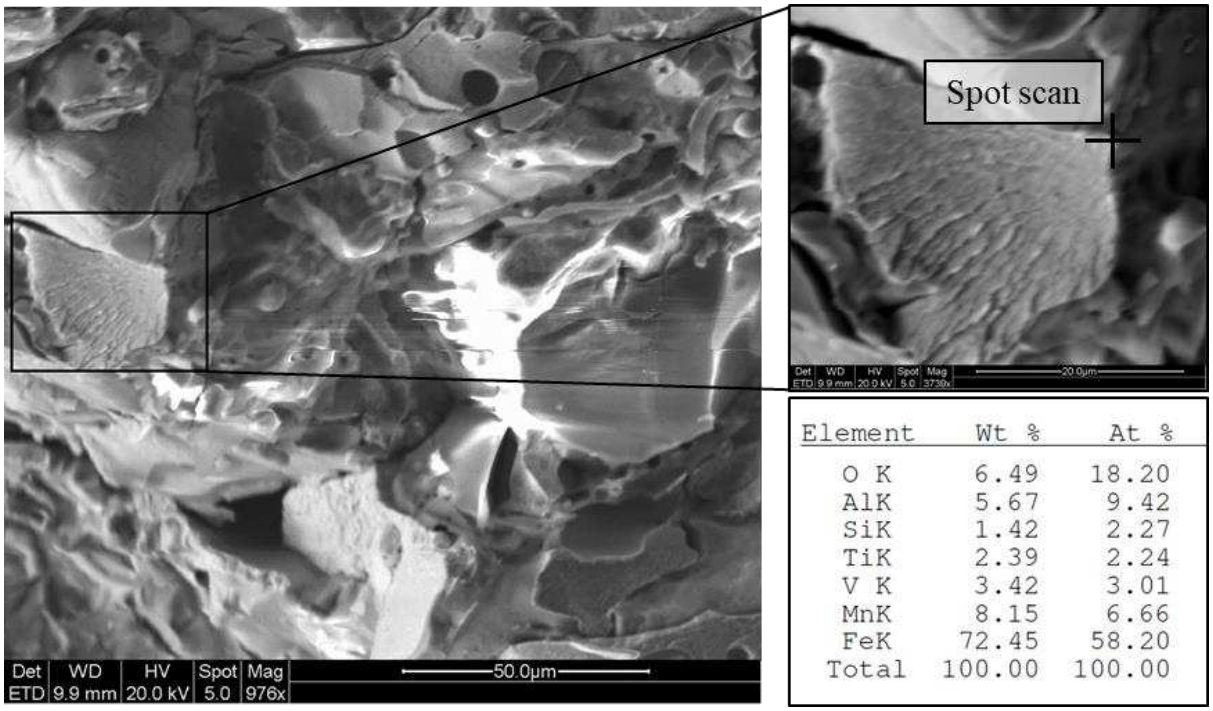

Figure 4.20 Cleaved splat showing river lines with spot scan taken at apparent initiation point.

4.1.7 Wear Test – HH1

Two wear tests were performed on the 31.5V and 36.5V voltage conditions with results provided in Table 4.5. Samples were tested for 1 hour at 200 revolutions per minute. Image of samples after test is provided in Figure 4.21.

Table 4.5 Wear Results.

Pressure Condition	Revolutions	Mass Loss (g)	Wear Rate (mm^3/Nm)	Average Wear
31.5V Test 1	12,000	1.244	1.21×10^{-4}	1.17×10^{-4}
31.5V Test 2	12,000	1.154	1.12×10^{-4}	
36.5V Test 1	12,000	1.108	1.08×10^{-4}	1.11×10^{-4}
36.5V Test 2	12,000	1.167	1.13×10^{-4}	

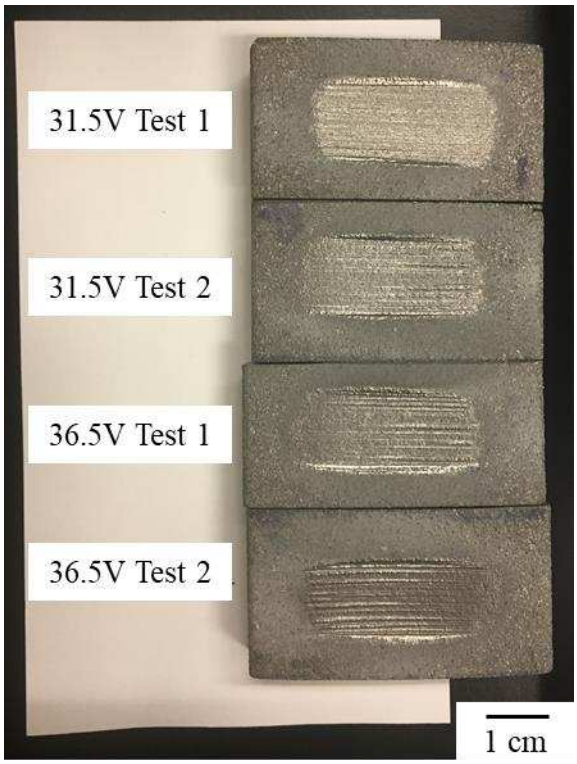

Figure 4.21 Image of wear test samples posttest.

4.2 Thermal Sprayed New Composition Coating

Samples were sprayed to a new composition as described in Section 3.7.1.2. Temperature was read approximately every 80 passes back and forth with the thermal spray gun using an infrared temperature gun to maintain the coating surface temperature under 93°C (200°F). Temperatures were observed to reach as high as 250°F during spraying at which point the coating was allowed to cool below 200°F before resuming thermal spraying.

4.2.1 Area Percent Defects

Area percent defects (oxides, pores, cracks) results are provided in Table 4.6 for varying spray pressures. Shown previously for the HH1 test pieces in Figure 3.4, three metallographic samples were taken along the center-line of each test piece and are identified as location 1, 2, and 3. Each metallographic sample had six images taken of the coating cross-section at the left-hand, middle, and right-hand side with one near the substrate identified and bottom and one near the coating surface identified as the top. Thus, the micrograph

naming convention for Table 4.6 is “test piece number” + “location number” + “left/right/middle” + “top/bottom”.

Table 4.6 Area Percent Defects for $Fe_{0.32}Co_{0.08}Cr_{0.2}Ni_{0.32}Mo_{0.07}Ta_{0.01}$ composition sprayed at varying pressures.

Test Piece	Location	Image	Top/Bottom	Micrograph Name	Percent Defects
1	1	Left	Top	TP1L1LT	21.41%
			Bottom	TP1L1LB	23.24%
		Middle	Top	TP1L1MT	19.71%
			Bottom	TP1L1MB	23.80%
		Right	Top	TP1L1RT	18.89%
			Bottom	TP1L1RB	25.56%
	2	Left	Top	TP1L2LT	23.40%
			Bottom	TP1L2LB	25.15%
		Middle	Top	TP1L2MT	25.81%
			Bottom	TP1L2MB	22.86%
		Right	Top	TP1L2RT	18.59%
			Bottom	TP1L2RB	27.16%
	3	Left	Top	TP1L3LT	23.87%
			Bottom	TP1L3LB	23.42%
		Middle	Top	TP1L3MT	22.16%
			Bottom	TP1L3MB	21.18%
		Right	Top	TP1L3RT	19.35%
			Bottom	TP1L3RB	21.26%
2	1	Left	Top	TP2L1LT	32.12%
			Bottom	TP2L1LB	31.92%
		Middle	Top	TP2L1MT	33.49%
			Bottom	TP2L1MB	32.64%
		Right	Top	TP2L1RT	29.79%
			Bottom	TP2L1RB	30.47%
	2	Left	Top	TP2L2LT	35.92%
			Bottom	TP2L2LB	31.77%
		Middle	Top	TP2L2MT	35.16%
			Bottom	TP2L2MB	34.64%
		Right	Top	TP2L2RT	34.13%
			Bottom	TP2L2RB	33.78%

Table 4.6 Continued

Test Piece	Location	Image	Top/Bottom	Micrograph Name	Percent Defects
2	3	Left	Top	TP2L3LT	30.82%
			Bottom	TP2L3LB	32.42%
		Middle	Top	TP2L3MT	34.55%
			Bottom	TP2L3MB	29.73%
		Right	Top	TP2L3RT	31.95%
			Bottom	TP2L3RB	29.91%
3	1	Left	Top	TP3L1LT	68.83%
			Bottom	TP3L1LB	60.11%
		Middle	Top	TP3L1MT	64.15%
			Bottom	TP3L1MB	64.51%
		Right	Top	TP3L1RT	60.29%
			Bottom	TP3L1RB	58.09%
	2	Left	Top	TP3L2LT	70.70%
			Bottom	TP3L2LB	60.25%
		Middle	Top	TP3L2MT	71.47%
			Bottom	TP3L2MB	65.46%
		Right	Top	TP3L2RT	69.14%
			Bottom	TP3L2RB	65.41%
	3	Left	Top	TP3L3LT	60.36%
			Bottom	TP3L3LB	56.89%
		Middle	Top	TP3L3MT	54.01%
			Bottom	TP3L3MB	61.81%
		Right	Top	TP3L3RT	57.70%
			Bottom	TP3L3RB	56.06%

4.2.2 Vickers Hardness

Vickers hardness was taken through the coating thickness with indents targeted to be within splats as discussed in Section 3.5.1. Figure 4.22 represents OM images compiled together showing indents taken through the coating thickness for the high (310 kPa) and low (172 kPa) spray pressure conditions. Due to the high oxidation present in the high spray pressure condition, taking an indent within a splat was difficult to accomplish with several indents cracking the surface, and thus, increasing the error of the measurements.

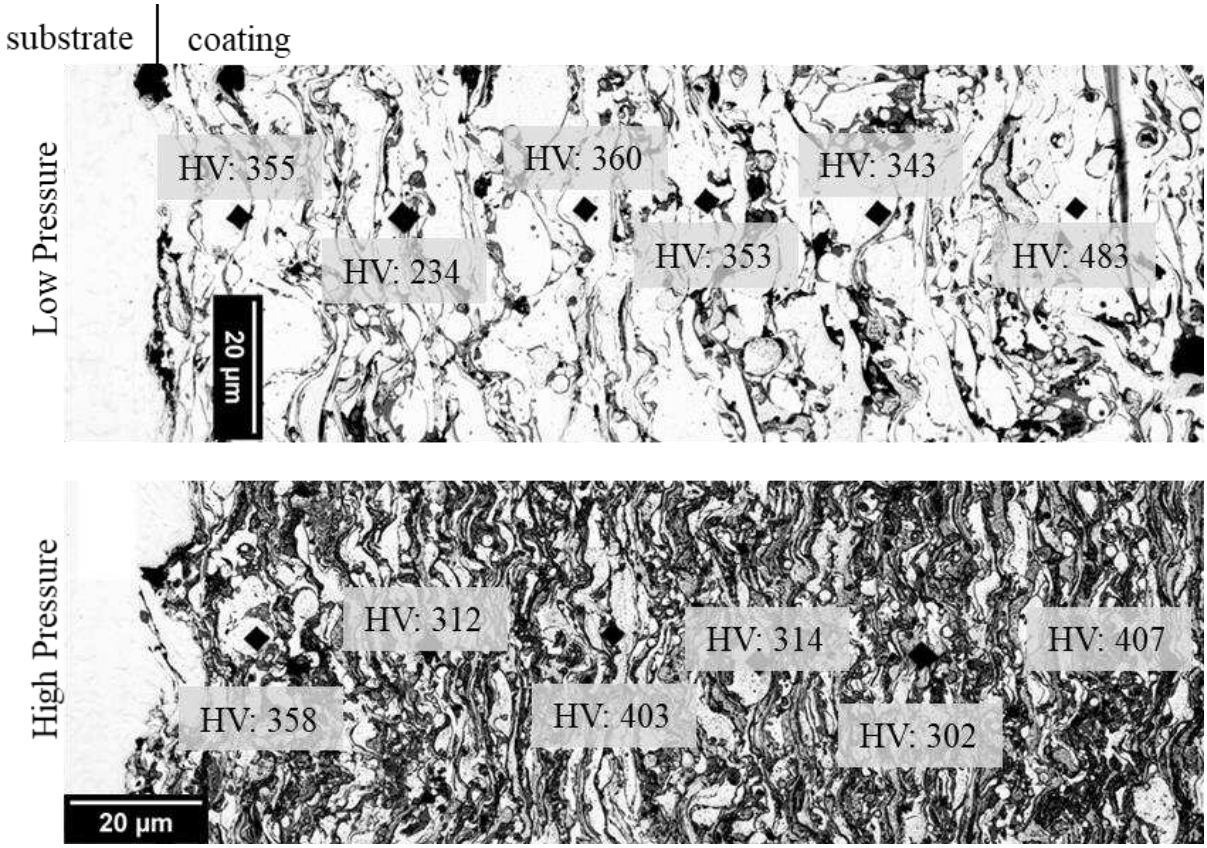

Figure 4.22 Vickers hardness taken through the coating thickness for the high and low pressure conditions.

4.2.3 SEM Images and Composition Maps

Composition maps were taken to identify major coating features. SEM and EDS details are provided in Section 3.3. Figure 4.23 shows composition maps taken of the 241 kPa pressure condition coating for Ni, Co, Fe, Cr, and O. Partially transparent compositional maps haven been overlaid on the SEM image to better show the elemental distributions within various splats.

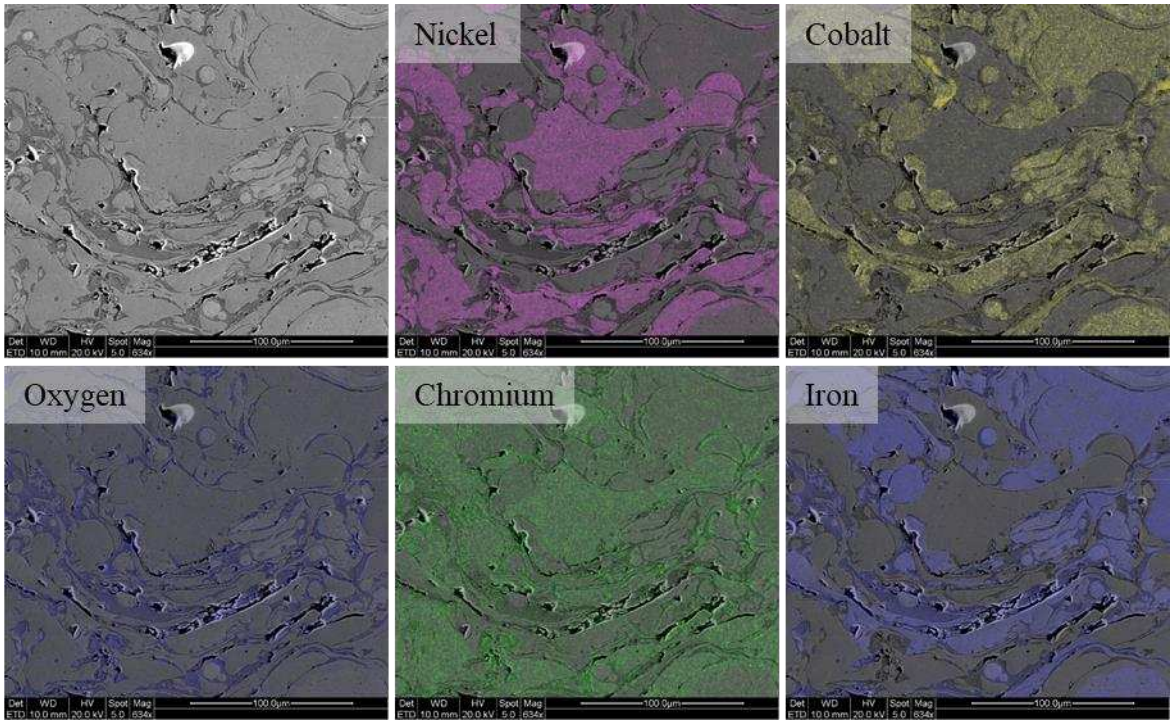

Figure 4.23 Compositional maps taken of the 241 kPa coating overlaid on the SEM image from the same location.

Additional composition maps were taken across the coating substrate interface as shown in Figure 4.24. Transparent composition maps are overlaid over the SEM image taken at the same location to help differentiate between the substrate and coating, different splat composition, and oxide types.

4.2.4 Four-Point Bending Results

As discussed in Section 3.6.1, samples were prepared for bend testing by water jet-cutting from the test pieces before sectioning, milling and surface grinding to final dimensions. However, instead of two samples per input voltage condition, there were three samples tested per spray pressure condition. Final dimensions were taken at locations shown in Figure 4.15 with a digital micrometer. Final sample dimensions for length, width, and thickness are provided in Table 4.7 with average values used to calculate stress and strain. The naming convention for the sample identification is first the spray pressure in psi and then the bend test number. For example, the first bend test sample of the 172 kPa (25 psi) spray condition was called "*25 BT1*".

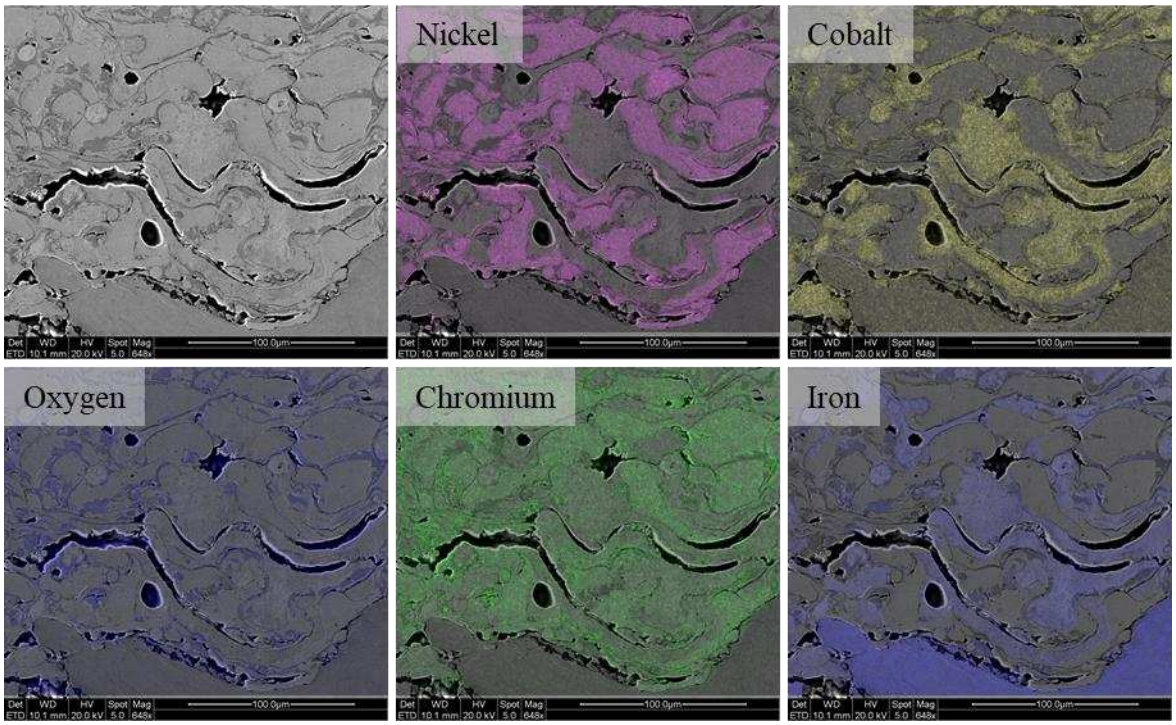

Figure 4.24 Compositional maps taken at the coating-substrate interface overlaid on the SEM image from the same location.

Table 4.7 Bend Sample Dimensions.

Sample ID	Width (mm) 1	Width (mm) 2	Width (mm) 3	Thickness (mm) 1	Thickness (mm) 2	Thickness (mm) 3	Length (mm)	Thickness Average	Width Average
25 BT1	11.940	11.930	11.930	4.510	4.290	4.470	79.450	11.933	4.423
25 BT2	11.960	11.960	11.960	4.380	4.040	4.290	79.590	11.960	4.237
25 BT3	11.960	11.950	11.950	4.450	4.080	4.190	79.560	11.953	4.240
35 BT1	11.960	11.950	11.960	4.320	4.040	4.230	79.540	11.957	4.197
35 BT2	11.950	11.950	11.950	4.240	4.060	4.210	79.410	11.957	4.170
35 BT3	12.370	12.350	12.370	4.270	4.120	4.190	79.440	12.363	4.193
45 BT1	11.960	11.950	11.960	4.210	3.930	4.160	79.360	11.957	4.100
45 BT2	11.960	11.960	11.960	4.240	4.090	4.240	79.380	11.960	4.190
45 BT3	12.340	12.350	12.370	4.270	4.130	4.240	79.540	12.353	4.213

Bend testing was conducted as discussed in Section 3.6.2 for each sample. DIC was not conducted on the new composition samples. Outer-fiber stresses were calculated and plotted using actual sample geometries. Figure 4.25 shows the outer-fiber stress versus strain for the low spray pressure condition. The second bend sample (*25 BT2*) was found to have a significantly lower stress achieved before cracking. It was found that an incorrect coating was prepared for bend testing as a result of preparing the wrong side of the substrate for testing. This is due to the substrates being coated on both sides as a way to save time and

material during the practice spraying of the new composition. For sample *25 BT2*, the correct side was marked incorrectly resulting in the wrong coating being prepared and tested.

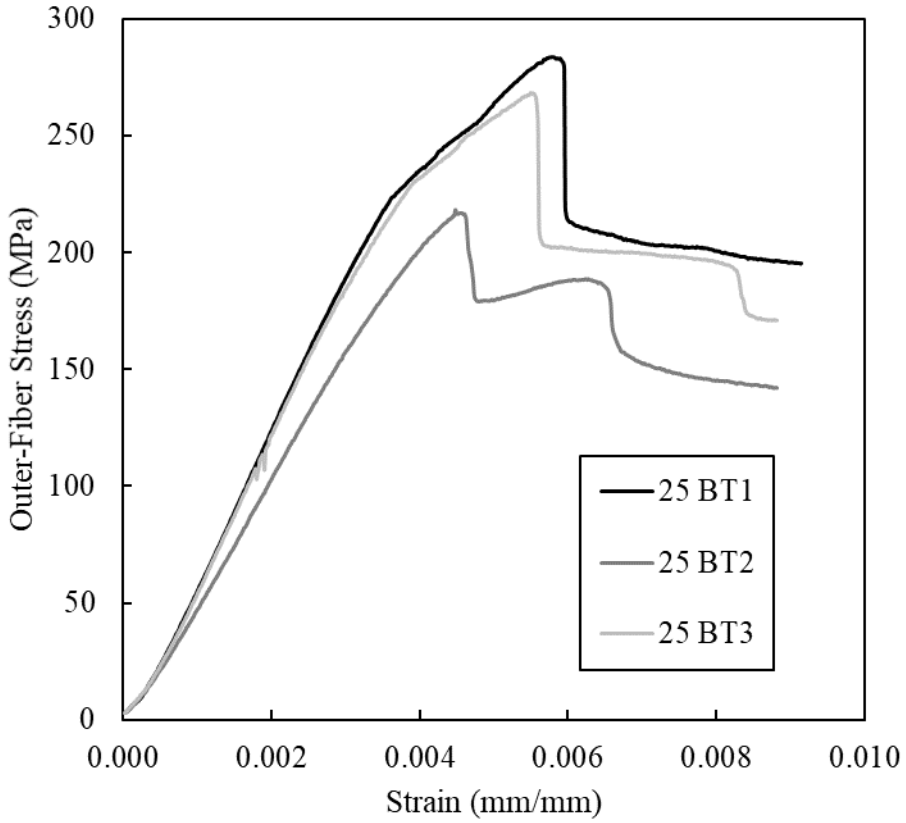

Figure 4.25 Low spray pressure bend samples outer-fiber stress versus strain.

The results for the other two spray pressure conditions are shown in Figure 4.26 with (a) representing the 241 kPa (35 psi) condition and (b) representing the 310 kPa (45 psi) spray condition. The first load drop occurred at the point when the coating cracks which was audible during the testing. All bend testing for the three spray pressure conditions was conducted on the same load frame discussed in Section 3.6.2 during the same testing session and set-up.

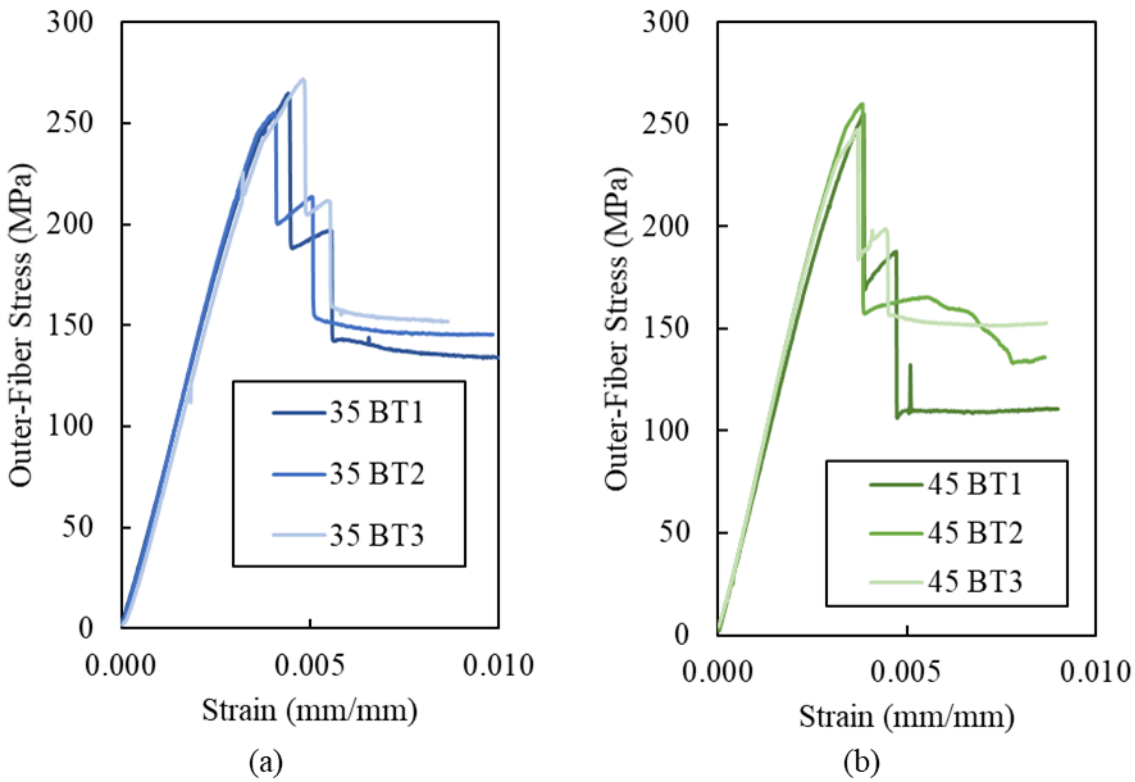

Figure 4.26 Outer-fiber stress versus strain for 241 kPa spray condition (a) and 310 kPa spray condition (b).

4.2.5 Wear Results – New Composition

Wear testing was conducted as discussed in Section 3.7.3.1. Results for each wear test are provided in Table 4.8. Wear rate was calculated by converting the mass loss to volume loss assuming $Fe_{0.32}Co_{0.08}Cr_{0.2}Ni_{0.32}Mo_{0.07}Ta_{0.01}$ has a density of 8.419 g/cm^3. The density (ρ) assumption was determined by the relationship $\rho = \sum c_i \rho_i$ using values provided in Table 3.3. Figure 4.27 shows the 241 kPa spray pressure condition wear sample posttest.

Table 4.8 Wear Results for New Composition.

Pressure Condition	Revolutions	Mass Loss (g)	Wear Rate (mm^3/Nm)
241 kPa	12,000	2.074	1.93×10^{-4}
310 kPa	12,000	2.029	1.89×10^{-4}

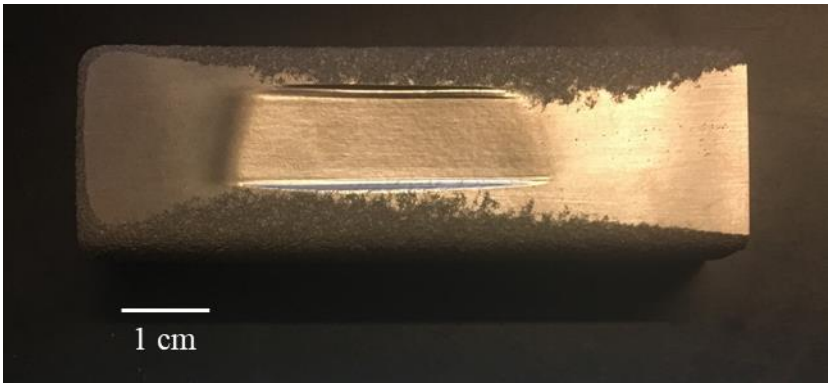

Figure 4.27 Post wear test sample of the 241 kPa spray pressure condition.

After wear testing, the 241 kPa spray pressure condition sample shown in Figure 4.27 was analyzed with SEM and EDS. Figure 4.28 shows the wear surface at increasing magnification from (a) to (c). The sliding direction of the rubber and sand wheel was from the top to the bottom of the image also noting the scratch direction in each image. Compositional maps were taken of the wear surface for Ni, Co, O, Cr, and Fe with results provided in Figure 4.29. The Mo composition map did not render and was excluded. Based on the compositional map results, spot scans were taken at various locations of interest with results provided in Figure 4.30.

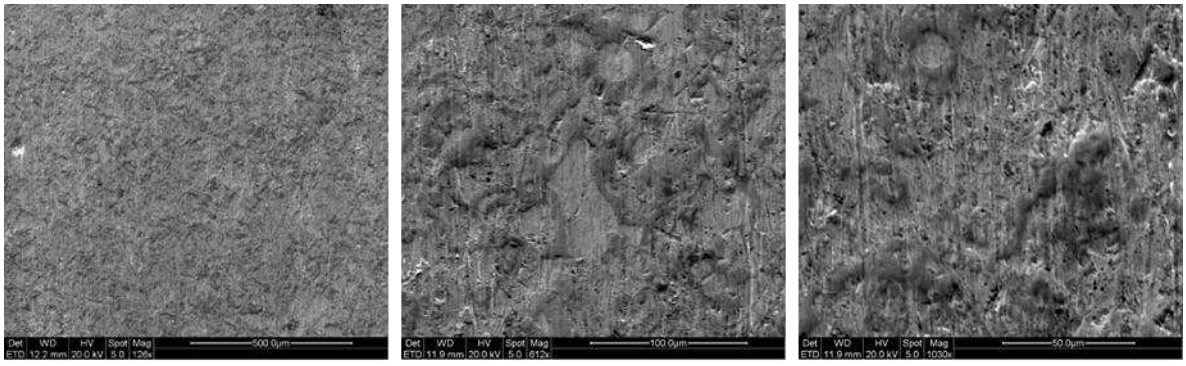

(a) (b) (c)

Figure 4.28 Wear surface of the 241 kPa spray pressure condition at different magnifications of (a) 126X, (b) 612X, and (c) 1030X.

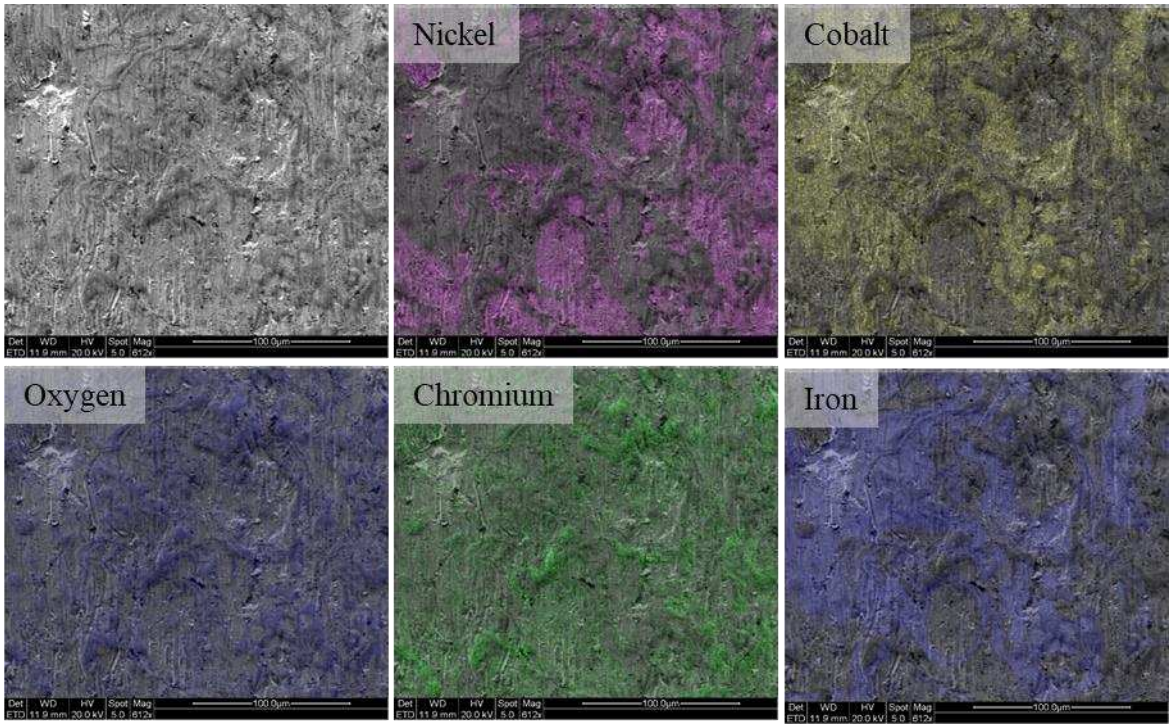

Figure 4.29 Compositional maps taken of the wear surface.

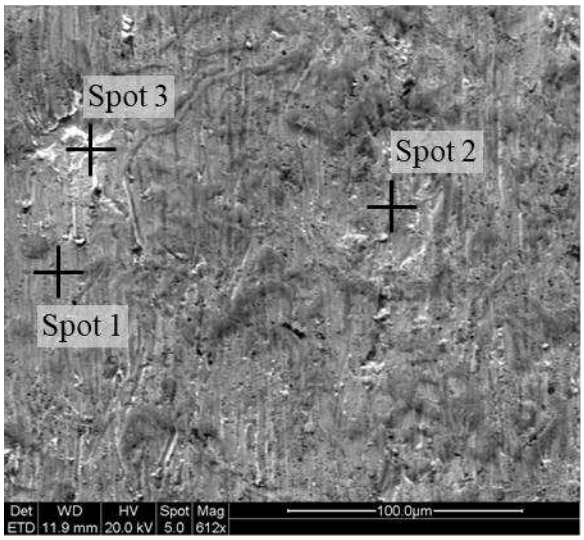

	Atomic Percent		
Element	Spot 1	Spot 2	Spot 3
Fe	44.86	15.68	21.42
Ni	0.86	19.32	5.61
Cr	9.18	17.28	6.73
Co	18.60	5.63	8.95
Mo	11.63	5.58	5.83
Ta	0.42	2.43	0.00
O	14.45	34.07	37.98

Figure 4.30 Location and result for spot scans taken of wear surface.

CHAPTER 5: DISCUSSION

This chapter will discuss the results presented in Chapter 4 starting with the experimentation conducted on the HH1 coating. The coating morphologies are discussed in connection with the in-flight and deposited droplet conditions to better understand the relationship among input voltage, droplet temperature, oxidation, and the final coating structures. The effect of the voltage parameter on mechanical properties was also investigated.

Results for the new composition are discussed in relationship to the HH1 coating and compared with the goal of achieving a tougher coating. The coating structure will be compared with the expected structure and wear rate. Coating microstructure and mechanical properties will be discussed in relationship to spray pressure.

5.1 Thermal Sprayed HH1 Coating

The objective of this study was to characterize the thermal spray coating as a function of input voltage and elucidate how the voltage affects the microstructure formation in the sprayed coatings. It has been reported for iron-based coatings (Fe-0.8 wt. %C), that increasing the input voltage from 27V to 40V resulted in the mean droplet temperature upon impact increasing by 150°C and mean droplet diameter decreasing by 56 μm [57, 58]. Adjusting the mean droplet size and temperature affects the coating structure and oxide content. The relationship between input-voltage and coating strength will be discussed and related to in-flight droplet characteristics and coating structure to better understand the connection between input voltages, coating structure, and coating mechanical properties.

5.1.1 Coating Porosity Analysis

Microstructural characterizations on the coatings under each voltage condition revealed a complex mixture of splats, oxides, pores, cracks, and regions of elemental segregation. As voltage increased, the measured area percentage porosity, gradually decreased as shown in Figure 5.1. However, by comparison with SEM images at the same location, it was found that most of the dark areas counted as pores in the OM analysis were actually oxides.

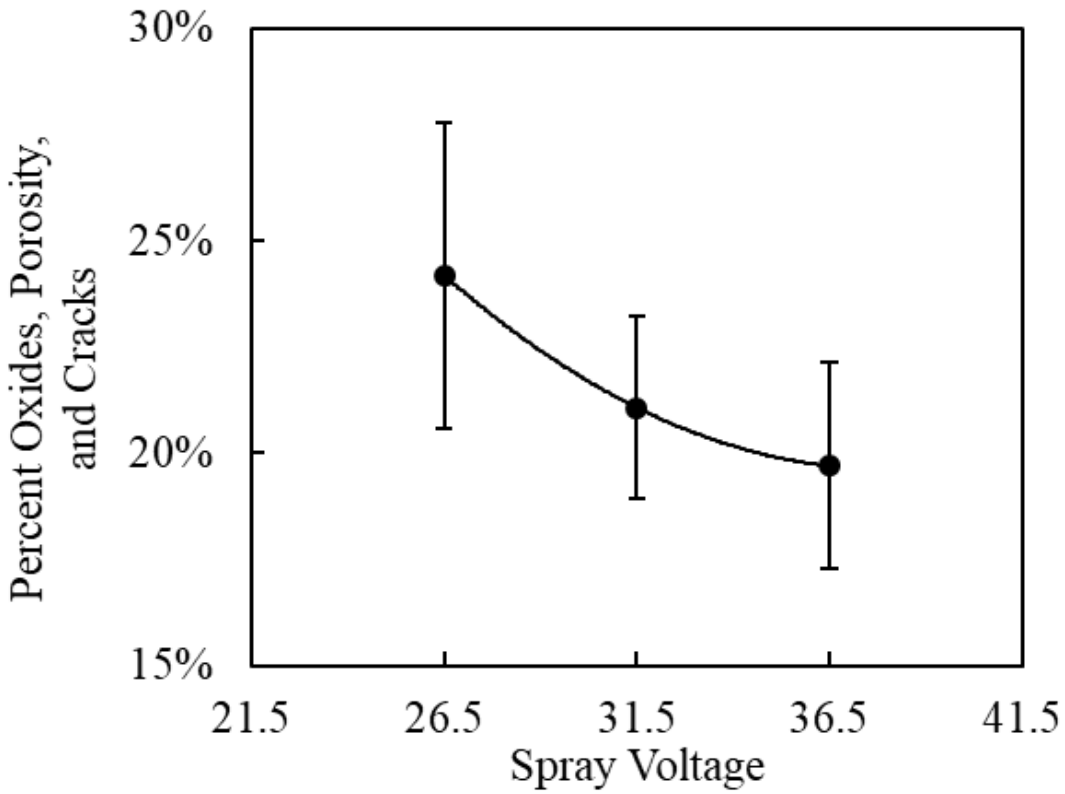

Figure 5.1 Graph showing the relationship between input parameter voltage and area percentage porosity.

Large oxides circled red in Figure 5.2 (a) show up as dark regions on the OM processed image but are revealed to be oxides by Figure 5.2 (b) SEM image taken from the same location. It is clearly shown that the majority of dark regions that were counted as porosity in the porosity analysis per the ASTM 2109 – 01 standard in Figure 5.2 (a) corresponds to the light colored oxide particles (~20 μm in size) in Figure 5.2 (b). Similar observations were reported for APS sprayed 316L austenitic stainless steel powders, where areas originally thought to be 'half-penny' shaped pores were oxides [30].

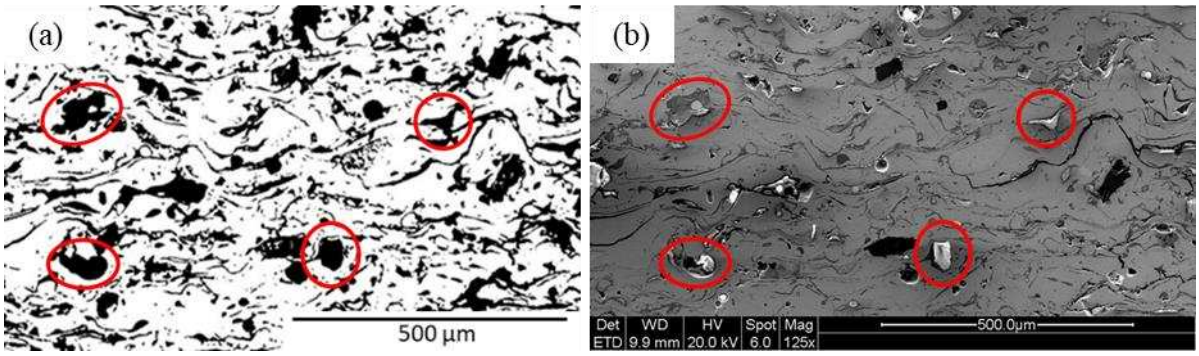

Figure 5.2 Processed image (a) and SEM (b) images taken from the same area of 26.5V voltage condition with red circles showing large oxides that show up as dark regions on the processed OM image.

In addition to the majority defect concentration of oxides, the coating contained a small volume of pores. The two main factors that influence porosity are droplet velocity and temperature. An increased droplet temperature decreases the viscosity and results in a reduced roughness and denser coating [105]. It has also been shown that for TWAS steel coatings with similar compositions to HH1, voltage reduces droplet size and increases droplet temperature on impact at this specific spray distance [57]. Thus, at higher voltages, the droplet would be hotter and smaller and are expected to produce a coating with less porosity as observed in Figure 5.1. A factor that would counteract the temperature is velocity. At the spray distance used, as voltage increases, droplet velocity decreases [57]. This results in less flattening and produces a less dense coating. The results of Figure 5.1 indicate that effects of voltage on droplet temperature and size are more significant than the effect of voltage on droplet velocity on coating porosity.

The distribution of the defects through the coating was evaluated by X-ray CT using the ZEISS 620 Versa 3D X-ray microscope as discussed in Section 3.4. A 3D rendered image for the 31.5 input-voltage condition is shown in Figure 5.3 compiled from the X-ray CT data. Based on the sample size, oxides smaller than 5 µm could not be resolved. The red regions represent oxides, pores, and crack content through the coating thickness. The defects, which are primarily oxides as shown in Figure 5.2, are distributed relatively evenly throughout the coating and constitute a large volume fraction consistent with the 22% measured from OM images of the same voltage condition as shown in Figure 5.1.

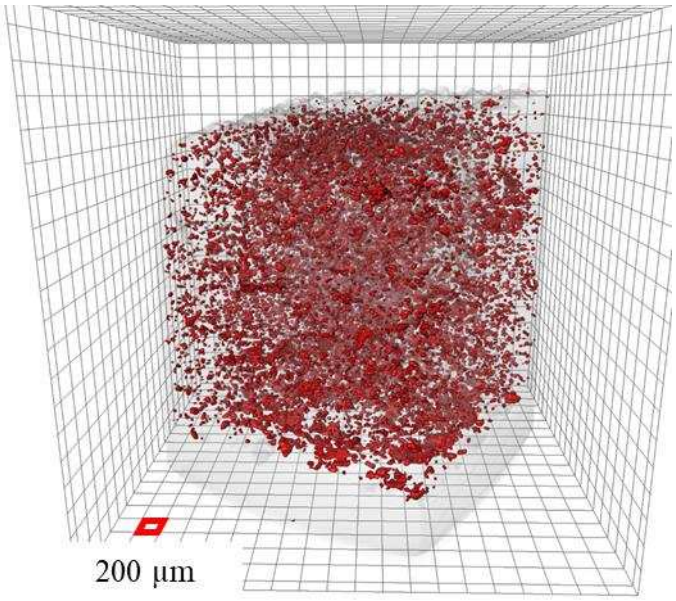

Figure 5.3 X-ray CT data of the HH-1 31.5 voltage condition rendered in 3D giving the distribution of oxides, pores, and cracks through the coating thickness.

5.1.2 Voltage Effects on Oxidation Behavior

Based on the results discussed in Section 5.1.1, the total number of oxides decreased as the voltage increased. TWAS oxidation can occur during in-flight and/or after droplet impact as the splat cools [30, 47]. It has been reported in a Fe-0.8 wt. %C system [57], which is similar to the composition studied here, that molten droplets impact the substrate at temperatures above 2200°C with the voltages increasing from 27V to 38V, the impact temperature increased by as much as 100°C [57]. Figure 5.4 (c) and (d) show a schematic of droplets impacting the substrate at these different temperatures. The melting temperature (T_m) of oxides such as silicon dioxide (SiO_2) and aluminum oxide (Al_2O_3) are 1710°C [106] and 2054°C [107] respectively. Thus, at these high droplet impact temperatures, oxide formation will occur primarily after droplet impact.

After droplet impacts and during splat cooling, splats exposed to oxygen of the compressed air form oxides on the surface. Depending on the time exposed to the jet before being covered by the next layer of splats will determine the amount of oxidation [47]. As voltage increases, the mean droplet diameter decreases with deposition rate remaining relatively unchanged as it relates to the amperage parameter [57]. For higher voltages, the smaller droplets will cover the splat layer faster and reduce the level of oxidation

after impact as observed in Figure 5.1. This is shown in Figure 5.4 (a) and (b) optical images of the 26.5V and 36.5V condition where the oxide layers between the splats are more defined in the lower voltage condition. An exaggerated illustration of this process is shown in Figure 5.4 (c) showing the low voltage condition and (d) showing the high voltage condition.

5.1.3 Coating Structure

Hardness values provided in Section 4.1.2 were taken within splats ranged between 523 and 934 HV indicating that the splats are composed of a fine martensitic structure. This is expected due to the rapid cooling of the molten droplet upon impact as well as observations in the literature of similar compositions TWAS studies [49, 51, 108]. Due to the complex mixture of oxides, element segregation and splat morphology, indenting the specimens within a droplet was difficult. Vickers hardness values that are below 500 HV were the result of the splat cracking as a result of indent placement to close to a splat-splat boundary.

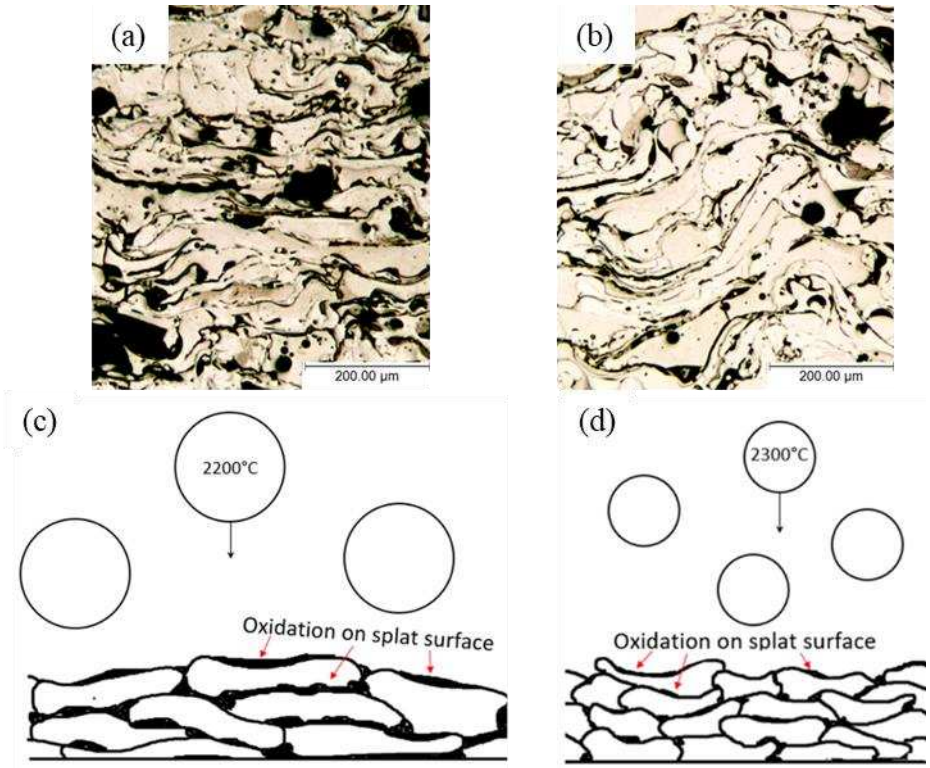

Figure 5.4 Optical image of the 26.5V (a) and 36.5V condition (b) comparing the oxidation on the splat surface. Schematic drawings (not-to-scale) showing droplet size and splat surface oxidation for the 26.5V (c) and 36.5V condition (d).

No clear effect of voltage on hardness was observed due to the wide range of values. This large variation in values, however, could have more to do with indent placement in relation to defects than an artifact of location within the coating thickness. It is also worth noting that the coating surface temperature was maintained below 93°C (200°F) and that droplets through the thickness of the coating would not have been exposed to temperatures high enough to temper the martensite after splat quench.

In addition to the oxides and martensitic splat structure, there were various regions of element segregation primarily of nickel and vanadium. Figure 5.5 shows an SEM image taken of a 36.5V sample with EDS maps of Ni and V overlaid showing the concentrated regions. Spot scan 1 in the Ni concentrated region estimates a composition of Fe-23 at.% Ni suggesting a face center cubic (FCC) phase [109]. Spot scan 2 in the V concentrated region estimates a composition of Fe-16 at.% V suggesting a (V, Fe) BCC phase [110]. The regions with higher elemental consecrations of elements such as Ni and V could be potentially caused by compositional variations inherent in the powder core wire. When the droplet impacts the substrate it spreads out and solidifies with an extremely high quench rate leaving little to no time for diffusion [12].

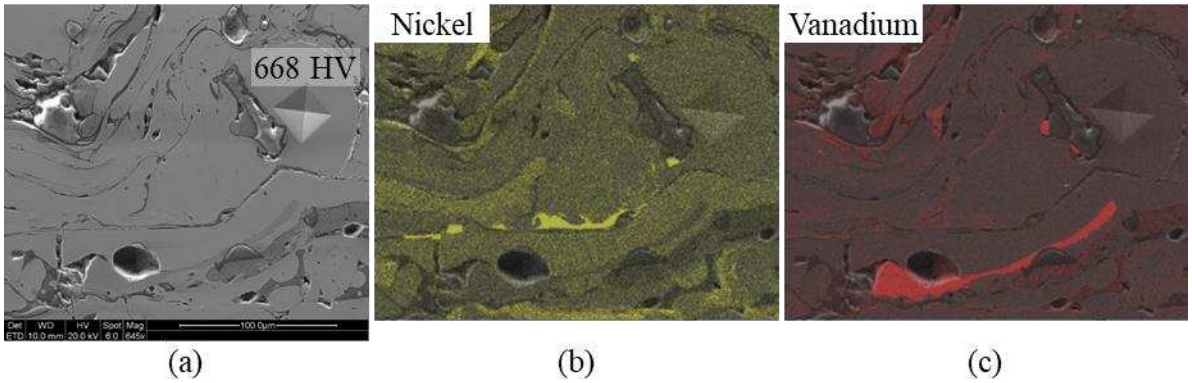

Figure 5.5 SEM image (a) and EDS maps of Ni (b) and V (c) of the 36.5V condition taken at the same location.

5.1.4 Oxide Morphologies

Oxide morphologies were determined by taking EDS maps of the various oxides observed. **Error! Reference source not found.** shows one EDS map taken of the 36.5V condition showing various oxides

formed with Al, Si, and Ti. Aluminum oxide (Al_2O_3) and silicon dioxide (SiO_2) were found to constitute most of the present oxides with titanium oxide present to a lesser extent. Al_2O_3 was found as long thin layers between splats. This is expected as Al_2O_3 forms as a stable high-temperature scale in iron systems [111, 112] and would form on the splat surface first after impact. Splats only exposed to the oxygen within the jet for a very short period of time (microseconds) will not oxidize much, as compared with portions of sprayed layers which can sometimes be exposed for up to a second allowing for an oxide scale to form [47]. This is shown in contrast between Figure 5.4 (a) and (b) where a thicker Al_2O_3 oxide layer is observed on the lower voltage condition because it has more time to form before the next droplet impacts and slows/stops the growth of the layer.

SiO_2 was observed to have large near-spherical oxide morphologies approximately 50 µm in diameter. The SiO_2, which has a lower melting point than Al_2O_3, forms after the Al_2O_3 with the remaining diffused oxygen [106, 107]. Given the silicon dioxide reaction:

$$Si + O_2 = SiO_2 \tag{5.1}$$

At the SiO_2 T_m of 1710°C the partial pressure of oxygen is on the order of 10-14 atm, well below the pressure of the system, resulting in the oxide not forming [113]. Silicon dioxide has many crystallographic forms. With the rapid cooling of the molten droplets, it is expected that silica glass, which forms on quenching from 1710°C, and cristobalite, the high temperature SiO_2 phase, would form [106]. This is observed in **Error! Reference source not found.** where EDS map show large near-spherical SiO_2 oxide morphologies unlike the thin layer morphologies of the Al_2O_3.

5.1.5 Effect of Voltage on Residual Stress

The coating-substrate interface consists of the A36 steel substrate and sprayed coating anchored onto the rough sand-blasted surface forming a mechanical bond [39]. Nano-indentation grids were taken across the interface to evaluate if the different voltage conditions had an influence on the hardness distribution into the substrate as previously discussed in Section 3.5.2. The plot in Figure 5.7 shows a comparison between each voltage condition for the average indentation value at various distances into the substrate

starting at the interface. It was observed that indentation values for every voltage condition decreased with distance from interface. This is expected, not due to the thermal spray coating, but due to the cold working of the surface from sandblasting. Thus, the indentation value was examined in order to see if differences in trends were observed between the three voltages.

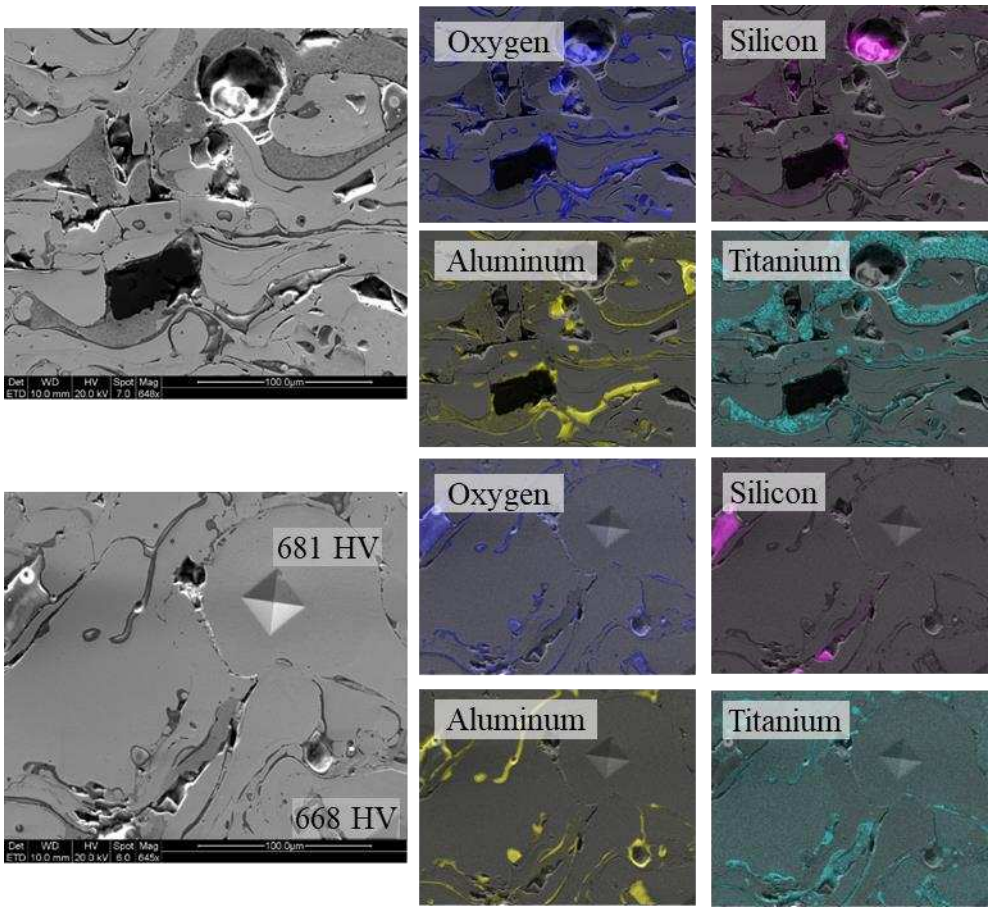

Figure 5.6 EDS Mapping of the 36.5V condition for O, Si, Al, and Ti.

No clear differences were observed between each voltage condition for hardness distribution. Due to the relationship existing between hardness and residual stress, this suggests that the applied residual stress from the coating was similar for each voltage condition due to the relationship between hardness and residual stress [94]. TWAS, unlike other spray processes, has minimal substrate heating and with the coating surface maintained under 93°C (200°F), there was not a distinct impact to the substrate mechanical properties from thermal spraying [9].

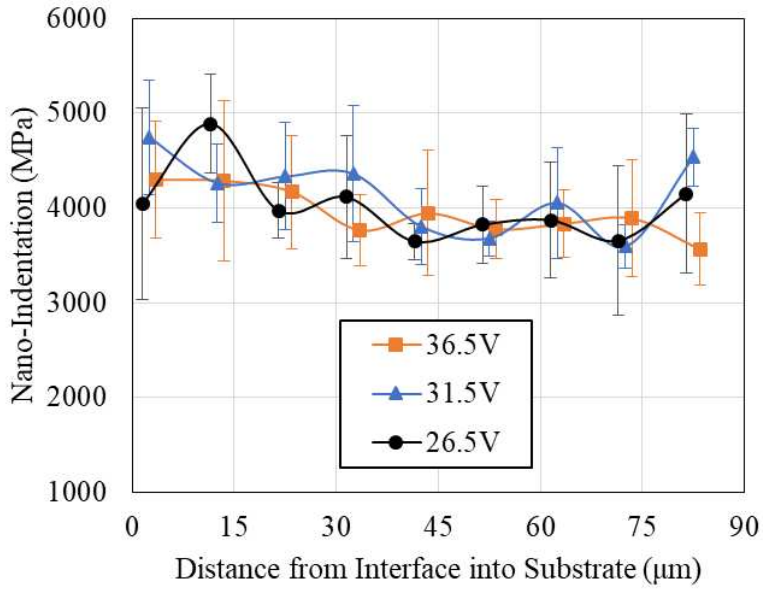

Figure 5.7 Average indentation values at various distances into the substrate starting at the interface.

5.1.6 Coating Strength

Four-point bend testing with DIC was performed on each sample of the three input-voltage condition with load versus time data provided in Figure 5.8. During each bend test there were several sharp load drops observed on each sample. Utilizing the DIC data, these load drops were correlated with each samples DIC strain data. Figure 4.17 shows the load vs time data for the second bend test of the 26.5 voltage condition with DIC strain maps of the sample one second before and after each load drop. Through this comparison we see that at 28 seconds the sample began to show higher strains at the right-hand side of the sample just below the right loading nose. Thus, the first load drop was caused by the coating cracking at this location which is evident from the posttest image which clearly shows the crack. The first crack continues to grow until 48 seconds at which point another load drop occurs. The second load drop show in Figure 4.17 compared with the DIC strain maps at 47 and 48 seconds shows that another crack develops in the coating at the left-hand side under the left loading nose. Both cracks propagate from the coating surface towards the substrate at which point the coating begins to pull away from the substrate as more loading is applied.

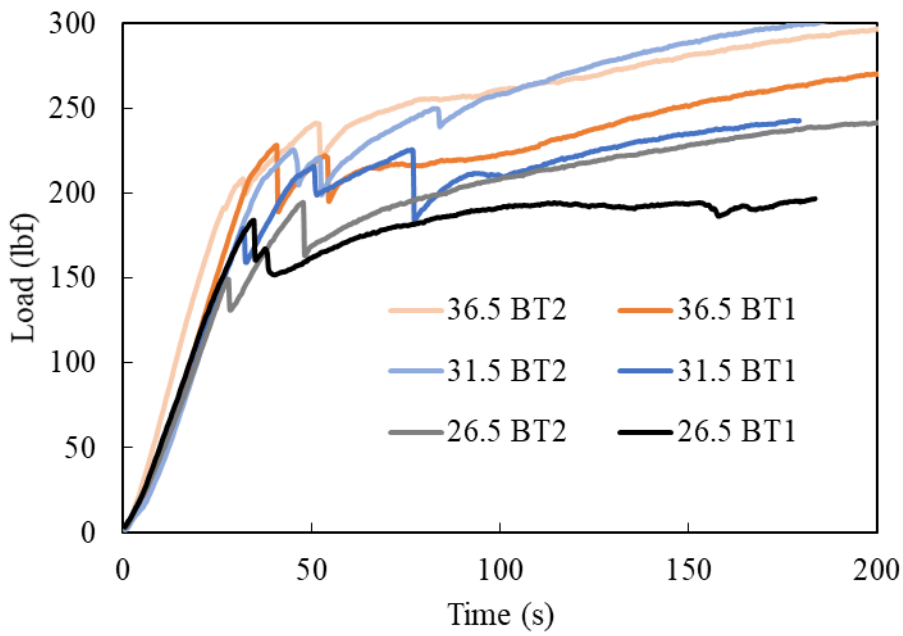

Figure 5.8 Load versus time for each bend sample. Each input voltage condition had two bend samples tested.

Looking at the averaged outer fiber stress versus strain for the three input-voltage conditions, it is observed that as voltage is increased the stress required to initiate a crack in the coating increases. This is shown in Figure 5.9 where the lowest outer fiber stress to crack the coating for the 26.5, 31.5, and 36.5 input-voltage condition was 88, 109, and 125 MPa respectively. The maximum outer-fiber stress can be calculated between the two central loading points that define the load span using the following equation:

$$S = \frac{3PL}{4bd^2} \tag{5.2}$$

where S is the outer-fiber stress throughout the load span in MPa, P is the load in Newtons, L is the length of the support span in millimeters, b is the average beam width in millimeters, and d is the average thickness in millimeters.

The increase in strength can be attributed to the higher voltage samples having a lower oxide content as discussed in Section 5.1.1 and finer solidified structure due to the smaller impinging droplet size [58]. It was shown in Figure 5.1 for sprayed HH-1 that the average oxide, porosity, and crack content decreases by

4% when increasing the input voltage from 26.5 to 36.5 V. For a similar sprayed material Fe – 0.8 wt. % C, it was observed that as voltage was increased from 28 to 40 V the mean droplet diameter decreased from 668 to 612 μm [58]. After the droplets impact the substrate surface, they are cooled to under 100°C within a few milliseconds [49, 51]. It has been reported that for a Fe-0.8 wt. %C system, which is similar to the composition studied here, molten droplets impact the substrate at temperatures of 2200°C and 2300°C for input voltages of 27V to 38V respectively [57]. Figure 5.10 shows the isothermal-transformation (I-T) diagram for type 1080 steel with a composition of Fe – 0.79 wt. % C – 0.76 wt. % Mn, grain size of 6 austenitized at 899°C [114]. This I-T diagram is used as a reference noting that a more accurate I-T diagram would need to account for factors that could affect the martensite start temperature (M_s) such as grain size [115] and quench rates [116].

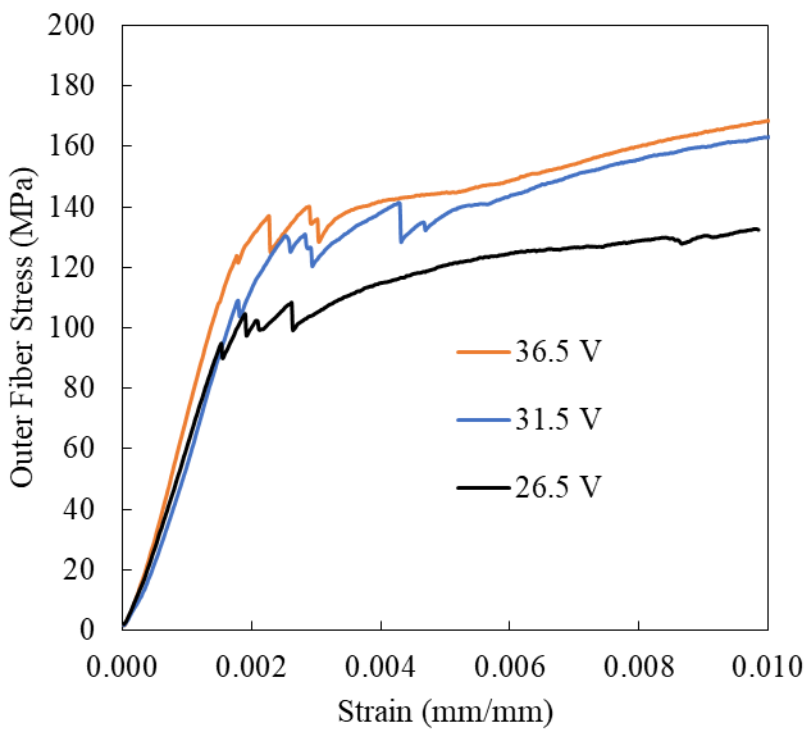

Figure 5.9 Average indentation values at various distances into the substrate starting at the interface.

As shown in Figure 5.10, the splat cools rapidly from the liquid state to below the M_s temperature within a few milliseconds. At some undercooling below the liquidus, by the peritectic reaction, austenite forms.

The droplet continues to rapidly cool below the on-cooling austenite transformation temperature (A_{r_1}) and avoids forming pearlite. The transformation kinetics are to slow to form ferrite (α) and cementite (Fe_3C) before the droplet is cooled to the maintained surface temperature of 93°C. The droplets instead cool below the M_s temperature and form a fine martensitic structure. Hardness values reported in Section 4.1.2 were taken within the deposited splats of the HH-1 coating and ranged between 523 and 934 HV which are similar to martensite values of steels containing similar carbon levels [117].

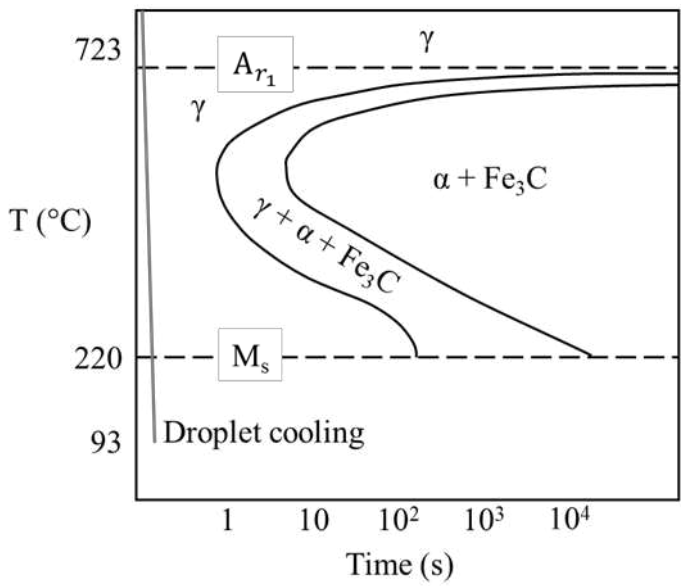

Figure 5.10 Schematic of the I-T diagram for type 1080 steel approximated for the twin-wire arc sprayed HH-1 [114].

5.1.7 Fracture Surface Analysis

Fracture surfaces of bend test samples were analyzed by SEM imaging. Figure 4.19 shows an image taken at 47x showing the full thickness of the coating. As was observed from the DIC data, the crack initiated at the coating surface and propagated towards the substrate. The crack propagation was chiefly affected by the fracture of splats from one layer to another utilizing weak points such as oxides, pre-cracks and pores within the lamella sprayed structure [118]. Near the substrate-coating interface the crack changed from propagating perpendicular to the bending stress to cracking horizontally. The coating is harder and more brittle than the A36 steel substrate and, once the crack propagates close enough to the substrate, the

coating holds it ridged shape and starts to pull away from the substrate. As shown in Figure 5.11, the coating does not pull directly away from the sand-blasted substrate but instead delaminates a first few splat layers up from the substrate along weak splat boundaries [119].

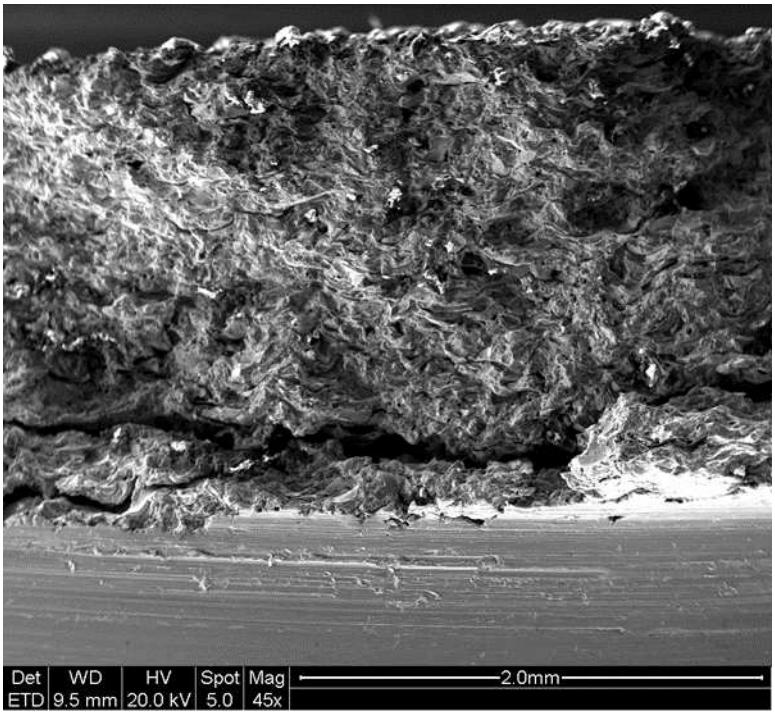

Figure 5.11 Fracture surface after bend test showing delamination from substrate.

Cracks initiated at oxides dispersed throughout the coating. Previously shown in Figure 4.20, an image was taken of the bend sample fracture surface where a splat failed by brittle cleavage fracture. The splat was subjected to tensile forces perpendicular to the image during testing. Further magnification of the cleaved splat surface revealed faceted ledges or river lines leading back to the initiation point [120]. A spot scan was taken at the initiation point where the river lines lead with results also shown in Figure 4.20. The spot was found to contain high amounts of aluminum and oxygen in close atomic ratio agreement to (Al_2O_3). The presence of aluminum oxides is expected as Al_2O_3 and SiO_2 are the most common oxides present in the HH1 coating.

Further spot scans taken along the fracture surface revealed that large amounts of oxides are present. Figure 5.12 shows several spot scans taken at various locations along the fractured surface near the substrate

where the crack began to propagate parallel to the bending stress. Spots a-d all contained high amounts of oxygen ranging from 40 to 49 at. % O and aluminum ranging from 12 to 16 at. % Al. This ratio suggests that the Al_2O_3 was present at the fracture which is expected as Al_2O_3 forms on the splat surface after molten steel droplets impact and cool. Thus, when the crack switched from propagating perpendicular to parallel to the bending stress, fracture occurred by the delamination along the splat surface. Similar findings were observed in the WC-FeCSiMn sprayed coating where many cracks were perpendicular to the bend stress between splat layers indicating that stress relaxation occurred by the delamination of weak splat boundaries [118].

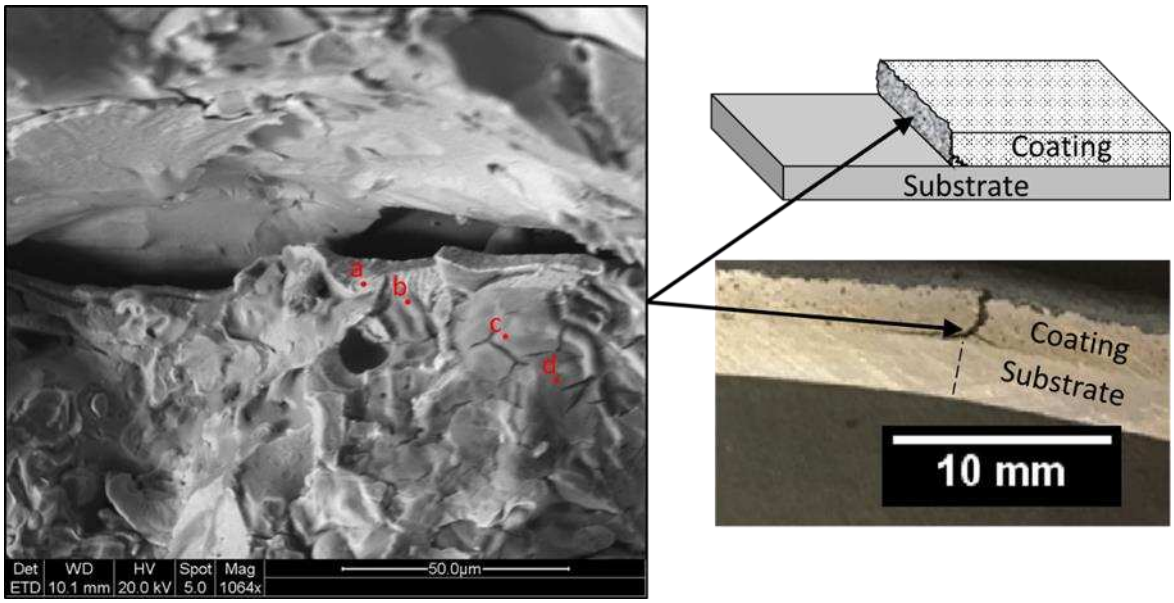

Figure 5.12 Spots scans taken along fracture surface with schematic showing where image was taken and photo of posttest bend sample showing where the crack changes from perpendicular to parallel to bend stress.

In addition to cracking initiated at Al_2O_3 oxides, it was also found that fracture occurred at other oxides including SiO_2 and TiO_2. Figure 5.13 (a) shows a splat that failed under tensile stress through the splat failing with brittle fracture. As shown in Figure 5.13 (a), at the location of the spot scan, there are radial marks directed at this location indicating the point where the crack initiated. Spot scans of this area revealed that this area was comprised primarily of silicon and oxygen indicating that the fracture started at a SiO_2 particle located within the splat. The SiO_2, which has a lower melting point than Al_2O_3, forms after the

Al_2O_3 forms as a thin layer on the spat surface after droplet impact [107]. The silicon reacts with the oxygen and forms near spherical SiO_2 oxide particles within the solidifying splat. These particles facilitate the brittle fracture through the splat cross-section. Titanium had a similar effect as silicon formed oxides within the spray. Figure 5.13 (b) shows a fractured surface where near the top of the image the failure was along splat boundaries before fracturing through several splat layers. The splat layers are easily visible with sharp angles between the splat surface and fracture surface. Radial marks on the splats fracture surface appear almost vertical pointing to the coating surface where max stress from bending occurs. A spot scan was taken at the top of a bowl-shaped fracture feature revealing that the particle at the top of the feature contained high amounts of titanium, aluminum and oxygen. To the left of the particle shows brittle fracture of the splat whereas the bowl-shaped feature appears to be the result of a bordering splat being pulled away (out of the page) leaving this crater surface. The presence of aluminum and oxygen within the bowl also suggest this was the case as Al_2O_3 was found primarily between splat layers.

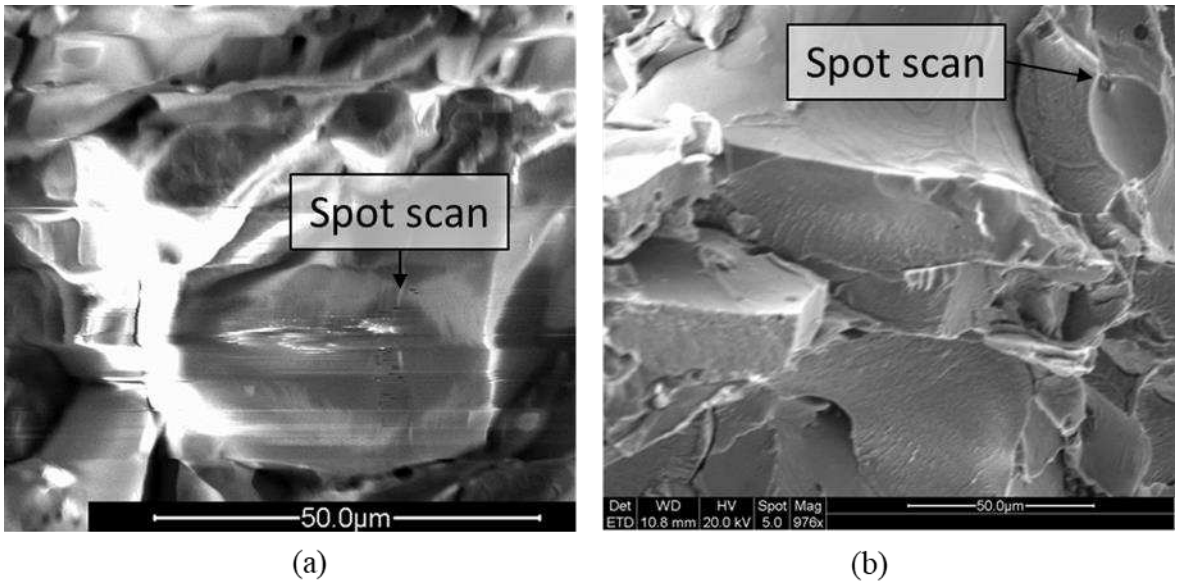

Figure 5.13 Fracture surface of post bend test samples showing location of spot scans at crack initiation points.

5.1.8 Wear Testing – HH1

Wear testing was conducted as previously discussed in Section 3.6.5. As reported in Table 4.5, the average wear rate decreased from 1.17×10^{-4} to 1.11×10^{-4} mm^3/Nm when input voltage increased from 31.5V to 36.5V. However, this difference is small and, without further repeated testing, no relationship can be confidently stated. It is expected, however, that the wear rate would increase with increased voltage due to the reduced oxide content observed in Figure 5.1. Oxides for HH1 were found to be primarily Al_2O_3, SiO_2, and TiO_2. Alumina (Al_2O_3) was observed to be the primary oxide formed between splat layers. Al_2O_3 has wear rates on the order of 10^{-12} mm^3/Nm which was reported for 450µm thick APS prepared Al_2O_3 coatings [121]. The decrease in oxides content from 31.5V to 36.5V was 1%, thus a significant difference in wear behavior between these two voltage conditions cannot be expected. This is not the case for the low voltage condition of 26.5V which saw a 5% decrease in oxide content which could have a more pronounced wear rate difference.

5.2 Thermal Sprayed New Coating Composition

As discussed in Section 5.1, adjusting the voltage influenced the oxide content and coating strength. However, in order to achieve a more significant increase in toughness, a new composition was developed based on findings by Li which found that a MPEA sprayed by APS formed an FCC solid solution with spinel oxides generating a coating with similar wear rates to HH1 [84]. The new composition ($Fe_{0.32}Co_{0.08}Cr_{0.2}Ni_{0.32}Mo_{0.07}Ta_{0.01}$) was determined based on material availability and Termo-Calc analysis previously discussed in Section 3.7.1.2. To generate this composition, two wires were arced together in the TWAS gun-head schematically shown in Figure 3.16. Spraying was conducted at three spray pressures in order to analyze the effect of droplet size on coating oxidation content, strength, and wire-mixing. It was hypothesized that increases in spray pressure would increase the oxide content which in turn would improve wear rate. This was observed for the $FeCoCrNiMo_{0.2}$ alloy where coatings produced by APS contained 47% oxide content and exhibited an order of magnitude improved wear resistance compared with an HVOF coating of the same alloy which contained only 12.7% oxide content [84]. However, based on the HH1 results, increased oxide content resulted in a decrease in coating strength and toughness. Thus, the tradeoff

between wear rate and coating toughness must be considered. This section will discuss the compositional, wear, and mechanical results of the $Fe_{0.32}Co_{0.08}Cr_{0.2}Ni_{0.32}Mo_{0.07}Ta_{0.01}$ coating.

5.2.1 Coating Features

Utilizing SEM imaging and EDS mapping per Section 3.3, two different splat compositions were observed in Figure 4.23 and Figure 4.24 which will be referred to as *Splat 1* and *Splat 2*. *Splat 1* was characterized by high concentrations of Ni and Cr as shown in Figure 5.14 (a). *Splat 2*, on the other hand, was characterized by high concentrations of Fe, Co, and Mo as shown in Figure 5.14 (a).

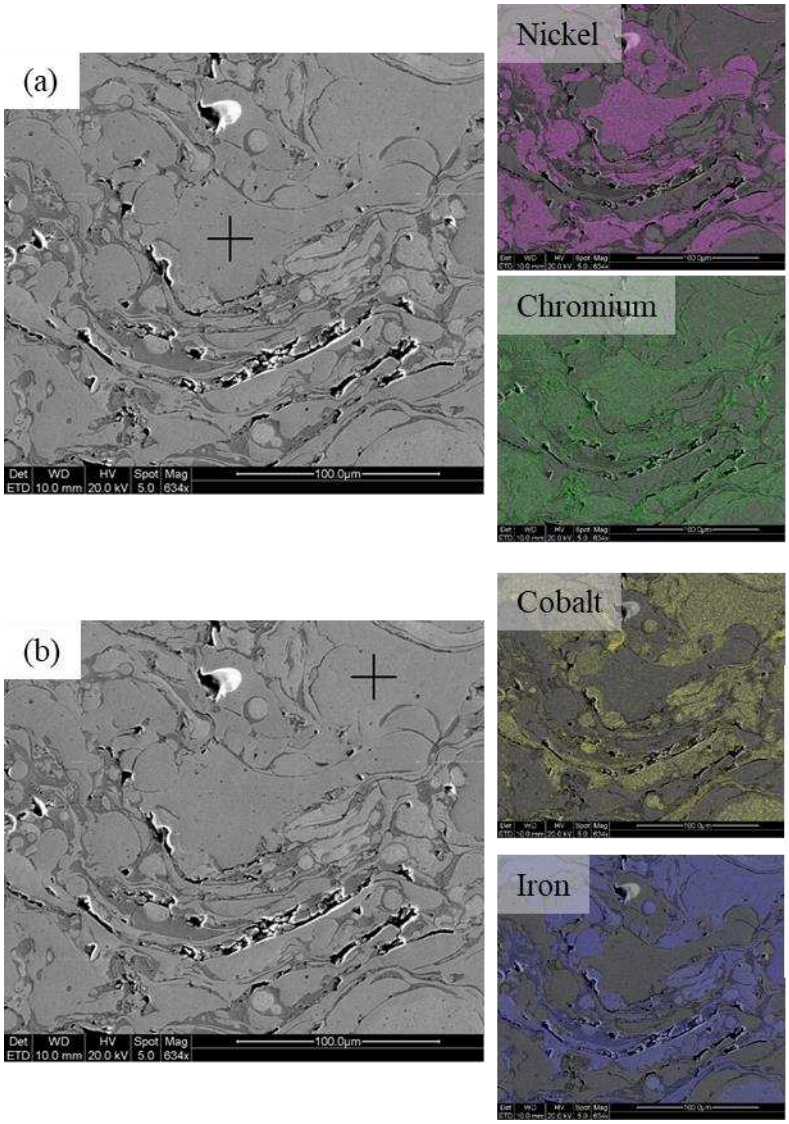

Element	Wt %	At %
O K	3.80	12.95
MoL	11.39	6.48
CrK	18.77	19.70
FeK	1.93	1.89
CoK	0.83	0.77
NiK	62.33	57.93
TaL	0.95	0.29
Total	100.00	100.00

Element	Wt %	At %
O K	3.83	13.38
MoL	21.53	12.55
CrK	8.28	8.90
FeK	44.00	44.05
CoK	18.39	17.44
NiK	3.81	3.63
TaL	0.15	0.05
Total	100.00	100.00

Figure 5.14 *Splat 1* (a) and *Splat 2* composition (b) with elemental maps and spot scans showing the distribution and composition of splat types for the 241 kPa spray pressure condition.

The spot scan within *Splat 1* revealed that the wt. % of Ni, Cr, Mo, and Fe was almost identical to that of the Inconel 625 solid wire with *Splat 2* having a composition closely matching that of the cored wire composition provided in Figure 3.16. This suggests that there was little to no mixing of the anode and cathode wires within the arc or of droplets colliding and mixing in-flight or upon impact. This was also observed for the lower and higher pressure conditions.

The lack of mixing within the arc can be attributed to the difference in arc attachment to the cathode and anode as previously discussed in Section 2.3.2. Due to the heating difference of the anode and cathode wires, the asymmetric arc behavior for TWAS in an inherent feature of the melting process [21]. For the anode, a sheet is created from molten metal that builds up at the wire tip as a result of a large portion of the wire being heated by the diffuse arc attachment. This anode sheet continues to stretch and spread itself downstream [122]. The cathode, however, has constricted arc attachment with more localized heating forming more obtuse sheets [123]. This is visualized in Figure 5.15 showing an image taken from high speed video of the formation of two distinct liquid metal sheets for the anode and cathode.

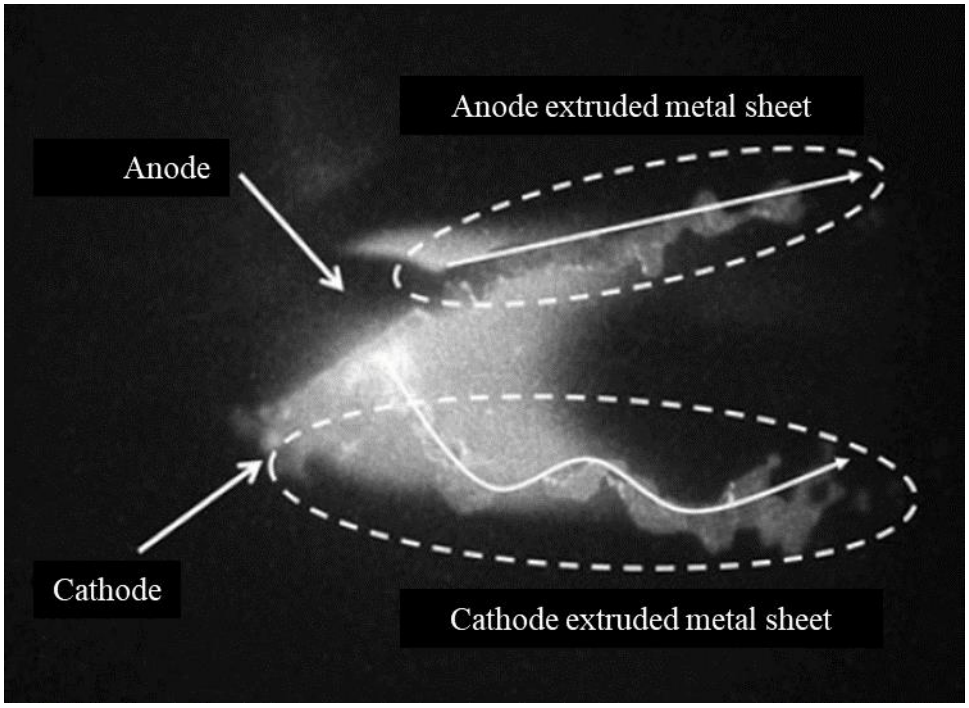

Figure 5.15 High speed image taken from the anode side of the metal breakup during TWAS [124].

Similar findings were observed for TWAS of 1.6 mm cored wires (AS850) and solid wires (Sprasteel) with composition in weigh percent of 4% Cr, <1% Mn, 1.4% Si, 2% C, 50% fused tungsten carbide WC-W_2C, and Fe balance and Fe-0.07% C, 0.96% Si, and 1.63 Mn, respectively [124]. It was found that melting behavior was different between cored wires and solid wires and that powder composition of the core wires played a significant role in metal disintegration. Solid wires exhibited longer metal sheets compared with cored wires due to the cross-sectional area differences between solid wire (2 mm^2) versus a metal sheath (0.38 mm^2) and propensity of powder, in the cored wire case, to be accelerated into the metal sheets causing early breakup.

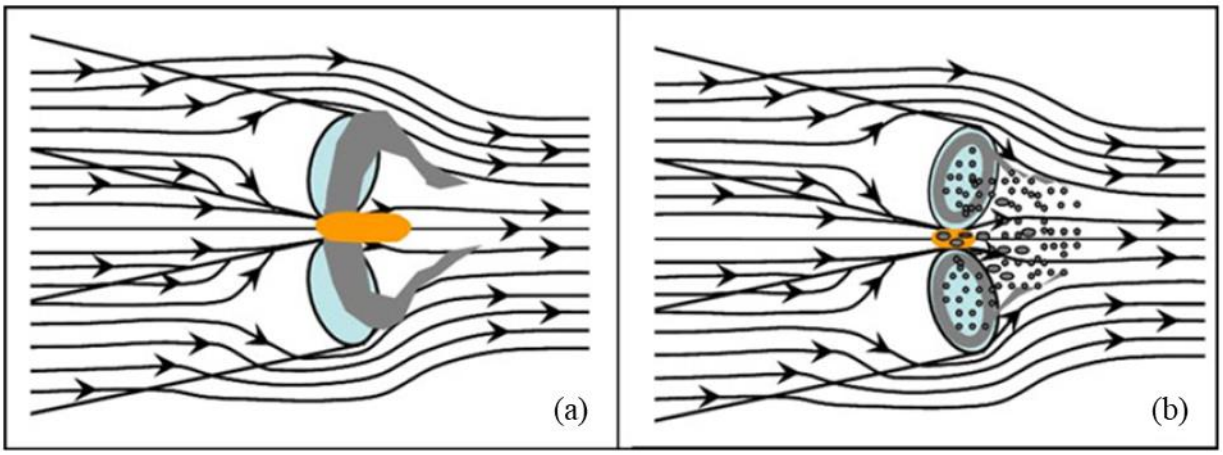

Figure 5.16 Jet flow melting behavior, and disintegration of solid wires (a) and cored wires (b) [124].

The new composition, however, was a combination of a cored wire and solid wire arced together as shown in Figure 3.16. It can be assumed that a combination of melting behavior would be achieved. Melting behavior and disintegration would consist of the behaviors shown in Figure 5.16 (a) and (b). By having the cored wire as the anode and solid IN625 wire as the cathode, no long metal sheets would form on the anode due to the cored wire sheath and powder breakup. Metal sheets could presumably form on the cathode side but only to a limited degree as the cathode has constricted arc attachment. The spot scan provided in Figure 5.14 (a) of *Splat 1* contained less than 1 wt. % Co suggesting that the powders within the powder core anode wire were not accelerated across the arc into the cathode sheet. This is contrary to the cross-over effect observed for the AS850 cored wires where the powder particles are accelerated by the atomizing gas and

penetrate against the extruded metal sheets as shown in Figure 5.17. This could be due to the short constricted arc attachment on the IN625 solid wire cathode not forming sheets long enough for the molten powders to interact based on the direction of the atomizing gas flow. The result was a coating composed of evenly distributed splats of two different materials forming an alloy composite shown in Figure 5.14.

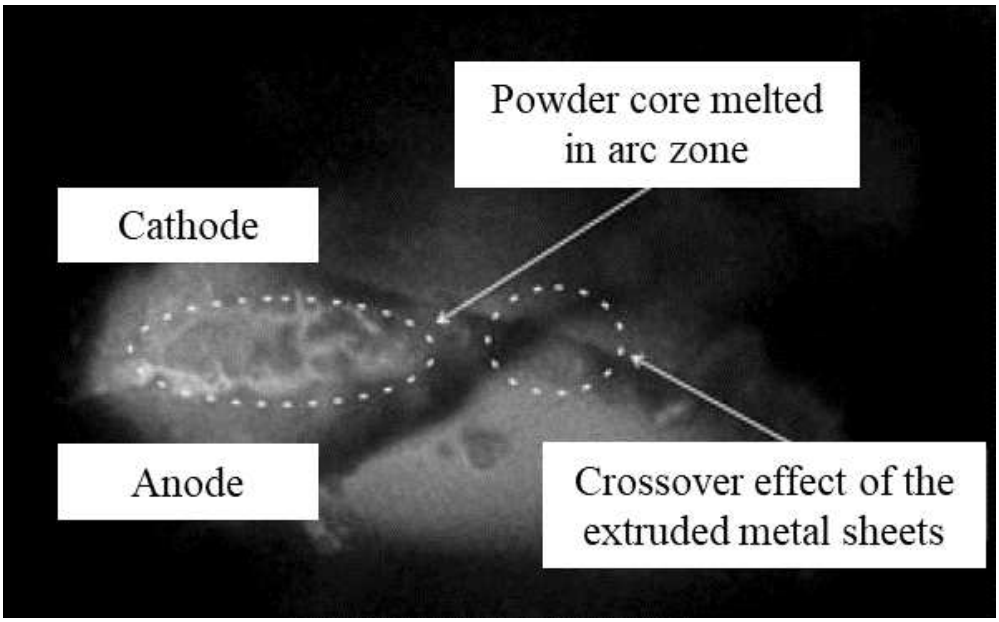

Figure 5.17 High speed image of TWAS of cored wires [124].

5.2.2 Coating Oxide Analysis

In addition to the two splat compositions, a significant amount of oxidation occurred. As previously discussed in Section 5.1.1, what was counted as porosity per ASTM 2109 measurements were actually mostly oxides. Spray pressure was found to have a significant effect on coating oxidation with average oxide content increasing from 21% to 64% when spray pressure was increased from 172 kPa to 310 kPa. Figure 5.18 shows the results of area percent oxide, pores, and cracks provided in Table 4.6 plotted versus spray pressure. The relationship was found to be non-linear where oxidation increased by 12% when increasing spray pressure from 172 to 241 kPa where the increase in oxidation from 241 to 310 kPa was almost three times this value at 31%.

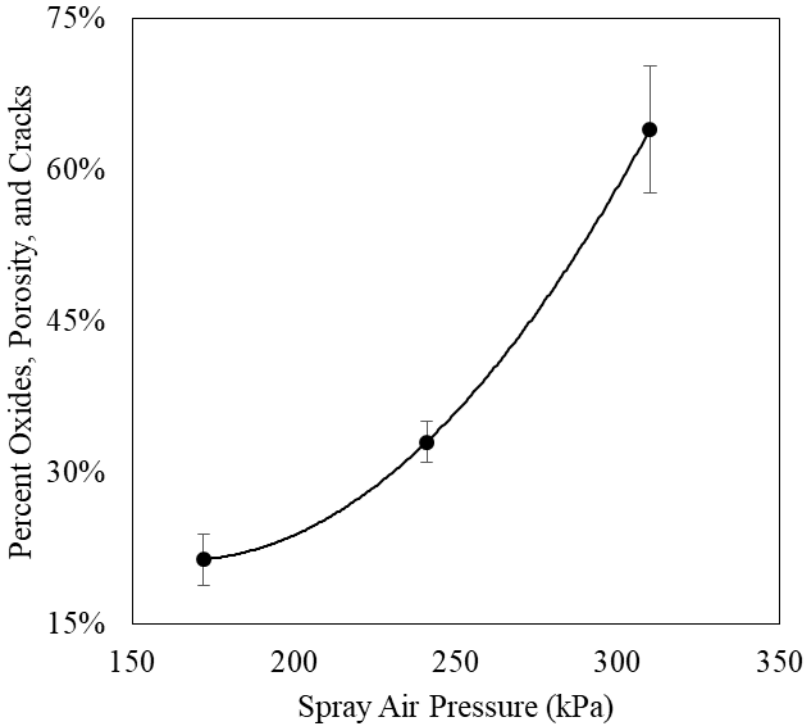

Figure 5.18 Graph showing the relationship between spray pressure and area percentage oxides, pores, and cracks.

This relationship can be easily visualized by three OM images taken at each pressure condition provided in Figure 5.19. The increase in spray pressure removes molten material from the wire tips more rapidly resulting in a significant reduction in droplet size as previously shown in Figure 2.31 [17, 58]. High atomizing air causes greater diffusion of oxygen into in-flight droplet and splat surface oxidation as the splats are propelled faster resulting in greater flattening [125].

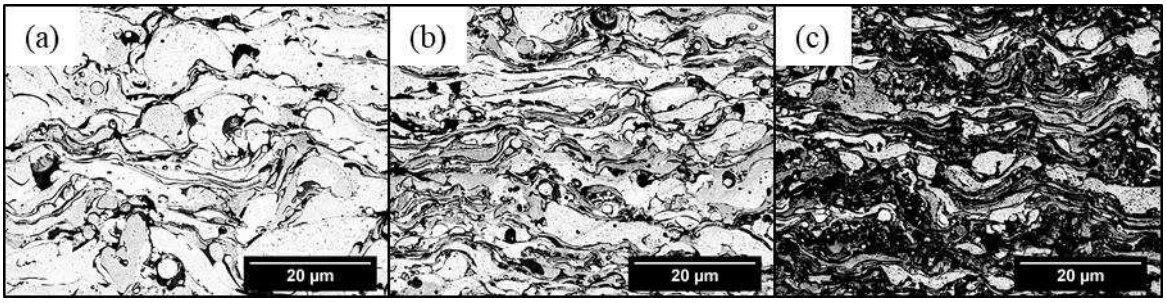

Figure 5.19 OM images of the 172 kPa (a), 241 kPa (b), and 310 kPa (c) spray pressure conditions.

Compositional maps and spot scans were used to estimate oxides present. Figure 5.20 shows the oxygen compositional map overlaid on an SEM image taken from the same area revealing the location of the oxides. Two spot scans found that the oxides are primarily composed of Fe, Cr, Mo, and Co. The base composition, discussed in Section 3.7.1.1, attributed the superior wear of the APS coating to the presence of spinel oxides AB_2O_4 (A = Fe, Co, Ni and B = Fe, Cr) with high solid solubility in each other. The atomic percentage recorded were 47.07% and 49.08% which is about 10% less oxygen than expected for the spinel. Though the desired spinel could have still formed, the results suggest the oxides present may be more complex and with the high atomic percentage of Fe present, Fe_3O_4 and Fe_2O_3 would be present as well. Additionally, the lack of Ni present within the spots suggests that the oxidation primarily occurred on the cored wire droplets which contained most of the present Fe. No large oxides were observed, like with the SiO_2 of the HH1 coatings, but instead oxidization was found to be primarily on the splat surfaces with thicker layers observed and higher pressures.

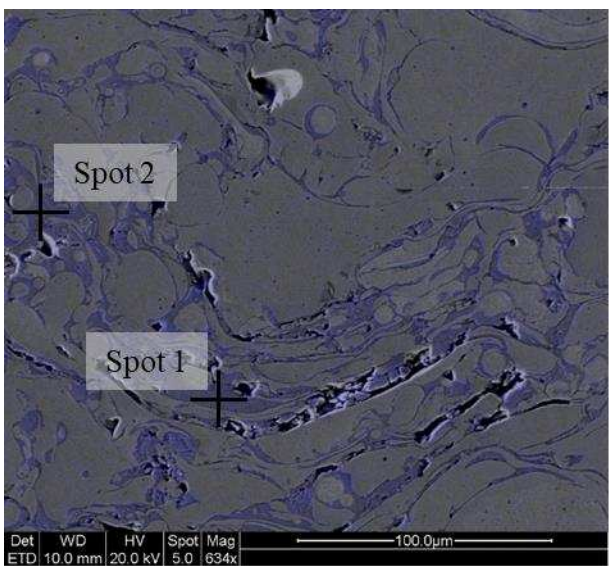

	Atomic Percent	
Element	Spot 1	Spot 2
O	47.07	49.08
Fe	31.68	29.23
Cr	7.96	8.35
Co	5.36	5.45
Mo	7.52	7.24
Ni	0.35	0.58
Ta	0.06	0.07

Figure 5.20 Oxygen compositional map overlaid on SEM image showing the location of two spot scans.

5.2.3 Mechanical Testing

5.2.3.1 Hardness

Hardness values presented in Section 4.2.2 ranged between approximately 300 and 500 HV for both the high and low spray pressure conditions. The large variation in values can be attributed to the two different splat compositions discussed in Section 5.2.1. *Splat 1* (IN625 splats) can be expected to have similar hardness values reported for selective laser melted (SLM) IN625 samples due to the similar cooling rates (10^6 k/s) [126]. SLW IN625 samples have a reported hardness of 343 HV which is within the range of hardness values observed within the TWAS new composition. High cooling rates for IN625 would result in most strengthening elements such as Mo and Nb remaining within the Ni matrix with a larger lattice distortion caused by point defects.

Splat 2 represents the combination of a 70 wt. % 430SS wire sheath (82% Fe and 18% Cr) filled with 15 wt. % Co and 15 wt. % Mo powders mixed together within the anode side of the TWAS arc. Looking at the Vickers hardness result for the low pressure condition presented in Figure 4.22, the difference between indents taken with *Splat 1* and *Splat 2* can be better estimated due to the larger splat size and lower presence of oxides. Of the six indents, four had values between 343 and 360 HV which have values consistent with *Splat 1*. Of the other two indents, one was taken on a splat boundary resulting in a lower hardness value of the 234 HV while the other had a value of 483 HV and was clearly within a splat. Thus, this last higher hardness value can be deduced to be within *Splat 2*. The reason so many of the indents appear to be within Splat 1 is suspected to be an artifact of how the indents were taken where indents were taken on even number of splats for the first five values and, due to the even distribution of splats with the coating, would favor sampling *Splat 1* over *Spat 2*.

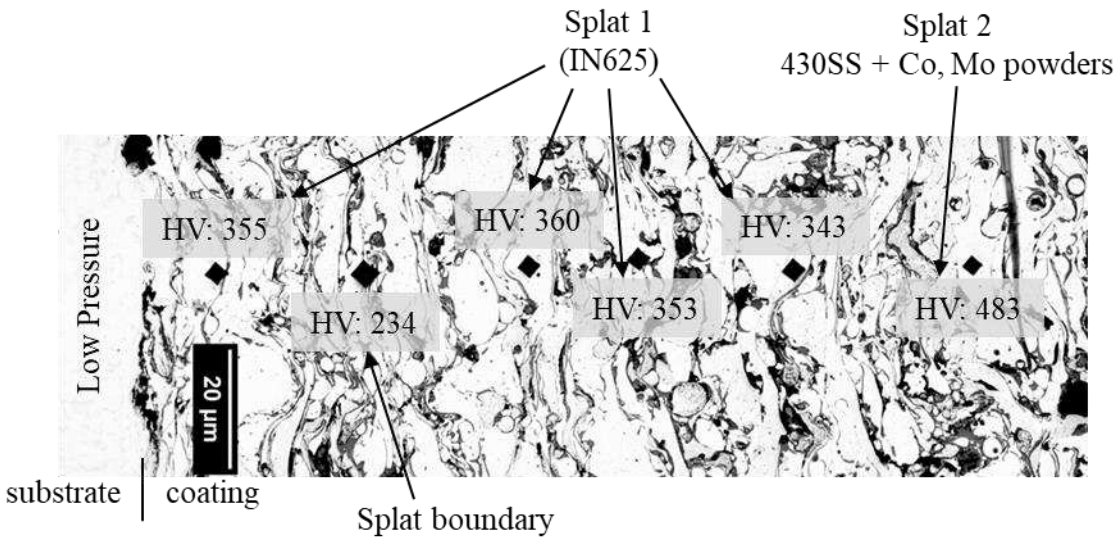

Figure 5.21 Vickers hardness values taken through the coating thickness of the low pressure condition showing which indents correspond to which splat type.

The phases present in *Splat 2* were estimated based on ternary phase diagrams for Fe-Co-Cr. Figure 5.22 (a) shows the ternary phase diagram at 1000°C with (b) showing the diagram at 700°C. *Splat 2* exists somewhere within the black triangle depending on degree of the Mo composition effect. It is observed that the splat cooled through the $(Fe, Co)_{ht}$ phase into a mixed phase region of $(Fe, Co)_{ht}$ and (Cr, Fe) phases or an FCC phase into a FCC + BCC phase region. The presence of a BCC phase could explain the higher 483 HV hardness observed.

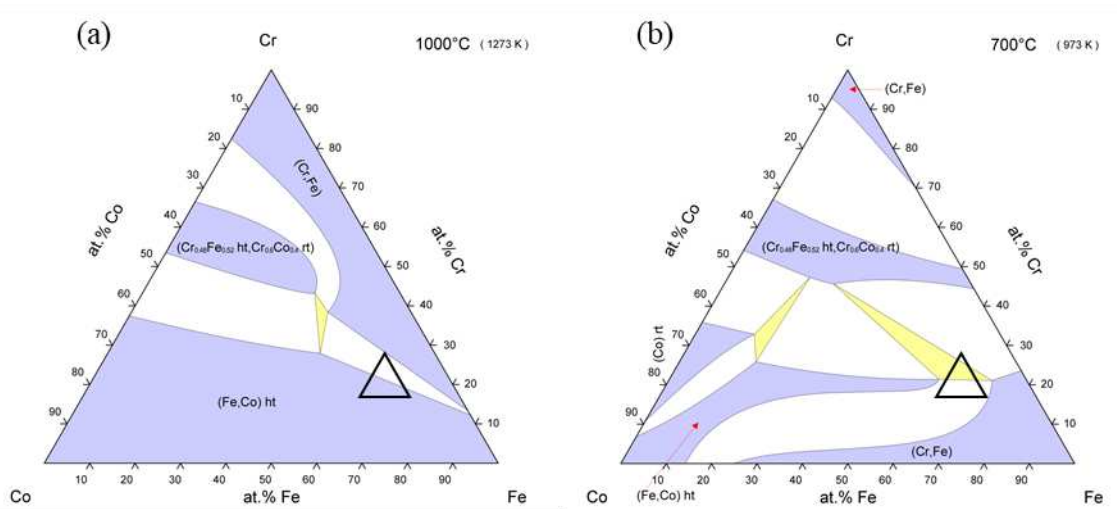

Figure 5.22 Fe-Co-Cr ternary phase diagrams at 1000°C (a) and at 700°C (b) [127].

5.2.3.2 Coating Strength

Bend testing performed on each pressure condition found that all coatings exhibited strength above 240 MPa as shown in Section 4.2.4. This is significantly higher than the highest strength observed for HH1 coating of 140 MPa. Figure 5.23 plots all of the outer-fiber stress versus strain for each pressure condition previously shown in Figure 4.25 and Figure 4.26 with the highest HH1 bent test result for HH1 previously shown in Figure 5.9 up to the point of the crack initiation where the stress dramatically drops. It was observed that all pressure conditions were stronger and tougher than the HH1 coating by a significant margin. It was also observed that as spray pressure increased from 172 kPa (25 psi) to 310 kPa (45 psi), the coating strength (and toughness) decreased from a maximum of 284 kPa for sample *25 BT1* to a low of 260 kPa. Additionally, the 172 kPa spray condition tests had a curved peak stress with material yielding before finally cracking, whereas the 310 kPa tests each had a sharp drop immediately following peak strength.

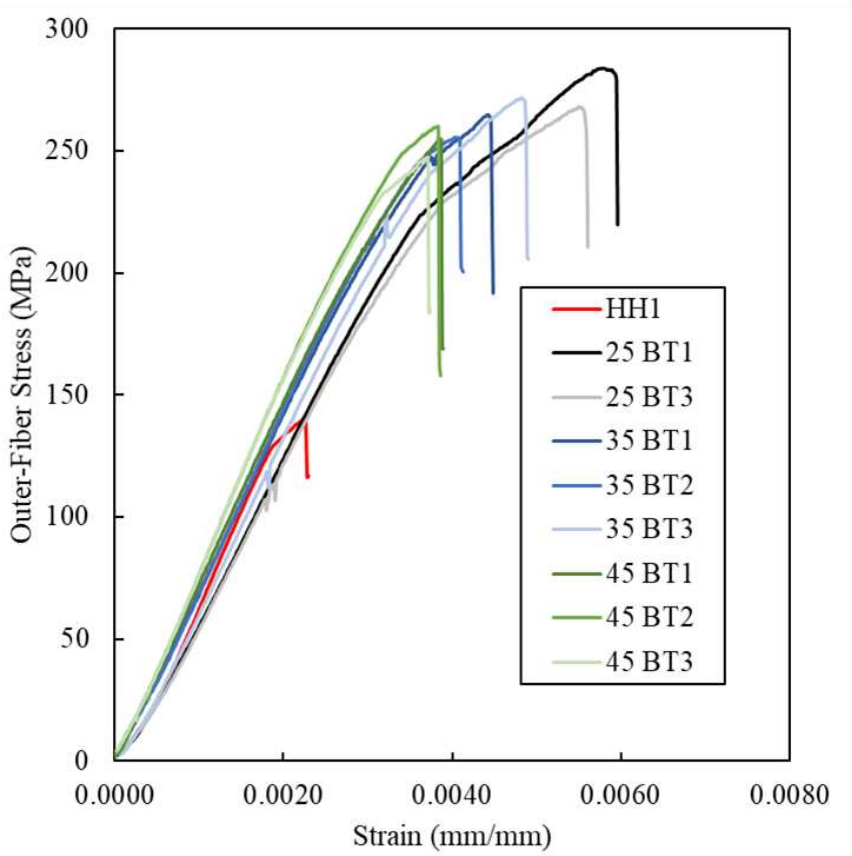

Figure 5.23 Bend test outer-fiber stress versus strain for each new composition spray pressure condition bend test plotted with HH1 coating results for comparison.

The higher strength observed from the low pressure condition is expected as this condition had the least amount of oxides as shown in Figure 5.18. However, even though the high pressure condition contained over three times the oxide content of the low pressure condition (21% versus 64% area percent oxides), the strength was decreased by only about 25 MPa or roughly 9%. This is contrary to the HH1 observations where a ~5% decrease in oxide content resulted in an almost 30 MPa (30%) increase in average stress before first crack initiation. This suggests that the oxides formed within the new composition coating adhered to the splat matrix better, resulting in a less pronounced oxide effect. No large spherical shaped oxides were found within the coating, like the large SiO_2 oxides found within the HH1 coating to help initiate fracture.

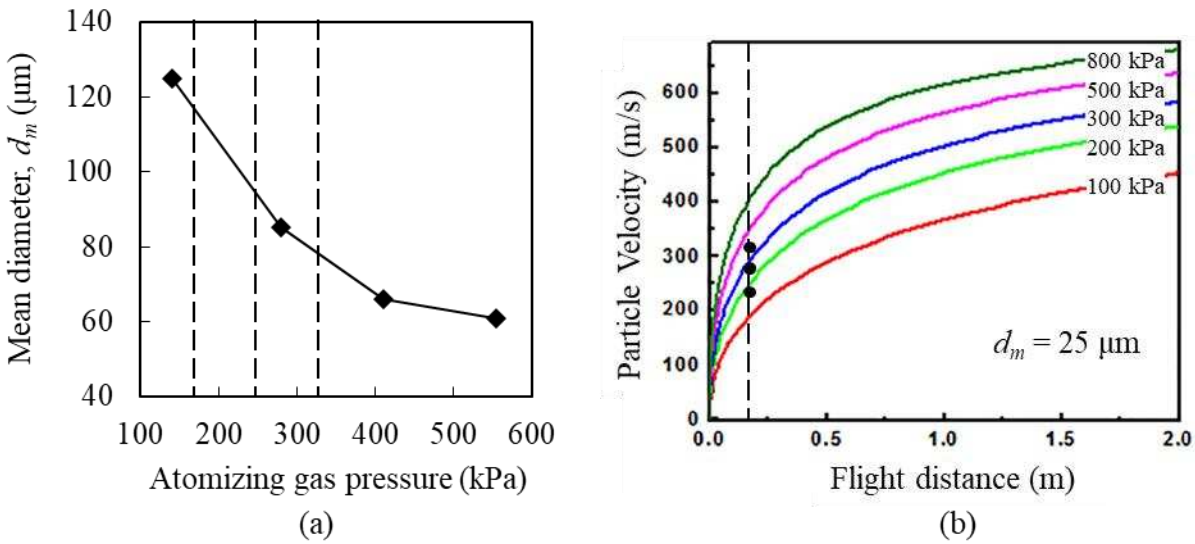

Figure 5.24 Effect of atomizing gas pressure on mean droplet diameter [58] (a) and effect of flight distance on particle velocity for various spray pressures [128] (b).

In addition to the oxide effect on strength, there also exists a particle size and velocity effect on strength. Increased pressure results in reduced droplet diameters and increased droplet velocities as shown in Figure 5.24 (a) and (b), respectively. Note that Figure 5.24 (a) represents the TWAS of Fe-0.8C steel wires whereas Figure 5.24 (b) represents the TWAS of Ni-Al. The dotted lines in Figure 5.24 (a) represent the three pressure conditions that the new composition was sprayed with showing the significant reduction in mean droplet diameter decreasing by over 30%. The dotted line on Figure 5.24 (b) represents the spray distance

(0.2 m) used for the new composition coatings with the black dots representing the three spray pressure conditions. Though this represents TWAS of a Ni-Al alloy with smaller droplet diameters reported for the Fe-0.8C alloy, the relationship of velocity with spray pressure would be similar. The increased velocities and reduced droplet size would result in a finer splat structure with a greater degree of flattening which, in part, would offset some of the detrimental effects of the increased oxide content.

5.2.3.3 Wear Testing – New Composition

Wear testing was performed on the 241 kPa and 310 kPa spray pressure conditions for the new composition coating ($Fe_{0.32}Co_{0.08}Cr_{0.2}Ni_{0.32}Mo_{0.07}Ta_{0.01}$) and compared with the reported HH1 wear rates, as well as, the results reported for the literature composition ($FeCoCrNiMo_{0.2}$) discussed in Section 3.7.1.1 used as the base for the new composition. Figure 5.25 shows the wear rates for the $FeCoCrNiMo_{0.2}$ coatings prepared by APS and HVOF, the wear reported by Devasco for the HH1 coating, and the two wear tests conducted on the new composition for two pressure conditions. The new composition coating wear rate fell between the reported values for the $FeCoCrNiMo_{0.2}$ coatings prepared by APS and HVOF. The 241 kPa new composition coating contained 33% oxides compared to the 12.7% oxide content of the HVOF coating and 47% oxide content of the APS coating [84]. The improved wear rate of the APS coating over the HVOF coating was attributed to the higher oxide content. Thus, it is reasonable to assume that the $Fe_{0.32}Co_{0.08}Cr_{0.2}Ni_{0.32}Mo_{0.07}Ta_{0.01}$ coating oxide content of 33% would have a wear rate in between these values, assuming similar oxides were formed. The result for the 310 kPa pressure condition contradicts this assumption having similar wear rates to the 241 kPa pressure condition even though the oxide content was almost doubled to 64% (higher than the APS coating). This suggests that the desired oxides responsible for the high wear rate of the APS $FeCoCrNiMo_{0.2}$ coatings were not forming.

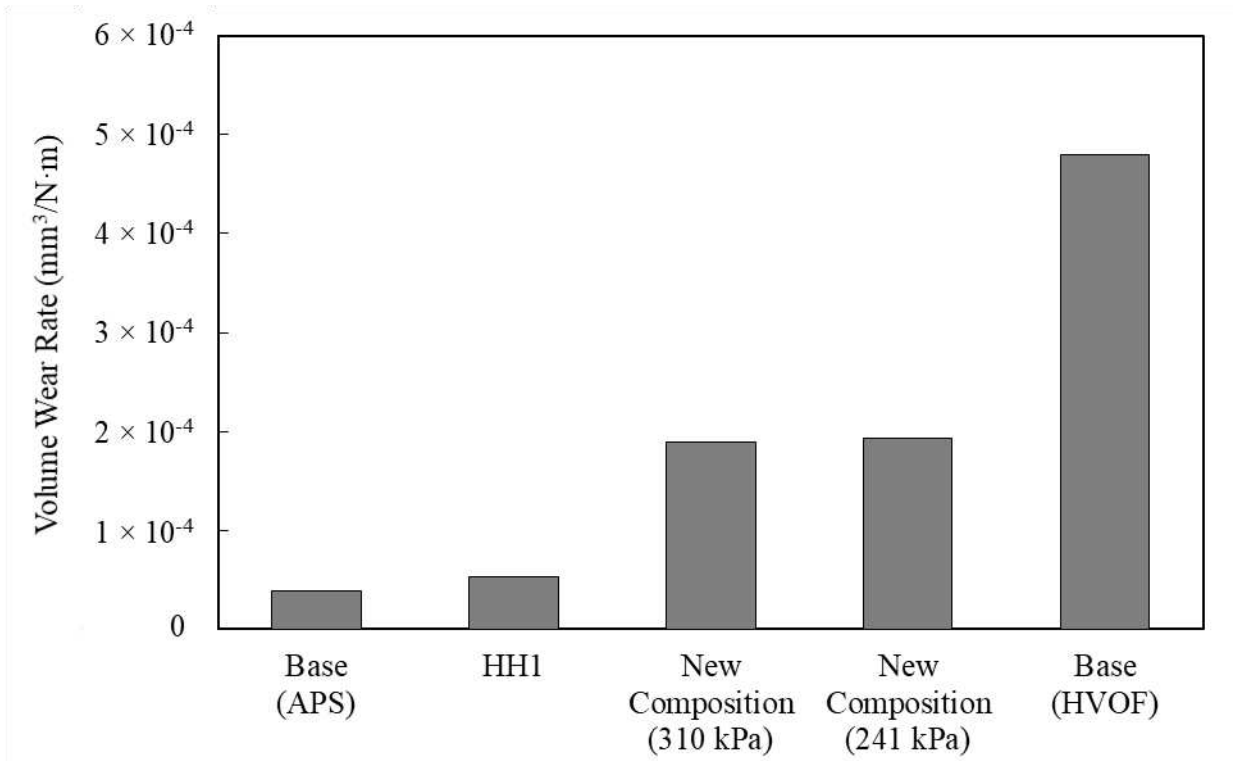

Figure 5.25 Volume wear rates for thermal sprayed coatings.

As previously discussed in Section 5.2.1 and 5.2.2, the two wires making up the $Fe_{0.32}Co_{0.08}Cr_{0.2}Ni_{0.32}Mo_{0.07}Ta_{0.01}$ composition did not mix resulting in a composite coating of splats formed either from the anode or cathode wires. However, each wire contained the elements necessary to form the desired spinel oxide AB_2O_4 (A = Fe, Co, Ni and B = Fe, Cr) with the exception of the anode not containing Ni. Figure 4.28 shows SEM images taken of the surface that reveal the presence of both abrasive and oxidation wear. Due to the presence of two splat materials, the wear was non uniform across the surface with visual regions of greater wear. Several almost perfectly circular regions are observed showing the presence of solidified droplets within the coating. In order to better characterize the worn surface, compositional maps were taken as shown in Figure 4.29. The regions protruding from the surface are shown to correspond to oxygen rich areas with the presence of oxides. This oxide layer prevents the sliding surfaces from direct metal-to-metal contact inhibiting abrasive wear [129]. Spot scan results presented in Figure 4.30 revealed regions with greatly different oxide compositions with oxygen varying from 14 to 38 at. % and Fe varying from 15 to 45 at. %. Spot scan 1 and 3 corresponded to a regions consistent with Splat 2

composition and exhibited abrasive wear with oxides high in Fe content. Higher wear in these regions could be caused by the formation of oxide scales which exhibit poor adhesion. Spot scan 2 was taken with a Splat 1 region and was found to contain 15-20 at. % of Fe, Ni, and Cr, 5-6 at. % Co and Mo and 34 at. % O. The presence of both Fe and Ni suggests that this represents the interface between Splat 1 and 2 where Splat 2 has worn down revealing Splat 2. Splat 1 has a lower hardness than Splat 2 and represents the IN625, thus it is not surprising that the Splat 1 region appears to be wearing at a greater rate.

Due to the lack of mixing of the anode and cathode wires, the FCC solid solution was not formed. The APS $FeCoCrNiMo_{0.2}$ coating wear rate was not achieved even with higher oxide contents, suggesting that the oxides formed within the $Fe_{0.32}Co_{0.08}Cr_{0.2}Ni_{0.32}Mo_{0.07}Ta_{0.01}$ coating were not of similar structures having high solid solubility within one another [99]. This results in oxides not compacting into an oxide layer by constant stress which acts to cause a lubrication effect as suggested for APS $FeCoCrNiMo_{0.2}$ coating [84, 91]. That said, the new composition ($Fe_{0.32}Co_{0.08}Cr_{0.2}Ni_{0.32}Mo_{0.07}Ta_{0.01}$) coating has an order of magnitude better wear rate than that of HVOF sprayed IN625 with a reported volume wear rate of 18.6×10^{-4} mm^3/Nm [130]. The wear rate of $Fe_{0.32}Co_{0.08}Cr_{0.2}Ni_{0.32}Mo_{0.07}Ta_{0.01}$ coating was actually closer to the wear rate of HVOF sprayed IN625 containing 42 wt. % tungsten carbide.

CHAPTER 6: CONCLUSION

6.1 HH1 Coating

In this work, the HH1 coating was characterized and tested with the effect of input-voltage parameter investigated. The HH1 coating was found to be a complex mixture of martensitic steel splats, oxides primarily of Al_2O_3 and SiO_2, and regions of elemental segregation. Splat hardness was found to be >500 HV from Vickers indents taken within splats. Al_2O_3 was primarily found as long thin layers between splats; whereas, SiO_2 was primarily found as large near-spherical shapes approximately 50 µm in diameter. Regions of element segregation were observed primarily of Ni and V. As voltage increased from 26.5V to 36.5V, the amount of defects primary oxides decreased from 24.2% to 19.7%. It is hypothesized that, because with increased voltage there is a decrease in mean droplet diameter and increase in droplet temperature with constant deposition rate, there would be less time for surface oxidation on the splat layers before being covered by the next layer.

Utilizing four-point bend testing, it was found that the stress required to initiate the first coating crack increased from 88 to 125 MPa when input-voltage was increased from 26.5 to 36.5V. DIC strain imaging with load vs time plots tracked the strains in the coating during the stress and were used to correlate load drops during the test with the specific crack initiation. Analysis of the bend test fracture surface revealed the presence of many oxides decorating the surface (Al_2O_3, SiO_2, and TiO_2). Fracture parallel to the bending stress was along splat boundaries which have high amounts of Al_2O_3 present resulting in delamination of the splats. Brittle fracture occurred through the splat commonly initiating at a silicon or titanium oxide particle.

6.2 New Composition Coating

A new MPEA composition ($Fe_{0.32}Co_{0.08}Cr_{0.2}Ni_{0.32}Mo_{0.07}Ta_{0.01}$) was prepared and tested with the objective to achieve increased strength and toughness while maintaining a wear performance comparable to HH1. The effect of spray pressure parameter was investigated. Findings were compared with results for the $FeCoCrNiMo_{0.2}$ literature composition which was used as the new composition base. It was found that the two different wires used in combination to achieve the desired composition did not mix within the arc,

in-flight, or on deposition. This resulted in a coating comprised of two different splat types correlating with the anode and cathode wire compositions. The cathode, comprised of a solid IN625 wire, generated splats with a hardness ranging from 310 – 360 HV. The anode, comprised of a cored wire with 430SS sheath material and 50/50 wt. % mixture of Mo and Co powder core, generated splats with a hardness ranging from 403 – 483 HV. As spray pressure was increased from 172 kPa to 310 kPa the oxide content increased from 21% to 64%. Oxides were found to exist in thin layers between splats. Oxides were primarily formed with Fe, Cr, Mo, and Co.

An increased spray pressure from 172 to 310 kPa resulted in an average strength decrease of 22 MPa or 8% decrease. Thus, the effect of pressure on coating strength was less than the effect of input-voltage on the HH1 coating which saw a 22% decrease in strength when reducing voltage from 36.5V to 26.5V. The volumetric wear rate of the 241 kPa spray pressure condition was 1.93×10^{-4} $mm^3/N\cdot m$ which fell between the APS and HVOF $FeCoCrNiMo_{0.2}$ base composition wear rates of 3.9×10^{-5} $mm^3/N\cdot m$ and 4.8×10^{-4} $mm^3/N\cdot m$, respectively. However, this wear rate was over four times the wear rate of HH1. The 310 kPa spray pressure condition, with approximately two times the oxide content of the 241 kPa spray pressure condition, had a wear rate of 1.89×10^{-4} $mm^3/N\cdot m$ which was virtually identical to the 241 kPa pressure condition test. It was suspected that, due to the anode and cathode not mixing, a more complex mixture of oxides formed than that of the $FeCoCrNiMo_{0.2}$ base composition's AB_2O_4 (A = Fe, Co, Ni and B = Fe, Cr) spinel oxides. This resulted in oxides that do not have high solid solubility in one another and would not form the oxide layer to which the APS $FeCoCrNiMo_{0.2}$ coating superior wear was attributed.

In conclusion, the new $Fe_{0.32}Co_{0.08}Cr_{0.2}Ni_{0.32}Mo_{0.07}Ta_{0.01}$ composition met the strength and toughness objective with stress achieved before cracking approximately doubling that observed of the HH1 coating. However, the wear rate objective was not met with the new composition having a wear rate almost four times that of the HH1. It cannot be concluded; however, that the $Fe_{0.32}Co_{0.08}Cr_{0.2}Ni_{0.32}Mo_{0.07}Ta_{0.01}$ MPEA would have this wear rate. The anode and cathode would need to be the same composition to evaluate if the Thermo-Calc predicted FCC solid solution splat structure would form. Thus, no conclusions can be drawn about the mechanical properties of a properly mixed $Fe_{0.32}Co_{0.08}Cr_{0.2}Ni_{0.32}Mo_{0.07}Ta_{0.01}$ MPEA.

CHAPTER 7: FUTURE WORK

7.1 HH1 Coating

Due to the limited scope of testing conducted for this work, additional modeling, characterization, and testing of the HH1 coating would prove useful. As previously discussed in Section 2.5 about solidification modeling, knowing the droplet diameter and temperature on impact with the substrate is critical to understanding the splat structure. A simple test that was conducted on a TWAS Fe-0.8 wt. %C steel to determine droplet size involved mounting the spray gun to the top of a 2.6 m long vertical chamber and spraying with the absence of a substrate so that droplets would solidify before reaching the base at which point the droplets/powder could be sieved [58]. As for the temperature, the use of an in-flight particle pyrometer has been employed which uses a two-color infrared pyrometer to give an average particle/droplet temperature over small measurement volume [57, 131, 132]. With accurate values for droplet size temperature of the HH1 composition, solidification modeling could be conducted. Values for residual stress could then be calculated using the elastoplastic model presented by Chen which takes into account the volume expansion for the martensitic phase transformation [51].

7.1.1 Bond Strength Test

The HH1 coating was reported to exhibit high bond strength with past attempts to use ASTM C 633 Standard Test Method for Adhesion or Cohesion Strength of Thermal Spray Coatings resulting in adhesive failure meaning that the exact value of the bond strength could not be determined [133]. An alternative test was designed and proposed that would be able to measure bond strength with a schematic shown in Figure 7.1. This test design is based in part on the “pin and ring” testing conducted on thermal sprayed WC-12Co coatings [134, 135]. The test works by aligning pin and ring top surfaces together and then sand blasting and thermal spraying to desired thickness. Once spraying is completed, the pin and ring can be fixed to the holders by fasteners screwed into the bottom of the ring. After the pin and ring are properly assembled into the holder, the set-up can be placed into a mechanical testing frame. The frame will load the sample pulling the pin away from the coating and by knowing the pin surface, the bond strength can be determined.

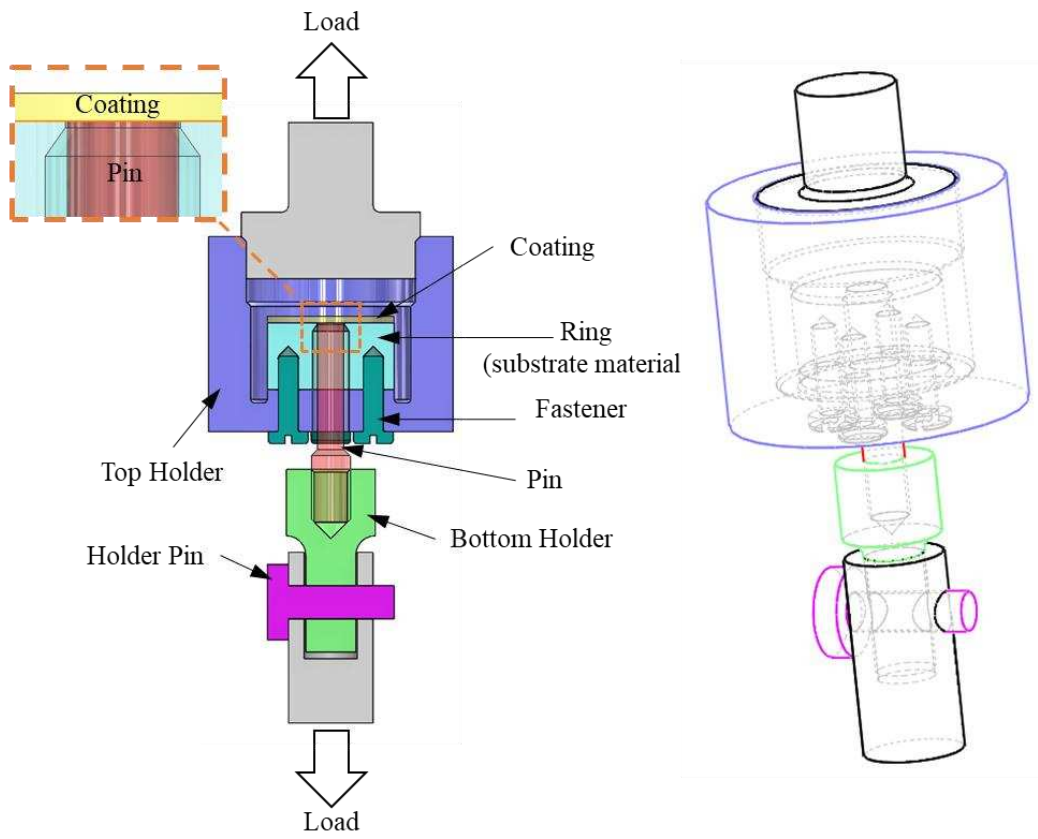

Figure 7.1 Schematic and transparent SolidWorks model of the pin and ring test proposed to measure the coating bond strength.

7.1.2 Residual Stress Testing

The HH1 coating did not have a direct measurement of residual stress performed. Performing residual stress measurements would be valuable to avoid coating peeling and in understanding the compressive or tensile influence on mechanical properties. Residual stress arises from quench stress and differential thermal contraction stresses [136]. These stresses can be measured by either non-destructive or destructive methods [137]. Non-destructive testing for the HH1 coating could be conducted by the curvature monitoring method or with neutron diffraction which would be capable of providing a through-thickness stress profile without having to perform layer removal [138]. The curvature monitoring method involves comparing strip samples before and after thermal spraying [139]. Testing conducted on vacuum plasma sprayed NiCr 80-20 coatings determined average residual stress by spraying a flat strip sample of known material and measuring the radius of curvature of the sample which developed after spraying as show in Figure 7.2.

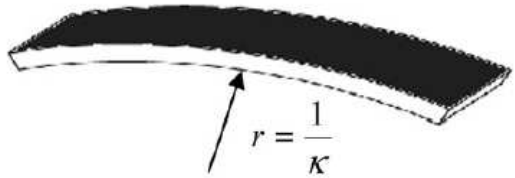

Figure 7.2 Sprayed sample showing curved radius developed after spraying with the definition of curvature parameter, *K* [139].

The following equations were proposed to calculate the average residual stress intensity (σ_R) of the coating [136, 139]:

$$K = \frac{6E_r E_s (t+T) t T \Delta\varepsilon}{E_r^2 t^4 + 4E_r E_s t^3 T + 6E_r E_s t^2 T^2 + 4E_r E_s T^3 t + E_s^2 T^4} \tag{7.1}$$

with

$$\sigma_R = \frac{E_r}{1-v} \times \Delta\varepsilon \tag{7.2}$$

or

$$\sigma_R = K \frac{E_r^2 t^4 + 4E_r E_s t^3 T + 6E_r E_s t^2 T^2 + 4E_r E_s T^3 t + E_s^2 T^4}{6tE_s(1+v)T(t+T)} \tag{7.3}$$

where, *K* is the curvature parameter after spraying, the Young's modulus of the coating and substrate are represented by E_r and E_s respectively, *T* represents the substrate thickness while *t* represents the coating thickness, and *v* being the Poisson ratio.

Residual stress can also be evaluated by destructive testing such as by the hole drilling method (ASTM E837) [140]. Thermal spray coatings like HH1 generally have non-uniform stresses through the thickness so a modification of ASTM E837 to perform incremental steps (20-40 µm) using an integral method is recommended [141]. Figure 7.3 (a) – (c) show the hole-drilling set-up, strain gauge rosette, and drill position. Due to issues with accurately measuring the drilling steps the results for this test were not included in this work. That said, proper testing using this measurement could prove useful in obtaining residual stress values and determining the effect of various spray parameters.

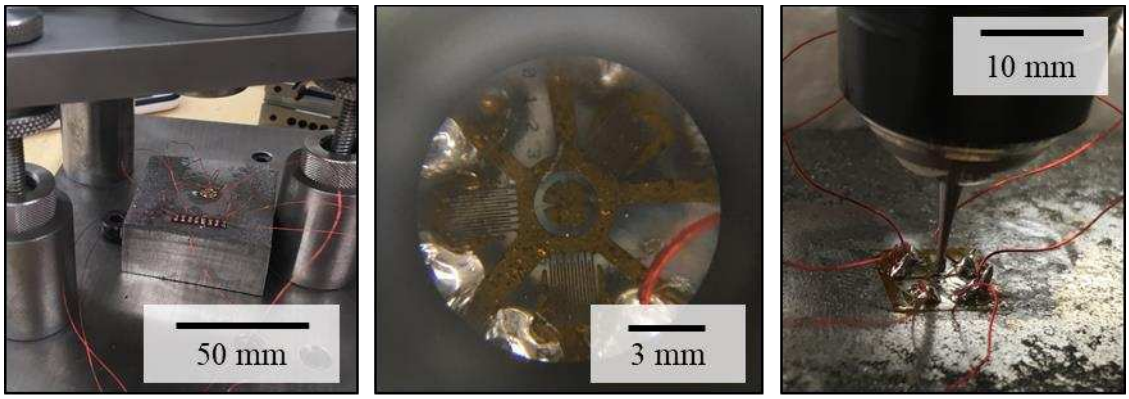

(a) (b) (c)

Figure 7.3 Hole-drilling set-up on the HH1 coating (a), magnified image of the strain gauge rosette (b), and image of drill positioned over the middle of the strain gauge.

7.2 New MPEA Composition

Due to the lack of wire mixing discussed in Section 5.2.1, the desired splat composition was not achieved. In order to evaluate the $Fe_{0.32}Co_{0.08}Cr_{0.2}Ni_{0.32}Mo_{0.07}Ta_{0.01}$ MPEA discussed in Section 3.7.1.2, anode and cathode wires would need to be of identical composition. By having identical wires, the splat structure could be compared with the Thermo-Calc predicted composition. If the TWAS $Fe_{0.32}Co_{0.08}Cr_{0.2}Ni_{0.32}Mo_{0.07}Ta_{0.01}$ coating forms similar oxides to the APS $FeCoCrNiMo_{0.2}$ coating, it is expected that the wear rate could be drastically increased from the 1.89×10^{-4} $mm^3/N \cdot m$ to the reported 3.91×10^{-5} $mm^3/N \cdot m$ [84]. It was shown that spraying at 310 kPa resulted in a coating with a greater oxide content than that of the APS meaning that wear rate could theoretically be further increased. Additionally, the strength was not significantly reduced at this spray pressure, leaving room for the possibility of a coating with improved wear and dramatically increased strength and toughness over the HH1 coating. Granted the cost would be significantly higher than that of HH1 due to the presence of Mo and Co. However, with the use of Thermo-Calc, these costly elements could be reduced resulting in a composition almost half the price of the $FeCoCrNiMo_{0.2}$ composition while still producing the primarily FCC solid solution.

REFERENCES

[1] Grijalva, O., Holzmann, J., Oppelt, J., Perozo, N., Paz, C., & Asgharzadeh, A. "Octg advancements in casing drilling: Where we have been and where are we going?"Review of. *Society of Petroleum Engineers. doi:10.2118/185102-MS*, 2017, March 27.

[2] True, M. E. W., P. D. "Optimum means of protecting casing and drillpipe tool joints against wear."Review of. *Journal of Petroleum Technology* 27, no. 02: pg.246-252, 1975.

[3] White, J. P. D., R. "Casing wear: Laboratory measurements and field predictions."Review of. *SPE Drilling Engineering* 2, no. 1: p.56-62, 1987.

[4] Tucker Jr, R. C. "2. Surface engineering." In *Asm handbook, volume 5a - thermal spray technology*: ASM International, 2013.

[5] Newbery, A. P., A. R. E. Singer, A. D. Roche*, et al. Electric arc sprayed self-lubricating coatings for the protection of drill string tool joints*. ASM International, Materials Park, OH (United States), 1995.

[6] Tucker Jr, R. C. "1. Introduction to thermal spray technology." In *Asm handbook, volume 5a - thermal spray technology*: ASM International, 2013.

[7] Vardelle, A., C. Moreau, J. Akedo*, et al.* "The 2016 thermal spray roadmap."Review of. *J Therm Spray Techn* 25, no. 8: 1376-1440, 2016.

[8] "Global thermal spray market-segmented by product type, by end-user industry, and geography-trends and forecasts (2019-2024)." Mordor Intelligence, 2018.

[9] Tucker Jr, R. C. "3. Thermal spray processes and coatings." In *Asm handbook, volume 5a - thermal spray technology*: Advanced Materials & Processes, 2015.

[10] Pawlowski, L. *The science and engineering of thermal spray coatings*. John Wiley & Sons, 2008.

[11] Toma, S. L., C. Bejinariu, R. Baciu*, et al.* "The effect of frontal nozzle geometry and gas pressure on the steel coating properties obtained by wire arc spraying."Review of. *Surf Coat Tech* 220: 266-270, 2013.

[12] Wang, X., J. Heberlein, E. Pfender*, et al.* "Effect of nozzle configuration, gas pressure, and gas type on coating properties in wire arc spray."Review of. *J Therm Spray Techn* 8, no. 4: 565-575, 1999.

[13] Thorpe, M. L. "Thermal spray industry in transition."Review of. *Advanced materials and processes* 143: 50-56, 1993.

[14] Newbery, A. P., and P. S. Grant. "Oxidation during electric arc spray forming of steel."Review of. *J Mater Process Tech* 178, no. 1-3: 259-269, 2006.

[15] Gedzevicius, I., and A. V. Valiulis. "Analysis of wire arc spraying process variables on coatings properties."Review of. *J Mater Process Tech* 175, no. 1-3: 206-211, 2006.

[16] "At-400 wire arc spray system sales brochure." edited by T. Inc.

[17] Hussary, N. A., and J. V. R. Heberlein. "Effect of system parameters on metal breakup and particle formation in the wire arc spray process."Review of. *J Therm Spray Techn* 16, no. 1: 140-152, 2007.

[18] Ashgriz, N. *Handbook of atomization and sprays: Theory and applications*. Springer Science & Business Media, 2011.

[19] Lavernia, E. J., and T. S. Srivatsan. "The rapid solidification processing of materials: Science, principles, technology, advances, and applications."Review of. *J Mater Sci* 45, no. 2: 287-325, 2010.

[20] Crapper, G., N. Dombrowski, and G. Pyott. "Kelvin–helmholtz wave growth on cylindrical sheets."Review of. *J Fluid Mech* 68, no. 3: 497-502, 1975.

[21] Hussary, N. A., and J. V. R. Heberlein. "Atomization and particle-jet interactions in the wire-arc spraying process."Review of. *J Therm Spray Techn* 10, no. 4: 604-610, 2001.

[22] Dombrowski, N., and W. Johns. "The aerodynamic instability and disintegration of viscous liquid sheets."Review of. *Chem Eng Sci* 18, no. 3: 203-214, 1963.

[23] Li, X. G., and U. Fritsching. "Process modeling pressure-swirl-gas-atomization for metal powder production."Review of. *J Mater Process Tech* 239: 1-17, 2017.

[24] Pilch, M., and C. A. Erdman. "Use of breakup time data and velocity history data to predict the maximum size of stable fragments for acceleration-induced breakup of a liquid-drop."Review of. *Int J Multiphas Flow* 13, no. 6: 741-757, 1987.

[25] Hsiang, L. P., and G. M. Faeth. "Near-limit drop deformation and secondary breakup."Review of. *Int J Multiphas Flow* 18, no. 5: 635-652, 1992.

[26] Guildenbecher, D. R., C. Lopez-Rivera, and P. E. Sojka. "Secondary atomization."Review of. *Exp Fluids* 46, no. 3: 371-402, 2009.

[27] Perrin, R., and J. P. Scharff. *Chimie industrielle* [in French]. Paris: Dunod, 1999.

[28] Neiser, R. A., M. F. Smith, and R. C. Dykhuizen. "Oxidation in wire hvof-sprayed steel."Review of. *J Therm Spray Techn* 7, no. 4: 537-545, 1998.

[29] Syed, A. A., A. Denoirjean, P. Denoirjean*, et al.* "In-flight oxidation of stainless steel particles in plasma spraying."Review of. *J Therm Spray Techn* 14, no. 1: 117-124, 2005.

[30] Deshpande, S., S. Sampath, and H. Zhang. "Mechanisms of oxidation and its role in microstructural evolution of metallic thermal spray coatings - case study for ni-al."Review of. *Surf Coat Tech* 200, no. 18-19: 5395-5406, 2006.

[31] Moreau, C., P. Gougeon, M. Lamontagne*, et al.* "Thermal spray industrial applications." Paper presented at the Proc. 7th Thermal Spray Conf., Boston, MA, 1994.

[32] Cochrane, R. F., P. V. Evans, and A. L. Greer. "Containerless solidification of alloys in a drop-tube."Review of. *Mater Sci Eng* 98: 99-103, 1988.

[33] Xu, Q., and E. J. Lavernia. "Influence of nucleation and growth phenomena on microstructural evolution during droplet-based deposition."Review of. *Acta Mater* 49, no. 18: 3849-3861, 2001.

[34] Liu, D. M., J. Z. Zhao, and H. Q. Ye. "Modeling of the solidification of gas-atomized alloy droplets during spray forming."Review of. *Mat Sci Eng a-Struct* 372, no. 1-2: 229-234, 2004.

[35] Liang, X., J. C. Earthman, and E. J. Lavernia. "On the mechanism of grain formation during spray atomization and deposition."Review of. *Acta Metall Mater* 40, no. 11: 3003-3016, 1992.

[36] Morris, D. G. "Glass-formation and crystallization in ni-si-b alloys .1. Glass formation-test of the avoidance of crystallization approach."Review of. *Acta Metallurgica* 31, no. 10: 1479-1489, 1983.

[37] Malik, M. "Plasma sprayed coatings in aircraft and engine components." Paper presented at the International Metal Spraying Conference in London, 1973.

[38] Amada, S., T. Hirose, and T. Senda. "Quantitative evaluation of residual grits under angled blasting."Review of. *Surf Coat Tech* 111, no. 1: 1-9, 1999.

[39] Crawmer, D. "5. Coating structures, proporties, and materials." In *Asm handbook, volume 5a - thermal spray technology*, edited by R. C. Tucker Jr: Advanced Materials & Processes, 2015.

[40] Sampath, S., and H. Herman. "Rapid solidification and microstructure development during plasma spray deposition."Review of. *J Therm Spray Techn* 5, no. 4: 445-456, 1996.

[41] Ruhl, R. C. "Cooling rates in splat cooling."Review of. *Mater Sci Eng* 1, no. 6: 313-320, 1967.

[42] Moreau, C., P. Cielo, M. Lamontagne*, et al.* "Temperature evolution of plasma-sprayed niobium particles impacting on a substrate."Review of. *Surf Coat Tech* 46, no. 2: 173-187, 1991.

[43] Sobolev, V. V., and J. M. Guilemany. "Flattening of droplets and formation of splats in thermal spraying: A review of recent work - part 1."Review of. *J Therm Spray Techn* 8, no. 1: 87-101, 1999.

[44] Moreau, C., P. Cielo, M. Lamontagne*, et al.* "Temperature evolution of plasma-sprayed niobium particles impacting on a substrate."Review of. *Thermal Spray Research and Applications*: 19-26, 1991.

[45] Doltsinis, I. S., J. Harding, and M. Marchese. "Modelling the production and performance analysis of plasma-sprayed ceramic thermal barrier coatings."Review of. *Arch Comput Method E* 5, no. 2: 59-166, 1998.

[46] Sobolev, V. V., and J. M. Guilemany. "Effect of oxidation on droplet flattening and splat-substrate interaction in thermal spraying."Review of. *J Therm Spray Techn* 8, no. 4: 523-530, 1999.

[47] Fauchais, P., A. Vardelle, and B. Dussoubs. "Quo vadis thermal spraying."Review of. *Thermal Spray 2001: New Surfaces for a New Millennium*: 1-32, 2001.

[48] Sobolev, V. V., and J. M. Guilemany. "Flattening of droplets and formation of splats in thermal spraying: A review of recent work - part 2."Review of. *J Therm Spray Techn* 8, no. 2: 301-314, 1999.

[49] Rayment, T., S. Hoile, and P. S. Grant. "Phase transformations and control of residual stresses in thick spray-formed steel shells."Review of. *Metall Mater Trans B* 35, no. 6: 1113-1122, 2004.

[50] Gill, S. C., and T. W. Clyne. "Stress distributions and material response in thermal spraying of metallic and ceramic deposits."Review of. *Metall Trans B* 21, no. 2: 377-385, 1990.

[51] Chen, Y. X., X. B. Liang, Y. Liu*, et al.* "Prediction of residual stresses in thermally sprayed steel coatings considering the phase transformation effect."Review of. *Mater Design* 31, no. 8: 3852-3858, 2010.

[52] Kuroda, S., T. Dendo, and S. Kitahara. "Quenching stress in plasma-sprayed coatings and its correlation with the deposit microstructure."Review of. *J Therm Spray Techn* 4, no. 1: 75-84, 1995.

[53] Vort, G. F. V. "Atlas of time-temperature diagrams for irons and steels."Review of. *ASM INTERNATIONAL, Materials Park, OH*: 16, 1991.

[54] Crawmer, D. "6. Process control and control equipment." In *Asm handbook, volume 5a - thermal spray technology*, edited by R. C. Tucker Jr: Advanced Materials & Processes, 2015.

[55] Chen, Y. X., X. B. Liang, S. C. Wei*, et al.* "Numerical simulation of the twin-wire arc spraying process: Modeling the high velocity gas flow field distribution and droplets transport."Review of. *J Therm Spray Techn* 21, no. 2: 263-274, 2012.

[56] Toma, S. L. "The influence of jet gas temperature on the characteristics of steel coating obtained by wire arc spraying."Review of. *Surf Coat Tech* 220: 261-265, 2013.

[57] Newbery, A. P., P. S. Grant, and R. A. Neiser. "The velocity and temperature of steel droplets during electric arc spraying."Review of. *Surf Coat Tech* 195, no. 1: 91-101, 2005.

[58] Newbery, A. P., and P. S. Grant. "Large arc voltage fluctuations and droplet formation in electric arc wire spraying."Review of. *Powder Metall* 46, no. 3: 229-235, 2003.

[59] Tillmann, W., E. Vogli, and M. Abdulgader. "Asymmetric melting behavior in twin wire arc spraying with cored wires."Review of. *J Therm Spray Techn* 17, no. 5-6: 974-982, 2008.

[60] Piers Newbery, A. "Electric arc spray forming of nickel alloys and nickel aluminides." University of Oxford, 1993.

[61] Madejski, J. "Solidification of droplets on a cold surface."Review of. *Int J Heat Mass Tran* 19, no. 9: 5, 1976.

[62] Ha, E. J., W. S. Kim, and G. D. Jeun. "A study on the impact and solidification of liquid metal droplets during thermal spray deposition onto a substrate with concentric grooves or ridges."Review of. *Heat Transfer Eng* 27, no. 3: 55-67, 2006.

[63] M.Pasandideh-Fard, R. B., S.Chandra, J.Mostaghimi. "Deposition of tin droplets on a steel plate: Simulations and experiments."Review of. *Int J Heat Mass Tran* 41, no. 19: 2929-2945, 1998.

[64] Tong, A. Y., and B. R. Holt. "Numerical study on the solidification of liquid metal droplets impacting onto a substrate."Review of. *Numer Heat Tr a-Appl* 31, no. 8: 797-817, 1997.

[65] Kothe, D. B., and R. C. Mjolsness. "Ripple - a new model for incompressible flows with free surfaces."Review of. *Aiaa J* 30, no. 11: 2694-2700, 1992.

[66] Brackbill, J. U., D. B. Kothe, and C. Zemach. "A continuum method for modeling surface-tension."Review of. *J Comput Phys* 100, no. 2: 335-354, 1992.

[67] Zhang, Y. G., S. Matthews, A. T. T. Tran*, et al.* "Effects of interfacial heat transfer, surface tension and contact angle on the formation of plasma-sprayed droplets through simulation study."Review of. *Surf Coat Tech* 307: 807-816, 2016.

[68] "Ansys fluent. 16.0, theory guide, ansys, inc., 2016."Review of.

[69] Wei Li, P. L. P. K. L. "Microstructures and properties of high-entropy alloy films and coatings: A review."Review of. *Materials Research Letters* 6:4: 199-229, 2018.

[70] Huang, K. B. Y., J. W. (advisor). "A study on the multicomponent alloy systems containing equal-mole elements. Masters' thesis." National Tsing Hua University, 1996.

[71] Macdonald, B. E., Z. Fu, B. Zheng*, et al.* "Recent progress in high entropy alloy research."Review of. *Jom-Us* 69, no. 10: 2024-2031, 2017.

[72] Hsu, W. L., H. Murakami, J. W. Yeh*, et al.* "On the study of thermal-sprayed ni0.2co0.6fe0.2crsi0.2alti0.2 hea overlay coating."Review of. *Surf Coat Tech* 316: 71-74, 2017.

[73] Tian, L. H., W. Xiong, C. Liu*, et al.* "Microstructure and wear behavior of atmospheric plasma-sprayed alcocrfeniti high-entropy alloy coating."Review of. *J Mater Eng Perform* 25, no. 12: 5513-5521, 2016.

[74] Miracle, D. B., and O. N. Senkov. "A critical review of high entropy alloys and related concepts."Review of. *Acta Mater* 122: 448-511, 2017.

[75] Gao, M. C. Y., J. W.; Liaw, P. K.; Zhang, Y. *High-entropy alloys fundamentals and applications*. Switzerland: Springer International Publishing, 2016.

[76] Pickering, E. J., and N. G. Jones. "High-entropy alloys: A critical assessment of their founding principles and future prospects."Review of. *Int Mater Rev* 61, no. 3: 183-202, 2016.

[77] Yeh, J. W. "Alloy design strategies and future trends in high-entropy alloys."Review of. *Jom-Us* 65, no. 12: 1759-1771, 2013.

[78] Yeh, J. W. C., S. K.; Lin, S. J.; Gan, J. Y.; Chin, T. S.; Shun, T.T.; Tsau, C. H.; Chang, S. Y. "Nanostructured high-entropy alloys with multiple principal elements: Novel alloy design concepts and outcomes."Review of. *Adv Eng Mater* 6, no. 5: 299-303, 2004.

[79] Zhang, Y., Y. J. Zhou, J. P. Lin*, et al.* "Solid-solution phase formation rules for multi-component alloys."Review of. *Adv Eng Mater* 10, no. 6: 534-538, 2008.

[80] Yeh, J. W., S. K. Chen, J. Y. Gan*, et al.* "Formation of simple crystal structures in cu-co-ni-cr-al-fe-ti-v alloys with multiprincipal metallic elements."Review of. *Metall Mater Trans A* 35a, no. 8: 2533-2536, 2004.

[81] Yeh, J. W. "Recent progress in high-entropy alloys."Review of. *Ann Chim-Sci Mat* 31, no. 6: 633-648, 2006.

[82] Tsai, K. Y., M. H. Tsai, and J. W. Yeh. "Sluggish diffusion in co-cr-fe-mn-ni high-entropy alloys."Review of. *Acta Mater* 61, no. 13: 4887-4897, 2013.

[83] "The united states patent and trademark office, www.Uspto.Gov/web/patents/classification/cpc/html/defc23c.Html."

[84] Li, T. C., Y. Liu, B. Liu*, et al.* "Microstructure and wear behavior of fecocrnimo0.2 high entropy coatings prepared by air plasma spray and the high velocity oxy-fuel spray processes."Review of. *Coatings* 7, no. 9, 2017.

[85] Wang, L. M., C. C. Chen, J. W. Yeh*, et al.* "The microstructure and strengthening mechanism of thermal spray coating nixco0.6fe0.2crysizalti0.2 high-entropy alloys."Review of. *Mater Chem Phys* 126, no. 3: 880-885, 2011.

[86] Wang, Y. F., S. G. Ma, X. H. Chen*, et al.* "Optimizing mechanical properties of alcocrfenitix high-entropy alloys by tailoring microstructures."Review of. *Acta Metall Sin-Engl* 26, no. 3: 277-284, 2013.

[87] Zhang, K. B., Z. Y. Fu, J. Y. Zhang*, et al.* "Characterization of nanocrystalline cocrfenitial high-entropy solid solution processed by mechanical alloying."Review of. *J Alloy Compd* 495, no. 1: 33-38, 2010.

[88] Chelliah, N., and S. V. Kailas. "Synergy between tribo-oxidation and strain rate response on governing the dry sliding wear behavior of titanium."Review of. *Wear* 266, no. 7-8: 704-712, 2009.

[89] Liu, B., J. S. Wang, Y. Liu*, et al.* "Microstructure and mechanical properties of equimolar fecocrni high entropy alloy prepared via powder extrusion."Review of. *Intermetallics* 75: 25-30, 2016.

[90] Lee, I., H. Park, J. Kim*, et al.* "Correlation of microstructure with tribological properties in atmospheric plasma sprayed mo-added ferrous coating."Review of. *Surf Coat Tech* 307: 908-914, 2016.

[91] Quinn, T. F. J. "Review of oxidational wear .1. The origins of oxidational wear."Review of. *Tribol Int* 16, no. 5: 257-271, 1983.

[92] Pourmousa, A., J. Mostaghimi, A. Abedini*, et al.* "Particle size distribution in a wire-arc spraying system."Review of. *J Therm Spray Techn* 14, no. 4: 502-510, 2005.

[93] "Astm standard e2109-01, 2000 (2014), "standard test methods for determining area percentage porosity in thermal sprayed coatings"." ASTM International, West Conshohocken, PA, 2014, DOI: 10.1520/E2109-01R14.

[94] Tosha, K. "Influence of residual stresses on the hardness number in the affected layer produced by shot peening." Paper presented at the Proceedings of the Second Asia-Pacific Forum on Precision Surface Finishing and Deburring Technology, Seoul, Korea, July, 2002.

[95] Lu, Z. K., Y. H. Feng, G. J. Peng*, et al.* "Estimation of surface equi-biaxial residual stress by using instrumented sharp indentation."Review of. *Mat Sci Eng a-Struct* 614: 264-272, 2014.

[96] ASTM. "Standard test method for flexural properties of unreinforced and reinforced plastics and electrical insulating materials by four-point bending. D6272." Paper presented at the ASTM, 2002.

[97] Mao, L., M. Cai, and G. Wang. "Effect of rotation speed on the abrasive–erosive–corrosive wear of steel pipes against steel casings used in drilling for petroleum."Review of. *Wear* 410: 1-10, 2018.

[98] International, A. "Astm g65-16e1 standard test method for measuring abrasion using the dry sand/rubber wheel apparatus." West Conshohocken, PA, 2016.

[99] Rost, C. M., E. Sachet, T. Borman*, et al.* "Entropy-stabilized oxides."Review of. *Nat Commun* 6, 2015.

[100] Hume-Rothery, W. "The structure of metals and alloys."Review of. *Indian Journal of Physics* 11: 74-74, 1969.

[101] Hume-Rothery, W. "Atomic theory for students of metallurgy."Review of., 1952.

[102] Guo, S., C. Ng, J. Lu*, et al.* "Effect of valence electron concentration on stability of fcc or bcc phase in high entropy alloys."Review of. *J Appl Phys* 109, no. 10: 103505, 2011.

[103] Winter, M. "Webelements: The periodic table on the www, vol. 2015."Review of. *The University of Sheffield and WebElements Ltd, UK*, 2015.

[104] "Astm a751-11, standard test methods, practices, and terminology for chemical analysis of steel products, astm international, west conshohocken, pa, 2011."

[105] Steffens, H. D., and K. Nassenstein. "Influence of the spray velocity on arc-sprayed coating structures."Review of. *J Therm Spray Techn* 8, no. 3: 454-460, 1999.

[106] Lamkin, M., F. Riley, and R. Fordham. "Oxygen mobility in silicon dioxide and silicate glasses: A review."Review of. *J Eur Ceram Soc* 10, no. 5: 347-367, 1992.

[107] Ansell, S., S. Krishnan, J. K. R. Weber*, et al.* "Structure of liquid aluminum oxide."Review of. *Phys Rev Lett* 78, no. 3: 464-466, 1997.

[108] Chen, Y. X., X. B. Liang, Y. Liu*, et al.* "Effect of heat treatment on microstructure and residual stress of wire arc sprayed high carbon steel coating."Review of. *Surf Eng* 26, no. 6: 407-412, 2010.

[109] Swartzendruber, L., V. Itkin, and C. Alcock. "The fe-ni (iron-nickel) system."Review of. *J Phase Equilib* 12, no. 3: 288-312, 1991.

[110] Lee, B. J., and D. N. Lee. "A thermodynamic study on the fe-v-c system."Review of. *Calphad* 15, no. 3: 293-306, 1991.

[111] Prescott, R., and M. J. Graham. "The formation of aluminum-oxide scales on high-temperature alloys."Review of. *Oxid Met* 38, no. 3-4: 233-254, 1992.

[112] Barbezat, G., A. R. Nicoll, and A. Sickinger. "Abrasion, erosion and scuffing resistance of carbide and oxide ceramic thermal sprayed coatings for different applications."Review of. *Wear* 162: 529-537, 1993.

[113] DeHoff, R. *Thermodynamics in materials science*. Second Edition ed.: CRC Press, 2006.

[114] Vander Voort, G. F. *Atlas of time-temperature diagrams for irons and steels*. ASM international, 1991.

[115] Yang, H. S., and H. K. D. H. Bhadeshia. "Austenite grain size and the martensite-start temperature."Review of. *Scripta Mater* 60, no. 7: 493-495, 2009.

[116] Nikravesh, M., M. Naderi, and G. H. Akbari. "Influence of hot plastic deformation and cooling rate on martensite and bainite start temperatures in 22mnb5 steel."Review of. *Mat Sci Eng a-Struct* 540: 24-29, 2012.

[117] Grange, R., C. Hribal, and L. Porter. "Hardness of tempered martensite in carbon and low-alloy steels."Review of. *Metallurgical Transactions A* 8, no. 11: 1775-1785, 1977.

[118] Tillmann, W., and J. Nebel. "Analysis of the mechanical properties of an arc sprayed wc-fecsimn coating: Compression, bending, and tension behavior."Review of. *J Therm Spray Techn* 20, no. 1-2: 317-327, 2011.

[119] Kovarik, O., J. Siegl, and Z. Prochazka. "Fatigue behavior of bodies with thermally sprayed metallic and ceramic deposits."Review of. *J Therm Spray Techn* 17, no. 4: 525-532, 2008.

[120] Becker, W., and S. Lampman. "Fracture appearance and mechanisms of deformation and fracture."Review of. *Materials Park, OH: ASM International, 2002.*: 559-586, 2002.

[121] Pantelis, D. I., P. Psyllaki, and N. Alexopoulos. "Tribological behaviour of plasma-sprayed al2o3 coatings under severe wear conditions."Review of. *Wear* 237, no. 2: 197-204, 2000.

[122] Mates, S. P., and G. S. Settles. "A study of liquid metal atomization using close-coupled nozzles, part 1: Gas dynamic behavior."Review of. *Atomization Spray* 15, no. 1, 2005.

[123] Steffens, H. "Haftung und schichtaufbau beim lichtbogen-und flammspritzen (adhesion and layer structure for arc and flame spraying)." Ph. D. Thesis, Technischen Hochschule Hannover, 1966.

[124] Tillmann, W., and M. Abdulgader. "Wire composition: Its effect on metal disintegration and particle formation in twin-wire arc-spraying process."Review of. *J Therm Spray Techn* 22, no. 2-3: 352-362, 2013.

[125] Jandin, G., H. Liao, Z. Q. Feng*, et al.* "Correlations between operating conditions, microstructure and mechanical properties of twin wire arc sprayed steel coatings."Review of. *Mat Sci Eng a-Struct* 349, no. 1-2: 298-305, 2003.

[126] Li, S., Q. S. Wei, Y. S. Shi*, et al.* "Microstructure characteristics of inconel 625 superalloy manufactured by selective laser melting."Review of. *J Mater Sci Technol* 31, no. 9: 946-952, 2015.

[127] Raynor, G. V., and V. G. Rivlin. "Phase equilibria in iron ternary alloys--a critical assessment of the experimental literature."Review of. *The Institute of Metals, 1 Carlton House Terrace, London SW 1 Y 5 DB, UK, 1988.*, 1988.

[128] Wang, J., Y. Wang, J. Liu, *et al.* "Microstructure and flight behaviors of droplet and its solidification in twin-wire arc sprayed ni-al composite coatings."Review of. *Materials Research*, no. AHEAD: 0-0, 2018.

[129] Lee, K.-y., S.-h. Lee, Y. Kim, *et al.* "The effects of additive elements on the sliding wear behavior of fe-base hardfacing alloys."Review of. *Wear* 255, no. 1-6: 481-488, 2003.

[130] Liu, Z., J. Cabrero, S. Niang, *et al.* "Improving corrosion and wear performance of hvof-sprayed inconel 625 and wc-inconel 625 coatings by high power diode laser treatments."Review of. *Surf Coat Tech* 201, no. 16-17: 7149-7158, 2007.

[131] Moreau, C., P. Gougeon, A. Burgess, *et al.* "Thermal spray science and technology."Review of. *ASM International*, 1995.

[132] Fincke, J., D. Haggard, and W. Swank. "Particle temperature measurement in the thermal spray process."Review of. *J Therm Spray Techn* 10, no. 2: 255-266, 2001.

[133] Testing, A. S. f., and Materials. "Standard test method for adhesion or cohesion strength of thermal spray coatings." 2001.

[134] Kaneko, K., and K. Higaki. "Delamination strength evaluation of thermal sprayed coating by torsion pin-test method."Review of. *Solid Mechanics and Materials* 5, no. 12: p 1042-1050, 2011.

[135] Inoue, Y., T. Ono, A. Noutomi, *et al.* "Evaluation method of interfacial strength of plasma spray coating by tensile pin test."Review of. *Japan Welding Society* 9, no. 1: p. 167-173, 1991.

[136] Clyne, T. W., and S. C. Gill. "Residual stresses in thermal spray coatings and their effect on interfacial adhesion: A review of recent work."Review of. *J Therm Spray Techn* 5, no. 4: 401-418, 1996.

[137] Ang, A. S. M., and C. C. Berndt. "A review of testing methods for thermal spray coatings."Review of. *Int Mater Rev* 59, no. 4: 179-223, 2014.

[138] Withers, P. J., and H. K. D. H. Bhadeshia. "Overview - residual stress part 1 - measurement techniques."Review of. *Mater Sci Tech-Lond* 17, no. 4: 355-365, 2001.

[139] Marot, G., P. Demarecaux, J. Lesage, *et al.* "The interfacial indentation test to determine adhesion and residual stresses in nicrvps coatings."Review of. *Surf Coat Tech* 202, no. 18: 4411-4416, 2008.

[140] ASTM, S. "Standard test method for determining residual stresses by the hole-drilling strain-gage method."Review of. *Book of Standards*, 2008.

[141] Valente, T., C. Bartuli, M. Sebastiani, *et al.* "Implementation and development of the incremental hole drilling method for the measurement of residual stress in thermal spray coatings."Review of. *J Therm Spray Techn* 14, no. 4: 462-470, 2005.